CORA Cork Open Research Archive
Cartlann Taighde Oscailte Chorcaí

Title	Area selective atomic layer deposition of Si-based materials
Authors	Filatova, Ekaterina A.
Publication date	2019
Original Citation	Filatova, E. 2019. Area selective atomic layer deposition of Si-based materials. PhD Thesis, University College Cork.
Type of publication	Doctoral thesis
Rights	© 2019, Ekaterina Filatova. - http://creativecommons.org/licenses/by-nc-nd/3.0/
Download date	2026-11-15 18:45:03
Item downloaded from	https://hdl.handle.net/10468/8091

UCC
University College Cork, Ireland
Coláiste na hOllscoile Corcaigh

Area selective atomic layer deposition of Si-based materials

Ekaterina Filatova
MSc

Thesis submitted for the degree of Doctor of Philosophy



NATIONAL UNIVERSITY OF IRELAND, CORK

TYNDALL NATIONAL INSTITUTE

March 2019

Supervisors: Dr. Simon D. Elliott,
Dr. Michael Nolan

Research supported by Lam Research Corporation under supervision of Dr. Dennis Hausmann

Contents

List of Figures iv
List of Tables x
Acknowledgements xv
Abbreviations xvi
List of publications xviii
Conferences and schools attended xix
Abstract xxii

1 Background, motivation and goals **1**
1.1 Overview of thin film deposition techniques 3
1.1.1 Physical vapor deposition (PVD) 3
1.1.2 Chemical vapor deposition (CVD) 4
1.1.3 Atomic layer deposition (ALD) 4
1.2 Area-selective ALD 8
1.3 Routes towards new ALD processes. Theoretical modelling . . . 10
1.4 Goals of this study 10

2 Current ALD processes for Si-based materials **12**
2.1 Motivation: applications of Si-based materials in semiconductor industry 12
2.2 Introduction to surface reaction mechanism during ALD 14
2.3 Silane precursors 15
2.4 Chlorosilane precursors 16
2.5 Alkoxide precursors 23
2.6 Aminosilane precursors 24
2.7 Silylamine precursors 28
2.8 Summary 30

3 Methodologies **32**
3.1 Challenges for modelling ALD processes 32
3.2 Theoretical modelling to describe ALD chemistry 34
3.3 Approaches for ALD modelling 35
3.3.1 Precursor screening 35
3.3.2 Adsorption of a precursor 36
3.3.2.1 Constructing surface model 37
3.3.3 Calculating activation energies 38
3.3.4 Nudged Elastic Band (NEB) approach 39
3.4 Density Functional Theory (DFT) 40
3.5 Simulations packages: TURBOMOLE and VASP 44
3.6 A practitioner's guide for DFT calculations 45
3.6.1 Choosing basis sets 45
3.6.2 Describing core and valence electrons: Pseudopotentials 46
3.6.3 Choosing approximation for exchange-correlation term . 47

4 Investigating the difference in nucleation during Si-based ALD on

different Si-based (Si, SiC, SiO_2, Si_3N_4) surfaces for area-selective deposition **49**
4.1 Introduction . . . 49
4.2 Methodology . . . 51
4.2.1 DFT modelling . . . 51
4.2.2 Experimental details . . . 54
4.2.3 Substrate preparation . . . 54
4.2.4 Material analysis . . . 55
4.3 Results . . . 55
4.3.1 DFT results on precursor adsorption . . . 55
4.3.2 Spectroscopic ellipsometry (SE) results on precursor adsorption . . . 60
4.3.3 Discussions . . . 62
4.3.4 Conclusion . . . 65

5 SiC precursor screening **67**
5.1 Abstract . . . 67
5.2 Introduction . . . 67
5.3 Methodology . . . 69
5.4 Results and discussion . . . 75
5.4.1 Model validation at CVD conditions, T=1000°C . . . 75
5.4.2 Precursor screening at ALD conditions, T=400°C . . . 77
5.5 Conclusion . . . 79

6 SiC PECVD **80**
6.1 Abstract . . . 80
6.2 Introduction . . . 80
6.3 Methodology . . . 82
6.4 Results . . . 85
6.4.1 Adsorption of the precursors on H-terminated and bare SiC surface . . . 86
6.4.2 Energy barriers of SiH_3 and SiH_2 reacting with H-SiC surface . . . 90
6.5 Discussion . . . 97
6.6 Conclusion . . . 100

7 DFT screening for ligand exchange mechanism for area-selective deposition **102**
7.1 Proposed strategy for achieving a non-growth area during thermal ALD via ligand-exchange mechanism . . . 103
7.2 Methodology . . . 104
7.3 Results . . . 107
7.3.1 ALD water pulse: hydrolysis . . . 108
7.3.2 ALD precursor pulse: ligand-exchange mechanism . . . 110
7.4 Discussions . . . 114
7.4.1 Bond dissociation energies (BDE) . . . 114
7.4.2 Temperature and entropy effects . . . 115

7.4.3 Experimental corroboration of the DFT results 116
7.5 Conclusion 116

8 Conclusions **119**
8.1 Summary 119
8.2 Future work 121

A Analysed reactions and calculated energies for SiC ALD **123**

B Optimized structures and adsorption energies of various Si and C precursors for SiC ALD **132**

List of Figures

1.1 Illustration of wafer and chip. The size of the wafer from 100-450 mm. 2
1.2 A schematic representation of ALD deposition cycle 5
1.3 A schematic representation of plasma-enhanced ALD (PEALD) deposition cycle 7
1.4 A schematic representation of the patterning step in microchip fabrication. (a) Conventional patterning; ALD-enabled patterning by (b) area-activation and (c) area-deactivation. 8

2.1 Examples of applications of ALD in semiconductor manufacturing. Source Lam Research Company. 13
2.2 SiO_2 ALD mechanism during $SiCl_4$ pulse. $SiCl_4$ precursor physisorbs on OH-terminated SiO_2 via H-bonding followed by direct substitution, *i.e.* concurrent cleavage of Si-Cl and O-H and formation of Si-O and H-Cl via a four-membered-ring transition state(TS) with pentacoordinate Si 18
2.3 ALD mechanism during H_2O pulse. H_2O physisorbs on surface Si-Cl via H-bonding followed by direct substitution, *i.e.* concurrent cleavage of Si-Cl and O-H and formation of Si-O and H-Cl via a four-membered ring transition state (TS). 19
2.4 Surface reaction mechanism during PEALD of SiN_x using SiH_2Cl_2 and NH_3 plasma. The TS is structure 3. Adapted with permission from [1]. Copyright 2018 American Chemical Society. 20
2.5 Chemical mechanism of SiO_2 ALD catalyzed by amine base during the (a), (b) $SiCl_4$ pulse and (c), (d) water pulse. H-bonding of a nucleophile ("Nu") such as an amine to surface OH or water increases the reactivity of oxygen in that group towards Si, facilitating chemisorption of (a) chlorosilane or (c) water, both via pentacoordinate Si in a 4-membered ring. Nucleophile with H (Nu-H) allows formation of a more stable 6-membered ring in (b) and (d). 22

3.1 Multiple scales and the nature of ALD processes models needed. 33
3.2 Silicon carbide bulk unit cell. Colour schemes: yellow=silicon, grey=carbon. 37
3.3 Different surfaces models. (a) slab silicon carbide cell, (b) cluster silicon nitride model with H groups on the surface. Colour schemes: yellow=silicon, grey=carbon, blue=nitrogen, white=hydrogen. 38
3.4 A schematic representation of the pseudopotential approximation for a silicon atom. The area in yellow is the ionic core that includes core electrons. The pseudopotential is the potential that is felt by the valence electrons interacting with the core. 47

4.1 Optimised precursor structures. (a) di(isopropylamino)silane (DIPAS), (b) di(sec-butylamino)silane (DSBAS), (c) bis(diethylamino)-silane (BDEAS), (d) tetrachlorosilane ($SiCl_4$), (e) tetrabromosilane ($SiBr_4$). Color scheme: yellow=silicon, green=chlorine, white=hydrogen, grey=carbon, blue=nitrogen, brown=bromine. 52
4.2 Optimised surface slabs (side view). (a) H-terminated Si (Si:H), (b) H-terminated SiC (SiC:H), (c) OH-terminated SiO_2 (SiO_2:OH) and (d) NH/NH_2-terminated Si_3N_4 (Si_3N_4:NH/NH_2) surfaces. Color scheme: yellow=silicon, white=hydrogen, grey=carbon, blue=nitrogen, red=oxygen. 52
4.3 Optimised structrures after precursors a) DIPAS/DSBAS b) BDEAS c) $SiCl_4$ d) $SiBr_4$ reacted with terminated Si:H, SiC:H, SiO_2:OH, Si_3N_4:NH/NH_2 surfaces (side view) and the ligands were eliminated. Color scheme: yellow=silicon, green=chlorine, white=hydrogen, grey=carbon, dark blue=nitrogen, brown=bromine, red=oxygen. 58
4.4 ΔE for aminosilane precursors reacting with Si:H, SiC:H, SiO_2:OH and Si_3N_4:NH/NH_2. ΔE values and chemical reactions are presented in Table 4.2. 59
4.5 ΔE for halide precursors reacting with Si:H, SiC:H, SiO_2:OH and Si_3N_4:NH/NH_2. ΔE values and chemical reactions are presented in Table 4.2. 60
4.6 SiN_x film thickness as a function of ALD cycle using DSBAS precursor and N_2 plasma as a co-reagent on SiO_2:OH (Si wafer with native oxide), Si:H (HF-last Si) and SiC:H (H_2 plasma treated SiC wafer) surfaces. The graph shows the thickness as a function of the number of the cycles measures by *in-situ* spectroscopic ellipsometry (SE). 61
4.7 Apparent thickness as measured after every DSBAS and N_2 half-cycles during PEALD of SiN_x at 150 °C. 62

5.1 Optimized structures for the possible precursors for ALD of SiC performed in TURBOMOLE. (a) methane (CH_4), (b) ethane (C_2H_6), (c) propane (C_3H_8), (d) n-butane (C_4H_{10}), (e) n-hexane (C_6H_{14}), (f) ethylene (C_2H_4), (g) propene (C_3H_6), (h) -2-butene (C_4H_8), (i) ethyne (C_2H_2), (j) propyne (C_3H_4), (k) carbontetrachloride (CCl_4), (l) iodomethane (CH_3I), (m) trichloromethane ($CHCl_3$), (n) chloromethane (CH_3Cl), (o) disilane (Si_2H_6), (p) silane (SiH_4), (q) monochlorosilane (SiH_3Cl), (r) dichlorosilane SiH_2Cl_2 (DCS), (s) trichlorosilane $SiHCl_3$ (TCS), (t) hexachlorodisilane (Si_2Cl_6), (u) tetrachlorosilane $SiCl_4$ (TET), (v) tetrafluorosilane (SiF_4), (w) dichlorosilacyclobutane ($SiCl_2(CH_2)_3$), (x) dimethyldichlorosilane ($Si(CH_3)_2Cl_2$), (y) bis(trichlorosilyl)methane ($(SiCl_3)_2CH_2$), (z) methylsilane (CH_3–SiH_3), (aa) 1,3-disilabutane(SiH_3–CH_2-SiH_2–CH_3), (bb) silacyclobutane ($SiH_2(CH_2)_3$), (cc) tetraethylorthosilicate $Si(OEt)_4$ (TEOS), (dd) diisopropylaminosilane $SiH_3N(iPr)_2$ (DIPAS), (ee) bis(diethylamino)silane $H_2Si[N(Et)_2]_2$ (BDEAS), (ff) methyltrichlorosilane $SiCH_3Cl_3$ (MTS). (Et) - ethyl group –CH_2–CH_3, (iPr) - iso-propyl group –$CH(CH_3)_2$. 73

5.2 Hess cycle representing screening approach for calculating ΔE using gas-phase cluster software (in our case TURBOMOLE) and periodic software (in our case VASP) with tetramethylsilane ($Si(CH_3)_4$) as a reference molecule for SiC. ΔE_3 is the desired energy, which is used to calculate Gibbs energy in eq. 5.3. . . . 74

5.3 Gibbs energies ΔG for reactions of various Si and C precursors at CVD temperatures (a) 1000°C and (b) 400°C. The most favourable reactions are those with the most negative ΔG (cells coloured in green). The least favourable reactions have the most positive ΔG (cells coloured in red). 76

5.4 Gibbs energies ΔG for decomposition reactions of single-source precursors containing both Si and C at CVD temperature 1000°C and at ALD temperature 400°C. The most favourable reactions are with the most negative ΔG (cells coloured in green). The least favourable reaction is with the positive ΔG (cells coloured in red). (Et) - ethyl group –CH_2–CH_3, (iPr) - iso-propyl group –$CH(CH_3)_2$. 78

6.1 Optimized structures. (a) silicon tetrachloride ($SiCl_4$), (b) disilane (Si_2H_6), (c) silane (SiH_4), (d) trichloromethane ($CHCl_3$), (e) ethyne (C_2H_2), (f) silyl (SiH_3), (g) propyne (C_3H_4), (h) carbon tetrachloride (CCl_4), (i) silylene (SiH_2), (j) bare silicon carbide (0 1 1) slab, (k) H- terminated silicon carbide (0 1 1) slab (side view). 83

6.2 Top (left column) and side (right column) view of the most thermodynamically favorable structures of the silicon precursors adsorbed on the bare silicon carbide surface. (a),(b) - tetrachlorosilane, (c),(d) - disilane, (e),(f) - silane. Color scheme: yellow=silicon, green=chlorine, white=hydrogen, grey=carbon 87

6.3 Top (left column) and side (right column) view of optimized the most favorable thermodynamically structures of the carbon precursors adsorbed on the bare silicon carbide surface. (a),(b) - trichloromethane, (c),(d) - propyne, (e),(f) - ethyne, (g),(h) - carbontetrachloride. Color scheme: yellow=silicon, green=chlorine, white=hydrogen, grey=carbon 89

6.4 Reaction pathway of SiH_3 stripping H from (a) C-H bond, (b) Si-H of the H-SiC 3C (0 1 1) surface producing SiH_4. I = SiH_3 is at infinity far from the surface, P=products, final configuration, SiH_4 produced; TS=transition state found using CI-NEB approach in VASP. R is similar to I and not shown. Small white spheres = hydrogen, large yellow spheres = silicon, small dark grey spheres = carbon. Red area = spin density at iso surface 0.008. 93

6.5 Reaction pathway of SiH_2 stripping H from (a) C-H bond, (b) Si-H of the H-SiC 3C (0 1 1) surface producing SiH_3 group on the surface. I = SiH_2 at infinity far from the surface, R = SiH_2 is at 2.74 Å from the Si of the surface, P = products, final configuration, SiH_3 produced; TS=transition state found using CI-NEB approach in VASP. Small white spheres = hydrogen, large yellow spheres = silicon, small dark grey spheres = carbon. Red area = spin density at isosurface 0.022. 94

6.6 Projected density of states (PDOS) (shifted for display purposes) on (a) Si and two H of molecule (c) H atom of Si-H bond of the surface obtained from VASP calculations. (b) Orbitals are plotted from TURBOMOLE calculations using SiH_4 model for the surface Si-H bond. (d) Geometric data for slabs: I = SiH_2 at infinity far from the surface, R = SiH_2 at 2.7 Å from the surface, TS = transition state, P = products, SiH_3 produced; Small light spheres = hydrogen, small dark spheres = carbon, large spheres = silicon. Iso surface plot at value 0.086. 96

7.1 A schematic of a full area-selective ALD cycle where non-growth area is achieved through ligand-exchange mechanism. Requirements to get the non-growth area are: 1) precursor exchanges its ligand with the surface termination group during precursor half-cycle ($\Delta E_{ex} < 0$), 2) transferred ligand remains on the surface after water half-cycle ($\Delta E_{hyd} > 0$). 103

7.2 Ligand exchange gas-phase model on the example of a) $HfCp(dma)_3$ (Air Liquide HyALD^{TM}) and b) TTiP ($Ti(O^iPr)_4$) precursor exposure step. OH-terminated Si surface is represented by a) $SiOH(dma)_3$ and b) $Si(OH)_4$ cluster models. Color scheme: white=hydrogen, grey=carbon, light blue=titanium, light blue=hafnium, yellow=silicon, red=oxygen, dark blue=nitrogen. Cp - cyclopentadienyl complex (C_5H_5), (^iPr) - iso-propyl group $–CH(CH_3)_2$, (dma) - dimethylamino group $–N(CH_3)_2$. 106
7.3 Hydrolysis gas-phase model on the example of a) HyALD and b) TTiP ALD water pulses. Si surface with Cp^- and O^iPr surface groups is represented by a) $SiCp(dma)_3$ and b) $Si(O^iPr)_4$ cluster models. Color scheme: white=hydrogen, grey=carbon, yellow=silicon, red=oxygen, dark blue=nitrogen. 107
7.4 ΔE of hydrolysis reaction during the water pulse. Surface with Cp^- or O^iPr groups after the successful ligand-exchange process during the precursor pulse are represented by molecules $m_1Cp(dma)_{x-1}$ and $m_1(O^iPr)_x$, respectively. m_2=Hf, Si, Ge, Ti, W, Co, Cu, Ru, Ta. x=4 for Hf, Si, Ge, Ti, W, x= 2 for Co, Cu, Ru and x=1 for Ta. ΔE_{hyd} values are shown in Table 7.2. 110
7.5 ΔE of precursor $m_1Cp(dma)_{x-1}$ exchanging a Cp^- ligand with surface OH group. Surface is represented by a molecule $m_2(OH)(dma)_{x-1}$. $m_{1,2}$=Hf, Si, Ge, Ti, W, Co, Cu, Ru, Ta, x=4 for Hf, Si, Ge, Ti, W, x= 2 for Co, Cu, Ru and x=1 for Ta. Example: $HfCp(dma)_3$ precursor reacting with OH-terminated Si surface, $HfCp(dma)_3$ + $(OH)Si(dma)_3$(surface) $\longrightarrow$ $(OH)Hf(dma)_3$ + $SiCp(dma)_3$(surface with Cp^- ligand), ΔE_{ex}=0.97 eV, i.e. Cp ligand transfer is not thermodynamically favorable from Hf to Si. 112
7.6 ΔE_{ex} of precursor $m_1(O^iPr)_x$ exchanging one O^iPr ligand with surface OH group. Surface is represented by a molecule $m_2(OH)_x$. $m_{1,2}$=Hf, Si, Ge, Ti, W, Co, Cu, Ru, Ta, x=4 for Hf, Si, Ge, Ti, W, x= 2 for Co, Cu, Ru and x=1 for Ta. Example: $TTiP(Ti(O^iPr)_4)$ precursor reacting with OH-terminated Si surface, $Ti(O^iPr)_4$ + $Si(OH)_4$(surface) $\longrightarrow$ $Hf(OH)_4$ + $Si(O^iPr)_4$(surface with O^iPr ligands), ΔE_{ex}=0.19 eV, i.e. O^iPr ligand transfer is not thermodynamically favorable from Ti to Si. 113
7.7 ALD growth of m_1O_y using $m_1Cp(dma)_{x-1}$ precursor and water is predicted to have a nucleation delay at o K on the surfaces marked as "x" (green color). "-" means that the requirements for non-growth surface considered in this chapter were not met. . . 117
7.8 ALD growth of m_1O_y using $m_1(O^iPr)_x$ precursor and water is predicted to have a nucleation delay at 0 K on the surfaces marked as "x" (green color). "-" means that the requirements for non-growth surface considered in this chapter were not met. 117

B.1 Optimized structure of $SiCl_4$ adsorbing on the bare SiC surface. Left column - top view, right column - side view. Calculated adsorption energies are presented in table B.1. 133
B.2 Optimized structure of Si_2H_6 adsorbing on the bare SiC surface. Left column - top view, right column - side view. Calculated adsorption energies are presented in table B.2. 134
B.3 Optimized structure of SiH_4 adsorbing on the bare SiC surface. Left column - top view, right column - side view. Calculated adsorption energies are presented in table B.3. 135
B.4 Optimized structure of $CHCl_3$ adsorbing on the bare SiC surface. Left column - top view, right column - side view. Calculated adsorption energies are presented in table B.4. 136
B.5 Optimized structure of C_3H_4 adsorbing on the bare SiC surface. Left column - top view, right column - side view. Calculated adsorption energies are presented in table B.5. 137
B.6 Optimized structure of C_2H_2 adsorbing on the bare SiC surface. Left column - top view, right column - side view. Calculated adsorption energies are presented in table B.6. 138
B.7 Optimized structure of CCl_4 adsorbing on the bare SiC surface. Left column - top view, right column - side view. Calculated adsorption energies are presented in table B.7. 139

List of Tables

2.1 Known SiO_2 and SiN_x ALD processes using silane precursors. GPC=growth per cycle. 15
2.2 Known SiC epitaxial growth processes (pulsed CVD) using silane precursors. GPC=growth per cycle. 16
2.3 Known SiC, SiO_2 and SiN_x ALD processes using chlorosilane precursors. GPC=growth per cycle. "-" =GPC is not reported. "Cat."=catalyst. 17
2.4 Known SiC, SiO_2 and SiN_x ALD processes using alkoxide precursors. GPC=growth per cycle, "cat."=catalyst, TEOS=tetraethoxysilane, Et= 24
2.5 Known ALD processes from aminosilanes. GPC=growth per cycle. BTBAS=bis(tert-butylamino)silane, 3DMAS=tris[dimethylamino]-silane, DSBAS=di(sec-butyl)aminosilane, BDEAS=bis(diethylamino)-silane, TEAS=tetrakis(ethylamino)silane, TIPAS=tris(isopropyl)-aminosilane, DIPAS=di(isopropylamino)silane, CSN-2=1,3-di-isopropylamino-2,4-dimethylcyclosilazane, BEMAS=bis(ethylmethyl-amino)silane, TDMAS= tris(dimethylamino)silane, BDMAS=bis(di-methylamino)silane, pl.ex.H_2O=plasma-excited water vapor. . 25
2.6 Known ALD processes of Si-based materials using silylamine precursors. GPC=growth per cycle. $DTDN_2$–H_2=bis(dimethylamino-methylsilyl)(trimethylsilyl)amine ($C_9H_{29}N_3Si_3$). "-" = GPC not reported 29

4.1 PEALD SiN_x process conditions using DSBAS and N_2 plasma . . 55
4.2 Chemical reactions and adsorption energies of aminosilane (DIPAS, DSBAS, BDEAS) and halide ($SiCl_4$, $SiBr_4$) precursors reacting with H-terminated Si (Si:H), H-terminated SiC (SiC:H), OH-terminated SiO_2 (SiO_2:OH) and NH/NH_2-terminated Si_3N_4 (Si_3N_4:NH/NH_2) surfaces. Optimised precursor and surfaces structures are shown in Figure 4.1 and Figure 4.2, respectively. ^{i}Pr is for iso-propyl group, sBu is for sec-butyl group, Et is for ethyl group, index "S" is for the surface atoms. 57

6.1 Adsorption energies of silicon and carbon precursors on the bare silicon carbide surface. Optimized structures are shown in Figures 6.2 and 6.3. 86
6.2 Bond length of the SiH_3 and SiH_2 fragments and Si-H/C-H bonds of the surface involved in adsorption. Index "F" is for Si/C fragment atoms and index "S" is for the surface atoms. I= fragment at infinity from the surface, R= initial configuration, TS=transition state, P=final configuration as described in Figures 6.4, 6.5. 91

6.3 Magnetic moments of the systems SiH_3 and SiH_2 approaching Si-H/C-H bonds of the surface involved in adsorption. I = fragment is at infinity from the surface, R= initial configuration, TS=transition state, P=final configuration as described in Figures 6.4, 6.5. 92
6.4 Summary of activation (ΔE_{act}) and adsorption (ΔE_{ads}) energies for SiH_3, SiH_2, CH_3 and CH_2 plasma fragments reacting with C-H and Si-H bonds of the H-SiC 3C (0 1 1) surface."-" means energies were not calculated. Index "S" is for the surface atoms. "DB" - surface dangling bond. 95

7.1 Bond lengths of the optimized precursor ($m_1Cp(dma)_{x-1}$, $m_1(O^iPr)_x$) and surface models with Cp and O^iPr groups (m_2 $Cp(dma)_{x-1}$, $m_2(O^iPr)_x$) 108
7.2 ΔE_{hyd} of hydrolysis reaction during the ALD water pulse computed using eq. 7.2a and 7.2b. Surface with Cp^- or O^iPr groups after the successful ligand-exchange process during the precursor pulse are represented by molecules $m_2Cp(dma)_{x-1}$ and $m_2(O^iPr)_x$, respectively. m_2=Hf, Si, Ge, Ti, W, Co, Cu, Ru, Ta (x=4 for Hf, Si, Ge, Ti, W, x= 2 for Co, Cu, Ru and x=1 for Ta). 109
7.3 m_1/m_2-Cp and m_1/m_2-O bond experimental bond dissociation energy (BDE) measured at T=298 K and 1 atm pressure. "-" BDE was not found. 114

A.1 List of the analysed reactions and calculated energies (chapter 5, eq. 5.3) at T=1000°C 123
A.1 List of the analysed reactions and calculated energies (chapter 5, eq. 5.3) at T=1000°C 124
A.1 List of the analysed reactions and calculated energies (chapter 5, eq. 5.3) at T=1000°C 125
A.1 List of the analysed reactions and calculated energies (chapter 5, eq. 5.3) at T=1000°C 126
A.1 List of the analysed reactions and calculated energies (chapter 5, eq. 5.3) at T=1000°C 127
A.2 List of the analysed reactions and calculated energies (chapter 5, eq. 5.3) at T=400°C 128
A.2 List of the analysed reactions and calculated energies (chapter 5, eq. 5.3) at T=400°C 129
A.2 List of the analysed reactions and calculated energies (chapter 5, eq. 5.3) at T=400°C 130
A.2 List of the analysed reactions and calculated energies (chapter 5, eq. 5.3) at T=400°C 131

B.1 Adsorption energies of $SiCl_4$ on the bare SiC surface. Optimized structures are presented in figure B.1. "(S)" for surface atoms. 133

B.2 Adsorption energies of Si_2H_6 on the bare SiC surface. Optimized structures are presented in figure B.2. "(S)" for surface atoms. 134
B.3 Adsorption energies of SiH_4 on the bare SiC surface. Optimized structures are presented in figure B.3. "(S)" for surface atoms. 135
B.4 Adsorption energies of $CHCl_3$ on the bare SiC surface. Optimized structures are presented in figure B.4. "(S)" for surface atoms. 136
B.5 Adsorption energies of C_3H_4 on the bare SiC surface. Optimized structures are presented in figure B.5. "(S)" for surface atoms. 137
B.6 Adsorption energies of C_2H_2 on the bare SiC surface. Optimized structures are presented in figure B.6. "(S)" for surface atoms. 138
B.7 Adsorption energies of CCl_4 on the bare SiC surface. Optimized structures are presented in figure B.7. "(S)" for surface atoms. 138

I, Ekaterina Filatova, certify that this thesis is my own work and has not been submitted for another degree at University College Cork or elsewhere.

_____

Ekaterina Filatova

To my parents Alexander and Ludmila

Acknowledgements

I would like to express my deepest gratitude to my supervisor Dr. Simon D. Elliott. His ideas, guidance and stress-free working environment enormously improved my thesis. I have been extremely lucky to have such a patient, understanding and supportive supervisor.

I am very grateful to my co-supervisor Dr. Dennis Hausmann from Lam Research Corporation for his constant guidance on this project and for giving me very fruitful industrial feedback on the project. I am also very grateful to my second supervisor Dr. Michael Nolan for helping me to carry on with my thesis. Thank you for his encouragements and suggestions during my thesis writing.

I am thankful to Lam Research Corporation for providing funding for this project and providing me an opportunity to gain industrial collaboration experience. Thank you to HERALD for providing funding for STSM collaboration in Eindhoven University of Technology. Thank you to the ICHEC and Tyndall National University cluster support teams for providing me computational resources and for their constant support with my calculations.

I thank the members of my PhD committee in Tyndall, Dr. Mary Manning and Dr. Joe O'Brien, for giving me valuable feedback during the review meetings. I am very grateful to all MMD group members, current and former, for their help and scientific discussions. Thank you to Hayrensa, Yasheng, Gangotri, Pedram, Alfonso, Hadi, Anna, Thomas, Merid, Glen, Conor, Christian, Suresh and many others for your help and your friendship.

My sincere acknowledgement to my collaborators in PMP group, Eindhoven University of Technology, Netherlands. I am particularly grateful to Prof. Adrie Mackus for his great contribution to the experimental part of my project. I am sincerely grateful to Dr. Alfredo Mameli for his great assistance in the experiment and further help and discussions on the project. I would also like to thank Prof. Fred Roozeboom and Dr. Tahsin Faraz for their insightful comments and suggestions on the experimental results.

Thanks to my mom Ludmila, my dad Alexander and my sister Nastya for all your love and support through all these years. Without you I would not be who I am today. I am very thankful to my husband Silviu for his encouragement, patience and constant support during my PhD writing. He made an enormous help to proof-read the text of my thesis countless number of times. I also would like to thank my great friend and colleague Ida for her support and motivation during our scientific coffee breaks.

I owe my deepest gratitude to Prof. Alexandre Reily Rocha, my Master's supervisor, for his inspiration and motivation during my Master's thesis and for encouraging me to pursue my PhD studies.

Abbreviations

Chemical formulas	
3DMAS	tris[dimethylamino]silane
$DTDN_2$–H_2	bis(dimethylaminomethylsilyl)(trimethylsilyl)amine
BDEAS	bis(diethylamino)silane
BDMAS	bis(dimethylamino)silane
BEMAS	bis(ethylmethylamino)silane
BTBAS	bis(tert-butylamino)silane
Cp	cyclopentadienyl
CSN-2	1,3-di-isopropylamino-2,4-dimethylcyclosilazane
DIPAS	di(isopropylamino)silane
dma	dimethylamino group
DSBAS	di(sec-butyl)aminosilane
Et	ethyl group
HyALD	tris(dimethylamido)cyclopentadienyl hafnium
^{i}Pr	iso-propyl group
MTS	methyltrichlorosilane
TCS	trichlorosilane
TDMAS	tris(dimethylamino)silane
TEAS	tetrakis(ethylamino)silane
TEOS	tetraethoxysilane
TET	tetrachlorosilane
TIPAS	tris(isopropyl)aminosilane
TTiP	titanium isopropoxide

ALD	atomic layer deposition
ALE	atomic layer epitaxy
APC	automated pressure controller
AS-ALD	area-selective atomic layer deposition
BDE	bond dissociation energy
Cat.	catalyst
CI-NEB	climbing image nudged elastic band
CVD	chemical vapor deposition
DB	dangling bond
DFT	density functional theory
FinFET	fin field-effect transistor
FTIR	Fourier transform infrared spectroscopy
GGA	generalized gradient approximation
GPC	growth per cycle
GTO	Gaussian-type orbital
HERALD	hooking together European research in atomic layer deposition
HOMO	highest occupied molecular orbital
HVM	high-volume manufactoring
IC	integrated circuit
ICHEC	Irish centre for high-end computing
ICP	inductively-coupled plasma source
LDA	local density approximation
LUMO	lowest occupied molecular orbital
MEP	minimum energy path
NEB	nudged elastic band
PAW	projector augmented wave
PBE	Perdew-Burke-Ernzerhof
PDOS	projected density of states
PEALD	plasma-enhanced atomic layer deposition
pl.ex.	plasma-excited
PVD	physical vapor deposition
PW91	Pedrew and Wang
RF	radio frequency
RI	resolution of identity
SAM	self-assembled monolayer
SCF	self-consistent field
SE	spectroscopic ellipsometry
STO	Slater-type orbital
STSM	short-term scientific mission
TS	transition state

List of publications

Peer-reviewed journal articles

- **Ekaterina A. Filatova, Dennis Hausmann, Simon D. Elliott**
  Understanding the Mechanism of SiC Plasma-Enhanced Chemical Vapor Deposition (PECVD) and Developing Routes toward SiC Atomic Layer Deposition (ALD) with Density Functional Theory
  ACS Applied Materials & Interfaces, 10, 15216 (2018)
- **Ekaterina A. Filatova, Dennis Hausmann, Simon D. Elliott**
  Investigating Routes Towards Atomic Layer Deposition of Silicon Carbide: Ab initio Screening of Potential Silicon and Carbon Precursors
  Journal of Vacuum of Science and Technology A, 35, 1-6 (2017)
- **Simon D. Elliott, Gangotri Dey, Yasheng Maimaiti, Hayrensa Ablat, Ekaterina A. Filatova, Glen N. Fomengia**
  Modeling Mechanism and Growth Reactions for New Nanofabrication Processes by Atomic Layer Deposition
  Advanced Materials, 28, 5367-5380 (2016)
  Contribution: Modeling the ALD of Silicon-Based Materials section
- **Rafaiel A. Ovanesyan, Ekaterina A. Filatova, Simon D. Elliott, David C. Smith, Dennis M. Hausmann, and Sumit Agarwal**
  Atomic Layer Deposition of Silicon-Based Dielectrics for Semiconductor Manufacturing: Current Status and Future Outlook
  Submitted to the Journal of Vacuum of Science and Technology A
  Contribution: Atomic Layer Deposition of SiO_2 section

Conferences and schools attended

Conference oral presentations

- **E. A. Filatova, A. Mameli, A. J. M. Mackus, F. Roozeboom, W.M.M. Kessels, D. Hausmann, S.D. Elliott**
  18th international conference on ALD, July 29-August 1, 2018, Incheon, South Korea
  Investigating the difference in nucleation during Si-based ALD on different surfaces (Si, SiC, SiO_2 and SiN_x) for future area-selective deposition

- **E. A. Filatova, A. Mameli, A. J. M. Mackus, F. Roozeboom, W.M.M. Kessels, D. Hausmann, S.D. Elliott**
  IEEE NANO 2018, July 23 – 26, 2018, Cork, Ireland
  Investigating the difference in nucleation during Si-based ALD on different surfaces for future area-selective deposition

- **Ekaterina A. Filatova, Simon D. Elliott, Dennis Hausmann**
  Atomic Layer Deposition: Russia - 2017 international workshop, September 25-28, 2017, St.Petersburg, Russia
  Ab initio modelling for understanding PECVD of silicon carbide and the routes towards ALD

- **Ekaterina A. Filatova, Simon D. Elliott, Dennis Hausmann**
  EuroCVD 21 – Baltic ALD 15 Conference, June 11-14, 2017, Linköping, Sweden
  Ab initio modelling for understanding PECVD of silicon carbide and the routes towards ALD

- **Ekaterina A. Filatova, Simon D. Elliott, Dennis Hausmann**
  Area Selective Deposition Workshop ASD17, April 20-21, 2017, Eindhoven, Netherlands
  Investigating the difference in nucleation of silicon-based materials Si, Si_3N_4, SiO_2 and C-doped SiO_2 during PECVD/PEALD for future selective area deposition (S-ALD)

- **Ekaterina A. Filatova, Simon D. Elliott**
  Tyndall Internal Conference, April 5, 2017, Cork, Ireland
  Putting atoms where we want them, 3 minutes pitch

- **Ekaterina A. Filatova, Simon D. Elliott, Dennis Hausmann**
  China ALD conference 2016, October 16 – 19, 2016, Suzhou, China
  Computational modelling of Atomic Layer Deposition of Silicon Carbide for future electronics

Conference posters

- **Ekaterina A. Filatova, Simon D. Elliott, Dennis Hausmann**
  Tyndall internal student poster competition, July 29, 2016, Cork, Ireland
- **Ekaterina A. Filatova, Simon D. Elliott, Dennis Hausmann**
  Irish Atomistic Simulators' Meeting (IASM) meeting, January 13-14, 2016, UCD, Dublin
- **Ekaterina A. Filatova, Simon D. Elliott, Dennis Hausmann**
  Paris International School on Advanced Computational Materials Science, August 28 – September 2, 2015, Campus Jussieu, Paris, France
- **Ekaterina A. Filatova, Simon D. Elliott, Dennis Hausmann**
  15^{th} international conference on ALD, July 1-2, 2015, Portland, US

Awards

- Best student presentation award
  EuroCVD 21 – Baltic ALD 15 Conference, June 11-14, 2017, Linköping, Sweden
- Tyndall internal student poster competition finalist
  Tyndall internal student poster competition, July 29, 2016, Cork, Ireland

Visits, Schools and Workshops

- Research collaboration
  August – October, 2017, Eindhoven University of Technology, Eindhoven Area, Netherlands
  SiNx plasma-enhanced atomic layer deposition (PEALD) growth and characterization (in-situ ellipsometry)
- School on effective research communications
  May 30 – June 02, 2016, DCU, Maynooth, RCSI, Dublin, Ireland
- ICHEC computational modelling school
  May 16 -20, 2016, ICHEC, Dublin, Ireland
- Research collaboration
  November 30 – December 25, 2015, St. Petersburg State Technological Institute, St. Petersburg, Russia
- Paris International School on Advanced Computational Materials Science
  August 28 – September 2, 2015, Campus Jussieu, Paris, France
- Lam Research process-engineer internship
  July – August, 2015, Tualatin, Oregon, US

Abstract

Modern electronics are very small and light yet extremely powerful. This is possible due to the constant integration of new techniques and novel materials into the electronics fabrication process. In the current project we are focusing on one of the most precise deposition fabrication techniques for microchip fabrication, called atomic layer deposition (ALD). In particular, we are interested in the applications of ALD for area-selective deposition, where the material is deposited only where it is needed allowing the lateral control of the grown film. We are using the quantum mechanical modelling, density functional theory (DFT) to investigate the chemical mechanism of the area-selective ALD processes for Si-based materials (SiC, SiO_2 and SiN_x), which are widely used in the semiconductor microchip fabrication process. We are also focusing on the possible SiC ALD mechanism in more detail, as this mechanism is very challenging and still not implemented in high-volume manufacturing in the semiconductor industry.

In order to investigate the possibility of area-selective deposition of Si-based materials on Si, SiC, SiO_2 and SiN_x substrates, the difference in adsorption energies of various aminosilane precursors was first analyzed by DFT. From DFT calculations we found that it is thermodynamically favorable for aminosilane precursors to react with SiN_x and SiO_2 substrates but not with SiC and Si. We further experimentally corroborate these results by depositing SiN_x on Si, SiO_2 and SiC substrates using di(sec-butylamino)silane precursor and N_2 plasma ALD and measuring the apparent SiN_x thickness by spectroscopic ellipsometry. Both DFT calculations and experiment show that the aminosilane precursor adsorbs selectively on SiO_2 not on Si and SiC substrates, however, after N_2 plasma pulse this selectivity is lost.

Further, we investigated the possibility of the ALD of SiC. First, we used DFT to screen various precursors in order to select the most favourable for SiC ALD. Then we expanded this study by analyzing how these precursors react with H-terminated and bare SiC surfaces. We predicted that precursors disilane (Si_2H_6), silane (SiH_4) or monochlorosilane (SiH_3Cl) with ethyne (C_2H_2), carbontetrachloride (CCl_4) or trichloromethane ($CHCl_3$) are the most promising for ALD of SiC. All of these precursors are predicted to react thermodynamically with bare SiC but not with the passivated surface. An additional activation step would be needed to sustain an ALD process. In order to analyze how silane plasma fragments will react with the passivated surface, the reaction pathways

of neutral silane plasma fragments SiH_3 and SiH_2 with the H-terminated surface were analyzed. Counterintuitively, it was found that silane plasma fragments SiH_3 and SiH_2 react selectivity with the Si-H bond rather than with the C-H bond of the H-terminated SiC surface.

Lastly, as a part of collaboration with Prof. Adrie Mackus from Plasma Materials Process group in Eindhoven Technological University, Netherlands, we used a DFT screening approach to determine the non-growth surface during ALD of transition metal oxides via a ligand-exchange mechanism in the precursor pulse. Two different precursors reacting with various OH-terminated metal surfaces were compared: a heteroleptic amidometallocene and a homoleptic alkoxide. A sample result is that HfO_2, SiO_2 and GeO_2 are predicted to show nucleation delay in ALD on OH-terminated W, Co and Cu surfaces. Depending on the ligands used in the ALD precursor, Ru-based or W-based substrates were predicted to resist the nucleation of all the metal oxides that were studied.

Chapter 1

Background, motivation and goals

The size of a computer has dramatically decreased over the years. Yet the power of the computer has massively increased. The major innovation that allowed this to happen was substitution of the heavy vacuum tubes used as switches with transistors within integrated circuits (IC)[1]. Modern computers are made of electronic devices based on the IC, or semiconductor chips. In the current electronic device fabrication process microchips are created on a thin slice of a semiconductor material, usually silicon, called a wafer. A sequence of various processing steps is used during the microchip fabrication process, allowing simultaneous fabrication of several million devices. A schematic representation of a wafer containing hundreds of chips is shown in Figure 1.1.

The main microchip fabrication process steps can be divided into four general categories: deposition (grow, coat, or transfer a material onto the wafer), removal (remove the material from the wafer), patterning (shaping of deposited materials) and modification of electrical properties (doping transistor sources and drains). Future scaling down of computers and improvement of characteristics requires improvements in each of these steps as well as application of new materials during these fabrication processes.

Our work is focused on a deposition technique called atomic layer deposition (ALD) for area-selective deposition of Si-based materials for microchip fabrication. For this reason, the steps of removal, patterning and modifications of electronic properties will not be covered. More detail about semiconductor device fabrication processes can be found in the *Semiconductor Devices* book by

[1] Integrated circuits are very advanced versions of an electric circuit, that are made from different electrical components, such as transistors, resistors, diodes and capacitors connected to each other.

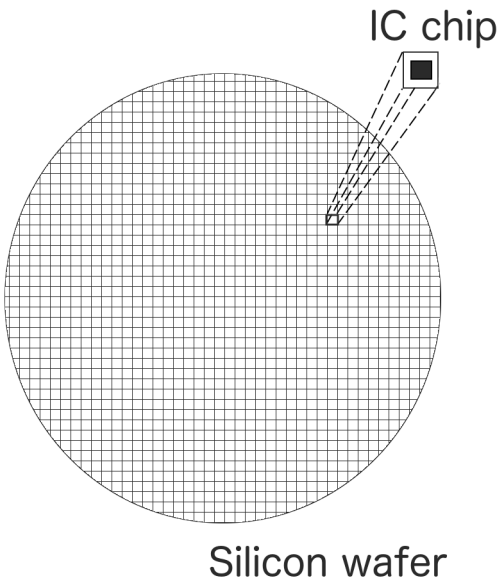


Figure 1.1: Illustration of wafer and chip. The size of the wafer from 100-450 mm.

Kano. [2] An overview of different deposition processes is presented below.

1.1 Overview of thin film deposition techniques

Thin films

As we are interested in applications of Si-based materials for electronics, we are considering layers of materials with thicknesses less than a micron, which are here called "thin films". Thin films exhibit unique properties compared to the bulk materials due to the large surface area to bulk volume ratio [3], [4]. Thin films are grown via a deposition process. The deposition process can influence the thin film material properties.

Thin film deposition processes

There are two main types of thin film deposition processes: *physical* and *chemical*. Each process technology has its own advantages and limitations and it is very important to understand them so as to choose the right deposition process. For the purpose of the current study, only a brief overview of the physical vapor deposition (PVD) fabrication technique will be presented. The main focus of this work will be on the chemical vapor deposition (CVD) process, and, in particular, atomic layer deposition (ALD). A detailed description of different thin film deposition processes can be found in the *Handbook of Thin Film Process Technology* [4].

1.1.1 Physical vapor deposition (PVD)

In physical vapor deposition (PVD) the material goes from condensed phase to a vapor phase and then back to condensed thin film. Different PVD processes differ in the methods used to generate and deposit material. The most common PVD processes are: *thermal evaporation* and *sputtering*. [5] In sputtering PVD the vapor is created through bombardment of the source with accelerated ions. In thermal PVD, the source evaporates by heating the material in vacuum. Depending on the application, PVD has some advantages over CVD. It does not require the use of specialized precursor materials. Also the PVD process is much cleaner environmentally compared to the chemical process. [6] However, thin films deposited using PVD can suffer from non-uniformity on high aspect ratio surfaces at the scale of hundreds of nanometers.

1.1.2 Chemical vapor deposition (CVD)

An alternative to the PVD technique for depositing more conformal thin films (i.e. the film thickness of the sidewalls is comparable to the thickness on the top) on high aspect ratio surfaces is chemical vapor deposition (CVD). [7] During CVD the thin film is formed by a chemical reaction of a volatile chemical, called a precursor, with the substrate. The chemical reaction can take place both in the gas phase and on the substrate. Various CVD types exist, which differ by the means by which the chemical reaction is initiated. CVD often operates at much higher temperatures (except the atomic layer deposition process, that will be described further) than PVD. This results in heating of the substrate that makes it challenging to use CVD for substrates that cannot tolerate high temperatures. A detailed description of CVD and its historical development can be found in the *Chemical Vapor Deposition* book by Hitchman and Jensen. [8]

1.1.3 Atomic layer deposition (ALD)

Atomic layer deposition (ALD) is a modification of the CVD technique, where thin films are grown layer by layer based on self-limiting chemical reactions. [9–12] ALD is one of the most precise deposition techniques used in the modern semiconductor fabrication process. ALD allows control of the thickness of the deposited film layer by layer and can achieve very high film conformality on high aspect ratio surfaces at low temperatures ($< 200\ ^{\circ}C$).

ALD was introduced independently twice under two different names: atomic layer epitaxy (ALE) by Suntola and Anston in Finland in 1977 (patent [9]) and as molecular layering by Aleskovskii in Soviet Union [10](in Russian). A review of the early publications of ALD can be found in [13].

Mechanism

A distinct feature of ALD is cyclic and self-limiting film growth. [11] One growth cycle consists of four steps (see Figure 1.2):

1. exposure to a pulse of the first precursor,
2. purge of the reaction chamber,
3. exposure to a pulse of the second precursor (also called co-reactant),
4. purge of the reaction chamber.

Individual gas-surface reactions in each pulse are called "half-reactions". The primary reaction steps in each half-reaction are the following: (1) molecular physisorption of a precursor into a surface, (2) molecular chemisorption, (3) local transfer of ligands between precursor and surface, (4) diffusion and reorganisation, (5) desorption of by-products. The chamber is purged with an inert carrier gas (typically N_2 or Ar) to remove any unreacted precursor or reaction by-products [12].

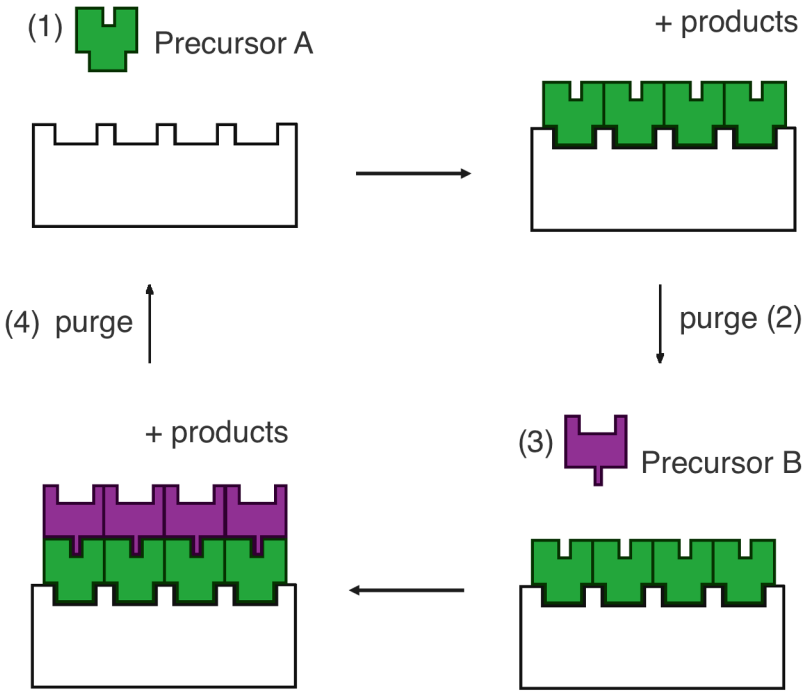


Figure 1.2: A schematic representation of ALD deposition cycle

After the formation of a layer no further adsorption takes place. This type of film growth is called self-limiting. It means that the amount of material deposited in each reaction cycle is constant. It explains the primary advantages of ALD, such as precise control of the film thickness during the deposition and excellent film conformality even on very high aspect ratio surfaces.

A review of ALD can be found in [14] by Riikka Puurunen, [11] by Steven George and [12] by Richard Johnson et al.

Precursor requirements

ALD precursors must fulfil a list of requirements. [12] First of all, the reactant that will deposit the desired material must be commercially available or synthe-

sized. Additionally, reactants should be volatile enough to be in the gas phase upon moderate heating. Furthermore, while in the gas phase they should not decompose until they have reached the surface. Neither the reactant nor its by-products, after reacting with the surface, should dissolve, etch or in any way damage the substrate, the growing film or ALD reactor. Finally, some reactants can be very expensive, which has economical implications as well [12]. Similar precursors can be used for CVD and ALD processes. Precursors that are commonly used for Si-based ALD as well as the precursor reaction mechanism during ALD will be described in detail in Chapter 2.

ALD types: thermal and plasma-enhanced

There are two types of ALD: thermal and plasma-enhanced ALD (PEALD), that differ by the way the energy for the chemical reaction is provided. In the thermal ALD process the necessary energy for the surface reaction is entirely provided by thermal energy from heating the substrate, while in PEALD additional chemical energy is provided by plasma.

Thermal ALD

Thermal ALD is very close to a standard CVD process based on a binary reaction (A + B$\rightarrow$ products). However, during thermal ALD precursors A and B are applied separately and sequentially [11]. A typical thermal ALD cycle is shown in Figure 1.2. The chemical reactions occur spontaneously at various temperatures and can be performed without the aid of plasma or radicals.

Plasma-Enhanced ALD

During plasma ALD additional chemical energy is provided by plasma. An overall PEALD process is similar to a thermal ALD process. The difference is that during the co-reactants step plasma[2] is generated. A schematic representation of a PEALD cycle is shown in Figure 1.3.

There are two different reactor layouts for PEALD: with a direct plasma generator and with a remote plasma generator.

Direct plasma

In the first type, plasma is generated at radio frequency (RF) between two electrodes. The substrate is placed on the grounded electrode and the powered electrode is placed above it. Such plasma is called “direct plasma”. Because of

[2]Plasma is a collection of free charged particles along with other gas-phase species that is on average electrically neutral. [15]

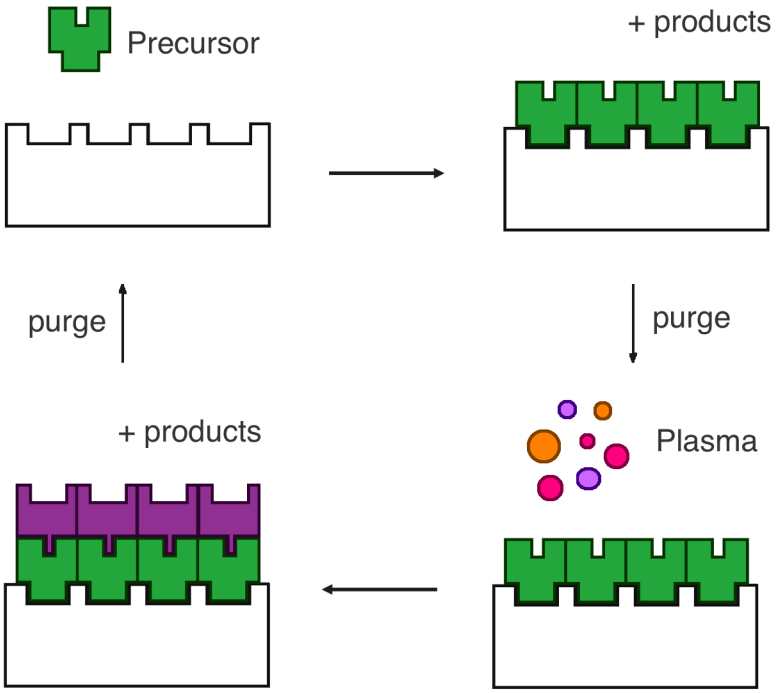


Figure 1.3: A schematic representation of plasma-enhanced ALD (PEALD) deposition cycle

the relatively simple reactor layout such plasmas are widely used in industrial tools. [16]

Remote plasma

In the second type, the plasma source is located remotely and the substrate is not involved in generation of plasma species. Such a plasma is called "remote plasma". The advantage of this configuration is that substrate and plasma properties can be varied independently. [16]

A plasma ALD process can be considerably more expensive and complex than thermal ALD due to addition of the plasma source. However, PEALD has a number of advantages over thermal ALD, such as a reduced process temperature, improved film properties due to more complete reaction with depositing film and reduced purge and nucleation time. [17]

An overview of PEALD can be found in [16] by Profijt et al. and in [17] by Hyungjun Kim and I.-K. Oh.

1.2 Area-selective ALD

For most applications in the microchip fabrication process it is required to control the lateral dimensions of the thin film. For example, patterned films are predominant in transistors and interconnect technology, where the main building blocks typically consist of the stack of patterned films of different materials. [18]

In the conventional microchip fabrication process, shaping of materials is done top-down, where a material that needs to be structured is first deposited on the substrate and then a resist layer is patterned on the film by using lithography (see Figure 1.4(a)). This processing step is called patterning. One of the delicate patterning steps is the lithography mask alignment step, which at smaller scale leads to edge placement error, which in turn leads to deterioration of device performance.

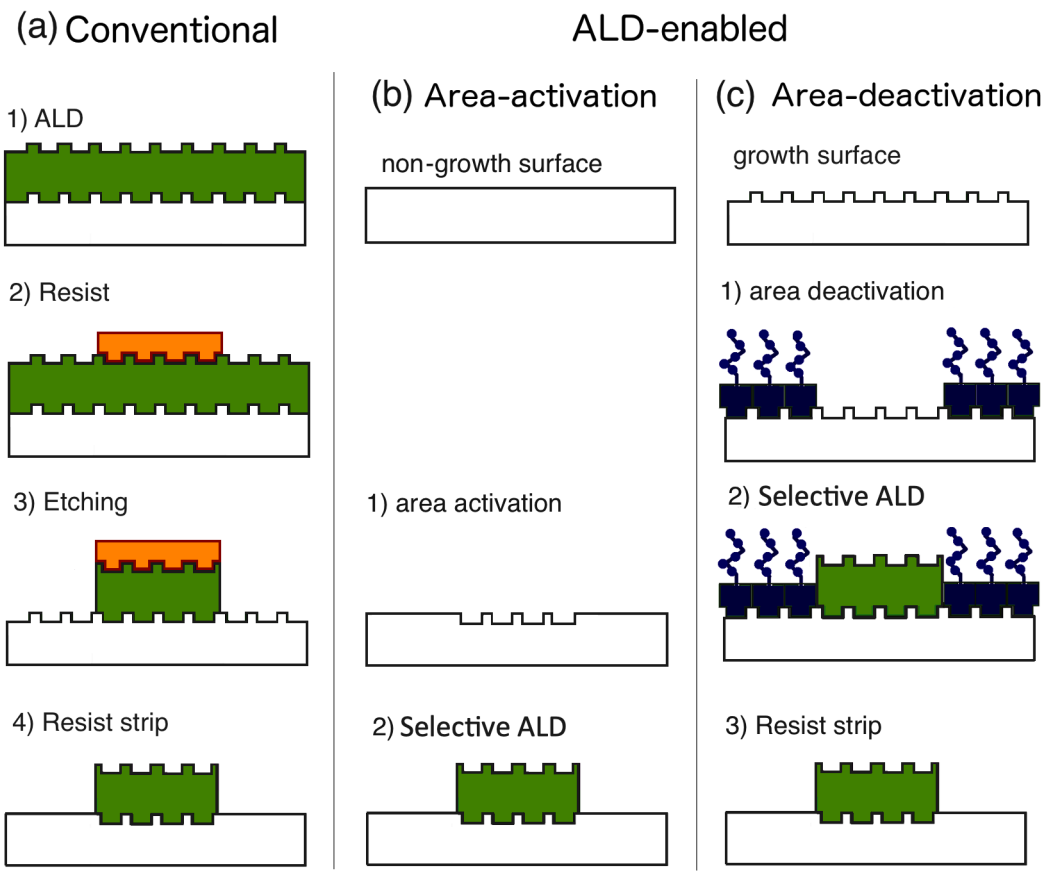


Figure 1.4: A schematic representation of the patterning step in microchip fabrication. (a) Conventional patterning; ALD-enabled patterning by (b) area-activation and (c) area-deactivation.

The alternative way is to use a bottom-up approach, where a material is grown only where it is needed. This is called area-selective deposition. ALD offers opportunities for patterning of sensitive materials, where deposition is required at low temperatures to prevent damage of the resist layer. [18]

ALD does not have the intrinsic ability to control lateral growth of the film. However, since ALD strongly depends on the surface chemistry it should be possible to modify the surface to enable area-selective ALD (AS-ALD). Local modification of the surface allows the control of lateral ALD growth in addition to precise thickness control. [18]

There are two main ways to enable AS-ALD: by area-activation and by area-deactivation, shown schematically in Figure 1.4(b),(c). As can be seen in Figure 1.4(b), the area-activation approach is much less complex than other approaches.

Area-activation can be achieved by patterning a layer so that it catalyzes the surface reactions of the ALD process. The main challenge of this approach is to create an ALD process that needs to be suppressed on the non-growth surface.

Area-selective ALD by area-deactivation is typically done by blocking the ALD growth by using self-assembled monolayers (SAMs). Typically SAMs are long organic molecules with reactive groups at both ends of the molecules. For example, octadecyltrichlorosilane (ODTS) molecules terminated with -CH_3 groups after reacting with an oxide substrate transform the surface from an OH-terminated hydrophilic surface into a CH_3 terminated hydrophobic surface. [19] The main challenges with the area-deactivation approach using SAMs are limited height of SAMs, which limits the control of the dimension of the pattern, and thermal stability of SAMs, that limits the thickness of the pattern, and defects in the SAM layer, which limits the selectivity.

A review of ALD-enabled patterning and conventional patterning process and applications can be found in [18]. Our results on the investigation of the possible area-selective ALD of Si-based materials are presented in Chapter 4.

1.3 Routes towards new ALD processes. Theoretical modelling

To investigate the routes towards new ALD processes a combination of experimental and theoretical research would ideally be used. Creating a new ALD process requires finding proper precursors and proper ALD process conditions, such as temperature and pressure. To understand which precursor is right for an ALD process we have to analyze the chemistry during the process. Computational modelling is a powerful tool that bridges theory and experiment. Computational modelling can simplify the investigation of a new ALD process and reduce the amount of development time in the laboratory. Nowadays, remarkable computation power is available in order to model chemical systems. In this work we are using computational modelling to investigate the routes towards new ALD processes for area-selective deposition applications.

Blocking or activation of material layers during area-selective ALD has limited lateral resolution. For this reason, exploiting inherent differences in nucleation on different substrates using theoretical modelling is of crucial importance for developing future area-selective ALD. A detailed computational methodology used in the current work will be described in the Chapter 3.

1.4 Goals of this study

As was mentioned above, area-selective ALD is a promising technology that can solve edge placement error and possibly reduce the number of patterning steps during the microchip fabrication process. Semiconductor companies, such as Lam Research Corporation[3], are paying more and more attention to area-selective ALD technology, however, it is still in the R&D stage. One of the main challenges of the AS-ALD is that generally the mechanism behind the technique is not fully understood. One of the key steps is to understand how to perform and control thin-film nucleation during AS-ALD, specifically how the molecules and the surface interact during the first ALD step. Computational modelling is a powerful tool which can be a solution to this challenge. By using computational modelling the chemistry during the first ALD step can be analyzed and further used for the understanding of nucleation.

[3]This project is fully funded by Lam Research Corporation

Hence, the goals of the current study are to understand the chemistry of the first ALD step of Si-based materials, by performing thermodynamical screening of various Si source precursors, presented in Chapter 4. In the current study we focus on four Si-based substrates: Si, SiN_x, SiC and SiO_2. SiC ALD is very challenging and still under active research as well. Thus, in Chapters 5 and 6 we focus on understanding the mechanism of SiC ALD and investigating why SiC surfaces are inert towards ALD-type reactions. Finally in Chapter 7 we use a similar theoretical screening approach in order to predict the non-growth surfaces during thermal ALD of metal-oxides via a precursor ligand-exchange mechanism. The goal of this chapter is thus to understand which metal precursors show a nucleation delay on which substrates, hence opening up routes towards thermal AS-ALD of metal oxides.

The thesis opens with a review of the existing ALD processes of Si-based materials in Chapter 2. Conclusions and directions for future work are presented in Chapter 8. Methods are presented in Chapter 3. Chapter 4 is under preparation for publication. Chapters 5 and 6 are published as articles in peer reviewed journals [20, 21].

Chapter 2

Current ALD processes for Si-based materials

2.1 Motivation: applications of Si-based materials in semiconductor industry

One of the ways to achieve the miniaturization of microelectronic devices is the implementation of advanced architectures. Examples of such a devices are fin field-effect transistors (FinFET) and 3D NAND memory (see Figure 2.1). The implementation of advanced architectures creates a need for the deposition of thin films of materials on high-aspect ratio surfaces at low temperatures. As was described in the previous chapter, ALD is an ideal technique for such applications.

In the current work we are interested in the possibility of area-selective ALD of Si-based materials. The most important Si-based materials for the microelectronics industry are silicon carbide (SiC), silicon oxide (SiO_2) and silicon nitride (Si_3N_4). These three materials are used for a variety of applications.

Si is commonly used as a semiconductor material in electronic devices, such as transistors, printed circuit boards and ICs. Si has a moderate band gap of 1.12 eV, which reduces the chance of leakage current. Crystalline Si used in electronics has a diamond like structure. For this reason pure silicon is highly stable at room temperature. One of the other advantages of Si is that it easily forms oxides and nitrides at high temperatures. SiO_2 is the most used insulator for IC due to its chemical stability compared to other oxides. [23]

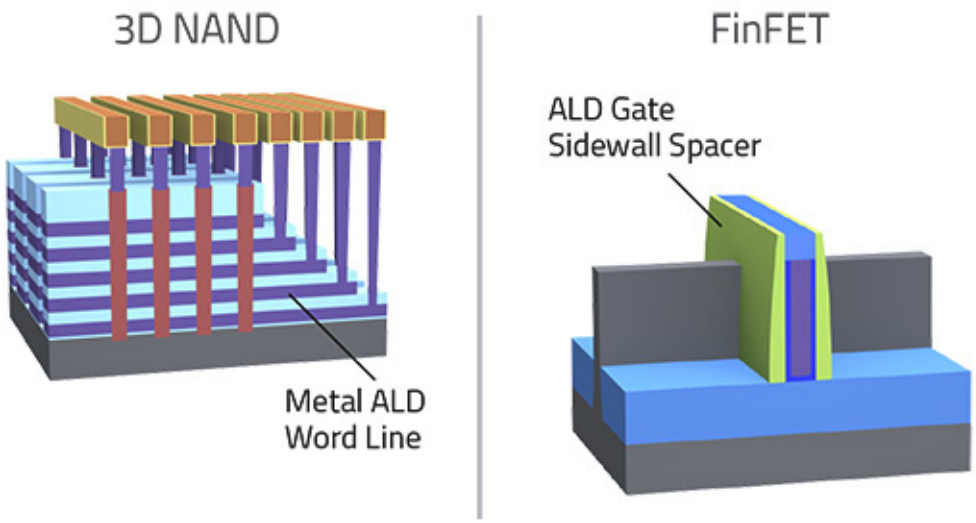


Figure 2.1: Examples of applications of ALD in semiconductor manufacturing. Source Lam Research Company.

Silicon nitride has excellent bending strength, high fracture toughness and good thermal conductivity. For this reason it is well suited for power electronic substrates. [22] Silicon nitride is superior to SiO_2 as it is a significantly better diffusion barrier against water molecules and sodium ions (the main sources of corrosion in electronics). [23] It is also used as a dielectric between polysilicon layers in capacitors in analog chips.

SiC has larger bandgap (2.3-3.2 eV, depending on polytype) than Si, which enhances the efficiency in energy transformation and it is also more robust when operating at higher temperatures when used for power devices. SiC also has a high breakdown electric field, high thermal conductivity and chemical robustness. [24–26]. Due to these properties SiC is used for power and sensor devices.

In microchip processing the low-permittivity electrically insulating SiC, SiO_2 and Si_3N_4 are used for liner and spacer applications. SiC is often used as a hard mask layer due to its robust resistance to chemical and plasma etching. [27] SiO_2 is chemically inert, scratch resistant, hard and has high optical transmittance. [28] Due to these properties SiO_2 thin films are used for sidewall spacers in FinFET transistors, [29] hard masks in self-aligned double pattering [30] and gap fill oxides for shallow trench isolation. Amorphous Si_3N_4 is hard and radiation resistant. [28] Si_3N_4 thin films are used as sidewall spacers, [31] trench

liners, gate stack encapsulation, [32] and air gap liners. [33]

Currently, among the Si-based films mentioned above, only SiO_2 thin films grown by ALD are integrated in semiconductor devices. SiC and Si_3N_4 ALD still faces substantial challenges for high-volume manufacturing (HVM). Existing SiO_2, SiN_x[4] and SiC ALD processes will be described below[5]. The ALD mechanism will be described where possible. Subsections below describe the main Si-based materials and their ALD precursors, such as silanes and silenes, chlorosilanes, alkoxides, aminosilanes and silylamines, followed by the summary.

2.2 Introduction to surface reaction mechanism during ALD

Future innovation for depositing Si-based materials by ALD requires an understanding of the surface reaction mechanism of current ALD processes. In order to understand the ALD mechanism the nature of each elementary step of the two ALD half-cycles must be understood. The primary reaction steps in each ALD half-cycle have so far been determined to be (i) molecular physisorption of a precursor onto a surface, (ii) molecular chemisorption, (iii) local transfer of ligands and/or fragments between precursor and surface, (iv) longer scale diffusion and reorganization and (v) desorption of by-products. [34] The reaction steps may be investigated by *in-situ* nano-characterization techniques (e.g. *in situ* Fourier transform infrared spectroscopy, FTIR) and by first principles computation (usually density functional theory, DFT). These techniques allow us to monitor the film composition, reactive surface sites and adsorbed surface species during each half-cycle.

The knowledge of the surface reaction mechanism can then inform substrate preparation, reactor conditions and choice of chemicals. Choosing the right precursor for an ALD process is a crucial factor in determining the viability of the process and the quality of the grown film. Detailed knowledge of the reaction steps can help in the selection of a chemistry that minimizes activation energies for the ALD reactions and avoids unwanted side reactions, enabling

[4]Deposited Si_3N_4 are rarely stoichiometric, for this reason Si_3N_4 deposited films here and after will be called SiN_x.

[5]Obtained via Web of Knowledge prior to August 2018

low temperature ALD.

2.3 Silane precursors

Existing ALD processes using silane precursors as the Si source are shown in Table 2.1. Typically, silane SiH_4 or disilane Si_2H_6 is used. $Si(SiH_3)_4$ was also used for ALD of SiN_x. [35] As can be seen from the table silanes as Si precursors were not reported for thermal SiO_2 and SiN_x ALD. Indeed, Mui et al. [36] calculated a high energy barrier of 3.25 eV for SiH_4 to react with an Si-H terminated surface during ALD of SiN_x using silane SiH_4 and NH_3. A high energy barrier of 2.56 eV was also calculated for NH_3 reacting with the Si-H terminated surface that is likely to exist after the SiH_4 pulse. Thus, only plasma-enhanced ALD processes were reported for SiO_2 and SiN_x using silanes with N_2 or NH_3 and CO_2 plasmas for SiN_x and SiO_2, respectively. The highest growth per cycle (GPC) was reported for the SiN_x ALD process using $Si(SiH_3)_4$ at 250-300 °C and SiH_4 at 400 °C.

Table 2.1: Known SiO_2 and SiN_x ALD processes using silane precursors. GPC=growth per cycle.

	Silane	Co-reagent	Temperature, °C	GPC, Å	Ref.
SiN_x plasma	SiH_4	N_2	250-400	0.06-2.5	[37, 38]
	SiH_4	N_2/H_2	350	0.1	[39]
	$Si(SiH_3)_4$	N_2	250-300	1.4	[35]
	$SiH(CH_3)_3$	NH_3	300-450	0.7-0.8	[40]
SiO_2 plasma	SiH_4	CO_2	250-400	0.25-2	[37]

ALD of SiC has proven to be extremely challenging. There are a few SiC thermal epitaxial growth processes reported usually operating at substrate temperatures > 850 °C (see Table 2.2).

Table 2.2: Known SiC epitaxial growth processes (pulsed CVD) using silane precursors. GPC=growth per cycle.

	Silane	Co-reagent	Temperature, °C	GPC, Å	Ref.
SiC thermal	Si_2H_6	C_2H_2	1000-1050	4-7	[41, 41]
	Si_2H_6	C_2H_2	1050	4-5	[42]
	Si_2H_6	C_2H_4	850-980	2.1	[43]
	$(C_2H_5)_2SiH_2$	-	590-675	0.2	[44]

The most common Si and C precursors are Si_2H_6 and C_2H_2 or C_2H_4. GPC higher than 2 Å suggests that the process may be not self-limiting and that a CVD process takes place. Plasma-enhanced ALD of SiC is usually not obtainable due to the tendency of Si- and C- containing plasmas to continuously deposit amorphous Si and C films. [45] Alternatively, a precursor containing both Si and C such as $(C_2H_5)_2SiH_2$ can be used. [44] However, Sadayuki et al. suggested that using $(C_2H_5)_2SiH_2$ single source precursor in ALD requires a subsequent surface modification either by using plasma or by a follow-up reconfiguration of the surface species using temperature modulation. Hence, the authors suggested that the growth occurred via CVD process not an ALD process.

One of the main challenges of achieving ALD of SiC is the lack of suitable carbon precursors for carbide deposition. Typical SiC CVD process proceeds using silane and light hydrocarbons, such as ethylene (C_2H_4) and propane (C_3H_8). [214] Hydrocarbons are good leaving groups in ALD chemistry, hence, are not suitable as a carbon precursor for ALD SiC.

2.4 Chlorosilane precursors

Chlorosilanes $SiCl_4$, SiH_2Cl_2 and Si_2Cl_6 are typically used as a source of Si during SiN_x and SiO_2 ALD. Chlorosilane precursors are easy to synthesize, cost-effective, and typically have a good thermal stability, which makes them very attractive for SiN_x ALD applications. [46] However, the unwanted chlorine impurities can cause a device-reliability issue. [47]

First of all an SiN_x PEALD process was introduced by Goto et al. [64] in 1996 using SiH_2Cl_2 with NH_3 plasma. Introducing N containing plasma decreased

Table 2.3: Known SiC, SiO_2 and SiN_x ALD processes using chlorosilane precursors. GPC=growth per cycle. "-" =GPC is not reported. "Cat."=catalyst.

	Chlorosilane precursor	Co-reagent	Temperature, °C	GPC, Å	Ref.
SiN_x thermal	$SiCl_4$	NH_3	427-627	2.4	[48]
	$SiCl_4$	NH_3	375, 550-600	0.9-1.5	[49–53]
	$SiCl_4$	NH_3	500	1.2	[54]
	SiH_2Cl_2	NH_3	375, 550	0.9	[55]
	SiH_2Cl_2	NH_3	500	1.2	[54]
	SiH_2Cl_2	NH_3	450-550	0.8	[56]
	Si_2Cl_6	NH_3	515-557	2.4-2.8	[57]
	Si_2Cl_6	NH_3	300	0.55	[58]
	Si_2Cl_6	N_2H_4	525-650	2.3	[59]
	Si_2Cl_6	N_2H_4	285	-	[60]
	Si_3Cl_8	NH_3	300-500	0.3-0.6	[61]
SiN_x plasma	SiH_3Cl	NH_3	400	-	[62]
	SiH_2Cl_2	NH_3	250-400	0.9	[63, 64]
	SiH_2Cl_2	NH_3	375	1.0	[65]
	SiH_2Cl_2	NH_3	500	-	[62]
	SiH_2Cl_2	NH_3	350-500	-	[66]
	SiH_2Cl_2	NH_3	350	0.24	[67]
	Si_2Cl_6	NH_3	350-450	1.2	[68]
	Si_2Cl_6& CH_3NH_2	N_2	400	0.9	[69]
	$SiCl_2(CH_3)_2$	NH_3	475	-	[45]
	HSi_2Cl_5	NH_3 or N_2/H_2	270–360	0.95	[70]
SiO_2 thermal	$SiCl_4$	H_2O	527, 327	0.75, 1.1	[71, 72]
	$SiCl_4$+cat.C_5H_5N	H_2O+cat.C_5H_5N	27	2.1	[73]
	$SiCl_4$+cat.NH_3	H_2O+cat.NH_3	27-65	2.16	[74]
	SiH_2Cl_2	O_3	300	2.5	[75, 76]
	SiH_2Cl_2	O_3/O_2	350-400	1.7-2.1	[77]
	Si_2Cl_6	O_3	403-453	3.2	[78]
SiC thermal	SiH_2Cl_2	C_2H_2	800-1050	4-9	[79, 80]

N precursor dosage and temperature to 250 - 400 °C, much lower than the thermal ALD process. However, the poor conformality and compositional uniformity of SiN_x deposited on high-aspect-ratio nanostructures, such as FinFETs, still remains an issue.

As can be observed from Table 2.3, the chlorosilanes are typically used with NH_3 plasma not with N_2 plasma during SiN_x ALD. It was found that using N_2 plasma with chlorosilane precursors not containing H, such as Si_2Cl_6, leads to the growth of poor-quality SiN_x films in a non-self-limiting manner and that the films oxidize rapidly to SiN_xO_y. [69] Furthermore, the chlorine of the chlorosilane precursor is not reactive with nitrogen of the undercoordinated bare SiN_x produced after the N_2 pulse. [58] Introducing the three step PEALD using

Si_2Cl_6 with an intermediate thermal step of CH_3NH_2 enables the use of N_2 plasma for high quality SiN_x growth deposition. [69] This process lowers the atomic H content and improves film conformality on high-aspect-ratio surfaces via the formation of Si-N-Si bonds during the intermediate CH_3NH_2 step.

S.M. George and co-workers made use of previous work on the reactivity of chlorosilanes with OH-terminated SiO_2 to develop a thermal SiO_2 ALD process. Sneh et al. [72] studied the high-temperature $SiCl_4$+H_2O process and confirmed that each surface half-reaction is complete and self-limiting. The main drawback was the need for high temperature (>600 K) and large reactant exposure (>10^9 L), consistent with prior work by Tripp and Hair [81]. The authors used literature data to explain the surface mechanism, as follows. In the $SiCl_4$ pulse, the precursor physisorbs via H-bonding on OH-terminated SiO_2, rather than dissociatively chemisorbing (Figure 2.2(a)).

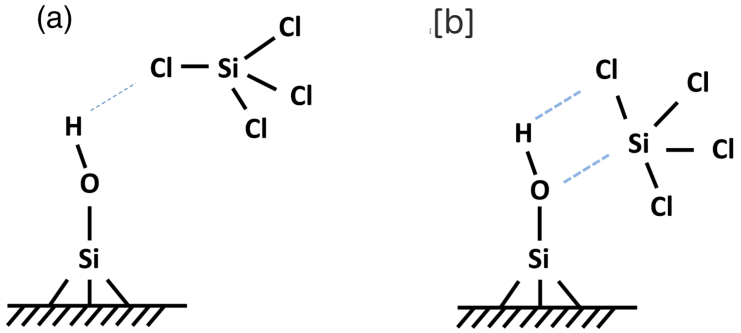


Figure 2.2: SiO_2 ALD mechanism during $SiCl_4$ pulse. $SiCl_4$ precursor physisorbs on OH-terminated SiO_2 via H-bonding followed by direct substitution, *i.e.* concurrent cleavage of Si-Cl and O-H and formation of Si-O and H-Cl via a four-membered-ring transition state(TS) with pentacoordinate Si

The subsequent reaction is direct substitution, *i.e.* concurrent cleavage of Si-Cl and O-H and formation of Si-O and H-Cl via four-membered-ring transition state (TS) (not intermediate) with pentacoordinate Si (Figure 2.2(b)). The result is chemical bonding of the chlorosilane fragment to the surface via O and formation of the by-product HCl. The authors suggested that a similar mechanism may be at play during the H_2O pulse (Figure 2.3a and 2.3b).

DFT calculations by Kang and Musgrave on OH-terminated Si(001) [82] provided evidence that individual molecules indeed adsorb and eliminate HCl in one step via a single four-membered-ring TS in both the $SiCl_4$ and H_2O pulses. No intermediates were detected. However a later DFT study of ALD onto OH-terminated α-SiO_2(0001) by Fang et al. [83] reported metastable intermediates

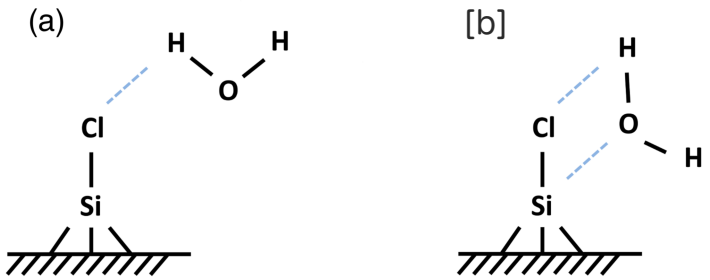


Figure 2.3: ALD mechanism during H_2O pulse. H_2O physisorbs on surface Si-Cl via H-bonding followed by direct substitution, *i.e.* concurrent cleavage of Si-Cl and O-H and formation of Si-O and H-Cl via a four-membered ring transition state (TS).

with pentacoordinate Si in both $SiCl_4$ and H_2O pulses. This conflicting evidence suggests that the local environment (i.e. surface orientation and electron donating groups) has a major influence on whether pentacoordinate Si is metastable or unstable. Further DFT studies of this process are reviewed by Fang et al. [84].

The first study of thermal SiN_x ALD using SiH_2Cl_2 and NH_3 was reported in 1997 by Morishita et al. [59] The SiN_x ALD surface reaction mechanism using SiH_2Cl_2 and NH_3 plasma was initially investigated by Yokoyama et al. [63]. Yokoyama et al. suggested a growth mechanism for the SiN_x PEALD using $SiCl_2H_2$ and NH_3 based on the FTIR measurements. They proposed that during the NH_3 plasma step the H-terminated Si surface becomes nitrided and H_2 molecules are produced as a by-product. This is followed by the $SiCl_2H_2$ adsorption leaving SiH_2Cl groups on the surface and producing H_2 or HCl by-products. At this step the coverage is less than one monolayer due to the size of the SiH_2Cl_2 molecule causing steric hindrance. In the second NH_3 step Si-H and Si-N surface groups are nitrided.

This was followed by FTIR studies of the thermal SiN_x ALD using $SiCl_4$ and NH_3 by Klaus et al. [48] Klaus et al. also used FTIR to analyze the reaction mechanism of thermal SiN_x ALD using SiH_2Cl_2 and NH_3. They found a reduction in the surface groups -SiCl after the SiH_2Cl_2 pulse and in $-NH_2$ after the NH_3 pulse concurrent with the growth of NH_2 and -SiCl. Furthermore, the half-reaction reaches completion with sufficient precursor exposure temperature at not less than 700 K.

A further chlorosilane SiN_x plasma ALD surface reaction mechanism was studied with FTIR by Ovanesyan. [45,68,69] Ovanesyan et al. suggested that Si_2Cl_6 reacts with the $-NH_2$ surface species to form -NH and $-Si_xCl_{2x-1}$(x = 1, 2). It

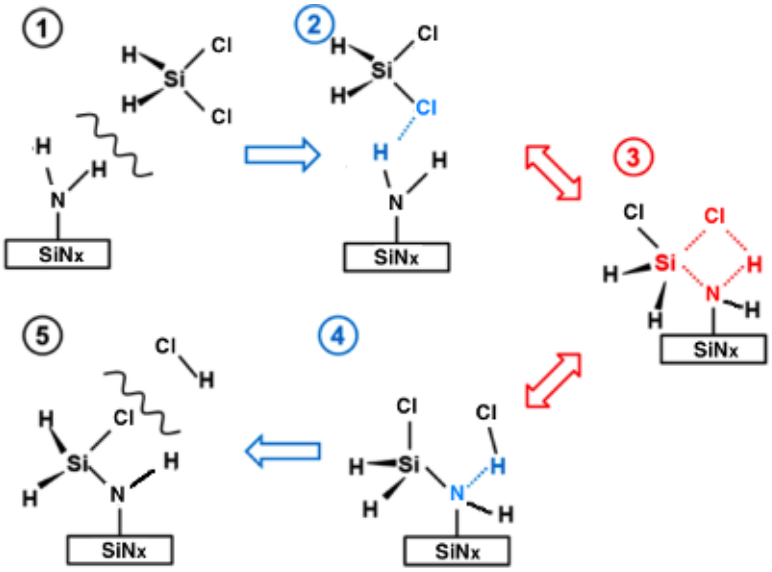


Figure 2.4: Surface reaction mechanism during PEALD of SiN_x using SiH_2Cl_2 and NH_3 plasma. The TS is structure 3. Adapted with permission from [1]. Copyright 2018 American Chemical Society.

was also suggested that the resulting surface-NH is the primary route to H incorporation in the SiN_x films.

Murray et al. used DFT to predict that SiH_2X_2 precursor molecules (X= particular functional group) react with H-Y surface groups (Y=O, NH, N) through a five-coordinated transition state (see Figure 2.4 for SiH_2Cl_2 example). Ovanesyan et al. used FTIR for the SiN_x PEALD using Si_2Cl_6 and NH_3 plasma to show that -NH_2 surface groups were more reactive to Si_2Cl_6 than =NH surface groups. [68] Furthermore, DFT modelling by Huang et al. [85] and Yusup et al. [58] showed that -NH_2 surface groups are more exposed to the incoming precursor than hindered =N–H groups making the incoming precursor first react with the -NH_2 surface group. Ovanesyan et al. confirmed using FTIR that Si_2Cl_6 will first react with the -NH_2 surface group via an overcoordinated Si atom resulting in Si_2Cl_5 and -NH groups on the surface and HCl as a by-product. [68] Other authors also suggested that removal of the Cl atom from the surface happens through the generation of HCl. [48, 59, 63]

Yusup et al. calculated reaction pathways of $SiCl_4$ and Si_2Cl_6 reacting with three different β- Si_3N_4 surfaces: undercoordinated bare Si_3N_4 surface, $NH/SiNH_2$ and NH/SiH terminated Si_3N_4 surfaces. [58]. High energy barriers were found for chlorosilanes reacting with the $NH/SiNH_2$ and NH/SiH terminated Si_3N_4 surfaces, i.e. an energy barrier of 3.55 eV for Si_2Cl_6 reacting with the $NH/SiNH_2$ terminated Si_3N_4 surface. The reaction was calculated to be

exothermic for $NH/SiNH_2$ terminated Si_3N_4 and endothermic for the NH/SiH terminated surface. However, an exothermic reaction with a very low energy barrier was found for chlorosilane precursors reacting with the undercoordinated bare S_3N_4 surface. The Si_3N_4 NH_2/NH or NH/SiH surface is produced after reacting with H containing NH_3 plasma, while the undercoordinated bare SiN_x surface is produced after N_2 plasma. In order to achieve a high precursor reactivity with undercoordinated bare surface a three step ALD was proposed by Yusup et al. [58] including an additional N_2 plasma step prior to the precursor pulse. This process increased the GPC from 0.59 Å to 1.1 Å showing a good agreement with DFT results and indicating that investigating the reactivity of the surface sites plays a very important role in improving the ALD process.

One of the ways to decrease the deposition temperature of the ALD process is to catalyse pulses with amines. Amine catalyst, such as pyridine that reacts strongly with surface functional groups and reactants, is added to each ALD half-reaction facilitating chemisorption. SiO_2 growth from multiple cycles of alternating alkylchlorosilane and water pulses catalyzed with amines was first reported in 1993 by Tripp and Hair, although not labelled as ALD. [81] This built on previous work where temperatures of at least 300 °C were found to be necessary for OH-terminated SiO_2 to react with chlorosilanes. Exposure to triethylamine allowed the surface reaction to proceed at room temperature. This is consistent with the mechanism proposed by Blitz et al. [86] whereby H-bonding of an amine base to surface –OH increases the nucleophilicity (i.e. electron donating power) of oxygen in the OH group, facilitating chemisorption of chlorosilane via pentacoordinate Si (see Figure 2.5). Catalyzed SiN_x ALD processes were not reported.

The George group also studied base-catalysed thermal SiO_2 ALD from $SiCl_4$+H_2O [73] and confirmed that co-dosing with pyridine in each pulse permitted lower temperature (27 °C) and smaller precursor fluxes (10^4 L) to be used. Fitting first order kinetics to the data revealed that the effective activation energy was halved by base-catalysis, and this dramatic drop in activation energy was later confirmed in DFT models by Chen et al. [87] It appears that O-H of H_2O is activated by an intermediate with H-bonded pyridine and pentacoordinate Si, as proposed by Blitz [86] (Figure 2.5).

Smaller bases were computed to show a stronger catalytic effect. [87] Consistent with this, ammonia was found experimentally to be about 10 times more effective as a catalyst for this reaction than pyridine. [74] Mayangsari et al. [88]

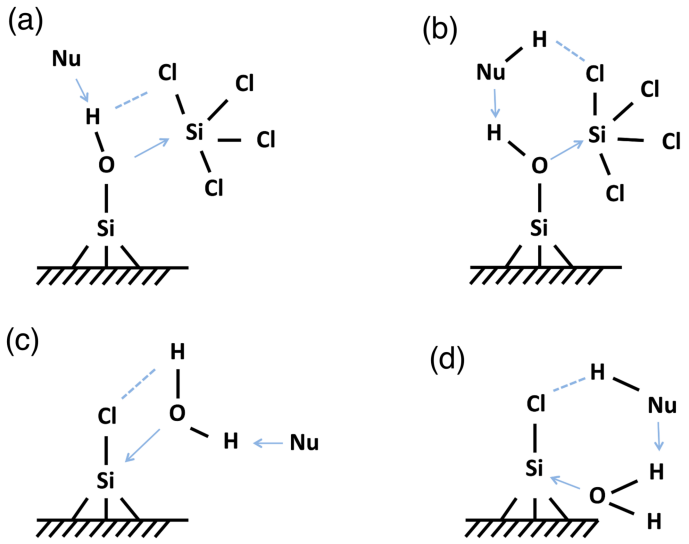


Figure 2.5: Chemical mechanism of SiO_2 ALD catalyzed by amine base during the (a), (b) $SiCl_4$ pulse and (c), (d) water pulse. H-bonding of a nucleophile ("Nu") such as an amine to surface OH or water increases the reactivity of oxygen in that group towards Si, facilitating chemisorption of (a) chlorosilane or (c) water, both via pentacoordinate Si in a 4-membered ring. Nucleophile with H (Nu-H) allows formation of a more stable 6-membered ring in (b) and (d).

used DFT to compare different alkylamine molecules in order to find an alternative for pyridine in the Si_2Cl_6 and H_2O ALD process. It was found that the catalysts with less steric hindrance such as pyridine would be more effective than bigger alkylamines during the Si_2Cl_6 pulse despite the lower nucleophilicity. However, during the H_2O pulse, the catalysts with a high nucleophilicity such as triethylamine (Et_3N) would be more efficient as the steric hindrance is less critical. It was also found that $(C_2H_5)_3N$ is expected to incorporate less amine salts than pyridine.

This sequence of studies on chlorosilanes shows how particular reagents may open up new mechanistic pathways and have a major effect on the viability of an ALD process. $SiCl_4$ can not chemisorb molecularly and faces a high barrier towards elimination of HCl, due to strain in the four-membered -Si-O-H-Cl-ring of the TS during SiO_2 ALD. Thermal ALD is then only possible above 300 °C. Co-dosing with a nucleophilic reagent (e.g. pyridine) increases the reactivity of the surface and allows $SiCl_4$ to adsorb molecularly as the pentacoordinate intermediate $–OSiCl_4$, lowering the barrier to HCl formation. The temperature where ALD is viable thus drops to room temperature. Co-dosing with a protic nucleophile (e.g. NH_3) changes the TS into a six-membered ring, further accelerating the reaction. H_2O is also a protic nucleophile and so the same effect

makes the H-bonded network of adsorbed H_2O molecules reactive towards the Cl-terminated surface. This explains why the H_2O pulse does not require high temperatures.

However, the catalyst-based ALD of SiO_2 film suffers from several drawbacks, such as chlorine and carbon impurities. In order to remove these impurities and improve the film quality, post-deposition processing such as high temperature oxidation may be required. [89]

Nagasawa et al. [79,80] used SiH_2Cl_2 as Si precursor and C_2H_2 as C precursor for epitaxial growth of SiC, which is extremely challenging, as was mentioned above. The films were deposited at extremely high temperatures and GPC was as high as 4-9 Å for 800-1050 °C, which suggests that it was not a self-limited process. This is similar to the case where Si_2H_6 was used for the epitaxial growth of SiC, as was described in the subsection 2.3.

2.5 Alkoxide precursors

Base-catalysis also seems to be key to achieving ALD of SiO_2 with the otherwise relatively unreactive tetraethoxysilane (TEOS). TEOS was used for SiO_2 and SiN_x ALD using NH_3 catalyst . [90] FTIR data indicate that NH_3 increased the nucleophilicity of oxygen in surface SiOH, possibly as shown for chlorosilanes (see Figure 2.5). Plasma-enhanced SiO_2 ALD using TEOS and O_2 plasma was also reported. [29] However, the GPC was lower at 50 °C compared to the thermal catalysed process. Moreover, at temperatures higher than 50°C there was no growth. The self-catalytic[6] precursor $H_2N(CH_2)_3Si(OEt)_3$ has also been used with H_2O or O_3 for low temperature SiO_2 ALD (120-200 °C). [91] It seems likely that the amino group of the precursor both improves adsorption and increases the reactivity of surface OH towards the alkoxide ligand.

[6] Self-catalytic - catalysis happens without adding extra catalyst, because of the activity of the precursor's own ligands.

Table 2.4: Known SiC, SiO_2 and SiN_x ALD processes using alkoxide precursors. GPC=growth per cycle, "cat."=catalyst, TEOS=tetraethoxysilane, Et=

	Precursor	Co-reagent	T, °C	GPC, Å	Ref.
SiO_2 thermal	TEOS+cat.NH_3	H_2O+cat.NH_3	27	0.7-0.8	[90]
	$H_2N(CH_2)_3Si(OEt)_3$	H_2O/O_3	120-200	0.6	[91]
SiO_2 plasma	TEOS	O_2	50-250	0.5 - no growth	[29]

2.6 Aminosilane precursors

Thermodynamically, amide ligands are predicted to be more reactive than chloride ligands with respect to elimination in SiO_2 and SiN_x ALD by about 0.5 - 0.7 eV per ligand according to DFT cluster calculations. [92] Aminosilane precursors can be divided into two categories: homoleptic silicon amides that have all identical ligands and heteroleptic silicon amides that have a mix of amide and hydride ligands attached to the central Si. The smallest homoleptic silicon amide, tetrakisdimethylaminosilane $Si(N(CH_3)_2)_4$, is found to be too sterically-hindered for adsorption during ALD. [93] A key question is therefore how precursor performance is affected by the ratio of amide to hydride ligands.

Tris[dimethylamino]silane (3DMAS) showed a higher growth rate at lower deposition temperatures (GPC of 1.13 Å/cycle at 100 °C) than at higher deposition temperatures (GPC of 0.11 Å/cycle at 350 °C). Similar performance was also found for bis(diethylamino)silane (BDEAS). The possible reason is the decreased precursor chemisorption at higher temperatures due to a lower –OH density after the plasma step. [103, 117]

In fact, Si-H is such a strong bond that H rarely behaves as a hydride leaving group. Many studies have confirmed that loss of the amine ligand is favoured over the loss of the hydride (i.e. to the by-product H_2) [118–120] when the precursor adsorbs onto OH-terminated SiO_2 surfaces. We understand this as meaning that heteroleptic aminosilanes can be viewed as a source of SiH, SiH_2 or SiH_3, leading to a saturated H-terminated Si surface. The saturated surface is therefore quite inert towards co-reagents such as H_2O for SiO_2 or NH_3 for SiN_x ALD and requires temperatures > 450 °C for reaction to proceed. [93] In-

Table 2.5: Known ALD processes from aminosilanes. GPC=growth per cycle. BTBAS=bis(tert-butylamino)silane, 3DMAS=tris[dimethylamino]-silane, DSBAS=di(sec-butyl)aminosilane, BDEAS=bis(diethylamino)silane, TEAS=tetrakis(ethylamino)silane, TIPAS=tris(isopropyl)aminosilane, DIPAS=di(isopropylamino)silane, CSN-2=1,3-di-isopropylamino-2,4-dimethylcyclosilazane, BEMAS=bis(ethylmethylamino)silane, TD-MAS= tris(dimethylamino)silane, BDMAS=bis(dimethylamino)silane, pl.ex.H_2O=plasma-excited water vapor.

	Aminosilane precursor	co-reagent	Temperature, °C	GPC, Å	Ref.
SiN_x plasma	BTBAS	N_2	80-500	0.16-0.93	[94–96]
	3 DMAS	N_2	350	0.11	[67, 97]
	DSBAS	N_2	100-500	0.12-0.2	[98]
	3 DMAS	NH_3	350	no growth	[67]
	BDEAS	NH_3	300	no growth	[99]
	TEAS	NH_3	300	no growth	[99]
	TIPAS	NH_3	300	no growth	[99]
	DIPAS	NH_3	300	no growth	[99]
	DIPAS	Ar & NH_3	300	0.4-0.7	[99]
	CSN–2	NH_3/N_2& N_2	200-500	0.43	[100]
SiO_2 plasma	$Si(N(CH_3)_2)_4$ and $Si(N(CH_3)_2)_3Cl$	O_2/N_2	100-250	0.2-0.4	[101]
	DIPAS	O_2	125-200	1.35	[102]
	3 DMAS	O_2	100, 200	1.13, 0.98	[103]
	BDEAS	O_2	100-300	0.8-1.7	[104–106]
	BTBAS	O_2	300	1.1	[105]
	DSBAS	O_2	300	1.3	[105]
	3 DMAS	O_2	150-300	0.9-1.15	[107]
	BEMAS	O_2	50-250	0.8	[29]
SiO_2 thermal	DIPAS	O_3	150-200	1.2-2.3	[108]
	TDMAS	O_3	100-400,	0.2-0.6	[109–113]
	TDMAS	H_2O_2	150-550	0.8-1.8	[93]
	BDMAS	O_3	250-400	0.8-0.98	[109, 113]
	BEMAS	O_3	320	1.2	[114]
	TEAS	O_3/O_2	478-514	1	[115]
	TDMAS	pl.ex.H_2O	15-25	0.75	[116]

deed, a high energy barrier of 2.56 eV was calculated for NH_3 reacting with the Si-H terminated surface. [36] By employing more agressive oxygen/nitrogen sources, such as O_2, O_3, N_2 or N_3 plasma, deposition is enabled at < 450 °C (see Table 2.5).

An aminosilane with three amino groups, such as tris(dimethylamino)silane ($SiH(N(CH_3)_2)_3$, TDMAS), would function as a source of SiH if it was to lose all the three amino ligands. However, it is computed by DFT that surface H transfer and loss of all three ligands is kinetically and thermodynamically im-

possible under ALD conditions [121]. It was found that the sequential dissociative chemisorption of TDMAS occurs only up to the second step so that a dimethylaminosilylenyl group is left on the surface, while further dissociation is energetically forbidden. This is consistent with FTIR data from Kinoshito et al. [111, 112] Oxidation of this remaining ligand in the co-reagent pulse may result in C and N impurities in the film.

Aminosilanes with two amino ligands (such as bis(*tert*-butylamino)silane $SiH_2[NHC(CH_3)_3]_2$, BTBAS or bis(diethylamino)silane $SiH_2[N(CH_2CH_3)_2]_2$, BDEAS) are a potential source of SiH_2. Indeed, DFT calculations predict that the most favourable reaction pathway during ALD of SiO_2 for both amide ligands to be cleanly removed. [122] The calculations showed that a variety of bridging arragements of the SiH_2 group are possible depending on which surface hydrogens combine with the amide ligands, and it is suggested that the resulting structures may lead to particular film microstructure (crystalline or amorphous). [122]

However, Bosch et al. showed using FTIR that when BTBAS precursor reacts with the surface during ALD of SiN_x, only one amino ligand is eliminated, while some of the ligands and fragments stay on the surface and are removed only during the subsequent N_2 plasma pulse. [96] Furthermore, H concentration in the deposited SiN_x originates from the BTBAS precursor and strongly depends on the deposition temperature. At lower deposition temperature the H concentration increases. The formation of an Si-NCH complex at the surface was observed during the N_2 plasma step. This complex is removed during the BTBAS pulse. The formation of the Si-NCH groups is thought to result from the redeposition process. [96] Similar results were achieved from FTIR of SiO_2 ALD using BTBAS, where it was suggested that the substrate temperature strongly affects the surface termination during the aminosilane pulse. For instance, deposition at 100 °C leads to formation of (-O-SiH_3), deposition at higher temperatures (> 300 °C) leads to formation of (-O_2-SiH_2) and the most stable mono hydride (-O_3-Si-H) is observed at 500 °C.

Huang et al. [123] calculated energetics for BDEAS and BTBAS reacting with NH and NH_2 β-Si_3N_4(0001) surface groups using DFT. It was suggested that the aminosilane ligand reacts with the NH surface group via the four-membered ring transition state that includes surface N, precursor Si and N and H from ligand. Activation energies were calculated to be 1.67 and 1.38 eV for NH and NH_2, respectively, which is lower than for $SiCl_4$ and Si_2Cl_6 mentioned above.

These barriers suggest that it is easier for aminosilane precursors to enter the transition state than for chlorosilane precursors. Even so, the reaction was calculated to be endothermic for aminosilanes suggesting that the reaction is not likely to proceed at lower temperatures. However, experimentally aminosilanes showed reactivity with SiN_x at temperatures as low as 80 °C [94–96], much lower than that of the chlorosilane precursors with reactions calculated to be exothermic.

With just one amide ligand, di(sec-butylamino)silane ($SiH_3(N^{sec}[C(CH_3)_3]_2$), DSBAS) should function as a source of SiH_3. DFT calculations show that SiO_2 ALD with DSBAS and O_3 is exothermic with low activation energy (0.26 eV) for the DSBAS adsorption step. [124] Mallikarjunan et al. [105] confirmed experimentally that DSBAS indeed shows SiO_2 ALD growth at lower temperature than BTBAS or BDEAS (150 °C vs. 250 °C). They also found that DSBAS gives a higher ALD growth rate, which was explained by better surface packing of the SiH_3 fragment of DSBAS after elimination of a single amine, relative to the corresponding $SiH_2(NR_2)$ fragments of BTBAS or BDEAS. Pena et al. [119] found that at > 400 °C surf-$OSiH_3$ can lose one or two hydrogens by reacting with surface hydroxyl. Penã et al. [125] also found using FTIR that PEALD of SiN_x with DSBAS requires both creation of the Si dangling bonds on the H-terminated surface and presence of the H-Si bonds for precursor ligand elimination. Dangling bonds can be created when surface H are eliminated by N_2 plasma treatment.

As was mentioned above, one of the challenges of PEALD of SiN_x with NH_3 plasma source is the significantly high silicon precursor exposure time, at least 100 times longer than that of the existing commercial SiO_2 PEALD process (with O_2 plasma source). In order to investigate this issue Murray et al. [126] used DFT to quantify how the identity of the amides affects ALD mechanism. The R group of amide was observed to have a major effect during molecular adsorption of the precursor via H-bonding to the SiO_2 surface, presumably due to steric crowding. As a general rule, larger R groups were found to hinder adsorption onto SiO_2, as seen in the adsorption energy sequence of -0.54, -0.44, -0.33 eV for R=Me (in SiH_2DMA_2), Et (in BDEAS), ^{i}Pr (in DIPAS) in the precursor family $SiH_2(NR_2)_2$. By contrast, adsorption of the same precursors on the Si_3N_4 surface was calculated to be only slightly exothermic (-0.08, -0.06, -0.11 eV for R=Me, Et and ^{i}Pr, respectively) and did not show a significant difference for the different R groups.

Thereafter, Murray et al. showed that the -NH_2 terminated Si_3N_4 surface is

less reactive than the -OH terminated SiO_2 when reacting with $SiH_2(NH_2)_2$, SiH_2DMA_2, BTBAS, BDEAS and DIPAS with a difference in adsorption energies of 0.23-0.46 eV. Murray et al. suggested that Si_3N_4 is less reactive due to the rigidity of the NH_2 groups that exist after the NH_3 pulse. This leads to less steric effect in the rather weak H-bonding interaction of the precursor during the precursor pulse compared to more flexible OH group during SiO_2 ALD. These results can help to explain why PEALD of SiO_2 is easier to achieve than PEALD of SiN_x.

Another challenge related to the SiN_x ALD process, that was mentioned above, is that aminosilanes in combination with NH_3 plasma do not lead to SiN_x film growth, while in combination with N_2 plasma they do lead to the film growth. In order to better understand this issue Ande at al. [127] used a combination of both experiment and DFT to study chemisorption of aminosilane precursors on several Si_3N_4 surfaces, such as β-Si_3N_4 surface with undercoordinated Si and N atoms, β-Si_3N_4 surface terminated exclusively with Si-NH and a β-Si_3N_4 surface terminated with Si–NH_2. Ande at al. showed that NH or NH_2 surface termination leads to a weak precursor-surface interaction, while the undercoordinated surface leads to a strong precursor-surface interaction. Furthermore, it was shown experimentally that the presence of H or NHx from NH_3, H_2, H_2–N_2 plasmas or NH_3 gas correlates with unfavorable precursor-surface interaction and poor growth, while N_2 plasma allows film growth to recover.

2.7 Silylamine precursors

Known Si-based material ALD processes using silylamine precursors are presented in Table 2.6. As can be seen from the table, silylamines are reported as Si sources only for SiNx PEALD processes. Furthermore, silylamine PEALD processes show high GPC with both NH_3 and N_2 plasmas. However, their prohibitively high cost means that their use for commercial PEALD SiNx processes is uneconomical.

Table 2.6: Known ALD processes of Si-based materials using silylamine precursors. GPC=growth per cycle. $DTDN_2$–H_2=bis(dimethylaminomethylsilyl)(trimethylsilyl)amine ($C_9H_{29}N_3Si_3$). "-" = GPC not reported

	Silylamine	Co-reagent	Temperature, °C	GPC, Å	Ref.
	$N(SiH_3)_3$	N_2	250-300	1.2	[35]
SiNx	$N(SiH_3)_3$	N_2	250	-	[67]
plasma	$N(SiH_3)_3$	NH_3	150-350	0.68	[128, 129]
	$N(SiH_3)_3$	N_2/H_2	300-400	1.3-2.1	[32]
	$DTDN_2$–H_2	N_2	250-400	0.36	[130]

2.8 Summary

SiO_2 and SiN_x thin films are deposited by both thermal and plasma-enhanced ALD processes. However only the SiO_2 ALD processes are commercially available. Many SiN_x ALD processes exist, however, it is still not implemented in high-volume semiconductor manufacturing due to the low conformality and compositional uniformity on high-aspect-ratio nanostructures. SiC thin films deposited by ALD are required by the semiconductor industry. However, only a few epitaxial processes using silane precursor Si_2H_6 with C_2H_2 or C_2H_4, chlorosilane precursors SiH_2Cl_2 with C_2H_2 or single-source precursor $(C_2H_5)_2SiH_2$ were reported, with the very high GPC and temperatures >850 °C suggesting that these processes may not be self-limiting.

The primary Si precursors used for ALD are aminosilanes, chlorosilanes, silanes, alkoxides and silylamines. Aminosilane and chlorosilane precursors are the most common Si sources for SiO_2 and SiN_x ALD. H_2O and O_3 are used as sources of oxygen for thermal SiO_2 ALD; CO_2 and O_2 plasma are used in PEALD SiO_2 processes. N precursors used for SiN_x ALD are typically NH_3 and N_2H_4 for thermal ALD and NH_3 and N_2 plasmas for PEALD. A recent review of the SiN_x ALD by Meng et al. can be found in [46].

The highest GPC (>2 Å) reported for SiO_2 ALD was for the chlorosilanes $SiCl_4$, Si_2Cl_6, SiH_2Cl_2 and the aminosilane DIPAS, including the room temperature thermal process with GPC of 2.1 Åusing $SiCl_4$ and H_2O catalysed by NH_3 or C_5H_5N. SiO_2 ALD using alkoxide precursors showed GPC of 0.5 Å at temperature 120 °C. Using O_2 plasma as a co-reagent or adding a catalyst allowed the process to run at room temperature with increased GPC of 0.8 Å or 0.5 Å, respectively. The silane precursor SiH_4 was used for PEALD of SiO_2 in combination with CO_2 at a deposition temperature > 250 °C and GPC of 0.25 Å, increasing to 2 Å at 400 °C.

The highest GPC (>2 Å) reported for SiN_x ALD processes was for thermal ALD using chlorosilane and for PEALD using silane and silylamine. However, these ALD processes operated at elavated temperatures (> 400 °C). The lowest temperatures of 80 and 100 °C were reported for PEALD SiN_x using the aminosilane precursors BTBAS and DSBAS, respectively, but the GPC of these processes was low (<0.2 Å). The PEALD process using silylamine $N(SiH_3)_3$ and ammonia at 150 °C showed a higher GPC of 0.68 Å.

SiN_x ALD is still facing challenges to be implemented as a commercial process.

First, the chlorosilanes are typically used with NH_3 plasma not with N_2 plasma. It was found that using N_2 plasma with chlorosilane precursors not containing H leads to the growth of poor-quality SiN_x films in a nonself-limiting manner, with rapid oxidation to SiN_xO_y. [69] Second, the GPC of the NH_3 plasma processes is generally higher than that of the N_2 processes. Third, aminosilanes in combination with NH_3 plasma do not lead to the SiN_x film growth.

Chapter 3

Methodologies

3.1 Challenges for modelling ALD processes

There are many different processes involved in ALD process across many length scales, e.g. pulsed flow of gases into meter-scale reactors, around millimetre-scaled geometries and chemical reaction between atoms. [131] However, it is impossible to describe explicitly all of these length scales in one model. To do so, one needs a "multi-scale" simulation. The problem of time scale is also important in ALD simulations, as a combination of fast (ps-ns) and slow reactions (μs-ms) contribute to film growth, and gases are pulsed and purged over second-long timescales. [132].

Simulations at each length scale are based on appropriate assumptions and are subject to characteristic limitations. The most precise are quantum simulations, but these are limited in size of system to a few thousand atoms. For larger systems of millions of atoms, the semi-empirical approach is used, where experimental data and approximations are included in atomistic-scale calculations. Using coarse-grained methods allows larger simulated systems to over 100 million atoms. [132] Fast reactions (ps-ns) are described by quantum mechanical and semi-empirical approaches, such as ab-initio and molecular dynamics simulations. Longer reactions (μs-ms) are described by multi-scale modelling approach, such as kinetic Monte-Carlo (KMC) method [252].

Examples relevant to ALD of systems at different scales needed are shown in Figure 3.1. Giving a detailed explanation of these methods is out of the scope of this work, as the current work is focused on quantum simulations only. More

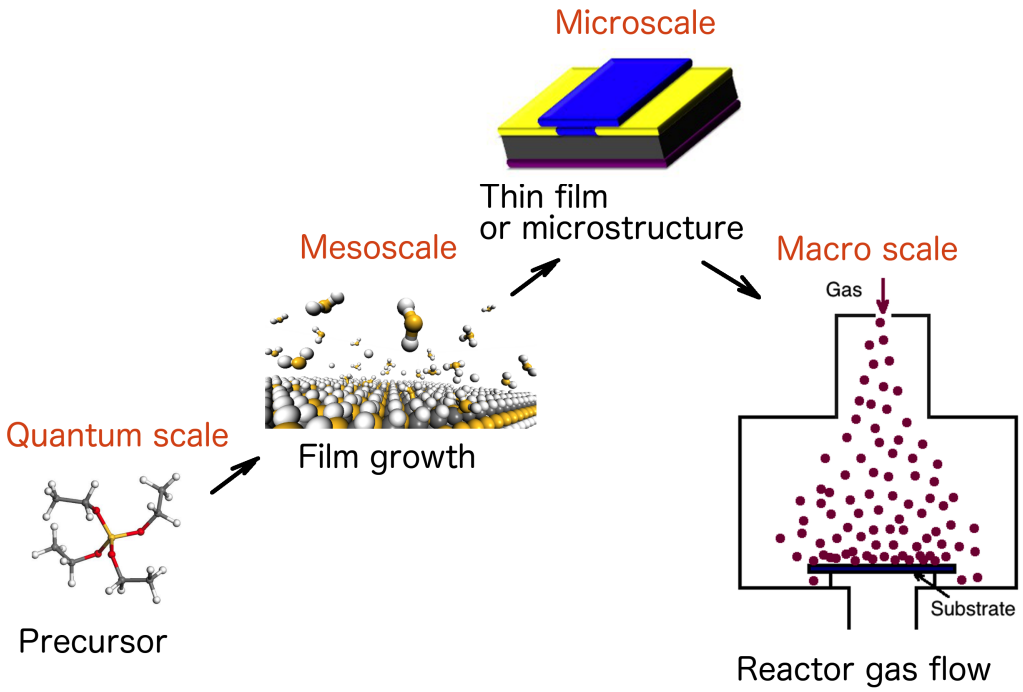


Figure 3.1: Multiple scales and the nature of ALD processes models needed.

information on different modelling approaches can be found in this book [133].

3.2 Theoretical modelling to describe ALD chemistry

Most commonly, theoretical modelling is used to describe the likely structure of an adsorbate[7] and its mode and energy of bonding to a surface. This can be done by calculating the relative stability of the adsorbate structures. In addition, orbital energies can be calculated that can be directly compared with spectroscopic measurements. [134]

The kinetics of the chemical reactions happening during the ALD process can be also computed. It is possible to calculate adsorption energies E_{ads} and energy barriers E_a of reactions within a theoretical model to predict whether a reaction is thermodynamically or kinetically favorable. In addition, it is also possible to perform a simple thermodynamic screening of different precursors for the ALD process by calculating Gibbs energies of CVD-like reactions. These approaches will be described in more detailed in the next section 3.3.

It is important to validate theoretical results by comparison with experimental data. However, it must be mentioned that this comparison is not always an easy task. One of the problems is that there usually exists little experimental information on adsorbate structures with atomic level detail. This what we usually get as a result of theoretical modelling in order to predict the likely adsorbate structures. [134]

In this work we are focused on describing chemical reactions of precursors reacting with a substrate and the growth of a thin film. For these purposes we are using quantum simulations using density functional theory (DFT), which nowadays is one of the most used quantum mechanical approaches for describing the electronic structure of a system. The theoretical background to the DFT approach will be described in the section 3.4.

[7] Here, the adsorbate is a precursor adsorbed on the surface.

3.3 Approaches for ALD modelling

3.3.1 Precursor screening

A thermodynamic screening of different precursors for an ALD process can be done by calculating Gibbs free energies for CVD like reactions. [20] The Gibbs free energy reflects the actual thermodynamics of a reaction and can be calculated using eq. 3.1:

$$\Delta G = \Delta E - T\Delta S + RT\ln Q, \tag{3.1}$$

where T is a temperature at which the reaction is performed, S - entropy, R - gas constant and Q - reaction quotient. Energies E and entropies S can be determined using quantum calculations.

Entropy can be computed by finding vibrational force frequencies from Hessian matrix (second derivatives of total energy). The Hessian matrix is found using ab-initio calculations, such as DFT.

For example, to determine if silicon precursor $SiCl_4$ and carbon precursor C_2H_6 are favorable for the ALD process of silicon carbide, the reaction:

$$2\,SiCl_4(g) + C_2H_6(g) \longrightarrow 2\,SiC(s) + 6\,HCl(g) + Cl_2(g) \tag{3.2}$$

can be written and the Gibbs energy for this reaction can be estimated. This reaction actually describes a CVD process for silicon carbide and the Gibbs free energy reflects the thermodynamics of a CVD process[8]. We know that in an ALD process these two precursors do not actually meet in the reactor at the same time. Findings to date are that formation of silicon carbide bond has a driving force for ALD reaction and that formation of by-product plays a secondary role. The CVD-like reaction is thus a way of measuring this driving force. [135] Therefore, for an ALD process estimating the Gibbs energy for a CVD-like reaction is still a valid model.

The CVD-like reaction involves both isolated molecules and solid. To describe solid material efficiently, a planewave basis set is used. For isolated molecules a local basis set is used. Basis sets will be described in detail in section 3.6. For

[8] If $\Delta G < 0$ the reaction is permitted and $\Delta G > 0$ means that it is not permitted

these reasons two different computational codes must be used for Gibbs energy calculations of a CVD-like reactions. However, it is possible to use a reference molecule in place of the solid material. The energy for reaction of the reference molecule to produce solid material can be estimated with planewave basis sets and then used as correction energy for the reactions of isolated molecules. In our example for silicon carbide material a reference molecule $Si(CH_3)_4$ can be used and an example equation can be rewritten in a form:

$$2\,SiCl_4(g) + C_2H_6(g) + 6CH_4(g) \longrightarrow 2\,Si(CH_3)_4(g) + 6\,HCl(g) + Cl_2(g).$$

This approach for ALD precursors screening is computationally not expensive, as energies and entropies are estimated for isolated molecules (i.e. computational codes with local basis sets computational codes can be used) and a surface is not included in calculations. However, it is important to remember that the absolute value of ΔG in this model has no meaning for the ALD reaction, i.e. $\Delta G > 0$ does not necessarily mean that ALD will not work and $\Delta G < 0$ does not necessarily mean that all the individual surface reactions take place. By computing ΔG thermodynamics of different precursors reacting with surfaces during ALD can be compared in order to define what precursor is more likely to react with the surface.

3.3.2 Adsorption of a precursor

Adsorption of a precursor into a substrate surface is the first stage in the ALD deposition process. Adsorption energies can be calculated using the formula:

$$E_{\text{ads}} = E_{\text{precursor+substrate}} - E_{\text{substrate}} - E_{\text{precursor}},$$

where $E_{\text{precursor+substrate}}$ is the total energy of a precursor adsorbed on the surface, $E_{\text{substrate}}$ is the total energy of a solid and $E_{\text{precursor}}$ is the total energy of the gas phase isolated precursor. These energies can be obtained from quantum mechanical calculations. As we are interested in surface reactions it is important to choose the right surface model for the calculations.

3.3.2.1 Constructing surface model

A perfect crystal in solid-state theory is introduced by a unit cell repeated to form an infinite three-dimensional array, called bulk. An example of a bulk model unit cell of SiC is shown in figure 3.2. In a surface model the 3D periodicity of the bulk crystal is broken, as the surface is periodic only in two directions. There are two main surface models used: supercell (also called slab) and cluster models (see figure 3.3).

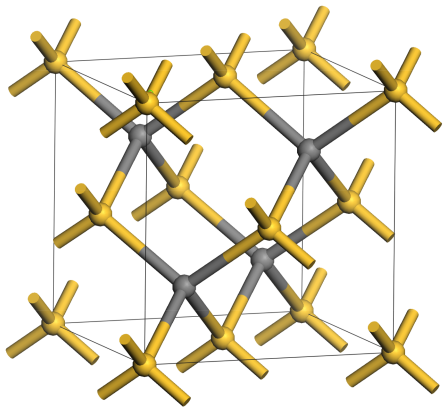


Figure 3.2: Silicon carbide bulk unit cell. Colour schemes: yellow=silicon, grey=carbon.

In slab model a unit cell consists of a 3D periodic slab of crystal and a vacuum region separating slab images, so that two dimensional periodicity can be achieved. The slab is infinite in the plane of the surface and finite in the direction perpendicular to the surface. There are two important things about the slab that must be considered. First, the slab thickness must be sufficient to assure that bulk and surface states can be distinguished. Second, the vacuum thickness must be large enough so that surfaces of consecutive slabs do not interact. [134]. Slab models are suitable for planewave basis sets. However, thick slabs can be computationally expensive. A slab unit cell for SiC(011) is presented in figure 3.3(a).

A cluster model (Figure 3.3b) treats the surface as a cluster of atoms with facets of the same symmetry analogously to an isolated molecule. Cluster models are ideal for describing local aspects, such as defects. The main advantages of cluster model is that it is computationally cheap for small clusters, as local basis sets can be used. The main disadvantages are that the cluster model have finite lateral size and that properties converge slowly with the cluster size.

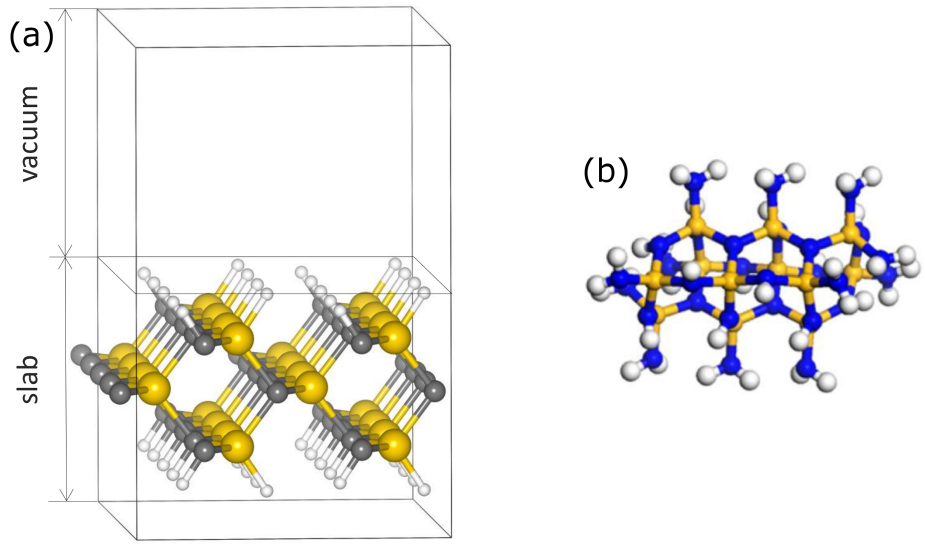


Figure 3.3: Different surfaces models. (a) slab silicon carbide cell, (b) cluster silicon nitride model with H groups on the surface. Colour schemes: yellow=silicon, grey=carbon, blue=nitrogen, white=hydrogen.

We use a perfect surface with no deffects as a typical model. It is possible to include surface deffects as well, however, it can increase the size of the unit cell requiring higher computational resources.

3.3.3 Calculating activation energies

ALD simulations are principally focused on calculating activation energies for reactions of precursors adsorbing/desorbing from the surface. Activation energies can be calculated using quantum mechanical calculations. ALD is mostly driven by kinetics not thermodynamics due to the irreversible loss of by-products into exhaust gases. [131] Calculating activation energies is a difficult task, as it involves bond making and bond breaking. These types of calculations are ab initio calculations, so the size of the system is limited to less than 1000 atoms. For this reason when computing activation energies it is important to compromise between the accuracy of calculations and the size of the system. [131]

Activation energy can be calculated by finding the lowest energy path, that is often called the minimum energy path (MEP), between reactants and products. The MEP connects the reactants and product through the transition state (TS). The transition state is a saddle point on the MEP between two minima of reac-

tants and products. After finding the transition state the activation energy can be determined by comparing the transition state and reactant energies. Many methods have been presented for finding saddle points. In the current work we use the nudged elastic band (NEB) method. [136] NEB is widely used for finding transition states, as it is particularly simple and easy to implement.

3.3.4 Nudged Elastic Band (NEB) approach

In the NEB approach [136] the minimum energy path and its saddle points are found by optimizing a number of intermediate images along the reaction path. Each of the images finds its lowest energy, while the space between the images is kept by a force constant (like an elastic band) and projecting out the force component perpendicular to the band. This type of optimization is called constrained optimization.

Climbing image Nudged Elastic Band (CI-NEB) approach

The CI-NEB approach [137] is a modification of NEB approach where the highest energy image is driven up to a saddle point. This image does not feel the spring force and the true force of this image along the tangent is inverted. This way the image maximizes its energy along the band. The number of images for CI calculations must be odd.

Practical recommendations for NEB calculations

NEB calculations can be quite challenging to converge. It is also computationally expensive as at the same time multiple images of a system are relaxed. Below are some recommendations on how to improve NEB performance in the VASP package. These recommendations are based on our experience with NEB calculations for the current project, i.e. finding reaction pathways for chemical reactions of a molecule adsorbing on silicon-based surfaces. The model representation of the surface is a slab with periodic boundary conditions.

Convergence time can be decreased by:

1. starting from NEB calculations and switching on CI-NEB only in the end, when system is almost converged (difference in energy for ionic step is about 0.5 eV/Å). This way a good estimate of the reaction co-ordinate around the saddle point is achieved and the highest image gets close to the saddle point;

2. turning off the symmetry (ISYM=0 VASP tag) of end points and NEB calculations;

3. freezing the bottom atoms of the slab.

Choosing optimization algorithm for NEB

The NEB approach uses a force projection in order to direct the optimizers towards minimum energy paths. For this reason, only optimizers that are solely based on the force (not on energy), can be used for NEB calculations. Such optimizers are the quasi-Newton (IBRION=1 tag in VASP) and quick-min for damped molecular dynamics optimization (IBRION=3 tag in VASP). The energy based conjugate-gradient method (IBRION=2 tag in VASP) cannot be used. A set of force-based optimizers from Henkelman's group can be also used. More information on different force-based optimization algorithms and their performance can be found in [138] and Henkelman's group website [139].

It is important to start NEB calculations from a soft optimizer, such as, for example, damped molecular dynamics optimization (IBRION=3 VASP tag) until the forces at the image are below 1 eV/Å. Then change to a more aggressive optimizer, for example quasi-Newton algorithm (IBRION=1 VASP tag). From our experience, if the system does not start to converge after 200 ionic steps it worth to try a different optimization algorithm.

Note, that it is important to run frequency calculations to confirm that the optimized structure is a transition state. As the transition state is a first order saddle point it must have only one imaginary frequency[9].

As was mentioned in this section, the energetics of an ALD reaction can be calculated using quantum mechanical calculations. In the current project the quantum mechanical approach that we are using is DFT, which will be described in the section below.

3.4 Density Functional Theory (DFT)

Most of the information we want to know about chemistry is in the electron density and electron energy, as well as atomic positions and atomic motion.

[9] A number of imaginary frequencies (negative square frequencies) correspond to an order of a saddle point. Transition state is a first order saddle point, so it must have only one imaginary frequency. For global minimum, for example, number of imaginary frequencies must be 0.

How can the electronic structure be calculated?

In 1925 Schrödinger suggested that particles behave as a wave and can be described by the wave function called Ψ. By determining this wave function one can get all the information about the state of these particles. In principle, to describe the electronic structure of a system, one would need to find the many-body wave function $\psi(r_i, R_j)$ for the electrons (coordinates r_i) and nuclei (coordinates R_j), which is an eigenstate of a Hamiltonian of the form:

$$\hat{H} = \hat{T} + \hat{V}, \tag{3.3}$$

where $\hat{T}$ is the kinetic energy operator and $\hat{V}$ is the potential energy operator. The solution satisfies the time-dependent Schrödinger Equation:

$$H|\psi\rangle = -i\hbar\frac{\partial|\psi\rangle}{\partial t} \tag{3.4}$$

The solution of this problem is extremely complicated for a large number of particles. For this reason some approximations must be applied to find a solution.

Born-Oppenheimer approximation

First, the Born-Oppenheimer approximation can be applied. It states that because of their significantly different masses, electrons and nuclei move on different time frames. So it is possible to assume that electrons can almost instantaneously accommodate to a specific configuration of nuclei and one need consider only the time evolution of the nuclei and separately the electronic structure at fixed nuclear coordinates.

Wave function is complicated

The Schrödinger Equation can be solved analytically only for the hydrogen atom. For bigger systems there is a need for approximations. For example, to describe electrons in the benzene molecule (C_6H_6) one would need a wave function of 168 coordinates(the benzene molecule has 42 electrons, each of which has 3 spatial coordinates plus 1 spin coordinate. 42x4=168). The computational complexity increases exponentially with the number of atoms, making the wave function complicated and difficult to interpret. What can be used instead of the wave function?

Using electron density instead of wave function: Thomas-Fermi theory

In 1927 Thomas [140], and independently Fermi (1928) [141] suggested that the full electron density[10] can be used instead of the wave function to describe all the information of the electronic system of interest and they derived a differential equation for the density. The electron density is a significantly simpler function than the wave function. This gave a basis for the later development of Density Functional Theory (DFT). However, the approximation they used for the kinetic energy was unable to sustain a bound state.

DFT fundamentals: Hohenberg and Kohn theorems

Further steps in developing DFT continued in 1964, when Hohenberg and Kohn formulated and proved theorems showing that the Thomas and Fermi approach was valid. In practical terms these theorems stated that if the energy functional is known there exists a variational principle on the density, where upon minimization, the energy obtained is that of the ground state and the corresponding density is the ground state density. After finding the ground state density any observables can be calculated. Unfortunately, these theorems did not give a prescription on how to obtain the energy functional[11] $E[n(r)]$.

DFT fundamentals: Kohn and Sham equations

This problem was partially solved in 1965 by Kohn and Sham [142], where they proposed a novel trick to make a practical application of the Hohenberg and Kohn theorems. The strategy was to separate the classical electrostatic energy into exchange and correlation contributions (see eq. 3.5) and to describe the kinetic energy using a system of non-interacting "electrons" with ground-state density the same as the real system.

$$E[n(r)] = T_S + V_{ne} + V_{ee} + V_{xc} \tag{3.5}$$

In eq. 3.5 T_S - kinetic energy term, V_{ne} - electron - nuclei interaction, V_{ee} - electron - electron Coulomb interaction, V_{xc} - exchange-correlation term. Correction terms in V_{xc} include corrections to all the errors appearing through positing a non-interacting system to calculate T ($\Delta T[n(r)]$) and employing classical electron-electron interaction term in $V_{ee}(\Delta V_{ee})$. Eq. 3.5 can be re-written in

[10] Electron density $n(r)$ is the number of electrons per unit volume

[11] Functional is a function that depends on another function. In this case the energy depends on the function electron density $n(r)$.

the more detailed form:

$$E[n(r)] = T[n(r)] + \Delta T[n(r)] + V_{ne}[n(r)] + V_{ee}[n(r)] + \Delta V_{ee}[n(r)] \quad (3.6)$$

In eq. 3.5 these corrections are represented by the term V_{xc}. The detailed theoretical background to the Kohn-Sham equations can be found in the book *Density Functional Methods in Physics*, p.265. [143]

Self-consistency

By expressing the Kohn-Sham energy functional $E[n(r)]$ in an orbital basis set, the eq. 3.7 can be obtained:

$$\begin{aligned} E[n(r)] = &\sum_{i}^{N} \left(\left\langle \chi_i \right| \nabla_i^2 \left| \chi_i \right\rangle - \left\langle \chi_i \right| \sum_{K} \frac{Z_K}{r_i - R_K} \left| \chi_i \right\rangle \right) \\ &+ \sum_{i}^{N} \left\langle \chi_i \right| \frac{1}{2} \int \frac{n(r')}{r_i - r'} dr' \left| \chi_i \right\rangle + V_{xc}[n(r)] \end{aligned} \quad (3.7)$$

where

- $\sum_{i}^{N} \left\langle \chi_i \right| \nabla_i^2 \left| \chi_i \right\rangle$ is kinetic energy over occupied orbitals, χ_i,
- $\sum_{i}^{N} \left\langle \chi_i \right| \sum_{K} \frac{Z_K}{r_i - R_K} \left| \chi_i \right\rangle$ is electron-nuclei attraction over occupied orbitals, where Z_K is atomic number, R_K is distance between electron and nuclei,
- $\sum_{i}^{N} \left\langle \chi_i \right| \frac{1}{2} \int \frac{n(r')}{r_i - r'} dr' \left| \chi_i \right\rangle$ is classical Coulomb repulsion for electron density interacting with orbitals that define this electron density,
- $V_{xc}[n(r)]$ is the exchange-correlation term.

We do not know what the density $n(r')$ is until we get a set of orbitals. After getting a new set of orbitals we calculate $n(r')$ again. For this reason, the method of solving this problem is called "self-consistent field" (SCF).

Exchange-correlation approximations

As described above, all the corrections appearing from positing a non-interacting system and employing the classical electron-electron interaction V_{ee} are included in the term V_{xc} (see eq. 3.7). To express this term we have to use

some approximations. The most used are local density (LDA) and generalized gradient approximation (GGA).

LDA

In the LDA, the exchange-correlation term V_{xc} can be found using eq. 3.8:

$$V_{xc}[n(r')] = \int d^3 r n(r)[\varepsilon_x[n(r)] + \varepsilon_c[n(r)]] \tag{3.8}$$

where $\varepsilon_x[n(r)]$ is exchange energy of uniform gas, which is calculated to be $-0.73856 n^{\frac{1}{3}}$ and $\varepsilon_c[n(r)]$ is correlation energy, that is obtained from Monte Carlo simulations for electron gas. Both $\varepsilon_x[n(r)]$ and $\varepsilon_c[n(r)]$ depend only on the density $n(r)$, which is a local property. That is why this approximation is called the local density approximation.

GGA

In the LDA a knowledge of the density at the point r is used. However, any real system is spatially inhomogeneous[12] and GGA includes information on the rate of this variation in the function. V_{xc} for GGA can be written in form:

$$V_{xc}^{GGA}[n] = \int d^3 r(n(r), \nabla n(r)). \tag{3.9}$$

Background on this DFT section was prepared using lectures by Professor Christopher J. Cramer at University of Minnesota, that can be found online [144] and in books [133], [143]. Different approaches can be realized while performing DFT calculations and they will be introduced in the next section.

3.5 Simulations packages: TURBOMOLE and VASP

For our calculations we used two different simulation packages: TURBOMOLE for local basis sets calculations, VASP for planewave basis sets. TURBOMOLE was used for calculating isolated precursor molecules, including their vibrational modes. VASP was used for calculating adsorption energies and activation energies for precursors adsorbing on the surface.

DFT calculation set up is described in each results chapter.

[12] Inhomogeneous system has a spatially varying density $n(r)$.

3.6 A practitioner's guide for DFT calculations

Before starting any DFT calculations there are following questions to answer:

- Which basis set to choose to expand the Kohn-Sham eigenfunctions?
- How to describe core and valence electrons in terms of interactions with the nuclei?
- Which approximation to choose for the exchange-correlation term?

This section is divided following the answers to these questions.

3.6.1 Choosing basis sets

In quantum mechanics the basis set refers to the set of nonorthogonal one-particle functions (called basis functions), that are used to describe molecular orbitals. In practice, we carry out DFT calculations using the Kohn-Sham equation for a non-interacting single-body system in potential $\nu(r)$:

$$\left[-\frac{1}{2}\nabla^2 + \nu(r)\right]\varphi_i(r) = \varepsilon_i\varphi_i(r). \tag{3.10}$$

The Kohn-Sham orbitals φ_i are expanded in suitable basis functions[13] χ_μ:

$$\varphi = \sum_\mu c_{i\mu}\chi_\mu. \tag{3.11}$$

The Kohn-Sham equation is solved for the coefficients $c_{i\mu}$. There are two main types of basis sets that are used in quantum mechanical calculations: local atomic orbital basis sets and planewave basis sets.

Atomic orbital basis sets are usually used for molecule calculations. Atomic orbitals can be described by Slater-type orbital (STO)[14] or Gaussian orbitals (GTO). STO accurately describe molecular orbitals. However, the computation of the integrals is greatly simplified when GTO's are used. Hense, GTO's are the most commonly used functions in computational chemistry as it is much less computationally expensive than STO's.

[13] Here to describe the molecular orbital φ, a linear combination of atomic orbitals (LCAO) is used. It is a commonly used approximation for molecular orbitals.

[14] Slater-type orbital (STO) are the exact hydrogen atomic orbitals

The smallest atomic orbital basis set, that is called a *minimum basis set*, is the one in which on each atom in the molecule a single basis function is used for each type of atomic orbital (s, p, d etc.). When two basis functions are used for each atomic orbital, basis sets are called *double-zeta* and when three basis functions are used, *triple zeta*. There is also a possibility to describe different atomic orbitals in different ways. For example, one may use one basis set for core atomic orbitals and a larger basis for the valence atomic orbitals. In this case, the basis set is called a *split-valence basis set*.

Planewave basis sets are commonly used for periodic boundary calculations, where orbitals are expanded into a finite number of plane-waves. The number of plane waves is described by a cut-off energy $E_{\text{cut–off}}$. It is computationally extremely expensive to describe core electrons using plane-wave basis sets, as core electrons tend to be concentrated close to the nuclei resulting in large wavefunction and density gradients with a much larger cut-off energy required. For this reason, in practice plane-wave basis sets are used in combination with effective core potentials, which are called pseudopotentials, which will be described in the subsection 3.6.2.

3.6.2 Describing core and valence electrons: Pseudopotentials

The computational time can be reduced by simplifying the many electron system by dividing electrons into two groups: outer valence electrons and inner core electrons. Valence electrons are responsible for chemical bonding. For this reason it is possible to ignore core electrons in a solid or large molecule and reduce each atom to an ionic core interacting with valence electrons. A schematic representation of this idea for the silicon atom is shown in Figure 3.4. The potential that is felt by the valence electron interacting with this ionic core is called the pseudopotential.

Pseudopotentials are derived from an atomic reference state. The pseudo- and all-electron valence eigenstates are required to have the same energies and amplitude outside a chosen core cut-off radius. Pseudopotentials with a larger cut-off radius are softer (more rapidly convergent), but at the same time less transferable (less accurate).

There are many different pseudopotentials, such as norm-conserving pseu-

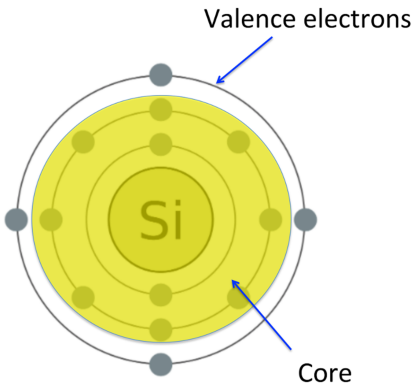


Figure 3.4: A schematic representation of the pseudopotential approximation for a silicon atom. The area in yellow is the ionic core that includes core electrons. The pseudopotential is the potential that is felt by the valence electrons interacting with the core.

dopotentials, [145] atomic pseudopotentials, [146] projector augmented wave method (PAW), [147] and ultra-soft pseudopotentials [148]. Different electronic structure software uses different pseudopotentials.

3.6.3 Choosing approximation for exchange-correlation term

More than 100 functionals have been invented for approximating exchange-correlation ($V_{\mathrm{xc}}[n(r)]$ in eq. 3.7), such as LDA, GGA or hybrid functionals. Any functional can be applied to any electronic structure problem. However, it is important to remember that no functional to date is accurate for all properties of interest. That is why to choose the right functional one must decide which properties of a studied material one is interested in and then use previous experience so as to choose the appropriate exchange-correlation functional for such kind of systems. For some systems and properties of interest LDA performs better, for some GGA. For other properties neither LDA nor GGA is adequate and other approximations must be introduced.

For many cases GGA seems to give reliable results for main types of chemical bonds, such as covalent, ionic, metallic and hydrogen bonds. However, for describing weak interactions, such as the van der Waals interaction, common GGA and LDA are not reliable, especially for total energy calculations and relaxations. To describe van der Waals interactions several specialized approaches have been developed. A description of these approaches can be found

in [149] and [150]. LDA and GGA also fail for strongly correlated systems (where electrons are strongly interacting), such as transition metal oxides and rare earth systems. This problem can be solved by introducing a strong intra-atomic interaction as an on-site adjustment to the LDA or GGA. For example, the LDA+U [151] method takes into account orbital dependence of the Coulomb exchange interactions, which is normally absent in the LDA.

LDA overbinds bond dissociation energies by about 1 eV/bond for thermochemistry. However, LDA typically underestimates bond lengths by 1% (unless involving an H atom). For total energy calculations LDA is accurate to about 7%. [152] GGA reduces LDA overbinding by 2-3% and overcorrects bond lengths to about +1%. [152]

Commonly used GGA functionals are: Pedrew and Wang (PW91) [153] and Perdew-Burke-Ernzerhof (PBE) [154] functionals. Data on performance of LDA and GGA approximations were analyzed in course of lectures of Dr. Kieron Burke and Dr. Lucas Wagner at Department of Physics and Chemistry, University of California, 2011, that can be found online in [155]. More examples on LDA and GGA performance can be found in article by Ziesche et al. [152].

Chapter 4

Investigating the difference in nucleation during Si-based ALD on different Si-based (Si, SiC, SiO_2, Si_3N_4) surfaces for area-selective deposition

4.1 Introduction

The cyclic nature of ALD gives an unparalleled control of the thickness of film deposited. The lateral dimensions of the thin film in the current microchip fabrication process are controlled by patterning. One of the delicate patterning steps is lithography mask alignment, which at smaller scale is prone to misalignment error, which in turn leads to deterioration of device performance. [18] Area-selective atomic layer deposition (AS-ALD) will allow nanostructures of arbitrary composition and lateral shape to be built with atomic precision on pre-selected substrate locations eliminating the misalignment error. Most current approaches for AS-ALD are based on local inhibition (e.g. with self-assembled monolayers) or activation. [18] However, for some applications of AS-ALD (e.g. in self-aligned fabrication) it is desirable to be able to exploit differences in chemical behavior of a pre-patterned substrate. For this reason, investigating inherent differences in nucleation on diverse substrates is of crucial importance for developing future AS-ALD processes.

One of the important criteria for ALD film growth is a self-limiting chemisorption of precursor during the first half-cycle. If the precursor chemisorption step is not efficient, the film growth can be delayed for several ALD cycles. Such a delay is often called nucleation-delay. Nucleation delay can be exploited for area-selective ALD. [156] This delay may reflect a difference in energetics for the precursors reacting with various surface terminations.

In this study we investigate the possibility of area-selective deposition of Si-based materials using aminosilane di(isopropylamino)silane (DIPAS), di(sec-butylamino)silane (DSBAS) and bis(diethylamino)silane (BDEAS) and halide $SiCl_4$ and $SiBr_4$ precursors by analysing the nucleation on four Si-based surfaces (Si:H, SiC:H, SiO_2:OH and Si_3N_4:NH_2/NH). In order to do so the difference in precursor adsorption on these surfaces was investigated by calculating their chemisorption energies using ab-initio modelling (density functional theory, DFT). We found that it is thermodynamically favourable for aminosilane precursors DIPAS, DSBAS and BDEAS to react with Si_3N_4:NH/NH_2 and SiO_2:OH, but not with SiC:H and Si:H suggesting that aminosilane precursors adsorb selectively on Si_3N_4:NH/NH_2 and SiO_2:OH, and not on SiC:H and Si:H.

In order to corroborate the DFT results, silicon nitride (SiN_x) was deposited using plasma-enhanced ALD (PEALD) from the DSBAS precursor and N_2 plasma on three Si-based surfaces. These are (1) H_2 plasma-exposed SiC wafer, (2) HF treated Si wafer and (3) Si wafer with layer of native SiO_2 at 150 °C. The experiment was performed in the Plasma & Materials Processing group in Eindhoven Technological University under the supervision of Dr. Adrie Mackus with collaboration of Dr. Alfredo Mameli during a short-term scientific mission (STSM) funded by COST Action MP1402 'Hooking together European research in atomic layer deposition (HERALD)', supported by COST (European Cooperation in Science and Technology). *In-situ* spectroscopic ellipsometry during the PEALD experiment SiN_x also showed that the DSBAS precursor adsorbs initially on the SiO_2:OH surface (c-Si with native SiO_2), but not on SiC:H (H_2 plasma exposed SiC) and Si:H (HF-last c-Si). Hence, both experiment and DFT calculations predict selective adsorption of DSBAS on SiO_2:OH not on SiC:H and Si:H surfaces. However, DSBAS converts the SiO_2:OH surface to Si-H by depositing its SiH_3 group on the surface and eliminating its amino ligand, after which the selectivity is lost.

4.2 Methodology

4.2.1 DFT modelling

First principles modelling using DFT was performed to calculate adsorption energies of aminosilane and halide precursors reacting with Si:H, SiC:H, SiO_2:OH or Si_3N_4:NH/NH_2 surfaces. Calculations were carried out using the Vienna *ab-initio* simulation package (VASP) [157] version 5.3.5. The Perdew - Burke - Ernzerhof (PBE) functional was used for the exchange-correlation term. The projector augmented wave (PAW) method [147, 157] was used to describe the core electrons of atoms. A plane wave basis set with a cut-off energy 400 eV was used for the valence orbitals. Spin polarized calculations were performed for all the structures. The difference between numbers of electrons in up and down spin components was not set initially. The structures of the gas-phase precursors were optimised in a 15 × 15 × 15 Å cubic cell using the Γ-point in the Brillouin zone. Optimised precursors and slab structures are shown in Figure 4.1 and Figure 4.2, respectively.

Bulk structures were optimised using a 4×4×4 k-point, 2×2×2 k-point, 3×3×3 k-point and 4 × 4 × 4 k-point grid within the Monkhorst - Pack scheme [158] (Γ-point shifted) for Si (001) 1x2, 3C-SiC (001), SiO_2 (001) and Si_3N_4 (100), respectively. The number of k-points was chosen based on k-point convergence tests. The minimum total energy for each optimised bulk material was found for lattice constants 5.43 Å for Si, 4.38 Å for SiC, a = 4.96, c = 5.46 Å for SiO_2 and a = 7.62, c = 2.91 Å for Si_3N_4 which are all in good agreement with experimental data (5.43 Å [159], 4.36 Å [160], a = 4.91, c = 5.41 Å [161] and a = 7.61, c = 2.91 Å [162] for Si, SiC, SiO_2 and Si_3N_4, respectively).

Convergence tests were carried out for bare slab surface energies with respect to slab thickness for different Si, SiO_2, 3C-SiC and Si_3N_4 surface orientations. Si (001) 1x2, 3C-SiC(011) and SiO_2(001) are calculated to have the smallest surface energies of each material, at 0.07 eV/$Å^2$, 0.18 eV/$Å^2$ and 0.12 eV/$Å^2$ [163], respectively. Bare Si_3N_4 (100) with N atoms exposed to the surface was calculated to have the smallest surface energy of 0.15 eV/$Å^2$, slightly smaller than that for the bare Si_3N_4 (001) slab (0.17 eV/$Å^2$). However, the Si_3N_4 (001) surface orientation was chosen for this work because the adsorption energy of the (100) slab did not converge, as will be described below. Si (001) 1x2, 3C-SiC(011), SiO_2(001) and Si_3N_4(001) surfaces were therefore constructed from

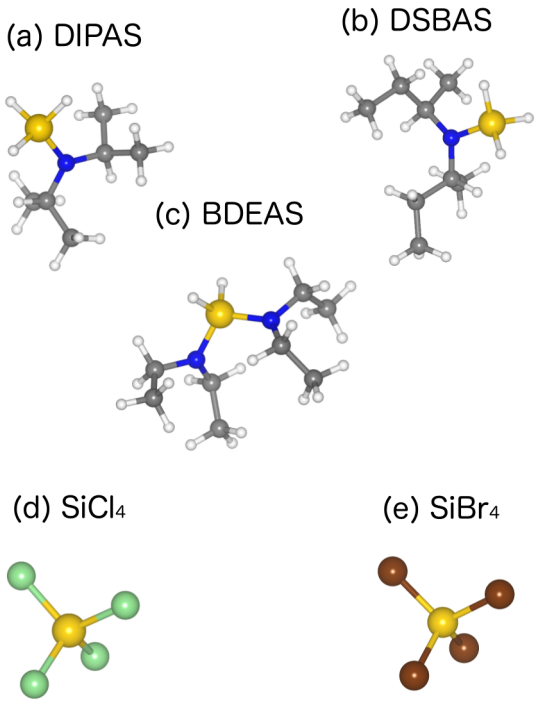


Figure 4.1: Optimised precursor structures. (a) di(isopropylamino)silane (DIPAS), (b) di(sec-butylamino)silane (DSBAS), (c) bis(diethylamino)silane (BDEAS), (d) tetrachlorosilane ($SiCl_4$), (e) tetrabromosilane ($SiBr_4$). Color scheme: yellow=silicon, green=chlorine, white=hydrogen, grey=carbon, blue=nitrogen, brown=bromine.

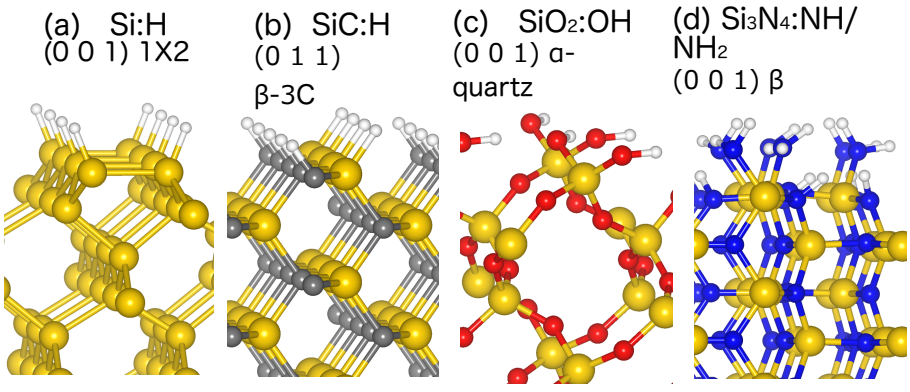


Figure 4.2: Optimised surface slabs (side view). (a) H-terminated Si (Si:H), (b) H-terminated SiC (SiC:H), (c) OH-terminated SiO_2 (SiO_2:OH) and (d) NH/NH_2-terminated Si_3N_4 (Si_3N_4:NH/NH_2) surfaces. Color scheme: yellow=silicon, white=hydrogen, grey=carbon, blue=nitrogen, red=oxygen.

the optimised Si, 3C-SiC, α-SiO_2 and β-Si_3N_4 bulk cells. Cell atoms were not fixed.

H atoms were attached to the bottom and top layer atoms of the Si and SiC slabs to remove their dangling bonds and create H-terminated surfaces. Equal numbers of OH groups were attached to both bottom and top layers of the SiO_2 slab to each Si dangling bond to create a stoichiometric OH-terminated SiO_2 surface. Likewise, equal numbers of NH_2 groups and H atoms were attached to the bottom and top layer atoms of Si and N dangling bonds of Si_3N_4 slab, giving a mixture of NH_2 and NH at the surface. Precursor molecules DIPAS, DSBAS, BDEAS, $SiCl_4$ and $SiBr_4$ were then introduced to the surface in a range of likely adsorption geometries.

A convergence test was done for adsorption energies of $SiCl_4$ reacting with the H-terminated surfaces for different slab thicknesses of two, three, four and five units thick. Our goal was to use the minimum thickness of slab that would give adsorption energies to an accuracy of at least 100 meV. In fact, the difference in adsorption energies between the chosen thickness and the next bigger thickness was less than 10 meV for Si, SiC and SiO_2. However, the adsorption energy for the Si_3N_4 (100) surface with NH_2/NH atoms exposed to the surface, which was calculated to have the smallest surface energy when bare, did not converge. The difference in energies between slabs four and five layers thick persisted at more than 200 meV. However, the Si_3N_4(001) orientation showed an acceptably converged difference in energy of 37 meV between slab thicknesses of three SiN units and four SiN units. The adsorption energy was thus considered to be converged for a slab thickness of 4 units for Si (001) (slab thickness 14.2 Å), of 2 units for SiC (011) (slab thickness 8.65 Å), 3 units for SiO_2 (slab thickness 18.7 Å) and 3 units for Si_3N_4 (001) (slab thickness 13.4 Å), all H-terminated. A vacuum thickness of 15 Å was chosen for the study for all the slabs. The total cell size was therefore 10.9 × 10.9 × 29.2 Å for the H-terminated Si slab, 8.7 × 12.3 × 22.3 Å for the H-terminated SiC slab, 9.9 × 8.6 × 33.7 Å for the OH-terminated SiO_2 slab and 15.2 × 13.2 × 28.4 Å for the NH_2/NH-terminated Si_3N_4 slab.

Adsorption energies ΔE were calculated using:

$$\Delta E = E_{\text{slab + precursor}} + E_{\text{by-products}} - E_{\text{slab}} - E_{\text{precursor}} \tag{4.1}$$

Thus, negative ΔE indicates a decrease in total energy for the system, implying

an exothermic process and energetically favourable adsorption at T=0 K. All energies are reported for T=0 K without consideration of entropy and pressure. No zero-point energy correction is included.

4.2.2 Experimental details

SiN_x PEALD was performed using an Oxford Instruments FlexAL reactor in the Plasma & Materials Processing group in Eindhoven Technological University. The reactor is equipped with a remote inductively-coupled plasma source (ICP), which operated at 600 W of radio frequency power at a frequency of 13.56 MHz. The reactor chamber base pressure of $\sim 10^{-6}$ Torr was obtained by using a turbo pump. A butterfly valve functioned as an automated pressure controller (APC). The chamber wall temperature was set to 150^{o}C. DSBAS precursor (> 99.3%) was synthesized and provided by Air Products and Chemicals Inc. Precursor condensation was prevented by heating the precursor delivery lines to 70^{o}C. The precursor was held at a bubbler temperature of 40^{o}C. Ar (25 sccm, purity 99.999%) was used as a carrier gas for the precursor. During the DSBAS dose the APC valve was completely closed. For the reaction step the APC valve was set to 10^o in order to reduce the effective pumping speed. Any residual gas was removed by purging the precursor delivery lines with 100 sccm of Ar. A continuous flow of inert N_2 gas (50 sccm, purity 99.9999%) was passed through the plasma tube during all process steps to reduce precursor adsorption in the tube. For the purge steps the APC valve was fully open (set to 90^o for maximum pumping).

The process conditions for PEALD of SiN_x using DSBAS and N_2 plasma developed by Faraz [98] were used. As compared to that recipe, precursor and plasma purge step times were increased to 2 s. The step sequence is shown in Table 4.1 and consists of: 1 s delivery line purge, 100 ms DSBAS dose time, 3 s reaction time, 2 s precursor purge time, 2 s preplasma time (gas stabilization prior to plasma ignition), 10 s plasma exposure time, and 1 s plasma purge time.

4.2.3 Substrate preparation

SiN_x growth on Si:H, SiC:H and SiO_2:OH was investigated in this study. The Si:H surface was represented by a Si wafer that was dipped in dilute HF

Table 4.1: PEALD SiN_x process conditions using DSBAS and N_2 plasma

bubbler temperature (°C)	40
precursor dose time (ms)	100
plasma (N_2) exposure time (s)	10
precursor reaction step (s)	3
precursor purge time (s)	2
plasma purge time (s)	2
plasma (N_2) pressure (mTorr)	80
plasma (N_2) gas flow (sccm)	100

(HF/H_2O = 1:100) for 4 min. SiC:H was represented by a SiC wafer cleaned by 5 min H_2 plasma exposure in the ALD load before the deposition. The SiO_2:OH surface was represented by a Si wafer with thin native oxide layer ($\sim$1.5 nm). Si substrates with a native oxide layer were cleaned by 5 min O_2 plasma exposure (8 mTorr O_2, 200 W) before the deposition. All substrates underwent 15 min heating prior to the deposition to ensure substrate temperature stabilization.

4.2.4 Material analysis

Apparent thickness was measured every half-cycle using in situ spectroscopic ellipsometry (SE) on a J.A.Woollam M2000D ellipsometer. The deposited SiN_x layer was fitted using Cauchy parameterization. For SiO_2 a thin native oxide layer 1.5 nm) and SiO_2 layer (440 nm) were added to the model for a Si substrate. The SiN_x substrate optical model consisted of a Si substrate layer, a thin native oxide layer (1.5 nm) and a SiN_x layer (1.2 nm) fitted using Cauchy parameterization. The surface roughness was assumed to be negligible for this process and was not taken into account.

4.3 Results

4.3.1 DFT results on precursor adsorption

The first deposited layer during ALD is of great importance for the nucleation delay during area-selective deposition. A H-terminated surface is likely to exist in growth experiments from the silane that is used during PECVD of Si and SiC.

Ozone or plasma-activated oxygen oxidize the surface intermediates and produce hydroxyl groups on the surface during SiO_2 ALD. Ammonia reacts with unsaturated Si and N sites of Si_3N_4 to form Si–NH_2 and N–H with NH_2 groups more exposed at the surface than NH species. [85] Therefore, in order to investigate the possibility of area-selective deposition of Si-based materials, we analyse the first reaction step of aminosilane (DSBAS, DIPAS, BDEAS) and halide ($SiCl_4$ and $SiBr_4$) precursors reacting with the four Si-based surfaces (Si:H, SiC:H, SiO_2:OH and Si_3N_4:NH_2/NH). Table 4.2 summarises energetics computed with DFT of the precursors reacting with these Si-based surfaces and their chemical reactions.

SiC (011) has both Si and C atoms on the surface and so SiC:H has both Si-H and C-H sites for adsorption. It was found previously that silane plasma fragments react more favourably with Si-H bonds rather than with C-H bonds. [20] With DFT we calculated the energetics for a neutral $SiCl_4$ molecule reacting with Si-H and C-H bonds of SiC:H and here found as well that it is more favourable for $SiCl_4$ to react with the Si-H bond than with the C-H bond with a calculated difference in ΔE of 0.94 eV. Based on this, we further restrict our study to precursors reacting only with the Si-H bond of SiC:H. As NH_2 groups are more exposed to the surface we consider chemical reactions of the precursors with NH_2 and not with NH on the NH_2/NH-Si_3N_4.

Aminosilanes

Many studies have confirmed that loss of the amine ligand is favoured over the loss of the hydride when precursor is adsorbed on the surface (see Chapter 2 section 2.6). [118–120]. Therefore, we calculated the thermodynamics of the first precursor adsorption step where a precursor first reacts with the surface bonds (H-Si of Si surface, H-Si of SiC surface, O-H of SiO_2 and N-H of Si_3N_4), eliminating a protonated amine ligand and leaving an SiH_3 or $SiRH_2$ group on the surface (see Table 4.2). Optimised final structures after the precursors reacted with the surface and ligands were eliminated are presented in Figure 4.3. ΔE are presented in Figure 4.4 and Table 4.2.

DIPAS and DSBAS aminosilanes have one amino ligand as shown in Figure 4.1(a, b). It is thermodynamically favourable for both DIPAS and DSBAS to react with SiO_2:OH and Si_3N_4:NH/NH_2 with calculated ΔE of -0.19 eV and -0.14 eV for DIPAS and -0.21 eV and -0.16 eV for DSBAS on SiO_2 and Si_3N_4, respectively. However, neither of the precursors reacts favorably with Si:H and SiC:H since the calculated ΔE are all positive: 0.10 eV and 0.49 eV for DIPAS

Table 4.2: Chemical reactions and adsorption energies of aminosilane (DIPAS, DSBAS, BDEAS) and halide ($SiCl_4$, $SiBr_4$) precursors reacting with H-terminated Si (Si:H), H-terminated SiC (SiC:H), OH-terminated SiO_2 (SiO_2:OH) and NH/NH_2-terminated Si_3N_4 (Si_3N_4:NH/NH_2) surfaces. Optimised precursor and surfaces structures are shown in Figure 4.1 and Figure 4.2, respectively. ^{i}Pr is for iso-propyl group, sBu is for sec-butyl group, Et is for ethyl group, index "S" is for the surface atoms.

Precursor	Surface	Reaction	ΔE, eV
DIPAS	Si	$H_3SiN(iPr)_2(g) + H–Si_S \longrightarrow HN(iPr)_2(g) + H_3Si–Si_S$	0.10
	SiC	$H_3SiN(iPr)_2(g) + H–Si_S \longrightarrow HN(iPr)_2(g) + H_3Si–Si_S$	0.49
	SiO_2	$H_3SiN(iPr)_2(g) + H–O_S \longrightarrow HN(iPr)_2(g) + H_3Si–O_S$	-0.19
	Si_3N_4	$H_3SiN(iPr)_2(g) + H–N_SH \longrightarrow HN(iPr)_2(g) + H_3Si–N_SH$	-0.14
DSBAS	Si	$H_3SiN(sBu)_2(g) + H–Si_S \longrightarrow HN(sBu)_2(g) + H_3Si–Si_S$	0.08
	SiC	$H_3SiN(sBu)_2(g) + H–Si_S \longrightarrow HN(sBu)_2(g) + H_3Si–Si_S$	0.46
	SiO_2	$H_3SiN(sBu)_2(g) + H–O_S \longrightarrow HN(sBu)_2(g) + H_3Si–O_S$	-0.21
	Si_3N_4	$H_3SiN(sBu)_2(g) + H–N_SH \longrightarrow HN(sBu)_2(g) + H_3Si–N_SH$	-0.16
BDEAS	Si	$H_2Si(NEt_2)_2(g) + H–Si_S \longrightarrow HNEt_2(g) + H_2SiNEt_2–Si_S$	-0.01
	SiC	$H_2Si(NEt_2)_2(g) + H–Si_S \longrightarrow HNEt_2(g) + H_2SiNEt_2–Si_S$	1.04
	SiO_2	$H_2Si(NEt_2)_2(g) + H–O_S \longrightarrow HNEt_2(g) + H_2SiNEt_2–O_S$	-0.18
	Si_3N_4	$H_2Si(NEt_2)_2(g) + H–N_SH \longrightarrow HNEt_2(g) + H_2SiNEt_2–N_SH$	-0.03
$SiCl_4$	Si	$SiCl_4(g) + H–Si_S \longrightarrow HCl(g) + Cl_3Si–Si_S$	0.64
	SiC	$SiCl_4(g) + H–Si_S \longrightarrow HCl(g) + Cl_3Si–Si_S$	1.17
	SiO_2	$SiCl_4(g) + H–O_S \longrightarrow HCl(g) + Cl_3Si–O_S$	0.35
	Si_3N_4	$SiCl_4(g) + H–N_SH \longrightarrow HCl(g) + Cl_3Si–N_SH$	0.12
$SiBr_4$	Si	$SiBr_4(g) + H–Si_S \longrightarrow HBr(g) + Br_3Si–Si_S$	0.58
	SiC	$SiBr_4(g) + H–Si_S \longrightarrow HBr(g) + Br_3Si–Si_S$	1.12
	SiO_2	$SiBr_4(g) + H–O_S \longrightarrow HBr(g) + Br_3Si–O_S$	0.28
	Si_3N_4	$SiBr_4(g) + H–N_SH \longrightarrow HBr(g) + Br_3Si–N_SH$	0.16

and 0.08 eV and 0.46 eV for DSBAS on Si and SiC, respectively (see Figure 4.4). We note that ΔE for DIPAS and DSBAS agree to within $\pm$0.05 eV across the range of substrates. This may be expected since the only difference is one extra CH_3 group on the eliminated by-product. Regarding substrates, the greatest difference in energies are between adsorption onto SiC and adsorption onto SiO_2 (differences of 0.68 eV and 0.67 eV for DIPAS and DSBAS, respectively, see Figure 4.4). This means that when DIPAS or DSBAS precursors are used for ALD of Si-based materials, a delay in growth on SiC compared to SiO_2 is expected.

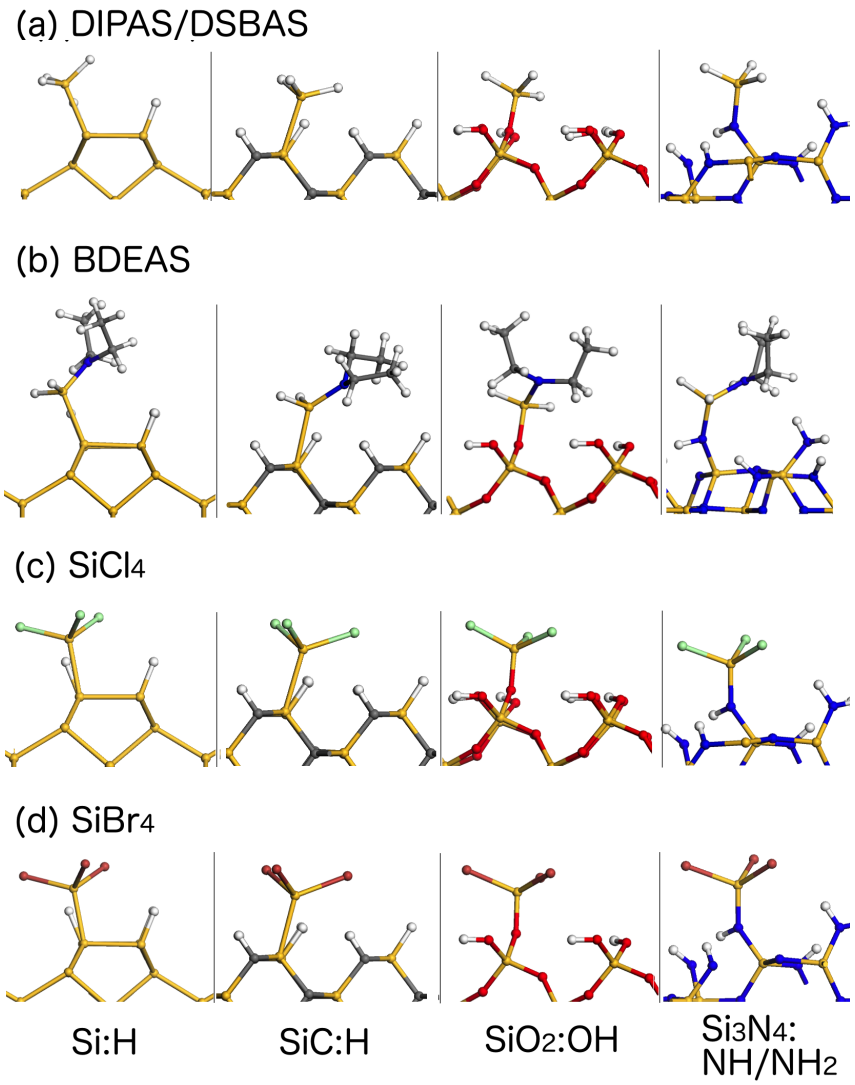


Figure 4.3: Optimised structrures after precursors a) DIPAS/DSBAS b) BDEAS c) $SiCl_4$ d) $SiBr_4$ reacted with terminated Si:H, SiC:H, SiO_2:OH, Si_3N_4:NH/NH_2 surfaces (side view) and the ligands were eliminated. Color scheme: yellow=silicon, green=chlorine, white=hydrogen, grey=carbon, dark blue=nitrogen, brown=bromine, red=oxygen.

BDEAS has two amino ligands as shown in Figure 4.1(c). We consider the first reaction step for the BDEAS precursor approaching the surfaces, where one ethylamino ligand is eliminated and the second is bonded to the surface group (see Figure 4.3(b)). On most substrates, BDEAS shows quantitatively a similar behaviour to DIPAS and DSBAS. ΔE of -0.18 eV for BDEAS reacting with the SiO_2:OH surface is nearly the same as for DIPAS. Slightly negative ΔE is also calculated for BDEAS reacting with the Si_3N_4:NH and Si:H surfaces (-0.03 eV and -0.01 eV, respectively). However, ΔE=1.04 eV is computed for BDEAS reacting with SiC, which is nearly 0.6 eV higher than that for DIPAS and DSBAS.

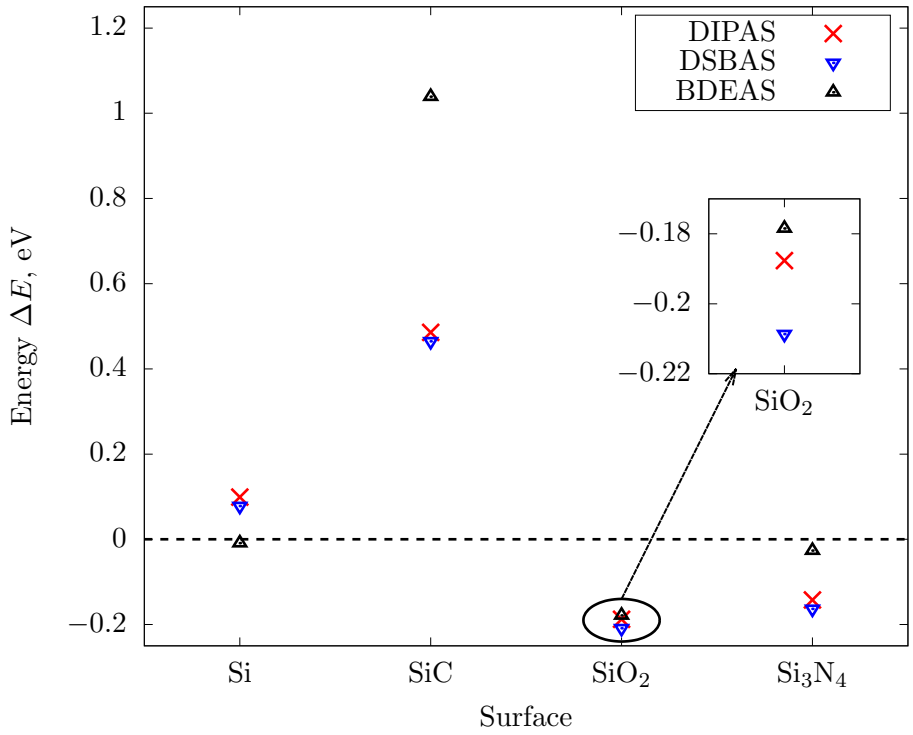


Figure 4.4: ΔE for aminosilane precursors reacting with Si:H, SiC:H, SiO_2:OH and Si_3N_4:NH/NH_2. ΔE values and chemical reactions are presented in Table 4.2.

Comparing substrates, the greatest difference in ΔE is again between SiC and SiO_2 (1.22 eV for BDEAS). Therefore for BDEAS, similar to DIPAS and DSBAS, a delay in growth is expected on SiC compared to SiO_2, and the same behaviour is likely for all aminosilane analogues.

Halides

It was calculated to be thermodynamically not favourable for either of the halide precursors $SiCl_4$ and $SiBr_4$ to react with all the considered surfaces at 0 K (see Figure 4.5 and Table 4.2). The most positive ΔE values were calculated for precursors reacting with the SiC:H (1.17 eV and 1.12 eV for $SiCl_4$ and $SiBr_4$, respectively) and Si:H (0.64 eV and 0.58 eV for $SiCl_4$ and $SiBr_4$, respectively) surfaces. The smallest ΔE was calculated for Si_3N_4:NH (0.12 eV and 0.16 eV for $SiCl_4$ and $SiBr_4$, respectively) with a slightly higher ΔE for SiO_2:OH (0.35 eV and 0.28 eV for $SiCl_4$ and $SiBr_4$, respectively). This means that, similar to the aminosilane case, the greatest difference in ΔE is calculated between Si_3N_4 and SiC (1.05 eV and 0.96 eV, respectively). We also note that ΔE for $SiCl_4$ and $SiBr_4$ agree to within ± 0.07 eV across the range of substrates.

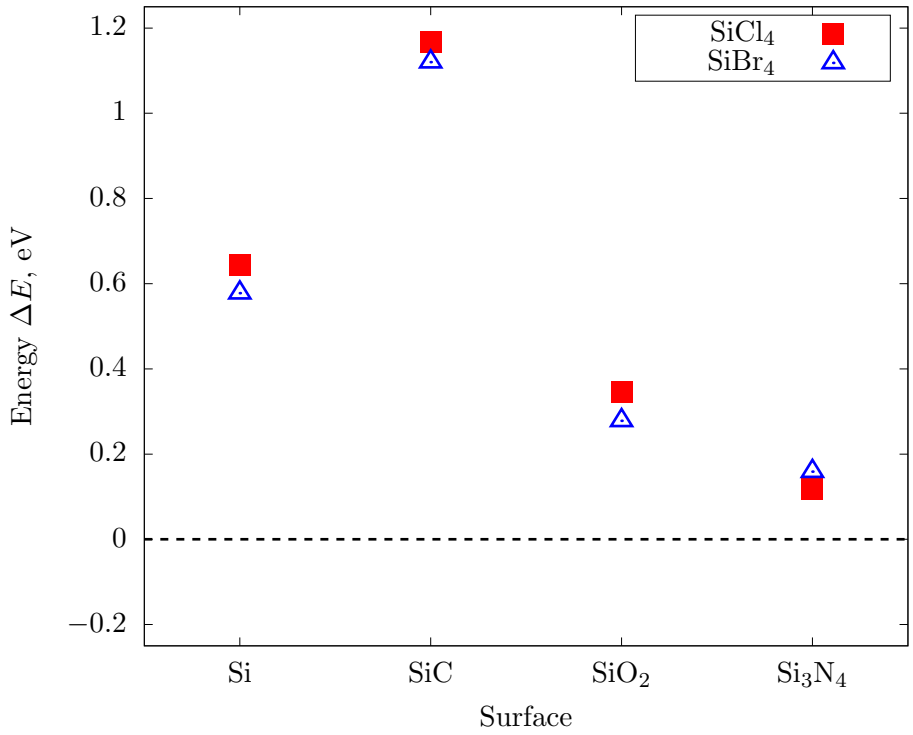


Figure 4.5: ΔE for halide precursors reacting with Si:H, SiC:H, SiO_2:OH and Si_3N_4:NH/NH_2. ΔE values and chemical reactions are presented in Table 4.2.

4.3.2 Spectroscopic ellipsometry (SE) results on precursor adsorption

To experimentally corroborate the DFT results, SiN_x was deposited using plasma-enhanced ALD from the DSBAS precursor and N_2 plasma at 150 °C. Deposition was done on the surfaces that closely represent our theoretical models, i.e. Si wafer with native oxide (SiO_2:OH) [164], HF-last Si (Si:H) [165, 166] and H_2 plasma treated SiC wafer (SiC:H) [167].

The thickness of SiN_x film as a function of number of ALD cycles measured by *in-situ* spectroscopic ellipsometry (SE) is presented in Figure 4.6. The graph shows that SiN_x grows without any nucleation delay on all the considered surfaces. A growth per cycle of approximately 0.12 Å was obtained. This growth per cycle corresponds to that of the existing SiN_x ALD process using DSBAS and N_2 plasma (see Chapter 2 section 2.6). [98]

In order to understand how SiN_x growth happens after the DSBAS and N_2 pulses, SE measurements were done after every ALD half-cycle. Apparent thickness as a function of half-cycle is presented in Figure 4.7. The SE signal is an

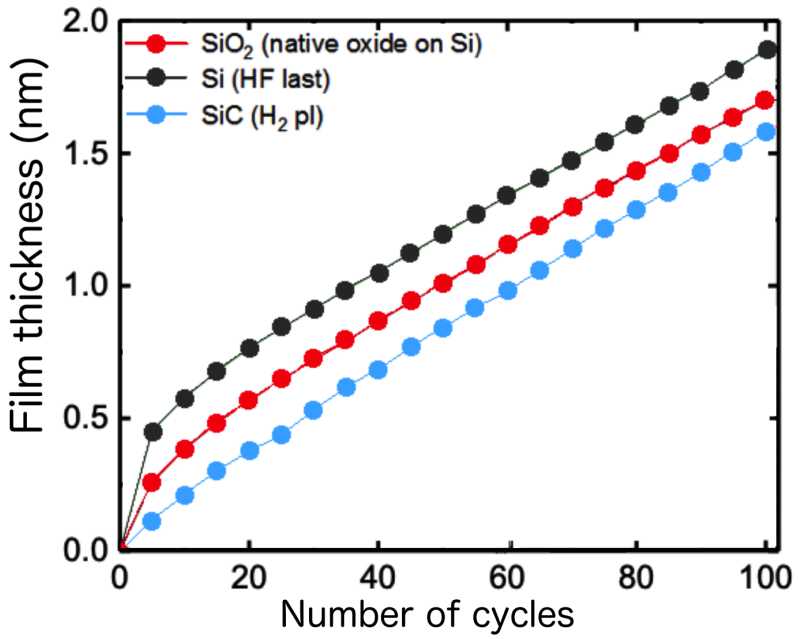


Figure 4.6: SiN_x film thickness as a function of ALD cycle using DSBAS precursor and N_2 plasma as a co-reagent on SiO_2:OH (Si wafer with native oxide), Si:H (HF-last Si) and SiC:H (H_2 plasma treated SiC wafer) surfaces. The graph shows the thickness as a function of the number of the cycles measures by *in-situ* spectroscopic ellipsometry (SE).

indirect measure of the amount of adsorbed material and therefore it is called apparent thickness. The dielectric function of the surface layers after every half-cycle is expected to be different from the bulk dielectric function. No separate surface layer is added to the model as the surface layer is very thick and cannot be easily distinguished from the bulk. Therefore, the changes in apparent thickness are a combination of a physical change in film thickness and a change in optical properties of the surface layer. The magnitude of such a change is only an approximation of the real change in physical thickness. [168]

The data for SiO_2 in Figure 4.7 show an apparent thickness increase after the first DSBAS dose suggesting that DSBAS adsorbs on the SiO_2 surface. The apparent thickness on Si and SiC after the first, second and third DSBAS half-cycles did not change. This suggests that DSBAS does not adsorb on the Si and SiC surfaces.

The apparent thickness for all the substrates increases during or after the N_2 pulse. This suggests that N_2 plasma adsorbs on the SiH_3 surface groups of all the considered surfaces. The apparent thickness for the Si:H substrate increases

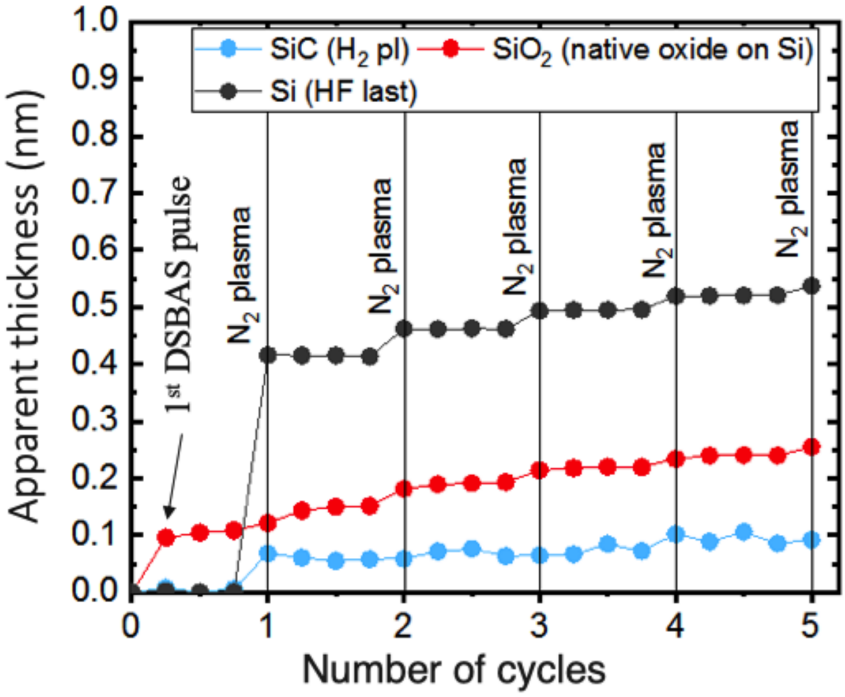


Figure 4.7: Apparent thickness as measured after every DSBAS and N_2 half-cycles during PEALD of SiN_x at 150 °C.

significantly after the first N_2 pulse compared to that for the SiC:H and SiO_2:OH surfaces.

4.3.3 Discussions

DFT calculations showed that it is not thermodynamically favourable for halide precursors $SiCl_4$ and $SiBr_4$ to adsorb on the Si, SiC, SiO_2 and Si_3N_4 surfaces. On the other hand aminosilane precursors were predicted to adsorb on SiO_2 and Si_3N_4 surfaces. The differences between the most negative ΔE for $SiCl_4$ and the most positive ΔE for DSBAS was estimated to be 0.53 eV for the SiO_2 surface and 0.32 eV for the Si_3N_4 surface. Murray et al. [92] also predicted that amide ligands are themodynamically more reactive than chloride ligands with respect to elimination in SiO_2 and SiN_x ALD by about 0.5 - 0.7 eV per ligand according to DFT cluster calculations. Huang et al. [123] used DFT to suggest that it is easier for aminosilane precursors BDEAS and BTBAS to enter the transition state than for chlorosilane precursors. Activation energies for aminosilane precursors adsorbing onto NH_2-Si_3N_4 were calculated to be 1.38 eV, which is lower than for chlorosilanes (an activation energy of 3.55 eV was calculated for Si_2Cl_6

reacting with NH_2-Si_3N_4 [58]). Hence, even at the high temperatures where aminosilanes can overcome the barrier for adsorption (1.38 eV), it will still be unfavourable for halide precursors to adsorb onto the NH_2-Si_3N_4 surface, as this requires an even higher barrier (3.55 eV) to be overcome.

Based on DFT calculations at 0 K we predicted that DSBAS will adsorb selectively on SiO_2:OH and not on SiC:H and Si:H surfaces. It was found in experiment that the apparent thickness of the grown film increases for SiO_2:OH surface and does not change for the Si:H and SiC:H substrate surfaces after the first DSBAS pulse. This validates the DFT calculations.

The difference in reactivity of the DSBAS precursor can be explained by different polarities of the surface groups, which can be crudely written as O^-–H^+ bond on SiO_2, N^-–H^+ on SiN_x, and Si^+–H^- on Si and SiC surfaces. The slightly negative nitrogen of the DSBAS precursor [169] has no difficulties approaching and hydrogen bonding with the slightly positive H atom of the SiO_2 and SiN_x surfaces. In contrast the H surface atom of Si:H and SiC:H surfaces is slightly negative and access of DSBAS to its electron pair is hindered. The even higher ΔE values for DSBAS interacting with H-Si bond of SiC surfaces compared to H-Si of Si:H surface (0.46 eV and 0.08 eV, respectively) can be explained by different electonegativity of the Si and C atoms. The surface carbon atom has higher electronegativity (2.2 [170]) than the Si atom (1.6 [170]) making the Si atom of Si-C bond slightly positive, which therefore pulls electrons from the H surface atom of the H-Si bond.

The apparent thickness has increased for all the surfaces when measured after the N_2 plasma pulse. This means that N_2 plasma reacts with the SiH_3 surface groups on all the considered surfaces allowing the SiN_x growth. Figure 4.6 shows SiN_x growth on SiO_2:OH, Si:H and SiC:H surfaces with a growth rate of 0.12 Å/cycle. This means that even though the DSBAS adsorbs selectively on the SiO_2:OH surface, N_2 plasma nitridates all surfaces allowing the growth. The selectivity of the surfaces is lost after the DSBAS dose. DSBAS is predicted to not adsorb on Si:H and SiC:H surfaces, as these are both terminated with Si-H bonds. However, DSBAS adsorbs on SiO_2:OH and SiN_x:NH/NH_2 converting these surface to Si-H terminated surfaces as well. Hence, all the surfaces after the DSBAS dose are predicted to be terminated with Si-H bonds (see Figure 4.3), which further are reacting with N_2 plasma and being turned into SiN_x surfaces.

DFT predicts DSBAS to adsorb on the SiO_2:OH surface during the first precursor

half-cycle leaving a silicon oxide surface covered with SiH_3 groups and eliminating its amino ligands. The apparent thickness increases after the first DSBAS dose indicating that SiH_3 groups indeed adsorb on the surface (see Figure 4.7). Hence, the dielectric function of the bulk silicon oxide before the DSBAS half-cycle clearly differs from the dielectric function of the bulk silicon oxide covered with SiH_3 groups after the DSBAS half-cycle. By contrast, for Si:H and SiC:H such a change in apparent thickness is not observed, which can be interpreted as meaning that DSBAS did not react with the surfaces. However, it is worth bearing in mind that adsorption of DSBAS would lead to the deposition of a layer of SiH_3 groups. The dielectric function for Si:H before the DSBAS pulse and an SiH_3-covered surface afterwards possibly will not differ and thus would not be detected by SE.

The N_2 plasma is expected to nitridate the surface. Hence, after the first N_2 plasma pulse all the surfaces are expected to be SiN_x surfaces. DFT predicts that DSBAS will adsorb on SiN_x surfaces with calculated ΔE = -0.16 eV. On all substrates one would therefore expect an increase of the apparent thickness after the DSBAS pulse in the second cycle. However the experimental SE results do not confirm this. Figure 4.7 shows that the apparent thickness does not change after the N_2 pulse for the Si:H surface. Furthermore, during the subsequent N_2 pulses, the apparent thickness continues to increase for the Si:H surface. This suggests that the first N_2 pulse was not sufficiently long to fully nitridate the substrate, leaving a mixture of Si-H and N-H groups on the surface. Thus, the dielectric function of the Si-SiH_3 and NH-SiH_3 surfaces after the second DSBAS half-cycle does not apparently differ from the dielectric function of the Si substrate with a mixture of Si-H and N-H groups on the surface.

This interpretation of the SE results is consistent with the DFT data, but does not provide definitive validation. We suggest that alternative experimental characterization is required in order to confirm that DSBAS does not react with Si:H and SiC:H surfaces and does react with SiN_x surfaces, such as FTIR.

It can be observed that DFT calculations of minima at 0 K predicted the experimental results at 150 °C well. Thus, bonding at 0 K is enough to predict selective deposition at low ALD temperatures. In general, the temperature and entropy effects can be included using the formula $\Delta G = \Delta E - T\Delta S$ (see Chapter 5). The entropy for the surfaces can be assumed to be zero. Hence, in order to evaluate ΔS of the reactions, the entropies of precursor and by-product must be calculated. For precursors with one amino ligand, such as DIPAS and DSBAS,

the entropy of the by-product ($HN(^iPr)_2$ or $HN(sBu)_2$ for DIPAS and DSBAS, respectively) and precursor are expected to be similar and ΔS is expected to be very small. Hence, including temperature and entropy effects is not expected to appreciably change the calculated ΔE. For BDEAS the entropy of the two by-product molecules ($HNEt_2$) is expected to be higher than the entropy of the BDEAS precursor. Thus, including $T\Delta S$ will decrease the calculated ΔE possibly shifting all the calculated ΔE towards negative values and losing the predicted selectivity for BDEAS adsorption. That is why low temperature is of a crucial importance for area-selective deposition. Including the entropy of the halide precursors is expected to increase the calculated ΔE values, making reactions more endothermic. For example, the entropies of the $SiCl_4$ precursor and HCl by-product were calculated to be 0.005 eV/K and 0.002 eV/K, respectively, at 400 °C (see Chapter 5). Hence, for $SiCl_4$ reacting with all the considered surfaces, including entropy (ΔS=-0.003 eV/K) and temperature effects at 400 °C will increase the calculated ΔE by 2.02 eV.

4.3.4 Conclusion

In order to investigate the possibility of area-selective deposition of Si-based materials using aminosilane and halide precursors, nucleation on four different Si-based surfaces (Si:H, SiC:H, SiO_2:OH and Si_3N_4:NH_2/NH) was analysed. The difference in precursor adsorption on these surfaces during exposure to the aminosilane and the halide precursors by calculating their chemisorption energies was analyzed using DFT. The theoretical results were corraborated by measuring the apparent thickness of the SiN_x film deposited by PEALD from the DSBAS precursor and N_2 plasma after every ALD half-cycle using *in-situ* spectroscopic ellipsometry.

Both DFT calculations and PEALD experiments show the selective adsorption of the DSBAS aminosilane precursor on SiO_2:OH and not on the Si:H and the SiC:H surfaces. However, after DSBAS is adsorbed on the SiO_2:OH surface and amino ligands are eliminated, the SiO_2:OH surface gets covered with SiH_3 groups leaving it terminated with Si-H, similar to the Si:H and the SiC:H surfaces, which means that the selectivity is lost. N_2 plasma further converts these Si-H terminated surfaces to reactive SiN_x surfaces. These results illustrate that it is generally difficult to achieve area-selective PEALD of nitrides, because of the nitridation of all exposed substrate surfaces during the plasma step. In ad-

dition, aminosilane precursors remove selectivity with respect to H-terminated Si surfaces, because they act as sources of Si-H.

Our results highlight the role of DFT calculations in predicting possible routes towards area selective ALD process development. It was shown that quick and simple thermodynamic DFT calculations of minima at 0 K are enough to predict the selective precursor adsorption at 150 °C well. This approach can be also used for the high-throughput precursor screening for the future area-selective ALD applications, since after the surface energies are obtained, the energetics of various gas-phase precursor molecules reacting with each surface can be rapidly evaluated. We make use of this approach for metal oxide ALD in Chapter 7.

It was also shown that in order to definitively detect the adsorbed species after every ALD half-cycle, extra surface characterization is needed as an alternative to spectroscopic ellipsometry. For example, SE results do not measure the growth of SiN_x on the SiN_x surface that is predicted by DFT and expected to be present on all of the considered surfaces after the first N_2 plasma step. Furthermore, this SE model is possibly not sensitive enough to measure whether there are SiH_3 groups on the surface after the first DSBAS half-cycle on the Si:H and the SiC:H surfaces.

Chapter 5

SiC precursor screening

5.1 Abstract

Silicon carbide SiC is a promising material for electronics due to its hardness, ability to carry high currents and high operating temperature. SiC films are currently deposited using chemical vapour deposition (CVD) at high temperatures 1500 - 1600°C. However, there is a need to deposit SiC-based films on the surface of high aspect ratio features at low temperatures. One of the most precise thin film deposition techniques on high-aspect-ratio surfaces that operates at low temperatures is atomic layer deposition (ALD). However, there are currently no known methods for ALD of SiC. Herein, we present a first-principles thermodynamic analysis so as to screen different precursor combinations for SiC thin films. We do this by calculating the Gibbs energy ΔG of the reaction using density functional theory (DFT) and including the effects of pressure and temperature. This theoretical model was validated for existing chemical reactions in CVD of SiC at 1000°C. The precursors disilane (Si_2H_6), silane (SiH_4) or monochlorosilane(SiH_3Cl) with ethyne (C_2H_2), carbontetrachloride (CCl_4) or trichloromethane ($CHCl_3$) were predicted to be the most promising for ALD of SiC at 400°C.

5.2 Introduction

Silicon carbide SiC is a promising material for electronic devices. It is harder than Si and can sustain higher voltages, carry higher currents and operate at

higher temperatures. There is a need to deposit SiC-based films on the surface of high aspect ratio features for various applications for electronics, e.g. low-k spacers/liners and air gap liners for interlayer dielectric, exploiting the low dielectric constant (<5) and low wet etch rate of SiC.

SiC occurs naturally in different crystal polytypes. The most common polytypes being developed for electronics are 3C, 4H and 6H. [171]

SiC-based films are currently deposited using chemical vapour deposition (CVD). This technique is operated at elevated temperatures 1500 - 1600°C and may suffer from non-uniformity due to fast surface reactions. [12] As explained in chapter 1, one of the most precise thin film growth techniques is a variant of CVD called atomic layer deposition (ALD). Thin films deposited by ALD or plasma-enhanced ALD (PEALD) are highly conformal even on high-aspect-ratio surfaces and are grown at low temperatures (e.g. < 400°C). However, there are currently no known low temperature methods for ALD of SiC.

The most commonly used precursors in SiC CVD growth are silane (SiH_4) [172–174] as a silicon precursor, and propane (C_3H_8) [172, 174–177] or ethylene (C_2H_4) [178, 179] as a carbon precursor. [180] They provide a better morphology and higher growth rate than other precursors. [181] However, many different precursors apart from those mentioned above were used for CVD of SiC. Nine different carbon precursors (methane (CH_4), ethane (C_2H_6), ethyne (C_2H_2), ethylene (C_2H_4), propane (C_3H_8), propene (C_3H_6), propadiene (C_3H_4), propyne (C_3H_4), butane (C_4H_{10})) with silane (SiH_4) were analysed by C. Hallin *et al.* [173] for the CVD growth of 4H and 6H SiC epitaxial layers, in the temperature range 1550 -1600°C. The most stable growth at high growth rates was achieved with propane (C_3H_8). [173] For silicon precursors besides silane (SiH_4) the most commonly used are chlorosilanes, such as dichlorosilane SiH_2Cl_2 (DCS), [174] trichlorosilane $SiHCl_3$ (TCS), [178] methyltrichlorosilane $SiCH_3Cl_3$ (MTS) [182] and tetrachlorosilane $SiCl_4$ (TET) [183]. TET ($SiCl_4$) and TCS ($SiHCl_3$) are the most common. [181] A review of chloride-based CVD growth of SiC was done by Pedersen *et al.*. [184] Single-source precursors (containing both Si and C in the same molecule) have also been used for CVD of SiC. [185] These precursors include: MTS ($SiCH_3Cl_3$), methylsilane (CH_3–SiH_3), [186] diethylmethylsilane ($(C_2H_5)_2SiHCH_3$), [187] tetramethylsilane ($Si(CH_3)_4$), [188] hexamethyldisilane ($Si_2(CH_3)_6$), [188] silacyclobutane ($SiH_2(CH_2)_3$), [189] and 1,3-disilabutane (SiH_3–CH_2–SiH_2–CH_3). [185]

As was mentioned above, experimentalists are facing difficulties in growing SiC films by ALD or PEALD. Theoretical modelling of ALD using density functional theory (DFT) provides a complementary view to the experimental techniques. DFT is usually used to calculate the pathways for precursor adsorption, ligand migration and by-product formation on the surface, yielding reaction energies and activation energies for each step of the ALD cycle. A review of previous theoretical studies of Si-based materials can be found in [135]. In this paper we present a theoretical thermodynamic analysis of different precursor combinations for SiC deposition thin film by calculating Gibbs energy ΔG using DFT as implemented in TURBOMOLE [190] and VASP [157] software. The effects of CVD conditions (1000°C) and ALD conditions (400°C) are evaluated. It is found that chemical reactions of disilane (Si_2H_6), silane (SiH_4), monochlorosilane (SiH_3Cl) or DCS (SiH_2Cl_2) precursors with all suggested carbon precursors are thermodynamically favourable. The most negative ΔG are for disilane (Si_2H_6), silane (SiH_4), monochlorosilane (SiH_3Cl), ethyne (C_2H_2), carbontetrachloride (CCl_4) and trichloromethane ($CHCl_3$). Hence, silane (SiH_4), disilane (Si_2H_6), monochlorosilane (SiH_3Cl), ethyne (C_2H_2), carbontetrachloride (CCl_4) and trichloromethane ($CHCl_3$) can be predicted to be the most favourable precursors for ALD of SiC thin films.

5.3 Methodology

Atomic-scale modelling was performed to investigate routes towards the ALD of SiC-based films using first principles calculations based on DFT. All precursors were modelled as isolated molecules in vacuum using the TURBOMOLE software. [190] Optimized structures of the Si and C precursors are shown in Fig. 5.1. The generalized gradient approximation to DFT [191] was implemented by using the exchange correlation functional of Perdew, Burke and Ernzerhof (PBE) [191]. The atom-centred basis set def2-TZVPP was used for all the atoms [192] along with an auxiliary basis set for the density within the resolution of identity (RI) approximation. [193, 194]

The energy for SiC-3C bulk was obtained using the Vienna ab-initio simulation package (VASP) [157] also with the PBE exchange-correlation functional. The projector augmented wave (PAW) method [147, 157] was used to describe the core electrons of atoms. A plane wave basis set with a cut-off energy 400 eV was used for the valence orbitals. An 8x8x8 k-point grid within the Monkhorst–Pack

scheme in the Brillioun zone was employed. Full geometry relaxation was carried out using the conjugate gradient method for energy minimization at convergence level of 0.01 eV/Å on each ion.

Reaction energetics for SiC from various silicon and carbon precursors were evaluated using the general formula in eq. 5.1, assuming that by-products of the reactions were CH_4, HCl, Cl_2 and H_2 where applicable. For the purpose of this analysis, competing reactions to formation of SiC are not considered.

$$\begin{aligned} n\mathrm{Si}_a\mathrm{X}_b + a\mathrm{C}_n\mathrm{Y}_m \longrightarrow an\mathrm{SiC} + am\mathrm{XY} + \frac{nb-am}{2}\mathrm{X}_2 \\ \text{if } nb > am; \\ n\mathrm{Si}_a\mathrm{X}_b + a\mathrm{C}_n\mathrm{Y}_m \longrightarrow an\mathrm{SiC} + nb\mathrm{XY} + \frac{am-nb}{2}\mathrm{Y}_2 \\ \text{if } nb < am. \end{aligned} \tag{5.1}$$

For example, for $SiCl_4$ (X=Cl, a=1, b=4) and C_2H_6 (Y=H, n=2, m=6) eq. 5.1 becomes:

$$2\,\mathrm{SiCl}_4 + \mathrm{C}_2\mathrm{H}_6 \longrightarrow 2\,\mathrm{SiC} + 6\,\mathrm{HCl} + \mathrm{Cl}_2 \tag{5.2}$$

A list of all the analysed reactions is presented in Appendix A.

Gibbs energies ΔG were calculated for these reactions using eq. 5.3:

$$\Delta G = \Delta E - T\Delta S + RT\ln Q \tag{5.3}$$

where $\Delta E = \sum E_{\text{products}} - \sum E_{\text{reactants}}$ using ground state energies obtained from DFT calculations, ΔS are entropies at temperature T obtained from DFT calculations in TURBOMOLE, assuming that S_{SiC}=0, and reaction quotient $Q = \prod P^{\mu}_{\text{products}} / \prod P^{\mu}_{\text{reactants}}$, where partial pressures of products are P_{products}=0.01 Torr, partial pressures of reactants $P_{\text{reactants}}$=1 Torr and μ are stoichiometric coefficients. Partial pressures were chosen in correspondence with experimental ALD data. ΔG indicates whether a reaction is thermodynamically favourable.

In VASP the one-electron orbitals are expressed in plane wave basis sets, which makes it inefficient and time-consuming for calculating gas-phase molecules, while bulk SiC can be easily simulated with VASP. Therefore we use a refer-

ence gas-phase molecule to estimate energies for bulk SiC in TURBOMOLE. We choose gas-phase tetramethylsilane $Si(CH_3)_4$ as a reference molecule for SiC. It contains Si-C bonds like SiC. First ΔE_1 is computed with VASP for decomposition of the reference molecule using eq. 5.4:

$$Si(CH_3)_4(g) \longrightarrow SiC(s) + 3\,CH_4(g) \tag{5.4}$$

Calculations for $Si(CH_3)_4(g)$ and $CH_4(g)$ molecules were done at single Γ - point in the Brillioun zone at convergence level for the forces on each ion of 0.01 eV/Å. The size of the cell was chosen as 15x15x15 Å. ΔE_1 is calculated only once. Then ΔE_2 is computed for the gas-phase reaction to the reference molecule with TURBOMOLE for each X and Y using eq. 5.5:

$$\begin{aligned} n\mathrm{Si}_a\mathrm{X}_b(g) + a\mathrm{C}_n\mathrm{Y}_m(g) + 3an\mathrm{CH}_4(g) &\longrightarrow \\ an\mathrm{Si}(\mathrm{CH}_3)_4(g) + am\mathrm{XY}(g) + \frac{nb-am}{2}\mathrm{X}_2(g) & \\ \text{if } nb > am; & \\ n\mathrm{Si}_a\mathrm{X}_b(g) + a\mathrm{C}_n\mathrm{Y}_m + 3an\mathrm{CH}_4(g) &\longrightarrow \\ an\mathrm{Si}(\mathrm{CH}_3)_4(g) + nb\mathrm{XY}(g) + \frac{am-nb}{2}\mathrm{Y}_2(g) & \\ \text{if } nb < am. & \end{aligned} \tag{5.5}$$

For the example above eq. 5.5 becomes:

$$\begin{aligned} 2\,SiCl_4(g) + C_2H_6(g) + 6\,CH_4(g) &\longrightarrow \\ 2\,Si(CH_3)_4(g) + 6\,HCl(g) + Cl_2(g) & \end{aligned} \tag{5.6}$$

The final corrected ΔE_3 that we use for calculating Gibbs energy ΔG in eq. 5.3 will be a sum of ΔE_2 and ΔE_1. This approach can be represented as a Hess cycle; see Fig. 5.2 for the example of $2\,SiCl_4 + C_2H_6 \longrightarrow 2\,SiC + 6\,HCl + Cl_2$. The difference between ΔE computed in VASP and in TURBOMOLE for this sample reaction of eq. 5.6 is just 0.0002 eV, well within the precision of the method.

Including the effects of temperature allowed us to validate the approach for known precursor combinations for CVD at 1000°C. Furthermore, reaction energetics were calculated at 400°C to predict precursors for ALD of SiC at around this temperature.

ΔG (A(g) + B(g) $\longrightarrow$ AB(s) + C(g)) reflects the actual thermodynamics of the CVD reaction. If $\Delta G < 0$ the reaction is permitted and $\Delta G > 0$ means that it is not permitted. By contrast, in an ALD process, reactants A(g) and B(g) do not meet in the reactor, but ΔG (A(g) + B(g) $\longrightarrow$ AB(s) + C(g)) is still relevant for describing the ALD process. Our finding so far with ALD has been that formation of A-B bonds in the solid product is the main driving force for the process (and that formation of by-product C plays a secondary role). The A+B reaction is thus a way of measuring this driving force. [135] The actual surface reaction steps in each ALD cycle are (i) unknown for SiC, (ii) expected to be quite complex and (iii) dependent on kinetics of each step (because ALD is performed at lower T than CVD). It is therefore not possible to screen a wide range of chemicals for their actual detailed behaviour in ALD. Instead, we use the simple ΔG model. However, we bear in mind that the absolute value of ΔG has no meaning for the ALD reaction, i.e. $\Delta G > 0$ does not necessarily mean that ALD will not work and $\Delta G < 0$ does not necessarily mean that all the individual surface reactions take place.

Therefore the same gas-phase reactions were used to investigate ALD and CVD processes. In both cases a surface was not introduced in the model.

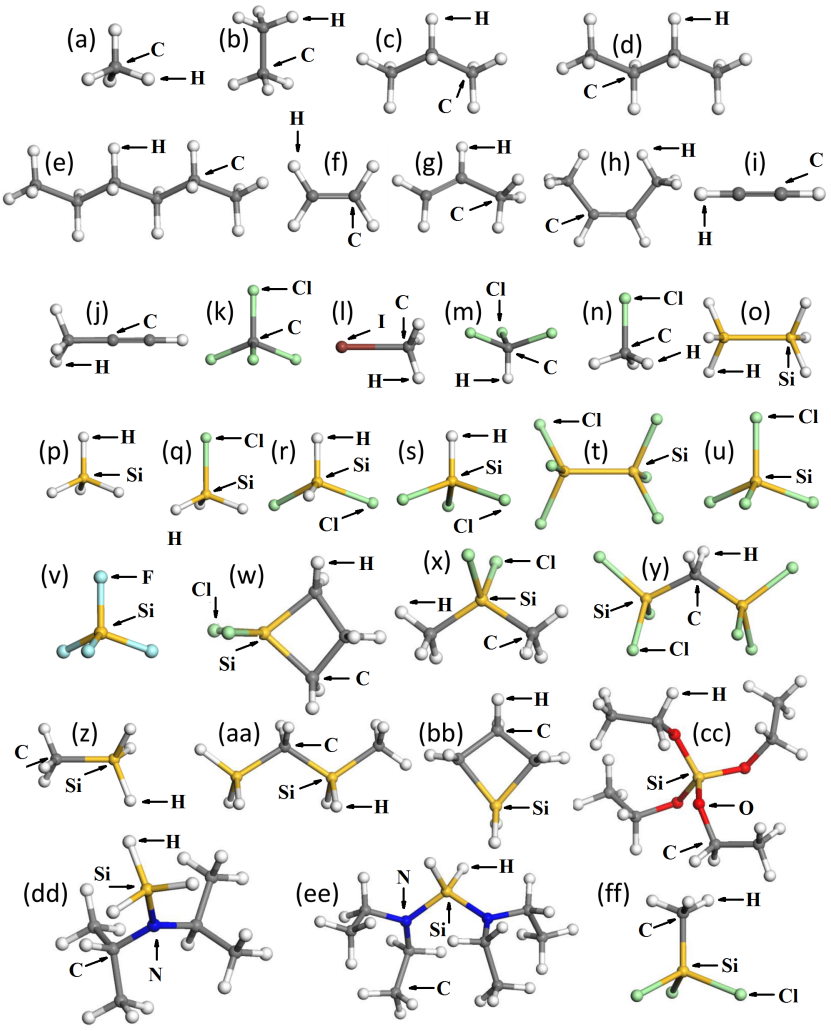


Figure 5.1: Optimized structures for the possible precursors for ALD of SiC performed in TURBOMOLE. (a) methane (CH_4), (b) ethane (C_2H_6), (c) propane (C_3H_8), (d) n-butane (C_4H_{10}), (e) n-hexane (C_6H_{14}), (f) ethylene (C_2H_4), (g) propene (C_3H_6), (h) -2-butene (C_4H_8), (i) ethyne (C_2H_2), (j) propyne (C_3H_4), (k) carbontetrachloride (CCl_4), (l) iodomethane (CH_3I), (m) trichloromethane ($CHCl_3$), (n) chloromethane (CH_3Cl), (o) disilane (Si_2H_6), (p) silane (SiH_4), (q) monochlorosilane (SiH_3Cl), (r) dichlorosilane SiH_2Cl_2 (DCS), (s) trichlorosilane $SiHCl_3$ (TCS), (t) hexachlorodisilane (Si_2Cl_6), (u) tetrachlorosilane $SiCl_4$ (TET), (v) tetrafluorosilane (SiF_4), (w) dichlorosilacyclobutane ($SiCl_2(CH_2)_3$), (x) dimethyldichlorosilane ($Si(CH_3)_2Cl_2$), (y) bis(trichlorosilyl)methane ($(SiCl_3)_2CH_2$), (z) methylsilane (CH_3–SiH_3), (aa) 1,3-disilabutane(SiH_3–CH_2SiH_2–CH_3), (bb) silacyclobutane ($SiH_2(CH_2)_3$), (cc) tetraethylorthosilicate $Si(OEt)_4$ (TEOS), (dd) diisopropylaminosilane $SiH_3N(iPr)_2$ (DIPAS), (ee) bis(diethylamino)silane $H_2Si[N(Et)_2]_2$ (BDEAS), (ff) methyltrichlorosilane $SiCH_3Cl_3$ (MTS). (Et) - ethyl group –CH_2–CH_3, (iPr) - iso-propyl group –$CH(CH_3)_2$.

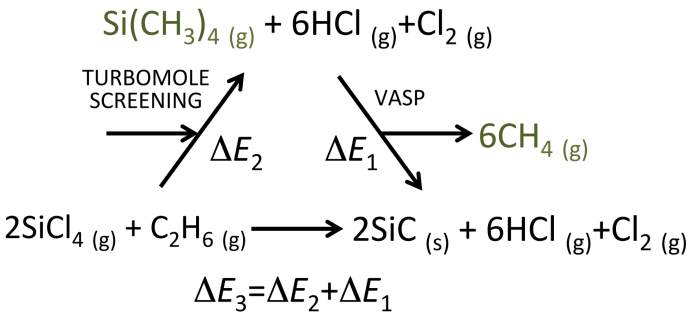


Figure 5.2: Hess cycle representing screening approach for calculating ΔE using gas-phase cluster software (in our case TURBOMOLE) and periodic software (in our case VASP) with tetramethylsilane ($Si(CH_3)_4$) as a reference molecule for SiC. ΔE_3 is the desired energy, which is used to calculate Gibbs energy in eq. 5.3.

5.4 Results and discussion

Different Si and C precursors for ALD of SiC were screened with respect to their thermodynamic reactivity towards forming SiC. Gibbs energies ΔG of chemical reactions between different Si and C precursors were calculated to investigate which chemical reactions are more thermodynamically favourable (Fig. 5.3(a, b).

5.4.1 Model validation at CVD conditions, T=1000°C

First, Gibbs energies were calculated at CVD conditions T=1000°C and partial pressures P_{products}=0.01 Torr and $P_{\text{reactants}}$=1 Torr of products and reactants, respectively, to validate the proposed theoretical model for screening (see Fig. 5.3(a), Table A.1 in Appendix A). At T=1000°C ΔG is negative for reactions of disilane (Si_2H_6), silane (SiH_4), monochlorosilane (SiH_3Cl), DCS (SiH_2Cl_2) and TCS($SiHCl_3$) with all the analysed carbon containing precursors (marked in green color in Fig. 5.3(a)). That corresponds very well with experimental results, where silane is the most common silicon precursor for SiC CVD. [172–174] Monochlorosilane together with propane (C_3H_8) gave a growth rate of SiC of 20 μm/h [177] and, consistent with this, the calculated ΔG for monochlorosilane (SiH_3Cl) and propane is negative (ΔG=-3.3 eV/SiC). Besides, for CVD of SiC using DCS with propane growth rates up to 100 μm/h were achieved at 1750°C, [174] where we estimate ΔG=-4.8 eV for DCS reacting with propane at 1750°C.

The most positive ΔG (marked in red in Fig. 5.3(a)) are computed for reactions of TET ($SiCl_4$) and tetrafluorosilane (SiF_4). For tetrafluorosilane (SiF_4) ΔG is positive for reactions with all suggested carbon precursors, and is also positive for TET ($SiCl_4$) with ethylene, propene, -2-butene, propyne and carbontetrachloride. In experiment TET ($SiCl_4$) together with TCS ($SiHCl_3$) are the most commonly used chlorosilane precursors for CVD of SiC. [184] The use of TET ($SiCl_4$) with hexane (C_6H_{14}) for epitaxial growth of 6H-SiC was demonstrated at 1850°C with a growth rate 3.6-7.2 μm/h. [195] Propane was also used with TET ($SiCl_4$) at high temperatures up to 1850°C yielding growth rates up to 200 μm/h. [196] Our model shows near-zero exothermicity for TET reacting with propane and hexane at 1000°C (ΔG -0.3 eV and 0.0 eV respectively), but much more negative values at 1850°C (-2.9 eV and -2.6 eV respectively, not shown in

(a) ΔG, [eV]/SiC unit, 1000°C (CVD)		methane	ethane	propane	n-butane	n-hexane	ethylene	propene	-2-butene	ethyne	propyne	carbon-tetrachloride	iodo-methane	trichloro-methane	chloro-methane
		CH_4	C_2H_6	C_3H_8	C_4H_{10}	C_6H_{14}	C_2H_4	C_3H_6	C_4H_8	C_2H_2	C_3H_4	CCl_4	CH_3I	$CHCl_3$	CH_3Cl
disilane	Si_2H_6	-3.5	-3.7	-3.8	-3.8	-3.8	-3.1	-3.3	-3.5	-5.5	-2.9	-6.8	-4.3	-6.5	-4.5
silane	SiH_4	-3.9	-4.0	-4.0	-4.0	-4.0	-3.4	-3.5	-3.7	-5.8	-3.2	-8.1	-4.7	-6.9	-4.9
monochlorosilane	SiH_3Cl	-3.2	-3.3	-3.3	-3.3	-3.4	-2.7	-2.8	-3.0	-5.1	-2.5	-5.5	-4.0	-6.2	-4.2
dichlorosilane (DCS)	SiH_2Cl_2	-2.5	-2.6	-2.6	-2.6	-2.7	-2.0	-2.1	-2.3	-4.4	-1.8	-2.9	-3.3	-3.6	-3.5
trichlorosilane (TCS)	$SiHCl_3$	-1.8	-1.9	-2.0	-2.0	-2.0	-1.3	-1.5	-1.6	-2.8	-0.5	-0.3	-2.6	-1.0	-2.8
hexachlorodisilane	Si_2Cl_6	-1.6	-1.7	-1.5	-1.3	-1.2	-0.1	-0.3	-0.5	-1.6	0.7	1.0	-1.4	0.3	-1.6
tetrachlorosilane (TET)	$SiCl_4$	-1.5	-0.6	-0.3	-0.2	0.0	1.0	0.8	0.6	-0.5	1.8	2.0	-1.2	1.3	-0.6
tetrafluorosilane	SiF_4	0.6	3.2	4.0	4.5	4.9	6.5	6.3	6.1	6.7	8.4	8.6	2.6	8.5	3.2

(b) ΔG, [eV]/SiC unit, 400°C (ALD)		methane	ethane	propane	n-butane	n-hexane	ethylene	propene	-2-butene	ethyne	propyne	carbon-tetrachloride	iodo-methane	trichloro-methane	chloro-methane
		CH_4	C_2H_6	C_3H_8	C_4H_{10}	C_6H_{14}	C_2H_4	C_3H_6	C_4H_8	C_2H_2	C_3H_4	CCl_4	CH_3I	$CHCl_3$	CH_3Cl
disilane	Si_2H_6	-1.5	-1.8	-1.9	-1.9	-2.0	-1.9	-1.9	-2.1	-5.0	-2.0	-4.8	-2.3	-4.5	-2.5
silane	SiH_4	-1.8	-2.0	-2.0	-2.0	-2.1	-2.0	-2.0	-2.2	-5.1	-2.1	-6.0	-2.5	-4.8	-2.8
monochlorosilane	SiH_3Cl	-1.1	-1.3	-1.3	-1.3	-1.4	-1.3	-1.3	-1.5	-4.4	-1.4	-3.4	-1.8	-4.1	-2.1
dichlorosilane (DCS)	SiH_2Cl_2	-0.3	-0.5	-0.6	-0.6	-0.6	-0.6	-0.6	-0.8	-3.7	-0.7	-0.8	-1.1	-1.4	-1.3
trichlorosilane (TCS)	$SiHCl_3$	0.4	0.2	0.1	0.1	0.1	0.1	0.1	-0.1	-2.1	0.6	1.8	-0.4	1.2	-0.6
hexachlorodisilane	Si_2Cl_6	0.5	0.2	0.5	0.6	0.7	1.1	1.1	0.9	-1.0	1.6	2.9	0.7	2.3	0.5
tetrachlorosilane (TET)	$SiCl_4$	0.7	1.5	1.8	1.9	2.0	2.4	2.4	2.2	0.2	2.9	4.1	1.0	3.4	1.6
tetrafluorosilane	SiF_4	1.8	4.6	5.5	6.0	6.4	7.4	7.5	7.2	7.3	9.3	10.9	4.1	10.5	4.7

Figure 5.3: Gibbs energies ΔG for reactions of various Si and C precursors at CVD temperatures (a) 1000°C and (b) 400°C. The most favourable reactions are those with the most negative ΔG (cells coloured in green). The least favourable reactions have the most positive ΔG (cells coloured in red).

the tables), corresponding very well with the experimental finding.

Experimentally, SiC films were grown by CVD using TCS ($SiHCl_3$) and ethylene (C_2H_4) precursors with a growth rate of 100 μm/h at 1600°C. [178] Our calculations found TCS ($SiHCl_3$) reacting with all of the carbon precursors to be thermodynamically favourable.

The above data include the effects of pressure via the $RT\ln Q$ term of eq. 5.3. We find that this is important: in general, including the effects of pressure makes the reactions more thermodynamically favourable, as seen in ΔG becoming more negative by an average of 0.6 eV/SiC at T=1000°C and by 0.3 eV/SiC at T=400°C.

It is important also to include the effects of entropy. The above data include the effects of entropy via $T\Delta S$. Including $T\Delta S$ makes the reactions more thermodynamically favourable by decreasing ΔG by an average of 1.3 eV/SiC for T=1000°C and 1.0 eV/SiC for T=400°C depending on the size of the molecules. For example, for small C_2H_2 reacting with different silicon precursors, including $T\Delta S$ decreased ΔG by an average of 0.1 eV/SiC for T=1000°C and 0.2 eV/SiC for T=400°C, while for the bigger molecule C_6H_{14} including $T\Delta S$ decreased ΔG by an average of 1.8 eV/SiC for T=1000°C and 1.2 eV/SiC for T=400°C.

5.4.2 Precursor screening at ALD conditions, T=400°C

To evaluate the viability of these precursors for ALD of SiC, Gibbs energies ΔG at T=400°C and partial pressures P_{products}=0.01 Torr and $P_{\text{reactants}}$=1 Torr of products and reactants, respectively, were calculated and are presented in Fig. 5.3(b) and Table A.2 in Appendix A. In general, we can see that most of the reactions are less favourable at this lower T, compared to ΔG at higher T presented in Fig. 5.3(a), which may be one reason why ALD of SiC is difficult. Nevertheless, direct chemical reactions of disilane (Si_2H_6), silane (SiH_4), monochlorosilane (SiH_3Cl) or DCS (SiH_2Cl_2) Si precursors with all suggested carbon precursors are thermodynamically favourable which suggests that these precursor combinations may give viable indirect reactions in ALD. The most negative ΔG are for ethyne (C_2H_2), carbontetrachloride (CCl_4) and trichloromethane ($CHCl_3$).

A quite different process for low temperature silicon carbide ALD was proposed by Thompson using silicontetrachloride and trimethylaluminium (TMA)

		ΔG, [eV]/SiC unit, 1000°C (CVD)	ΔG, [eV]/SiC unit, 400°C (ALD)
dichlorosilacyclobutane	$SiCl_2(CH_2)_3$	0.1	0.9
dimethyldichlorosilane	$Si(CH_3)_2Cl_2$	-2.6	-0.6
bis(trichlorosilyl)methane	$(SiCl_3)_2CH_2$	-2.4	-0.4
methylsilane	CH_3-SiH_3	-3.8	-1.9
1,3-disilabutane	SiH_3-CH -SiH_2-CH_3	-3.5	-1.7
silacyclobutane	$SiH_2(CH_2)_3$	-4.5	-3.8
TEOS	$Si(OEt)_4$	-8.0	-2.3
DIPAS	$SiH_3N(iPr)_2$	-6.7	-4.6
BDEAS	$H_2Si[N(Et)_2]_2$	-5.4	-0.9
methyltrichlorosilane (MTS)	$SiCH_3Cl_3$	-1.8	0.2

Figure 5.4: Gibbs energies ΔG for decomposition reactions of single-source precursors containing both Si and C at CVD temperature 1000°C and at ALD temperature 400°C. The most favourable reactions are with the most negative ΔG (cells coloured in green). The least favourable reaction is with the positive ΔG (cells coloured in red). (Et) - ethyl group –CH_2–CH_3, (iPr) - iso-propyl group –$CH(CH_3)_2$.

as precursors. [197] We postulated that the corresponding chemical reaction is $3\,SiCl_4 + Al(CH_3)_3 \longrightarrow 3\,SiC + AlCl_3 + 9\,HCl$ and found that ΔG for this reaction at 400°C is -0.54 eV per SiC. This is of the same magnitude as ΔG for the other ALD processes that we have computed to be viable, and thus provides further validation for our approach.

Single-source precursors screening

To assess single-source precursors, the thermodynamics of their decomposition into SiC and by-products was calculated at T=400°C and T=1000°C. The corresponding ΔG are presented in Fig. 5.4 and Tables A.1 and A.2 in Appendix A. We find that unimolecular decomposition of most of these precursors is thermodynamically favourable at low temperature. The most negative ΔG are for decomposition of DIPAS ($SiH_3N(iPr)_2$) and silacyclobutane ($SiH_2(CH_2)_3$). The most positive ΔG is for dichlorosilacyclobutane ($SiCl_2(CH_2)_3$).

Experimentally, growth of SiC by CVD using single-source precursors was shown for 1,3-disilabutane (SiH_3–CH_2–SiH_2–CH_3) (low pressure CVD, 750°C), [185] silacyclobutane ($SiH_2(CH_2)_3$) (T=800 - 1200°C), [189] methylsilane (CH_3–SiH_3) (T=800°C) [186] and MTS (T=1570°C) [198]. Our calculations show that decomposition of 1,3-disilabutane, silacyclobutane and methylsilane is thermodynamically favourable at T=1000°C with ΔG= -3.5, -4.5, -3.8 eV/SiC, respectively. For decomposition of the MTS precursor we got negative

ΔG=-1.8 eV/SiC at 1000°C. Experimentally it was shown that growth of SiC using MTS is favourable only at 1570°C. Indeed our theoretical estimation of the Gibbs energy for MTS at 1570°C gives negative ΔG = -3.4 eV/SiC. This shows that our theoretical results correspond to experimental studies in all of the cases.

Unimolecular decomposition is undesirable as a reaction strategy for ALD because it does not allow surface reactions to self-limit. It is therefore important to check whether proposed ALD precursors can decompose and lead to non-ALD growth. The data in Fig. 5.4 show that the precursors that are the most resistant towards decomposing at 400°C are dichlorosilacyclobutane ($SiCl_2(CH_2)_3$) and MTS ($SiCH_3Cl_3$) with ΔG = 0.9 eV/SiC and 0.2 eV/SiC, respectively. On the other hand, the precursors silacyclobutane ($SiH_2(CH_2)_3$) and DIPAS are the most likely to decompose at 400°C.

5.5 Conclusion

In conclusion, we carried out a theoretical thermodynamic analysis of different precursor combinations for SiC thin film by calculating Gibbs energy ΔG including the effects of pressure and temperature ($G = \Delta E - T\Delta S + RT\ln Q$). The theoretical model was validated for existing chemical reactions in CVD of SiC process at 1000°C and partial pressures P_{products}=0.01 Torr and $P_{\text{reactants}}$=1 Torr. Single source precursors were also computed. In all of the cases our theoretical results correspond to experimental studies. For ALD of SiC at 400°C and P_{products}=0.01 Torr and $P_{\text{reactants}}$=1 Torr, the precursors disilane (Si_2H_6), silane (SiH_4) or monochlorosilane (SiH_3Cl) with ethyne (C_2H_2), carbontetrachloride (CCl_4) or trichloromethane ($CHCl_3$) are predicted to be the most promising.

Chapter 6

SiC PECVD

6.1 Abstract

Understanding the mechanism of SiC chemical vapor deposition (CVD) is an important step in investigating the routes towards future atomic layer deposition (ALD) of SiC. The energetics of various silicon and carbon precursors reacting with bare and H-terminated 3C-SiC (011) are analyzed using *ab-initio* density functional theory (DFT). Bare SiC is found to be reactive to silicon and carbon precursors, while H-terminated SiC is found to be not reactive with these precursors at 0 K. Furthermore, the reaction pathways of silane plasma fragments SiH_3 and SiH_2 are calculated along with the energetics for the methane plasma fragments CH_3 and CH_2. SiH_3 and SiH_2 fragments follow different mechanisms towards Si growth, of which the SiH_3 mechanism is found to be more thermodynamically favorable. Moreover, both of the fragments were found to show selectivity towards the Si-H bond and not C-H bond of the surface. Based on this, a selective Si deposition process is suggested for silicon versus carbon-doped silicon oxide surfaces.

6.2 Introduction

Silicon carbide (SiC) as a semiconductor has unique properties that give it significant advantages compared to silicon. It can carry high currents and operate at a higher temperature than silicon. Moreover, silicon carbide has the lowest wet etch rate compared to other silicon-based materials, such as silicon dioxide

or silicon nitride. This makes it an ideal candidate for barrier applications in the semiconductor industry, for example, for low-k spacers/liners and air gap liners for the interlayer dielectric. The most common silicon carbide polytypes used in electronics are 3C, 4H and 6H, where C refers to cubic and H to hexagonal structure. [171]

Using silicon carbide for spacer and liner applications implies the ability to deposit thin layers of the material on high-aspect-ratio structures at low temperatures. Currently, silicon carbide films are deposited by the chemical vapor deposition (CVD) technique at 1500°C - 1600°C, commonly using silane (SiH_4) [173, 174, 199] as a silicon precursor, and propane (C_3H_8) [172, 174–177] or ethylene (C_2H_4) [178, 179] as a carbon precursor. In addition to the fact that these techniques operate at elevated temperatures, thin films deposited by CVD may suffer from non-uniformity.

One way to lower the deposition temperature is to use plasma-enhanced CVD (PECVD). A gas mixture of silane (SiH_4) and methane (CH_4) is typically used. It is possible to achieve deposition temperatures as low as 200°C for amorphous silicon carbide films. [200, 201] The crystallinity of silicon carbide films increases with deposition temperature. [202] Crystalline silicon carbide films were deposited by PECVD at temperatures 650-1000°C. [203]

Understanding the PECVD process requires knowledge of the reactive constituents of the plasma. The silane radicals SiH, SiH_2 and SiH_3 are formed under PECVD conditions in addition to atomic silicon and hydrogen. [204] Higher silanes, such as di- and trisilane may be produced in smaller quantities. SiH_3 and SiH_2 are the primary and secondary constituents of the plasma. SiH_3 is longer-lived and less reactive, while SiH_2 together with SiH and Si radicals are reactive short-lived species. [205]

Numerous theoretical studies have been performed on silane plasma fragments reacting with silicon and silicon carbide surfaces during the PECVD process. Kuwahara *et al.* used tight-binding quantum chemical molecular dynamics to show that the SiH_2 crystal growth mechanism is different from that of SiH_3 during silane plasma PECVD of silicon on H-terminated Si(001)-(2 $\times$ 1). [206] The latter requires at least two SiH_3 radicals for generating a Si-Si bond, while SiH_2 can be directly adsorbed onto Si of the H-terminated surface. In another paper by Kuwahara *et al.* a mechanism for dangling bond diffusion on Si (0 1 1) was suggested, where the dangling bond diffuses rapidly along an upper layer consisting of Si–H_3 sites and then migrates from the upper layer to

a lower layer consisting of Si–H sites. [207] Quantum chemical molecular dynamics and density functional theory (DFT) calculations were used to support the model and explain why layer-by-layer growth occurs during silicon PECVD. The probability of H abstraction and silicon dangling bond formation induced by SiH_3 on Si(011)(2 $\times$ 1) was estimated using *ab-initio* Car-Parrinello simulations. [208] Kalered *et al.* used a DFT cluster model to compare activation energies for the SiH_2 and $SiCl_2$ species that are likely to exist during silicon carbide PECVD with chlorine addition. It was found that SiH_2 binds more strongly to the H-terminated (0 0 0 $\bar{1}$) SiC surface than $SiCl_2$. [209]

One of the most precise thin film deposition techniques that operates at low temperatures is atomic layer deposition (ALD). Using ALD or plasma-enhanced ALD (PEALD) to deposit SiC would solve the temperature and film uniformity issues that are discussed above. However, currently, there is no known high volume manufacturing ALD process for silicon carbide.

For this reason, following our previous study on screening of the possible silicon carbide ALD precursors in chapter 5, [20] we perform a theoretical study on how various silicon and carbon precursors react with bare 3C-SiC (0 1 1) surface (where silicon and carbon atoms are exposed) and H-terminated 3C-SiC (0 1 1) surfaces and how silane plasma fragments react with H-Si and H-C bonds of the H-terminated 3C-SiC (0 1 1) surface. This is done by calculating adsorption energies and energy barriers of these reactions with DFT. In addition, the adsorption energies of methane plasma fragments CH_3 and CH_2 are estimated. The precursors analyzed are silicon tetrachloride ($SiCl_4$), disilane (Si_2H_6), silane (SiH_4), trichloromethane ($CHCl_3$), propyne (C_3H_4), ethyne (C_2H_2) and carbon tetrachloride (CCl_4). We find that all the precursors react spontaneously with the bare silicon carbide surface and none with H-terminated silicon carbide surface. The neutral plasma fragments are silyl (SiH_3) and silylene (SiH_2). We find that these silane plasma fragments react selectively with the Si-H bond, not with the C-H bond of the H-terminated SiC surface.

6.3 Methodology

First principles modelling using DFT was performed to calculate adsorption energies and energy barriers of various C and Si precursors and plasma fragments

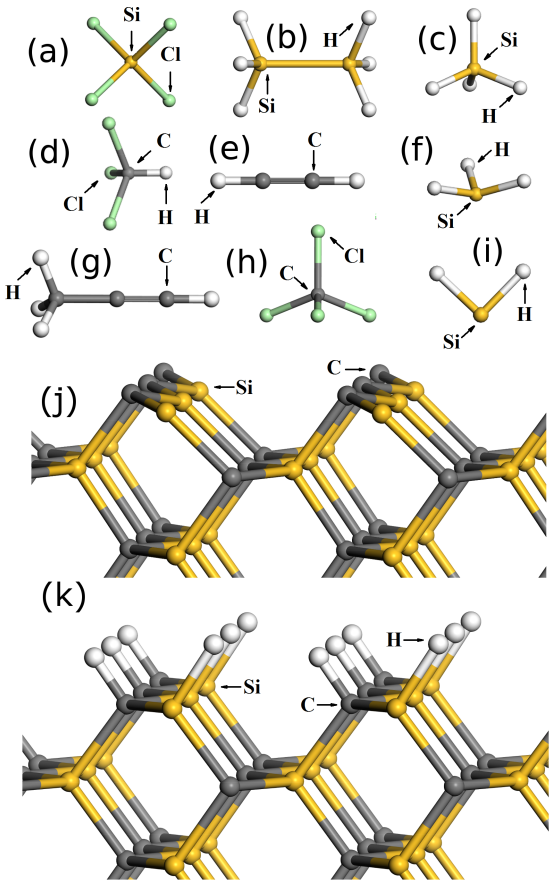


Figure 6.1: Optimized structures. (a) silicon tetrachloride ($SiCl_4$), (b) disilane (Si_2H_6), (c) silane (SiH_4), (d) trichloromethane ($CHCl_3$), (e) ethyne (C_2H_2), (f) silyl (SiH_3), (g) propyne (C_3H_4), (h) carbon tetrachloride (CCl_4), (i) silylene (SiH_2), (j) bare silicon carbide (0 1 1) slab, (k) H- terminated silicon carbide (0 1 1) slab (side view).

reacting with bare and H-terminated SiC surfaces. Calculations were carried out using the Vienna *ab-initio* simulation package (VASP) [157] version 5.3.5. The Perdew - Burke - Ernzerhof (PBE) functional was used for the exchange-correlation term. The projector augmented wave (PAW) method [147, 157] was used to describe the core electrons of atoms. A plane wave basis set with a cut-off energy 400 eV was used for the valence orbitals. Spin polarized calculations were performed for all the structures. Optimized precursors, silane plasma fragments and slab structures are shown in Figure 6.1.

Bulk 3C-SiC was optimized using a $2 \times 2 \times 2$ k-point grid within the Monkhorst - Pack scheme. [158] 3C-SiC was chosen as the total energy of the optimized 3C-SiC bulk was calculated to be the lowest compared to 4H and 6H SiC. The minimum total energy for the optimized bulk was found for lattice constant

4.38 Å that is in a good agreement with experimental data (4.36 Å) [160]. Energies of different SiC surface orientations were calculated. A SiC (0 1 1) is calculated to have the smallest surface energy of 0.18 eV. A SiC (0 1 1) surface was therefore constructed from the optimized 3C-SiC bulk cell.

H atoms were attached to the bottom and top layer Si and C atoms of the slab to remove their dangling bonds and create an H-terminated SiC surface. A convergence test was done for adsorption energies of SiH_3 reacting with the H-terminated SiC surface for slab thicknesses of two, three and four SiC units thick. The difference in adsorption energies between two and three Si-C unit slabs was just 0.003 eV. The adsorption energy was thus considered to be converged for a slab thickness of two Si-C units. A vacuum thickness of 8 Å and slab thickness of two Si-C units (8.65 Å) was therefore chosen for the rest of the study. The total cell size was 8.7 $\times$ 12.3 $\times$ 20.3 Å and 8.7 $\times$ 12.3 $\times$ 22.3 Å with the total number of ions 80 and 112 for bare SiC and H-terminated SiC, respectively. SiC and H-SiC slab geometries were optimized using a 2 $\times$ 2 $\times$ 1 k-point grid.

The structures of the gas-phase precursors and silane plasma fragments were optimized in a 15 $\times$ 15 $\times$ 15 Å cubic cell using the Γ-point in the Brillouin zone. The difference between numbers of electrons in up and down spin components was not set initially and was defined by full relaxation. The net magnetic moment calculated in VASP is defined as the difference between spin up and spin down magnetic moments.

Optimized structures of precursors were introduced to the SiC and H-SiC surface at various sites and adsorption energies of spontaneous reactions with the surface were calculated. Energies were obtained by full geometry relaxation using the conjugate gradient method with a convergence level of 1 meV/Å on each ion.

Adsorption energies E_{ads} were calculated using eq. 6.1:

$$E_{\text{ads}} = E_{\text{slab + precursor}} - E_{\text{slab}} - E_{\text{precursor}} \tag{6.1}$$

Thus, negative E_{ads} indicates a decrease in total energy for the system, implying an exothermic process and energetically favorable adsorption at T=0 K. All energies are reported for T=0 K without consideration of entropy. No zero-point energy correction is included.

In order to understand how silane plasma fragments silyl (SiH_3) and silylene (SiH_2) react with the H-terminated SiC surface, optimized fragments were introduced to the H-SiC surface and energy barrier calculations were carried out using the climbing nudged elastic band (CI-NEB) [137] tool implemented in VASP. Seven images including initial and final configurations were used. The initial configuration is a precursor molecule around 2-4 Å away from the surface (hereafter called "R"). The final adsorption configuration is a precursor molecule reacted with the surface ("P"). Energies are plotted relative to the energies of a precursor molecule located at infinity from the surface, that is the sum of the energy of the isolated precursor and isolated slab ("I"). Initial R and final P configurations were optimized in the same way as was described above. Only one vibrational mode is found with an imaginary frequency at the transition state.

Some of the geometries were transferred to a cluster DFT model for ease of inspection of the molecular orbitals at the Γ-point. To do this, single point calculations were carried out using the TURBOMOLE package [210] and the same PBE functional. The atom-centered basis set def2-TZVPP [192] was used for all the atoms along with an auxiliary basis set for the density within the resolution of identity (RI) approximation. [193, 194] Molecular orbitals were visualized using Tmolex.

6.4 Results

Following our previous work on the thermodynamical screening of precursors for silicon carbide low-temperature ALD (chapter 5) [20], we were interested in the thermodynamics of how the most favorable precursors react with bare and H-terminated silicon carbide surfaces. To do so, we computed the reaction pathways and the kinetic parameters of the reaction of precursors silicon tetrachloride ($SiCl_4$), disilane (Si_2H_6), silane (SiH_4), trichloromethane ($CHCl_3$), propyne (C_3H_4), ethyne (C_2H_2) and carbon tetrachloride (CCl_4) with the surfaces. In order to understand how the silane plasma fragments silyl (SiH_3) and silylene (SiH_2) react with an H-terminated 3C-SiC (0 1 1) surface, adsorption and activation energies of species reacting with the surface were calculated. One molecule/fragment per cell was introduced to the top surface of the slab, giving a coverage of 0.93 adsorbates per nm^2.

Table 6.1: Adsorption energies of silicon and carbon precursors on the bare silicon carbide surface. Optimized structures are shown in Figures 6.2 and 6.3.

		ΔE_{ads}, eV
silicon tetrachloride	$SiCl_4$	-3.3
trichloromethane	$CHCl_3$	-4.1
carbon tetrachloride	CCl_4	-4.8
disilane	Si_2H_6	-7.6
silane	SiH_4	-4.4
propyne	C_3H_4	-2.6
ethyne	C_2H_2	-3.2

6.4.1 Adsorption of the precursors on H-terminated and bare SiC surface

An H-terminated surface is likely to exist in growth experiments due to the HF cleaning of the SiO_2 substrate or from the silane that is used during PECVD. Therefore, first of all, the adsorption of the precursor was calculated on the H-terminated silicon carbide surface. It was found that none of the precursors reacted spontaneously with the H-terminated surface. Furthermore, since all Si and C atoms at the H-terminated surface are coordinatively saturated, there are no obvious sites at which the precursors could adsorb via thermal activation (activation of the silane precursor as a plasma is considered in next section).

On the other hand, it was found to be thermodynamically favorable for all of the precursors to react with the bare surface, yielding the optimized structures shown in Figures 6.2 and 6.3 for the most favorable structures and Figures B.1 to B.7 in Appendix B for all of the considered structures. Most of the precursors adsorb dissociatively, donating one or more H or Cl to adjacent surface atoms. Adsorption energies for the most favorable structures are shown in Table 6.1. Adsorption energies for all the considered structures are shown in Tables B.1 to B.7 and Figures B.1 to B.7 in Appendix B.

Chlorinated precursors: A chlorine atom was found to favor adsorbing on the silicon surface atom, not on the carbon surface atom, with a difference in adsorption energies of 0.8 eV. The Si-Cl bond length was calculated to be 2.08 Å. Silicon tetrachloride dissociatively chemisorbs on the bare surface (Figure

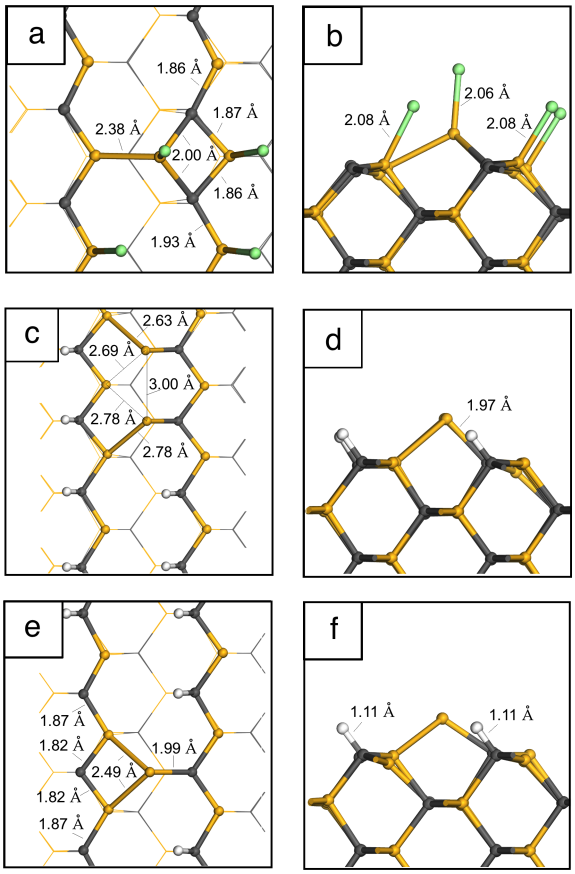


Figure 6.2: Top (left column) and side (right column) view of the most thermodynamically favorable structures of the silicon precursors adsorbed on the bare silicon carbide surface. (a),(b) - tetrachlorosilane, (c),(d) - disilane, (e),(f) - silane. Color scheme: yellow=silicon, green=chlorine, white=hydrogen, grey=carbon

6.2 a, b), donating three Cl to the surface silicon atoms to form Si-Cl bonds, resulting in an adsorption energy of -3.3 eV. Si forms an Si–Cl bond (2.06 Å), an Si-Si bond (2.38 Å) with a surface silicon and two C-Si bonds (1.93 Å) with a surface carbon atoms. Donating two or one chlorine atoms to the surface is thermodynamically less favorable with adsorption energies -2.8 eV and -2.2 eV, respectively (see Appendix B Figure B.1 (c, d) and (a, b), respectively). Trichloromethane, donating three chlorine to the surface, adsorbs more strongly than silicon tetrachloride, with an adsorption energy of -4.1 eV (see Figure 6.3 (a, b)). The final structure is similar to the silicon tetrachloride structure with a carbon atom from the precursor forming an C–Si bond (2.05 Å) and two C–C bonds (1.72 Å) with surface atoms. It is more favorable for trichloromethane to donate three chlorine atoms to the surface than to donate two (adsorption energy -3.1 eV) or one (adsorption energy -2.0 eV) (see Ap-

pendix B Figure B.4 (a - d)).

The greatest adsorption energy (-4.8 eV) for chlorinated precursors was calculated for carbon tetrachloride. CCl_4 dissociatively chemisorbs on the silicon carbide surface, donating all four chlorines to the surface silicon atoms and forming C–C (1.28 Å) and Si–C bonds (1.83 Å) with the surface atoms (Figure 6.3 g, h). Donating two chlorine atoms to the surface and bonding a CCl_2 group to the surface carbon atom is thermodynamically less favorable with the adsorption energy of -3.5 eV (see Appendix B Figure B.7 (a - d)).

Silane and disilane:

It is more thermodynamically favorable for a H atom to adsorb on surface carbon than on surface silicon with calculated difference in adsorption energies of 1.0 eV. The formed C–H bond length is 1.11 Å. The SiH_3 group was found to be more likely to form a bond with surface carbon, rather than with surface silicon, with an energy difference of 1.2 eV. Disilane and silane dissociatively chemisorb on the surface donating hydrogen atoms to the surface with adsorption energies -7.6 eV and -4.4 eV, respectively (see Figure 6.2 (c-f)). In this way, the bare silicon carbide surface becomes passivated by hydrogen from the precursors.

For disilane it is more thermodynamically favorable to donate all six hydrogen atoms to carbon atoms of the surface (Figure 6.2 (c, d)). The distance between the two adsorbed silicon atoms is 3.00 Å. Each of the silicon atoms forms Si–Si bonds (2.63 Å, 2.69 Å, 2.78 Å and 2.78 Å) with two surface silicon atoms and a C–Si bond (1.97 Å) with one surface carbon atom. The adsorption geometry that is least favorable in energy (-1.6 eV) is the disilane donating one hydrogen to the surface and forming a C–SiH_2–SiH_3 group with surface carbon. Energies of disilane donating two hydrogen atoms and three hydrogen atoms to the surface and the Si atom bridging surface silicon and carbon atoms are computed to yield -3.6 and -4.6 eV, respectively. For all the structures see Appendix B Figures B.2 (a - h).

Silane has a very similar behavior to disilane. The adsorption energy for silane (-4.4 eV) is nearly the same as disilane. Silane donates all four hydrogen atoms to the surface (Figure 6.2(e, f)). Silicon bonds to the surface silicon and carbon atoms forming Si–Si (2.49 Å) and C–Si (1.99 Å) bonds and a silicon dangling bond. Adsorption energies for silane donating one, two and three H atoms to the surface are -2.4 eV, -3.6 eV and -4.1 eV, respectively.

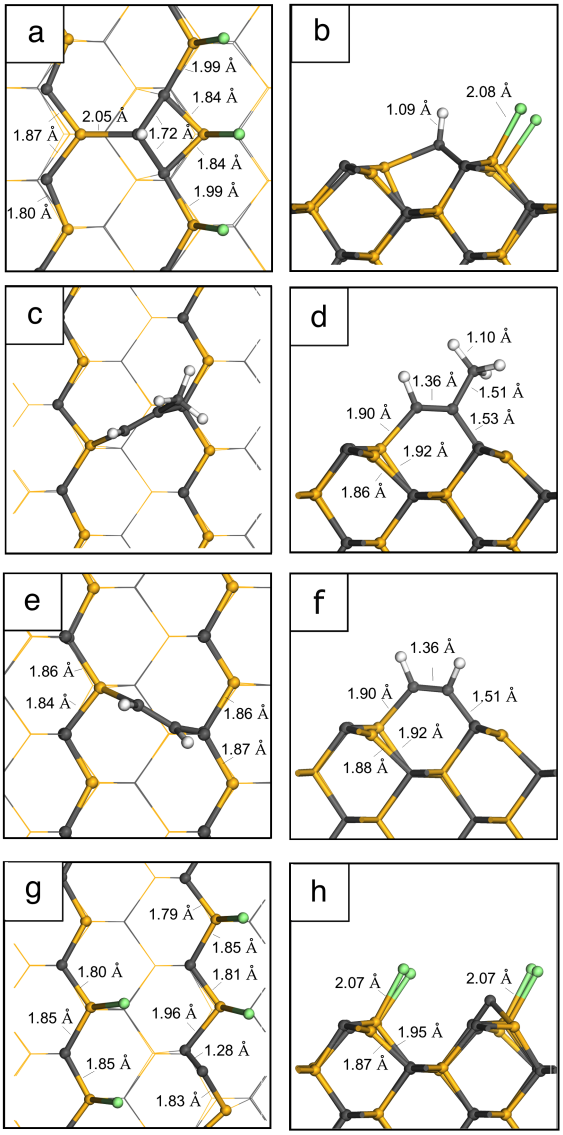


Figure 6.3: Top (left column) and side (right column) view of optimized the most favorable thermodynamically structures of the carbon precursors adsorbed on the bare silicon carbide surface. (a),(b) - trichloromethane, (c),(d) - propyne, (e),(f) - ethyne, (g),(h) - carbontetrachloride. Color scheme: yellow=silicon, green=chlorine, white=hydrogen, grey=carbon

Propyne and ethyne:

For propyne and ethyne reacting with the bare silicon carbide surface, dissociation of the C-C triple bond during chemisorption is less thermodynamically favorable. Instead, C-C triple adds across surface SiC to form silicon-carbon and carbon-carbon single bonds and carbon-carbon double bonds, resulting in a C(surface)-CH(precursor)=CR(precursor)-Si(surface) bridge (see Figure 6.3

(c - f)).

The carbon-carbon bond length (1.36 Å) of the adsorbed propyne (for carbons involved in adsorption) indicates double bond character, as it is only 0.03 Å longer than the calculated carbon-carbon bond of isolated ethylene (1.33 Å). The carbon-silicon (1.90 Å) and carbon-carbon (1.51 Å) bonds formed by a propyne carbon atom adsorbed on the surface are negligibly shorter compared to silicon carbide and diamond bulk bond lengths optimized with DFT (1.89 Å for silicon-carbon bond and 1.55 Å for carbon-carbon bond). Similar to propyne, the silicon-carbon (1.90 Å) and carbon-carbon (1.51 Å) bonds formed when ethyne adsorbs on the surface are the same length as silicon carbide and diamond bulk bonds optimized with DFT. The adsorption energies for propyne and ethyne are -2.6 eV and -3.2 eV, respectively. Donating hydrogens to the surface is less likely for both propyne and ethyne with adsorption energies -2.3 eV and -3.1 eV, respectively (see Appendix B Figure B.5 (c, d) and Figures B.6 (a, b), respectively). For both propyne and ethyne, reacting with a chain of surface carbon atoms is thermodynamically less favorable with adsorption energies -2.1 eV and -2.3 eV, respectively (see Figure A5 (e,f) and Figure A6 (c,d), respectively).

To summarise, the most negative adsorption energies are for disilane and carbon tetrachloride (-7.8 eV and -4.8 eV, respectively), which means that disilane and carbon tetrachloride are the most likely to adsorb on the bare silicon carbide surface at T=0 K. All the precursors that we tested show exothermic reactions with bare SiC. Therefore all are potential ALD precursors if such a bare surface can be generated. However, after these precursors adsorb, the reactive bare surface becomes hydrogen or chlorine passivated, covered with precursor fragments and therefore inert.

6.4.2 Energy barriers of SiH_3 and SiH_2 reacting with H-SiC surface

As was mentioned above, the H-terminated silicon carbide surface is not reactive, while the bare surface shows reactivity towards various carbon and silicon precursors and becomes passivated by hydrogen due to dissociative chemisorption. Bearing this in mind, an investigation of how to strip the hydrogen from the H-terminated surface was carried out. Plasma fragments are known to be highly reactive. Silane plasma is often used for PECVD of SiC. Therefore, ad-

Table 6.2: Bond length of the SiH_3 and SiH_2 fragments and Si-H/C-H bonds of the surface involved in adsorption. Index "F" is for Si/C fragment atoms and index "S" is for the surface atoms. I= fragment at infinity from the surface, R= initial configuration, TS=transition state, P=final configuration as described in Figures 6.4, 6.5.

			Bond length Å			
			I	R	TS	P
SiH_3	C - H	Si_F - H_F	1.49	1.49	1.49	1.49
		C_S - H_S	1.11	1.11	1.62	-
		Si_F - H_S	-	2.85	1.62	1.49
		Si_F - C_S	-	3.90	3.21	4.11
	Si - H	Si_F - H_F	1.49	1.49	1.50	1.49
		Si_S - H_S	1.50	1.50	1.52	-
		Si_F - H_S	-	3.81	2.50	1.49
		Si_F - Si_S	-	4.94	3.77	4.31
SiH_2	C - H	Si_F - H_F	1.54	1.54	1.51	1.49
		C_S - H_S	1.11	1.11	1.70	-
		Si_F - H_S	-	2.46	1.62	1.49
		Si_F - C_S	-	3.10	2.09	1.91
	Si - H	Si_F - H_F	1.54	1.53	1.52	1.50
		Si_S - H_S	1.50	1.61	2.00	-
		Si_F - H_S	-	1.71	1.51	1.50
		Si_F - Si_S	-	2.74	2.86	2.40

sorption of the silane radical fragments silyl SiH_3 and silylene SiH_2 on the H-SiC surface was analyzed. Thermodynamics of methane plasma fragments CH_3 and CH_2 were calculated as well. Energy barriers were calculated for SiH_3 and SiH_2 inserting into H-Si and H-C bonds of the surface in order to understand which reactions are the most kinetically likely. The zero reference energy is when the fragments are located at infinity from the surface, which is calculated as the sum of the energies of the isolated fragment and the isolated slab (denoted "I"). Energies for silane and methane plasma fragments are summarized in Table 6.4.

Silyl SiH_3

The Si-H bond lengths of the isolated silyl radical SiH_3 were calculated to be the same as those of silane (1.49 Å) (see Table 6.2) and the magnetic moment was calculated to be 1 μB (see Table 6.3). The reaction pathway of silyl reacting with C-H and Si-H bonds of the H-SiC surface is presented in Figure 6.4. In the initial state "I", the fragment is at infinity from the surface. Then at "R" the silyl fragment is at 2.85 Å and 3.81 Å from the surface hydrogen for reactions with

Table 6.3: Magnetic moments of the systems SiH_3 and SiH_2 approaching Si-H/C-H bonds of the surface involved in adsorption. I = fragment is at infinity from the surface, R= initial configuration, TS=transition state, P=final configuration as described in Figures 6.4, 6.5.

		Magnetic moment, μB			
		I	R	TS	P
SiH_3	C - H	1.00	0.94	1.00	0.95
	Si - H	1.00	0.97	0.99	1.00
SiH_2	C - H	0.00	0.09	0.00	0.00
	Si - H	0.00	0.05	0.00	0.00

C-H and Si-H bonds, respectively. In the final state ("P") of the reactions, one hydrogen atom desorbs from the surface and binds to the silane product.

The energy of the system at R was found to be -0.1 eV relative to I. This small minimum in energy can be explained by weak van der Waals interactions between the silyl and surface atoms. Due to the small difference between R and I, R can be ignored and is not presented in Figure 6.4.

It was found that SiH_3 abstracting a hydrogen from the C-H bond of the surface is thermodynamically unfavorable with a reaction energy of +0.47 eV. However, for abstracting hydrogen from the Si-H bond this reaction is thermodynamically favorable (ΔE= -0.13 eV). For CH_3 methane plasma fragment abstracting H from C-H and Si-H surface bonds the energies were calculated to be more thermodynamically favorable (-0.41 eV and -0.99 eV, respectively). The energy barriers for silyl reactions are 0.56 eV and 0.02 eV for C-H and Si-H, respectively. This means that the reaction of silyl with the Si-H bond of the H-SiC surface producing silane is essentially barrierless. Therefore, silyl will first react with the Si-H bond, leaving C-H of the surface unreacted, until all H has been stripped from Si. However, SiH_3 also bonds with an Si dangling bond, leading to Si–SiH_3 at the surface. Continued abstraction of H and replacement with SiH_3 thus leads ultimately to growth of Si.

It is important to notice that the reverse reaction for silane donating H to the dangling bond of a C atom at the surface is thermodynamically favorable and the energy barrier is small (0.08 eV). On the other hand, for silane to donate H to a Si dangling bond costs 0.13 eV at T=0 K.

Silylene SiH_2

The gas-phase silylene (SiH_2) fragment is calculated to have an Si-H bond length of 1.54 Å (see table 6.2) and a magnetic moment of 0 μB (see Table

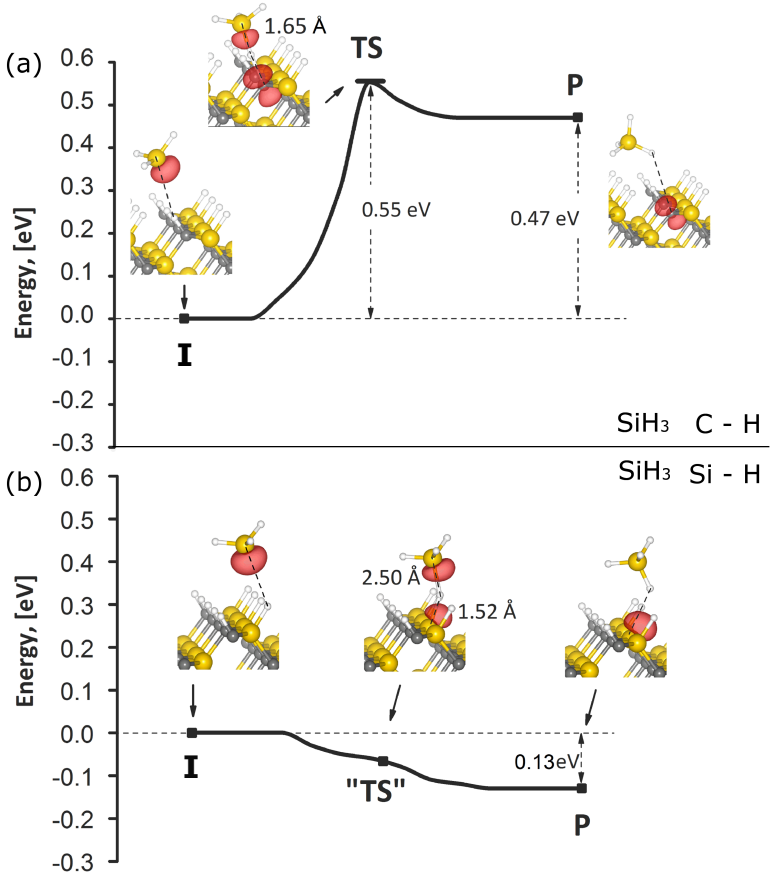


Figure 6.4: Reaction pathway of SiH_3 stripping H from (a) C-H bond, (b) Si-H of the H-SiC 3C (0 1 1) surface producing SiH_4. I = SiH_3 is at infinity far from the surface, P=products, final configuration, SiH_4 produced; TS=transition state found using CI-NEB approach in VASP. R is similar to I and not shown. Small white spheres = hydrogen, large yellow spheres = silicon, small dark grey spheres = carbon. Red area = spin density at iso surface 0.008.

6.3), i.e. silylene is found to be most stable in its singlet state. SiH_2 in its triplet state was calculated to be 0.71 eV higher in energy. This corresponds to experimental results, where SiH_2 was found to be a ground state singlet. [211] The reaction pathways of silylene reacting with the H-SiC surface are presented in Figure 6.5. It was found that SiH_2 first replaces one surface hydrogen, forming a C-Si or Si-Si bond, and then transfers the hydrogen to the adsorbing Si atom, so that the net effect is insertion of SiH_2 into the surface bond. Both C-H and Si-H bond insertion reactions were found to be thermodynamically favorable at T=0 K with ΔE= -2.04 and -2.30 eV, respectively. ΔE for CH_2 methane plasma fragments for similar reactions were calculated to be -3.78 and -4.66 eV for producing C and Si dangling bonds, respectively.

First, the SiH_2 fragment is at infinity from the surface ("I"). Then it gets closer

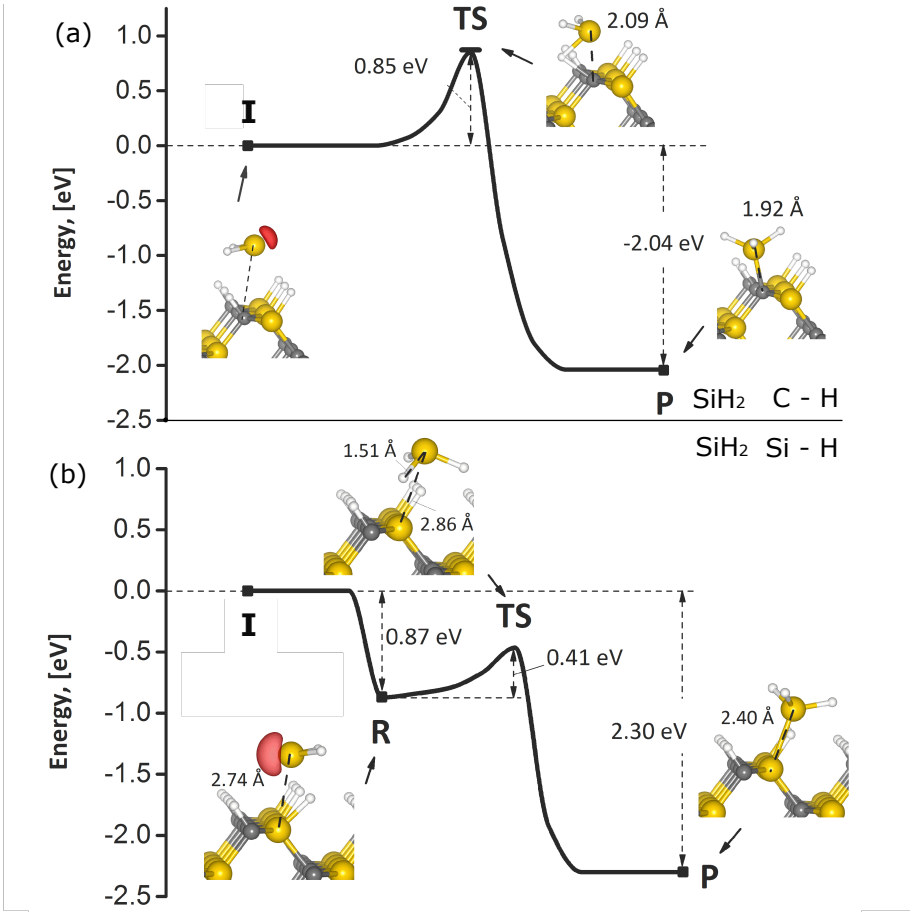


Figure 6.5: Reaction pathway of SiH_2 stripping H from (a) C-H bond, (b) Si-H of the H-SiC 3C (0 1 1) surface producing SiH_3 group on the surface. I = SiH_2 at infinity far from the surface, R = SiH_2 is at 2.74 Å from the Si of the surface, P = products, final configuration, SiH_3 produced; TS=transition state found using CI-NEB approach in VASP. Small white spheres = hydrogen, large yellow spheres = silicon, small dark grey spheres = carbon. Red area = spin density at isosurface 0.022.

and starts to interact with the surface ("R"), where the silicon atom of silylene is at approximately 3 Å from the C/Si of the surface. When silylene is close to the surface its magnetic moment was calculated to be 0.1 μB (see Table 6.3), which means that it remains predominantly in a singlet state. The energy of the system at state R was found to be -0.16 eV and -0.87 eV when approaching the C-H and Si-H bond, respectively. The former (-0.16 eV) can be explained as due to weak van der Waals forces and can be ignored, as for SiH_3 above. However, the interaction of SiH_2 with the surface Si-H bond at R is apparently much stronger (-0.87 eV) and of a different nature.

In order to explain the minimum R in the Si-H case, we analyze the atomic and electronic structure. At I the silylene molecule has bond lengths of 1.53 Å and

Table 6.4: Summary of activation (ΔE_{act}) and adsorption (ΔE_{ads}) energies for SiH_3, SiH_2, CH_3 and CH_2 plasma fragments reacting with C-H and Si-H bonds of the H-SiC 3C (0 1 1) surface."-" means energies were not calculated. Index "S" is for the surface atoms. "DB" - surface dangling bond.

Fragment	Reaction	ΔE_{act}, eV (TS)	ΔE_{ads}, eV (P)
SiH_3	$SiH_3(g) + H–C_S \longrightarrow SiH_4(g) + DB–C_S$	0.55	0.47
	$SiH_3(g) + H–Si_S \longrightarrow SiH_4(g) + DB–Si_S$	0	-0.13
	$2\,SiH_3(g) + H–C_S \longrightarrow SiH_4(g) + SiH_3–C_S$	-	-2.73
	$2\,SiH_3(g) + H–Si_S \longrightarrow SiH_4(g) + SiH_3–Si_S$	-	-2.99
SiH_2	$SiH_2(g) + H–C_S \longrightarrow SiH_3–C_S$	0.85	-2.04
	$SiH_2(g) + H–Si_S \longrightarrow SiH_3–Si_S$	0.41	-2.03
CH_3	$CH_3(g) + H–C_S \longrightarrow CH_4(g) + DB–C_S$	-	-0.41
	$CH_3(g) + H–Si_S \longrightarrow CH_4(g) + DB–Si_S$	-	-0.99
	$2\,CH_3(g) + H–C_S \longrightarrow CH_4(g) + CH_3–C_S$	-	-3.50
	$2\,CH_3(g) + H–Si_S \longrightarrow CH_4(g) + CH_3–Si_S$	-	-4.39
CH_2	$CH_2(g) + H–C_S \longrightarrow CH_3–C_S$	-	-3.78
	$CH_2(g) + H–Si_S \longrightarrow CH_3–Si_S$	-	-4.66

an Si-H-Si angle of 90.9°. At R the bond lengths are 1.54 Å and the Si-H-Si angle increases to 94.5°. At TS, the silylene Si-H decreases to 1.49 Å and Si-H-Si angle increases to 104.8°. At the same time, the surface Si-H lengthens significantly, from 1.50 Å in I to 1.61 Å in R, and this H is just 1.71 Å from the silylene Si at R. This indicates that the H is shared between silylene and surface silicons. The geometry of I, R and TS are shown in Figure 6.6 (d). Although not indicative of a chemical bond, these structural changes do suggest a change in electronic structure between I and R.

Analyzing the electronic structure of the slabs, the projected density of states (PDOS) was plotted for the adsorbing SiH_2 atoms (see Figure 6.6(a)) and for the H atom of the Si-H surface bond (see Figure 6.6(c)) for I, R, TS and P. At I, SiH_2 states are localized while those of the surface H are delocalised. At R the SiH_2 states get lower in energy and mix with surface H states, which localize at the same energy. At P the localized states become disperse bands. This SiH_2 - H interaction already at R seems to be the cause of the stabilization ΔE = -0.87 eV relative to I. In order to analyze the localized states at R,

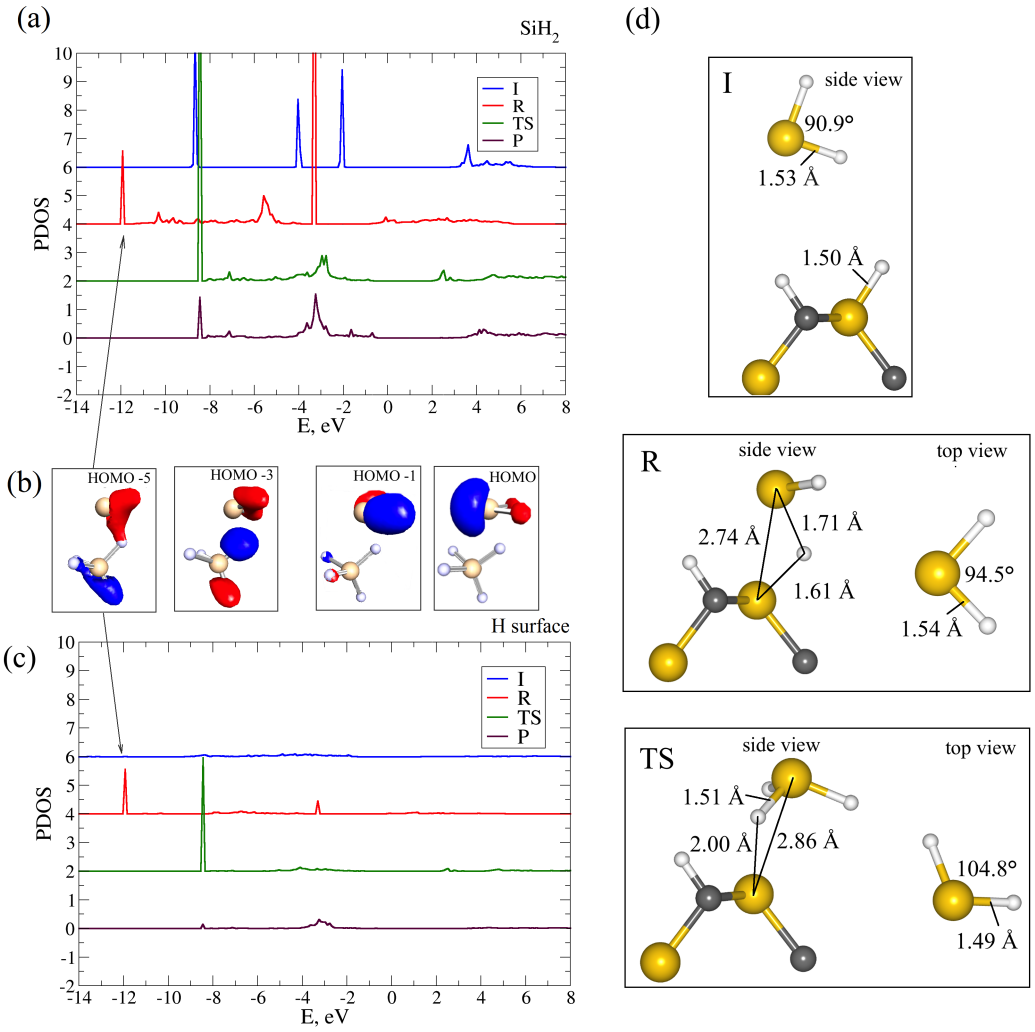


Figure 6.6: Projected density of states (PDOS) (shifted for display purposes) on (a) Si and two H of molecule (c) H atom of Si-H bond of the surface obtained from VASP calculations. (b) Orbitals are plotted from TURBOMOLE calculations using SiH_4 model for the surface Si-H bond. (d) Geometric data for slabs: I = SiH_2 at infinity far from the surface, R = SiH_2 at 2.7 Å from the surface, TS = transition state, P = products, SiH_3 produced; Small light spheres = hydrogen, small dark spheres = carbon, large spheres = silicon. Iso surface plot at value 0.086.

TURBOMOLE calculations were done for a cluster model of R and are shown in Figure 6.6 (b). SiH_4 was used as a cluster model for a surface Si-H bond (different spins were considered, but since the spin down PDOS was identical to spin up, it is not shown in the figure). From the orbital plot we can see that the presence of charge density in a gas-phase SiH_2 molecule (HOMO and HOMO -1 orbitals) above the surface Si-H allows localization of electrons onto the Si-H bond (HOMO -5 orbital), stabilizing the physisorbed complex "R" and facilitating homolytic cleavage of Si-H and ultimately transfer of hydrogen.

The energy barrier for SiH_2 approaching the C-H bond was calculated to be 0.85 eV (Figure 6.5(a)), which is more than twice as high as that for SiH_2 approaching the Si-H bond (0.41 eV). Silylene thus preferentially inserts into surface Si-H to produce surface Si–SiH_3. This may in part be due to the stabilization of "R" in the Si-H case.

In order to understand if the silane plasma growth reaction on Si-H terminated material is self-limiting, the thermodynamics of a further silylene molecule reacting with the new Si–SiH_3 surface group was calculated. The reaction to produce Si–SiH_2–SiH_3 was found to be thermodynamically favorable with ΔE of -3.04 eV. This means that this reaction is not self-limiting.

6.5 Discussion

We found that all of the considered silicon and carbon precursors react with the bare SiC surface. Precursor chemisorption on bare SiC was calculated before. Lespiaux and Langlais used published bond energies to estimate the chemisorption energy of C_2H_2 on bare 3C-SiC (111) at 298 K to be -4.25 eV and -4.30 eV on Si and C terminated surfaces, respectively. [212] Our DFT calculations of the chemisorption energy of C_2H_2 on the 3C-SiC (011) surface is -3.2 eV for C_2H_2 adsorbing on Si and C surface atoms and -2.2 eV for C_2H_2 adsorbing on two carbon surface atoms at 0 K. Inclusion of temperature effects is expected to decrease the adsorption energies and thus cannot explain the difference in the energies. However, this difference can be explained by the different methods used for calculations, where DFT can be regarded as more accurate. A chemisorption energy of -6.99 eV was calculated by Olander and Larsson for C_2H_2 adsorbing on 4H-SiC (0001) (silicon terminated) using DFT. [213] Due to the different polytypes used the discrepancy with our data is even higher, even

though the DFT method was used. This can probably be explained by the different polytypes surface orientation. In our calculations we used the bare (011) 3C-SiC surface, where both silicon and carbon dangling bonds are present at the surface, while on 4H-SiC (0001) only Si dangling bonds are present.

All of the considered precursors are computed to react with a bare SiC surface and passivate this surface with Cl and H atoms. Such a self-limiting reaction is desirable as one step of the ALD cycle. However, this passivated surface does not then react spontaneously with any of the other silicon and carbon precursors, which means that the ALD cycle for SiC can not be completed. Sukkaew *et al.* obtained similar results, calculating extremely large activation barriers for C-precursors adsorbing on H-passivated 4H-SiC (0001). [214] This means that SiC growth can only be sustained if the passivated SiC surface is activated.

One of the ways to activate the H-terminated surface is to generate a chain production of surface dangling bonds via a process called surface hydrogen abstraction, where surface hydrogen is abstrated by a gaseous hydrogen atom. [215] Such mechanism was studied for 4H-SiC CVD using C_2H_2, C_2H_4, CH_4 and CH_3 by Sukkaew *et al.* [214] An overall process was analyzed starting from surface hydrogen abstraction by an atomic hydrogen, followed by a C species adsorption into the formed dangling bond and finishing with adsorption of a H surface atom of the formed surface group at 1600^o C. It was found that for C_2H_2 and C_2H_4 the overall process is thermodynamically unfavorable, while for the CH_3 radical it is thermodynamically favorable.

H abstraction from the H-terminated 4H-SiC surface (Si-terminated and C-terminated) by gaseous H, Cl, Br and F radicals was studied by Olander and Larsson. [216] The energies were found to be more favorable for abstraction by a halogen radical compared to an H radical with the following order of energies H < Br < Cl < F. Furthermore, in most of the cases the reactions of abstraction of hydrogen from an Si-terminated surface were more exothermic than those for a C-terminated surface with an adsorption energy difference of 0.8 - 2.0 eV. This corresponds to our findings for H abstraction by the SiH_3 radical from Si-H and C-H bonds, where the difference in ΔE was calculated to be 0.6 eV. It was also shown by Olander and Larsson that the H-terminated surface is energetically stable to temperatures as high as 2300^{o}C, even in the presence of H or halogen radicals. This makes this mechanism unsuitable for low temperature ALD.

An alternative way to activate the deposition process at lower temperatures is to

use silane plasma. We analyzed how the neutral silane plasma fragments SiH_3 and SiH_2 react with the H-passivated SiC surface. Abstracting a H atom from the Si-H surface bond is thermodynamically favorable at 0 K with ΔE=-0.13 eV. However the next SiH_3 fragment reacts with this dangling bond producing an Si-Si bond. In contrast, just one SiH_2 can be directly adsorbed into the H-terminated surface, which again produces an Si-Si bond. ΔE for the Si growth multistep reaction using two SiH_3 fragments was calculated to be -2.73 eV and -2.99 eV (see Table 6.4) for C-H and Si-H bonds respectively. For comparison, Si growth from one SiH_2 fragment was calculated to be less favorable but still exothermic (-2.04 with C-H and -2.03 eV with Si-H bond). Both routes effect Si growth by transforming surface $-Si-H$ into surface $-Si-SiH_3$. It is thermodynamically favorable for further plasma fragments to react with a formed SiH_3 group, which means that these reactions are not self-limiting and can be described as a Si PECVD process, not an ALD process. A similar mechanism was described by Kuwahara *et al.* [217] for the silane PECVD process on H-Si(001)-(2x1), where it was also shown that SiH_3 radicals produce a Si film of a higher quality compared to that from SiH_2. Kalered *et al.* [209] used a cluster model to calculate the energetics of a SiH_2 plasma fragment reacting with the C-H surface bond of 4H-SiC (000-1) surface. The adsorption energy was -2.22 eV and the energy barrier was 0.79 eV, which is quite close to our calculated energies (-2.04 eV and 0.85 eV, respectively).

It is important to mention that including temperature effects is expected to decrease the adsorption free energies of a precursor. Sukkaew *et al.* showed that including 1600 ^{o}C temperature decreased most of the adsorption free energies of C_2H_2, C_2H_4, CH_4 and CH_3 on 4H-SiC, with the effect of favoring desorption for some of the reactions. [214] Kalered *et al.* [209] found that including partial pressure of 0.0004 atm and T = 1600 ^{o}C also decreased the adsorption free energy of SiH_2 onto SiC. This shows that when estimating energies for such reactions at high temperatures including thermal effects is of a crucial importance. On the other hand at the low temperatures typical of ALD (e.g. 300 ^{o}C) the adjustment to the free energy is relatively minor and is not expected to change our conclusions.

One may naively expect that a plasma is too indiscriminate and energetic a reagent to show any selectivity in its reactivity. However, our results indicate that at low temperature neutral silane plasma reacts selectively with a surface Si-H bond and not with a C-H bond. A substantial barrier of 0.85 eV and 0.55 eV exists for the C-H surface bond to react with SiH_2 and SiH_3, respectively. This

is in close agreement with the activation energy of 0.82 eV that was estimated for SiH_2 inserting into the C-H bond of CH_4 by Sawrey *et al.* and Davidson *et al.* based on rate measurements. [218, 219] It was suggested by Jasinski *et al.* that the difference between Si-H and C-H with respect to SiH_2 insertion is related to the different polarities of the bonds. [220] The electrophilic SiH_2 has no difficulty approaching the slightly negative H of the Si^+-H^- bond, which is consistent with the localisation and sharing of electrons that we observed as SiH_2 approaches Si-H. By contrast, in the case of less polar C-H, access of silylene to the desired electron pair is hindered. Experimental bond dissociation energies (BDE) for the Si-H of silane in gas phase [221] and the C-H of methane in the gas phase [221] are 3.92±0.05 eV and 4.55±0.004 eV, respectively. This indicates that it is 0.63 eV harder to break C-H than Si-H in the gas phase. We computed the difference in ΔE for breaking Si-H and C-H surface bonds and forming silane to be 0.60 eV, which corresponds well to the experimental BDE data for the molecules.

In this study we computed one surface of SiC with Si and C sites. The two types of site seem to behave independently. Therefore, we suggest that the results can be generalised to other substrates that feature Si, Si-H, C and C-H surface sites. For instance, the results can be used for future area-selective PECVD of Si on Si-H and C-H surfaces. Examples of these materials can be HF-last Si (Si-H terminated) and carbon-doped silicon oxide (C-H terminated). We predict that silane plasma will preferentially deposit Si onto the Si substrate and leave the doped oxide bare. Low temperatures are preferable for selective deposition as higher temperatures might allow the high-energy barrier of C-H to be overcome.

6.6 Conclusion

In order to understand the mechanism of ALD/PECVD of SiC for future SiC applications, a theoretical study of various silicon and carbon precursors reacting with the bare and H-terminated 3C-SiC (011) surface and silane plasma fragments reacting with the H-Si and H-C surface bonds was performed using *ab-initio* density functional theory (DFT).

We found that all of the considered silicon and carbon precursors (silicon tetrachloride, disilane, silane, trichloromethane, propyne, ethyne and carbon tetrachloride) are thermodynamically likely to react with bare SiC at 0 K, passivating

the surface with Si or Cl atoms from the precursor. However, none of these precursors are thermodynamically likely to react with the passivated surface. An additional activation step would be needed to sustain an ALD process.

One of the ways to activate the non-reactive surface is to use plasma. The reaction pathways of neutral silane plasma fragments SiH_3 and SiH_2 with the H-terminated surface were analyzed. Moreover, thermodynamics of methane plasma fragments reacting with the H-terminated surface were calculated. It was found that the SiH_3 and SiH_2 reaction mechanisms are different. Two SiH_3 fragments are required to form each new Si-Si bond for Si growth, while in contrast, only one SiH_2 fragment is needed. Both overall reactions were found to be thermodynamically favorable. However, none of these reactions are self-limiting, which means that they constitute a PECVD rather than an ALD process.

Moreover, silane plasma fragments SiH_3 and SiH_2 are found to show kinetic selectivity towards reacting with the Si-H bond rather than the C-H bond of the H-terminated SiC surface at 0 K. This seems to be due to the greater polarisability of the Si-H bond. Based on this, we suggest that silane will grow Si selectively by PECVD on a material terminated with Si-H rather than with C-H, such as HF-last silicon versus carbon-doped silicon oxide. Plasma surface chemistry is not as indiscriminate as might be assumed.

Chapter 7

DFT screening for ligand exchange mechanism for area-selective deposition

The screening approach described in the Methodology Section 3.3.1 and in Chapter 5 can be also used for determining the non-growth surfaces for area-selective ALD growth based on a ligand-exchange mechanism. The ligand-exchange screening mechanism using DFT was introduced in ref. [222] for predictions of the composition of ALD-grown ternary oxides. Prof. Adrie Mackus from Eindhoven Technological University, Netherlands, suggested using a similar approach for area-selective deposition applications. Elements relevant for the semiconductor industry, such as Hf, Si, Ge, Ti, W, Co, Cu, Ru and Ta were considered with the ligands $Cp(dma)_{x\text{-}1}$ and $O^{i}Pr$ (Cp^{-} - cyclopentadienyl complex $C_5H_5^{-}$, dma - dimethylamino group $–N(CH_3)_2$, (^{i}Pr) - iso-propyl group –CH(CH3)2, x = number of ligands) that were selected based on the existing $HfCp(dma)_3$ (Air Liquide HyALD^{TM}) precursor used for the HfO_2 ALD process [223, 224] and $Ti(O^{i}Pr)_4$ (TTiP) precursor used for the TiO_2 ALD process. [225, 226] The following chapter will present the results obtained during the short term scientific mission (STSM) collaboration with Eindhoven Technological University via HERALD.

7.1 Proposed strategy for achieving a non-growth area during thermal ALD via ligand-exchange mechanism

Murray et al. [222] used DFT to predict the composition of ALD-grown ternary oxides by computing thermodynamics of the metal oxide ALD. One of the possible mechanisms of metal oxide ALD growth that was analyzed is a rapid exchange of ligands from the precursor metal centre to the surface metal centre occurs, followed by elimination of the ligand from the surface during the combustion step. After the combustion step the surface is covered with OH groups, that function as a source of protons during the subsequent precursor step, allowing the ligands to be eliminated before the subsequent combustion step so that ALD growth proceeds.

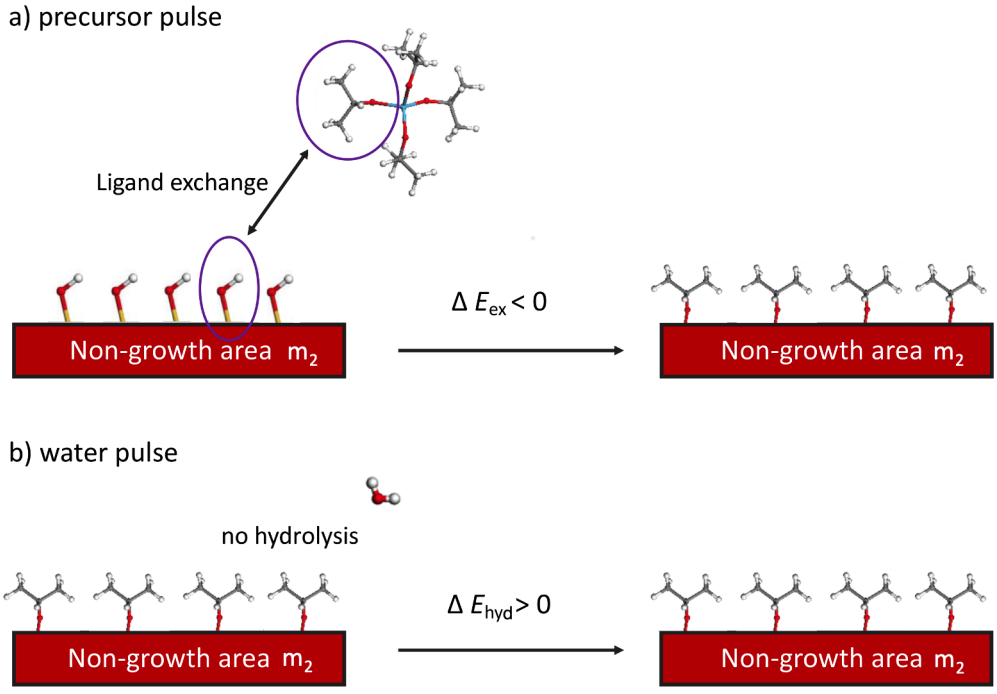


Figure 7.1: A schematic of a full area-selective ALD cycle where non-growth area is achieved through ligand-exchange mechanism. Requirements to get the non-growth area are: 1) precursor exchanges its ligand with the surface termination group during precursor half-cycle ($\Delta E_{\text{ex}} < 0$), 2) transferred ligand remains on the surface after water half-cycle ($\Delta E_{\text{hyd}} > 0$).

A similar approach is used in this chapter to determine the non-growth area during selective ALD. The strategy suggested is as follows. If the ligand ex-

change takes place during the precursor pulse, but the ligand transferred to the surface is not eliminated during the water pulse, then the surface will remain covered with those ligands instead of with OH groups. OH is necessary as a source of protons for further ligand elimination and ALD growth. The ligand-covered surfaces thus resist ALD. This idea of achieving the non-growth area during area-selective ALD using the ligand-exchange mechanism is shown schematically in Figure 7.1. The non-growth surface during ALD, thus, can be achieved if two requirements are met: 1) a precursor exchanges its ligand with OH surface group during precursor pulse (see Figure 7.1a), 2) the exchanged ligand remains on the surface during the water pulse (see Figure 7.1b). This will cause the film growth delay for the next several ALD cycles until sufficient reactive species accumulate on the surface for nucleation to start. This delay in film growth is often called nucleation delay. [156]

DFT is accurate in predicting the bond making and bond breaking during the surface ALD reactions. [227] For this reason we are using DFT for predicting whether ligand-exchange and hydrolysis reactions will happen during ALD. We use simple gas-phase molecules to represent surfaces and these have been shown to be sufficient to describe the key bond making/breaking processes which allows a larger number of chemical systems to be considered. [228], [229]

Therefore, we use DFT to screen various precursors with metal center cation m_1 (m_1=Hf, Si, Ge, Ti, W, Co, Cu, Ru or Ta) with an anionic ligands $Cp(dma)_{x-1}$ and $(O^iPr)_x$ for the possibility of the ligand-exchange mechanism reacting with various OH-terminated metal oxide surfaces with metal centre m_2 (m_2=Hf, Si, Ge, Ti, W, Co, Cu, Ru or Ta) and further hydrolysis reaction with the surface to determine which surfaces can be the non-growth surfaces during area-selective ALD. It is appreciated that many of the precursors presented in this work are experimentally not available and included for completeness.

7.2 Methodology

The energetics per ligand for the ligand-exchange reaction ΔE_{ex} from a precursor with metal centre m_1 with an OH-terminated surface with metal centre m_2 (precursor exposure half-cycle, see Figure 7.1a) are calculated using equations 7.1a for Cp^- ligand transfer and 7.1b for O^iPr ligand transfer, where x=number

of ligands of metal centre m_1 or m_2 (x=4 for Hf, Si, Ge, Ti, W, x= 2 for Co, Cu, Ru and x=1 for Ta):

$$\Delta E_{ex} = E_{m_1(OH)(dma)_{x-1}} + E_{m_2Cp(dma)_{x-1}} - E_{m_1Cp(dma)_{x-1}} - E_{m_2(OH)(dma)_{x-1}} \quad (7.1a)$$

$$\Delta E_{ex} = [E_{m_1(OH)_x} + E_{m_2(O^iPr)_x} - E_{m_1(O^iPr)_x} - E_{m_2(OH)_x}]/x \quad (7.1b)$$

The number of the ligands was chosen based on the common oxidation states of metal centres. Examples of the gas-phase models for $HfCp(dma)_3$ precursor (m_1 = Hf) and $Ti(O^iPr)_4$ (m_1 = Ti) precursor with OH-terminated Si oxidesurface (m_2 = Si) are shown in Figure 7.2 (a) and (b), respectively.

The second condition for the non-growth surfaces after the ligand is transferred from a precursor to the surface is that the remaining ligand is not removed by water during the water pulse (water ALD half-cycle, see Figure 7.1b)). The energetics of the hydrolysis reaction are calculated using equation 7.2a for surface terminated with Cp^- surface group and 7.2b for surface terminated with O^iPr surface group.

$$\Delta E_{hyd}/\text{ligand} = E_{m_2(OH)(dma)_{x-1}} + E_{Cp-H} - E_{m_2Cp(dma)_{x-1}} - E_{H_2O} \quad (7.2a)$$

$$\Delta E_{hyd}/\text{ligand} = [E_{m_2(OH)_x} + E_{O^iPr-H} - E_{m_2(O^iPr)_x} - E_{H_2O}]/x \quad (7.2b)$$

Values of ΔE_{ex} and ΔE_{hyd} in the range of -0.1 eV to 0.1 eV are not reliable as this is the likely level of the DFT error. Hence, these values will not be considered.

Models for precursors were chosen based on the existing $HfCp(dma)_3$ and $Ti(O^iPr)_4$ precursors. In order to describe the mechanism of a $m_1Cp(dma)_{x-1}$ precursor exchanging its one Cp ligand with an OH surface group, the molecule $m_2OH(dma)_{x-1}$ was chosen to represent the surface. $Ti(O^iPr)_4$ is a homoleptic precursor, hence, in order to describe the mechanism of $m_1(O^iPr)_x$ precursor exchanging one O^iPr ligand with a surface OH group, the $m_2(OH)_x$ molecule was chosen to represent the surface. Calculated ΔE_{ex} and ΔE_{hyd} for O^iPr ligand-exchange mechanism are further divided by the number of the ligands, as shown in eq. 7.1b and 7.2b.

Examples of the gas-phase models for hydrolysis reaction of the surface with Cp

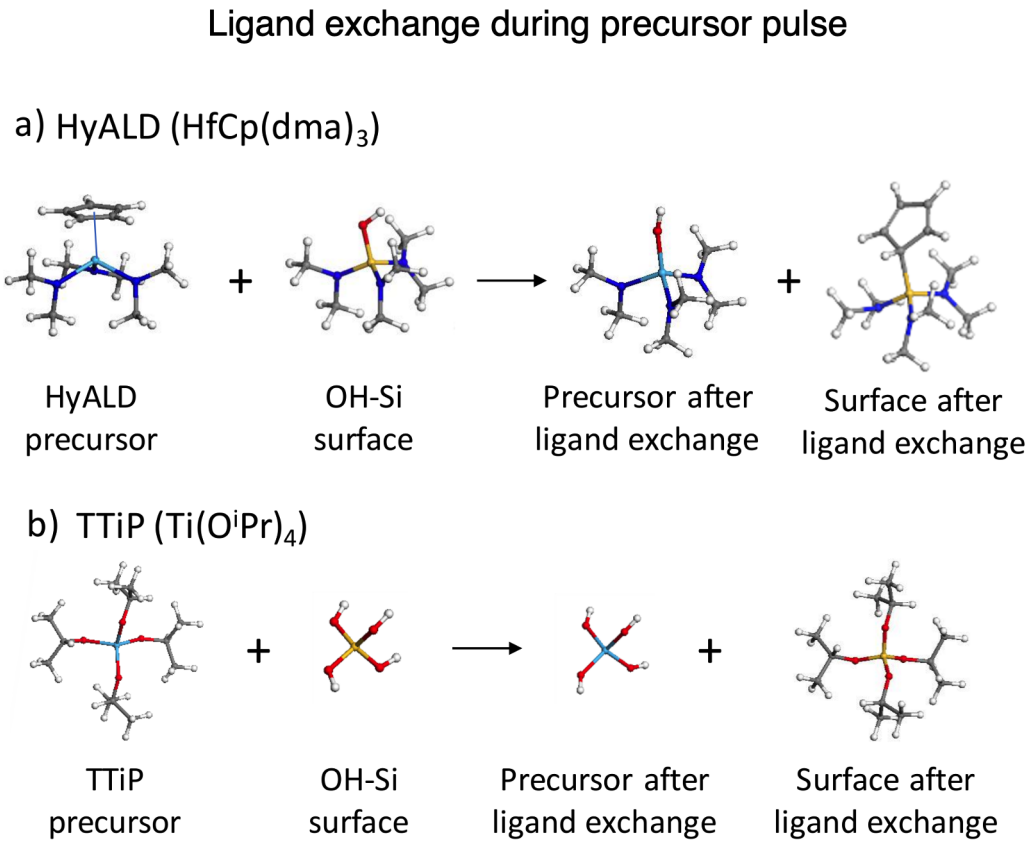


Figure 7.2: Ligand exchange gas-phase model on the example of a) $HfCp(dma)_3$ (Air Liquide HyALD^{TM}) and b) TTiP ($Ti(O^iPr)_4$) precursor exposure step. OH-terminated Si surface is represented by a) $SiOH(dma)_3$ and b) $Si(OH)_4$ cluster models. Color scheme: white=hydrogen, grey=carbon, light blue=titanium, light blue=hafnium, yellow=silicon, red=oxygen, dark blue=nitrogen. Cp - cyclopentadienyl complex (C_5H_5), (^iPr) - iso-propyl group $–CH(CH_3)_2$, (dma) - dimethylamino group $–N(CH_3)_2$.

and O^iPr ligands on it during the water pulse are shown in Figure 7.3.

Precursors and surfaces were modelled as isolated molecules in vacuum using the Vienna ab-initio simulation package (VASP). [157] Cluster models were used to represent the surface. The generalized gradient approximation to DFT [191] was implemented by using the exchange correlation functional of Perdew, Burke and Ernzerhof (PBE) [191]. The projector augmented wave (PAW) method [147, 157] was used to describe the core electrons of atoms. A plane wave basis set with a cut-off energy 400 eV was used for the valence orbitals. Molecules were optimized at single Γ-point using the conjugate gradient method for energy minimization at convergence level of 0.01 eV/Å on each ion. The size of the cell was chosen as 15x15x15 Å.

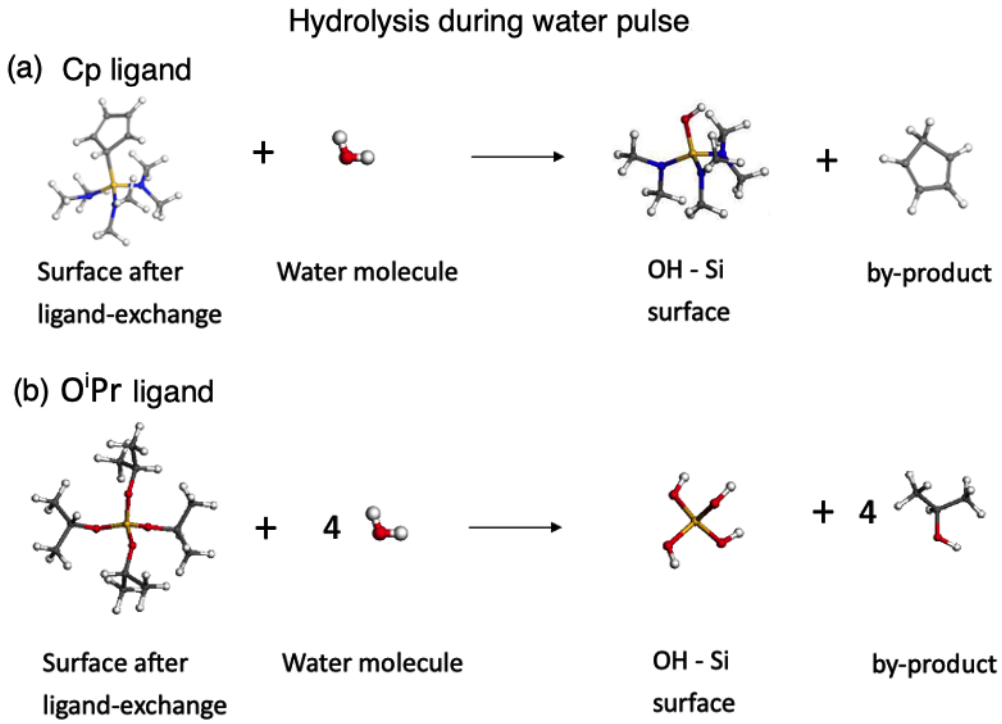


Figure 7.3: Hydrolysis gas-phase model on the example of a) HyALD and b) TTiP ALD water pulses. Si surface with Cp^- and O^iPr surface groups is represented by a) $SiCp(dma)_3$ and b) $Si(O^iPr)_4$ cluster models. Color scheme: white=hydrogen, grey=carbon, yellow=silicon, red=oxygen, dark blue=nitrogen.

7.3 Results

We use ΔE as a metric for the ligand elimination from the precursor during ligand-exchange reaction or from the surface during the water pulse. Therefore, the absolute value of ΔE is not of a significant importance. However, the relative value of ΔE allows us to compare the reactivity of various precursors. The more negative ΔE_{ex} the more likely is the precursor to transfer its ligand to the surface. Similarly, the more negative ΔE_{hyd} the more likely that the transferred ligand is to be eliminated from the surface during the water pulse. Conversely, the more positive ΔE_{ex} is, the more stable is the precursor and the less likely to exchange its ligand with the surface; the more positive ΔE_{hyd} is the more stable is the surface complex with the transferred ligand on it and the less likely for hydrolysis to take place during the water cycle.

Optimized geometries

Examples of optimized $HfCp(dma)_3$ and $Ti(O^iPr)_4$ precursors and surface mod-

els structures before and after ligand-exchange can be found in Figures 7.2 and 7.3. Bond lengths m_1/m_2-Cp and m_1/m_2-O of optimized precursors and surfaces models are shown in Table 7.1. The smallest bond lengths are calculated to be for the precursors with the smallest number of ligands (two) for Co, Cu and Ru (1.82, 1.86 and 1.78 Å, respectively). Bond lengths for Ta with three ligands and Hf, Si, Ge, Ti and W with four ligands are calculated to be very similar (2.04, 2.23, 2.05, 2.06, 2.09 and 1.99Å, respectively). m_1/m_2-O bond lengths do not follow similar trend.

The M-Cp ligand can have different bonding modes for different metal centres. The most common bonding mode is the η^5-coordination (metal centre binds to all Cp^- carbon atoms). Another bonding mode, relatively rare, is η^1 bonding (where metal centre binds to one Cp^- carbon atom). η^1 is common for group 14 elements, in our project Si and Ge. [230] η^1-bonded Si-Cp and Ge-Cp bond lengths (2.05 and 2.06 Å, respectively) are only slightly smaller than η^5-bonded Hf-Cp and Ti-Cp (2.23 and 2.09 Å, respectively) and slightly larger than η^5-bonded W-Cp (1.99 Å).

Table 7.1: Bond lengths of the optimized precursor ($m_1Cp(dma)_{x-1}$, $m_1(O^iPr)_x$) and surface models with Cp and O^iPr groups (m_2 $Cp(dma)_{x-1}$, $m_2(O^iPr)_x$)

	Bond length, Å	
Metal centre, m_1/m_2	M-Cp	M-O
Hf	2.23	1.95
Si	2.05	1.65
Ge	2.06	1.81
Ti	2.09	1.84
W	1.99	1.87
Co	1.82	1.73
Cu	1.86	1.76
Ru	1.78	1.81
Ta	2.04	1.91

7.3.1 ALD water pulse: hydrolysis

ΔE_{hyd} for hydrolysis reactions with Cp and O^iPr covered m_2 oxide surfaces are presented in Table 7.2 and Figure 7.4.

Table 7.2: ΔE_{hyd} of hydrolysis reaction during the ALD water pulse computed using eq. 7.2a and 7.2b. Surface with Cp^- or O^iPr groups after the successful ligand-exchange process during the precursor pulse are represented by molecules $m_2Cp(dma)_{x-1}$ and $m_2(O^iPr)_x$, respectively. m_2=Hf, Si, Ge, Ti, W, Co, Cu, Ru, Ta (x=4 for Hf, Si, Ge, Ti, W, x= 2 for Co, Cu, Ru and x=1 for Ta).

	ΔE_{hyd}, eV	
Metal centre m_2	Cp^- ligand	O^iPr ligand
Hf	-0.02	-0.03
Si	-0.99	-0.10
Ge	-0.45	-0.09
Ti	-0.09	0.09
W	0.92	0.24
Co	0.77	0.13
Cu	0.27	0.09
Ru	2.45	0.01
Ta	0.17	-0.13

Cp^- ligand

As shown in Figure 7.4 ΔE_{hyd} for the Cp^- ligand is strongly positive for W, Co, Cu, Ru and Ta oxide surfaces. Hence, Cp^- groups are predicted to remain on the W, Co, Cu, Ru and Ta oxide surfaces during the water pulse at 0 K. For Si, Ge and Ti oxide surfaces ΔE_{hyd} was calculated to be negative, predicting that hydrolysis is thermodynamically favorable on these oxide surfaces. ΔE_{hyd} is only slightly negative for Hf surface.

The difference between the most exothermic ΔE for Si oxide surface (ΔE_{hyd} = -0.99 eV) and the most endothermic ΔE_{hyd} for Ru oxide surface (ΔE_{hyd} = 2.45 eV) is predicted to be large (3.44 eV). This difference illustrates that the nature of the surface metal is of a high importance and that selectivity may be possible.

O^iPr ligand

ΔE_{hyd} values for O^iPr surface groups were found to be fairly similar to each other: slightly positive for Ti, W, Co and Cu oxide surfaces and slightly negative for Si, Ge and Ta oxide surfaces. Hence, it can be predicted that m_2(OiPr) surface will remain intact during the water pulse on the OH-terminated Ti, W, Co and Co surfaces. However, these values are only slightly positive (<0.24 eV), meaning that including the entropy and temperature effects may shift it towards negative values.

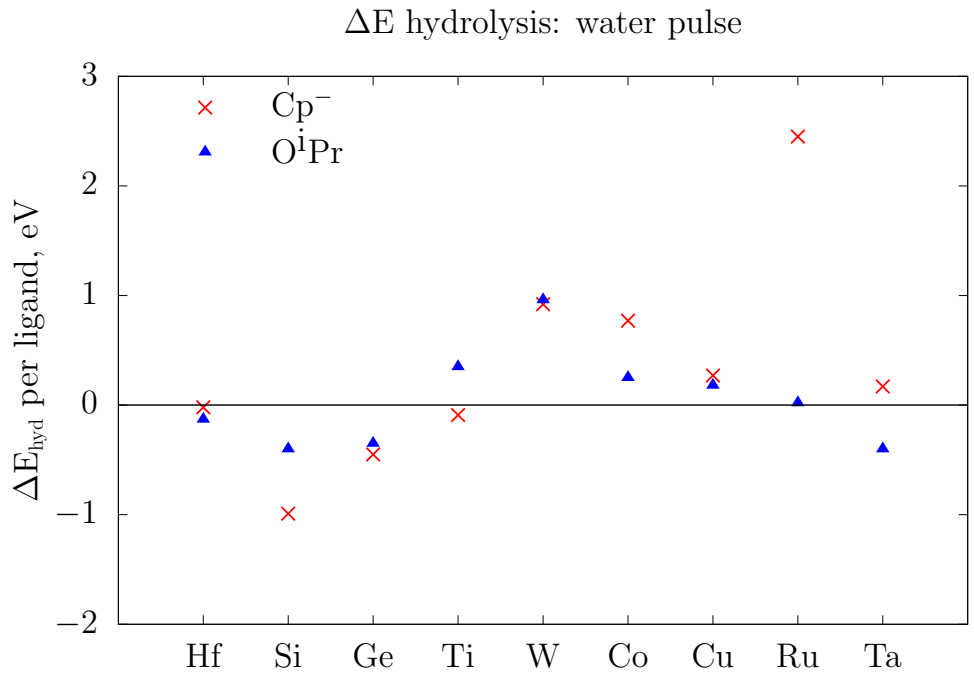


Figure 7.4: ΔE of hydrolysis reaction during the water pulse. Surface with Cp^- or O^iPr groups after the successful ligand-exchange process during the precursor pulse are represented by molecules $m_1Cp(dma)_{x-1}$ and $m_1(O^iPr)_x$, respectively. m_2=Hf, Si, Ge, Ti, W, Co, Cu, Ru, Ta. x=4 for Hf, Si, Ge, Ti, W, x= 2 for Co, Cu, Ru and x=1 for Ta. ΔE_{hyd} values are shown in Table 7.2.

In contrast to Cp ligand, for the O^iPr ligand, a much smaller difference of 0.37 eV is predicted between the most endothermic ΔE_{hyd} for W oxide surface (ΔE_{hyd} = 0.24 eV) and the most exothermic ΔE for the Ta oxide surface (ΔE_{hyd} = -0.13 eV). This illustrates that the identity of the surface metal is of less importance for hydrolysis of a surface with an O^iPr group on it. This ligand is thus less promising for area-selective ALD.

7.3.2 ALD precursor pulse: ligand-exchange mechanism

Focusing on the area-selective deposition applications, we are mostly interested in determination the non-growth surface during ALD using the considered precursors. As was mentioned in the introduction, in order to get a nucleation delay on the surface two requirements must be met: 1) precursor will exchange its ligand with the surface during the precursor step and 2) surface after ligand exchange will remain intact during the water pulse. Above, we analyzed ΔE_{hyd} for the second requirement for various surfaces and the considered precursors

and found that Cp groups remain on the OH-terminated W, Co and Ru oxide surfaces and O^{i}Pr groups remain on OH-terminated Ti, Ta, Co and Cu oxide surfaces at 0 K during the water pulse. For this reason, we will now be mostly focusing on whether these surfaces meet the first requirement.

$m_1Cp(dma)_{x-1}$ precursor

A matrix of ΔE_{ex} for the $m_1Cp(dma)_{x-1}$ precursor exchanging the Cp ligand with various OH-terminated m_2 surfaces is presented in Table 7.5. The most negative ΔE_{ex} values were calculated for $SiCp(dma)_3$ precursor donating the ligand to all the considered surfaces. The most positive values were calculated for the RuCp(dma) donating Cp to all the considered surfaces.

None of the precursors were predicted to exchange a Cp ligand with the OH-terminated Si surface. However, all of the considered precursors are expected to react with the OH-terminated Ru surface. Recalling that ΔE_{hyd} for Ru-Cp surface was calculated to be 2.45 eV (see Table 7.2). OH-Ru is therefore predicted to be a good candidate as the non-growth surface during ALD processes with all the considered precursors.

ΔE_{ex} were calculated to be negative for $HfCp(dma)_3$, $SiCp(dma)_3$, $GeCp(dma)_3$, $TiCp(dma)_3$, CuCp(dma) and $TaCp(dma)_2$ precursors reacting with W, Co and Ru surfaces.

The RuCp(dma) precursor was calculated to be stable against exchanging its Cp ligand with all the considered OH-terminated surfaces with strongly positive $\Delta E_{ex} > 1.54$ eV. It is indeed hard to deposit noble metal materials, such as Ru using ALD. For example, currently the most widely used Ru ALD precursor $Ru(EtCp)_2$ shows very long nucleation delays on SiO_2 and TaN surfaces for both Ru and RuO_2. [231–236] One of the possible explanations of this nucleation delay can be the strongly positive ΔE_{ex} ($\Delta E_{ex} = 3.44$ eV) for the Ru precursor to exchange its Cp ligand with OH-groups on the SiO_2, along with the positive ΔE_{hyd} for eliminating Cp. While OH groups are present on the surface, $Ru(EtCp)_2$ is not thermodynamically likely to transfer its Cp ligand to the surface, thus preventing growth. We also predict the CoCp(dma) precursor to be stable against exchanging its Cp ligand with most of the OH-terminated surfaces, except W and Ru. Experimentally Co_3O_4 growth is very slow (GPC 0.05 nm/cycle at 100 - 400 °C) [237] by ALD using $CoCp_2$ and O_2 plasma on SiO_2 (Si with native oxide or thermally grown SiO_2). This can be also explained by the strongly positive calculated $\Delta E_{ex} = 1.76$ eV and ΔE_{hyd} for the reactions

of the Cp ligand with the surface. OH groups can be presented after every O_2 pulse, further slowing down the precursor Co chemisorption during the precursor pulse. Using $CoCp_2$ precursor with H_2/N_2 [238, 239] and NH_3 [239, 240] plasma instead of O_2 plasma indeed increases the GPC (GPC=0.065 nm/cycle at 450 °C and GPC=0.097 nm at 300 °C for H_2/N_2 and NH_3 plasmas, respectively).

To summarize, when $m_1Cp(dma)_{x-1}$ precursor are used m_1O_x is predicted to have a nucleation delay on the OH-terminated W, Co, Cu, Ru and Ta surfaces for precursors with metal centres Hf, Si, Ge and Ti. OH-terminated W, Co and Ru surfaces are predicted to be non-growth surfaces when CuCp(dma) is used. OH-terminated W and Ru surfaces are predicted to be the non-growth surfaces when CoCp(dma) is used. The OH-terminated Ru surfaces is predicted to be a non-growth surface for the $m_1Cp(dma)_{x-1}$ precursors with all the considered metal centres (see Figure 7.7).

ΔE, eV		surface $M_2(OH)(dma)_{x-1}$								
		Hf	Si	Ge	Ti	W	Co	Cu	Ru	Ta
Precursor $M_1Cp(dma)_{x-1}$	Hf	0.00	0.97	0.43	0.07	-0.93	-0.79	-0.29	-2.47	-0.17
	Si	-0.97	0.00	-0.54	-0.90	-1.90	-1.76	-1.26	-3.44	-1.13
	Ge	-0.43	0.54	0.00	-0.36	-1.37	-1.22	-0.72	-2.90	-0.60
	Ti	-0.07	0.90	0.36	0.00	-1.00	-0.86	-0.36	-2.54	-0.24
	W	0.93	1.90	1.37	1.00	0.00	0.14	0.64	-1.54	0.77
	Co	0.79	1.76	1.22	0.86	-0.14	0.00	0.50	-1.68	0.62
	Cu	0.29	1.26	0.72	0.36	-0.64	-0.50	0.00	-2.18	0.13
	Ru	2.47	3.44	2.90	2.54	1.54	1.68	2.18	0.00	2.31
	Ta	0.17	1.13	0.60	0.24	-0.77	-0.62	-0.13	-2.31	0.00

Figure 7.5: ΔE of precursor $m_1Cp(dma)_{x-1}$ exchanging a Cp^- ligand with surface OH group. Surface is represented by a molecule $m_2(OH)(dma)_{x-1}$. $m_{1,2}$=Hf, Si, Ge, Ti, W, Co, Cu, Ru, Ta, x=4 for Hf, Si, Ge, Ti, W, x= 2 for Co, Cu, Ru and x=1 for Ta. Example: $HfCp(dma)_3$ precursor reacting with OH-terminated Si surface, $HfCp(dma)_3$ + $(OH)Si(dma)_3$(surface) $\longrightarrow$ $(OH)Hf(dma)_3$ + $SiCp(dma)_3$(surface with Cp^- ligand), ΔE_{ex}=0.97 eV, i.e. Cp ligand transfer is not thermodynamically favorable from Hf to Si.

$m_1(O^iPr)_x$ precursor

A matrix of ΔE_{ex} for $m_1(O^iPr)_x$ exchanging ligands with OH-terminated m_1 surfaces is presented in Figure 7.6. In general,these ΔE_{ex} are less negative than for the $m_1Cp(dma)_{x-1}$ precursor. The most negative ΔE_{ex} were calculated for the $Ta(O^iPr)_3$ precursor reacting with all the considered surfaces. However, for $Ta(O^iPr)_3$ exchanging ligands with OH-Si and OH-Ge, ΔE_{ex} was predicted to

be only slightly negative (-0.10 and -0.14 eV, respectively). Ligand exchange is predicted to take place for all the considered precursors with the OH-terminated W surface. Taking into account that the W-(O^iPr) surface is predicted to remain intact during the water pulse, ALD growth of oxides using all the considered precursors is expected to be delayed on the OH-W surface at 0 K. Based on the calculated positive values of ΔE_{hyd} and negative values of ΔE_{ex} described above, the ALD of m_1O_y using water and precursors $m_1(O^iPr)_x$ with metal centres Hf, Si, Ge and Ta and water is predicted to have a nucleation delay on the OH-terminated Ti, W, Co and Cu surfaces. These results are summarized in Figure 7.8.

Δ E/ligand, eV		Surface $M_2(OH)_x$								
		Hf	Si	Ge	Ti	W	Co	Cu	Ru	Ta
Precursor $M_1(O^iPr)_x$	Hf	0.00	0.07	0.05	-0.12	-0.27	-0.16	-0.13	-0.04	0.30
	Si	-0.07	0.00	-0.01	-0.19	-0.34	-0.23	-0.19	-0.11	0.10
	Ge	-0.05	0.01	0.00	-0.17	-0.33	-0.21	-0.18	-0.10	0.14
	Ti	0.12	0.19	0.17	0.00	-0.15	-0.04	-0.01	0.08	0.66
	W	0.27	0.34	0.33	0.15	0.00	0.11	0.15	0.23	1.12
	Co	0.16	0.23	0.21	0.04	-0.11	0.00	0.02	0.06	0.39
	Cu	0.13	0.19	0.18	0.01	-0.15	-0.02	0.00	0.04	0.34
	Ru	0.04	0.11	0.10	-0.08	-0.23	-0.06	-0.04	0.00	0.22
	Ta	-0.30	-0.10	-0.14	-0.66	-1.12	-0.39	-0.34	-0.22	0.00

Figure 7.6: ΔE_{ex} of precursor $m_1(O^iPr)_x$ exchanging one O^iPr ligand with surface OH group. Surface is represented by a molecule $m_2(OH)_x$. $m_{1,2}$=Hf, Si, Ge, Ti, W, Co, Cu, Ru, Ta, x=4 for Hf, Si, Ge, Ti, W, x= 2 for Co, Cu, Ru and x=1 for Ta. Example: TTiP($Ti(O^iPr)_4$) precursor reacting with OH-terminated Si surface, $Ti(O^iPr)_4$ + $Si(OH)_4$(surface) $\longrightarrow$ $Hf(OH)_4$ + $Si(O^iPr)_4$(surface with O^iPr ligands), ΔE_{ex}=0.19 eV, i.e. O^iPr ligand transfer is not thermodynamically favorable from Ti to Si.

Table 7.3: m_1/m_2-Cp and m_1/m_2-O bond experimental bond dissociation energy (BDE) measured at T=298 K and 1 atm pressure. "-" BDE was not found.

	BDE, eV	
Metal centre, m_1/m_2	M-Cp (Ref.)	M-O (Ref.)
Hf	4.27([241])	8.30([242], [221] p.686)
Si	-	8.22([243], [221] p.462)
Ge	-	6.84([244], [221] p.472)
Ti	3.29([241])	6.98([245], [221] p.669)
W	4.63([241])	7.46([246], [221] p.768)
Co	3.35([241])	3.99([247], [221] p.858)
Cu	-	2.98([248], [221] p.972)
Ru	-	5.47([242], [221] p.842)
Ta	-	8.22([249], [221] p.710)

7.4 Discussions

7.4.1 Bond dissociation energies (BDE)

The calculated ΔE_{ex} describe breaking and formation of M-ligand and M-O bonds for m_1 and m_2. The bond dissociation energy (BDE) describes the strength of the chemical bond when it is cleaved by homolytic dissociation. Hence, one would expect that the ligand-exchange mechanism can also be predicted by analyzing experimental or theoretical BDE of M-Cp and M-O for various metal centres. In order to understand if ΔE_{ex} corresponds to experimental BDE we compare our calculated ΔE_{ex} with experimental BDE values, presented at Table 7.3. BDE are measured at standard conditions (T=298 K and p=1 atm). BDE for M-Cp bonds are measured by evaluating the enthalpies of formation of bis-cyclopentadienyls (MCp_2) [241], BDE for M-O bonds measured using enthalpies of formation of metal oxides $M(O)_x$-O [221, 242–249].

As can be seen from Table 7.3, BDE do not show the same trend as the calculated ΔE_{hyd} and ΔE_{ex}. For example, the experimentally measured experimentally BDE for Hf-Cp is 4.27 eV and for Co-Cp 3.35 eV. Hence, one would expect ΔE_{hyd} for the Co-Cp surface to be more negative than ΔE_{hyd} of Hf-Cp. However, the calculated ΔE_{hyd} for the Co-Cp surface is 0.77 eV and for Hf-Cp is -0.02 eV. Similarly, for the M-O bonds in $m_1(O^iPr)_x$ the Hf-O BDE is 8.3 eV and the Co-O BDE is 3.99 eV; however the calculated ΔE_{hyd} is -0.03 eV and 0.13 eV, respectively. Furthermore, ΔE_{ex} was calculated to be the most negative for the

$Ta(O^iPr)_3$ precursor to react with all the considered surfaces. One would therefore expect the BDE of Ta-O BDE to be the smallest of all. However, it is one of the largest (8.22 eV). This disagreement can be explained by the difference in the geometry of the considered precursor and surface models and the geometry of the molecules actually used for experimental setup to determine BDE. The BDE for M-Cp bonds were measured for bis-cyclopentadienyls [241] and the BDE for M-O bonds was chosen as averaged BDE value [221], which differs from our models. The experimental values of BDE strongly varies depending on what kind of molecules or molecule cluster are considered for the measurements. Hence, the ligand-exchange mechanism introduced in this chapter can not be simply predicted based on the experimental BDE values.

7.4.2 Temperature and entropy effects

All the energies were calculated at 0 K. Thereby, it is important to bear in mind that including entropy and temperature effects via $T\Delta S$ may affect the predicted selectivity. Entropy and temperature effects can be included by calculating Gibbs energy using equation $\Delta G = \Delta E - T\Delta S$ (see Chapter 5). It can be assumed that entropy of the surfaces is equal to zero. Hence, for the ligand exchange reaction ΔS will be the difference between the entropy of the by-product $m_2OH(dma)_{x-1}$ and entropy of the precursor $m_1Cp(dma)_{x-1}$ (or by-product $m_2OH(O^iPr)_{x-1}$ and $m_2(O^iPr)_x$ precursor). The size of the precursor $m_1Cp(dma)_{x-1}$ and $m_2(O^iPr)_x$ molecules is similar, so the entropy ΔS is expected to be similar. Based on the entropy calculations in Chapter 5 for molecules of similar size, ΔS for the ligand-exchange reactions for both $m_1Cp(dma)_{x-1}$ and $m_2(O^iPr)_x$ precursors ΔS is estimated to be around -0.003 $\frac{eV}{K}$, which increases all ΔE_{ex} by 0.82 eV at room temperature. At 100 $^\circ$ ΔE_{ex} would therefore be even higher, increased by 1.12 eV. Hence, including temperature and entropy effects shifts all ΔE_{ex} towards more positive absolute values.

For ΔE_{hyd} ΔS will depend on the entropy values of Cp-H (O^iPr) by-products and water. The by-products CpH and HO^iPr are bigger than the water molecule, so the entropy for by-products is expected to be higher. Hence, entropy for these by-products and temperature effects are expected to shift all ΔE_{hyd} to more negative values. This can change all the endothermic hydrolysis reactions with slightly positive ΔE_{hyd} for the surface with O^iPr groups to exothermic reactions, allowing the ALD growth and removing any selectivity. For this reason it is

important to perform area-selective ALD at the lowest possible temperatures.

7.4.3 Experimental corroboration of the DFT results

For the existing TiO_2 ALD using the TTiP precursor and water, a negative ΔE_{ex} of -0.15 eV is calculated for the exchange of its O^iPr ligand with OH-W surface. Hydrolysis of W surfaces terminated with O^iPr groups was predicted to be thermodynamically unfavorable (ΔE_{hyd}=0.09 eV). Thus, for TiO_2 ALD using the TTiP precursor and H_2O a nucleation delay is expected on the OH-terminated W surface. Similarly, the existing HfO_2 ALD process using the HyALD precursor and water is predicted to have a nucleation delay on OH-terminated W, Co, Cu, Ru and Ta surfaces . However, HfO_2 (HyALD precursor plus water) [224] and TiO_2 (TTiP precursor plus water) [225,250] were successfully grown on Si substrates at T>300 °C.

Hence, in order to corroborate the obtained theoretical results, the following two experiments can be suggested: 1) ALD deposition of thermal HfO_2 using HyALD precursor and water and 2) ALD deposition of thermal TiO_2 using TTiP precursor and water on Si, W, Co, Ru and Ta surfaces measuring apparent film thickness every half-cycle using in-situ spectroscopic ellipsometry.

7.5 Conclusion

DFT calculations were used to determine the possibility of the growth delay on various OH-terminated metal and metal oxide surfaces during ALD of oxide m_1O_y using precursors $m_1Cp(dma)_{x-1}$ or $m_1(O^iPr)_x$ and water for area-selective deposition applications. Based on this approach, in order to get a non-growth surface during ALD two requirements must be met: 1) it must be favourable for a precursor to exchange its ligand with an OH surface group during the precursor pulse and 2) the exchanged ligand must remain on the surface during the water pulse. In order to perform this screening, the thermodynamics of ligand exchange reaction ΔE_{ex} and hydrolysis ΔE_{hyd} were calculated at 0 K.

It was predicted that when $m_1Cp(dma)_{x-1}$ precursor and water are used, m_1O_y will have a nucleation delay on the OH-terminated W, Co, Cu, Ru and Ta surfaces for precursors with metal centres m_1=Hf, Si, Ge and Ti. OH-terminated W, Co and Ru surfaces are predicted to be non-growth surfaces

Cp ligand

ALD grown material	Precursor	Substrate (OH-terminated surface)								
		Hf	Si	Ge	Ti	W	Co	Cu	Ru	Ta
HfO_x	$HfCp(dma)_3$	-	-	-	-	x	x	x	x	x
SiO_x	$SiCp(dma)_3$	-	-	-	-	x	x	x	x	x
GeO_x	$GeCp(dma)_3$	-	-	-	-	x	x	x	x	x
TiO_x	$TiCp(dma)_3$	-	-	-	-	x	x	x	x	x
WO_x	$WCp(dma)_3$	-	-	-	-	-	-	-	x	-
CoO_x	$CoCp(dma)$	-	-	-	-	x	-	-	x	-
CuO_x	$CuCp(dma)$	-	-	-	-	x	x	-	x	-
RuO_x	$RuCp(dma)$	-	-	-	-	-	-	-	-	-
TaO_x	$TaCp(dma)_2$	-	-	-	-	x	x	x	x	-

Figure 7.7: ALD growth of m_1O_y using $m_1Cp(dma)_{x-1}$ precursor and water is predicted to have a nucleation delay at o K on the surfaces marked as "x" (green color). "-" means that the requirements for non-growth surface considered in this chapter were not met.

O^iPr ligand

ALD grown material	Precursor	Substrate (OH-terminated surface)								
		Hf	Si	Ge	Ti	W	Co	Cu	Ru	Ta
HfO_x	$Hf(O^iPr)_4$	-	-	-	x	x	x	x	-	-
SiO_x	$Si(O^iPr)_4$	-	-	-	x	x	x	x	-	-
GeO_x	$Ge(O^iPr)_4$	-	-	-	x	x	x	x	-	-
TiO_x	$Ti(O^iPr)_4$	-	-	-	-	x	-	-	-	-
WO_x	$W(O^iPr)_4$	-	-	-	-	-	-	-	-	-
CoO_x	$Co(O^iPr)_2$	-	-	-	-	x	-	-	-	-
CuO_x	$Cu(O^iPr)_2$	-	-	-	-	x	-	-	-	-
RuO_x	$Ru(O^iPr)_2$	-	-	-	-	x	-	-	-	-
TaO_x	$Ta(O^iPr)_3$	-	-	-	x	x	x	x	-	-

Figure 7.8: ALD growth of m_1O_y using $m_1(O^iPr)_x$ precursor and water is predicted to have a nucleation delay at 0 K on the surfaces marked as "x" (green color). "-" means that the requirements for non-growth surface considered in this chapter were not met.

when the CuCp(dma) precursor is used. OH-terminated W and Ru surfaces are predicted to be the non-growth surfaces when the CoCp(dma) is used. The OH-terminated Ru surfaces is predicted to be a non-growth surface for the $m_1Cp(dma)_{x-1}$ precursors with all the considered metal centres. Predicted non-growth surfaces are summarised in Figure 7.7 and marked in green.

For ALD of m_1O_y using water and precursors $m_1(O^iPr)_x$ with metal centres Hf, Si, Ge and Ta is predicted to have a nucleation delay on the OH-terminated

Ti, W, Co and Cu surfaces. The OH-terminated W surface is predicted to be a non-growth surface for ALD of m_1O_y using precursors with all the considered metal centres. Predicted non-growth surfaces are summarised in Figure 7.8 and are marked in green. Selectivity is likely to be lost at elevated deposition temperatures.

Chapter 8

Conclusions

8.1 Summary

In the current work we use theoretical modelling in order to understand the chemistry of the thin-film nucleation during the initial step of area-selective ALD (AS-ALD). We focus on the AS-ALD of Si-based materials using aminosilane precursors on the Si, SiC, SiO_2 and Si_3N_4 surfaces that are widely used in the semiconductor industry. We are also investigating the routes towards possible ALD of SiC. Lastly, we perform the screening of a wide range of technologically-useful substrates for AS-ALD of metal oxides.

We found both theoretically and experimentally that aminosilane reacts selectively with Si_3N_4:NH_2/NH and SiO_2:OH, but not with SiC:H and Si:H surfaces (Chapter 4). However, aminosilanes are sources of Si-H groups. After reacting, aminosilane passivates the reactive Si_3N_4:NH_2/NH and SiO_2:OH surfaces with inert Si-H bonds and selectivity is lost. Thus, the inertness of the Si-H surface is a major obstacle towards developing thermal AS-ALD processes for Si-based materials using aminosilane precursors. Furthermore, in Si_3N_4 PEALD, the subsequent N_2 plasma half-cycle modifies the Si-H terminated surface into a reactive N-H terminated surface, thus allowing the SiNx growth on all the surfaces. These results illustrate that it is generally difficult to achieve area-selective PEALD for nitrides, because of the nitridation of all exposed substrate surfaces during the plasma step.

The inertness of the Si-H surface bond is also one of the possible reasons for why the ALD of SiC is so challenging. The precursors predicted to show the most fa-

vorable thermodynamics for ALD of SiC (see Chapter 5) were disilane (Si_2H_6), silane (SiH_4), monochlorosilane (SiH_3Cl), ethyne (C_2H_2), carbontetrachloride (CCl_4) and trichloromethane ($CHCl_3$). It was found that these precursors are likely to react with bare SiC, passivating the surface with H, and thus resulting in a surface covered with inert Si-H and C-H surface bonds. Also, none of these precursors were found to be reactive towards such a H-terminated surface (see Chapter 6). Hence, one of the ways towards the ALD of SiC is activation of the inert Si-H and C-H bonds on the SiC surface. In order to find a potential way to activate the non-reactive H-passivated SiC surface, the reaction pathways of neutral silane plasma fragments SiH_3 and SiH_2 were analyzed in the second part of Chapter 6. Silane plasma fragments SiH_3 and SiH_2 are found to show kinetic selectivity towards reacting with the Si-H bond rather than the C-H bond of the H-terminated SiC surface. Based on this, we suggest that silane plasma will grow Si selectively on a material terminated with Si-H rather than with C-H. However, silane plasma does not react with the surface in a self-limiting manner, which means that this constitutes a PECVD rather than a PEALD process. Furthermore, silane plasma still produces an inert Si-H surface, and so does not activate the surface as hoped for.

We also use the theoretical screening approach introduced in Chapter 5 for screening chemical reactions for various metal-centered precursors with typical ligands and various surfaces in order to define the non-growth surface required for future area-selective deposition applications (see Chapter 7). Based on this approach, in order to get a non-growth surface during ALD two requirements must be met: 1) a precursor is favorable to exchange its ligand with OH surface group during precursor pulse and 2) the exchanged ligand will remain on the surface during the water pulse. HfO_2, SiO_2 and GeO_2 are predicted to show a nucleation delay in ALD on OH-terminated W, Co and Cu surfaces when precursors with Cp(dma) and O^iPr ligands are used. Ru-based and W-based substrates were predicted to resist the nucleation of all the metal oxides from precursors with Cp(dma) ligands and O^iPr ligands respectively. Chemical specificity of this sort can be exploited for area-selective ALD.

Our results highlight the role of DFT calculations in predicting possible routes towards AS-ALD process development. It was shown that quick and simple thermodynamic DFT calculations of minima using a slab surface model are enough to predict the selective adsorption for Si-based materials using aminosilane precursors. An even simpler gas-phase precursor screening approach using a cluster molecule to represent the surface was used to predict the most favorable pre-

cursors for the initial ALD nucleation step for SiC (Chapter 5). This screening approach was further used to predict the non-growth surfaces during thermal ALD of a metal oxides. Such screening approaches can therefore also be used for high-throughput precursor screening for future AS-ALD applications, since after the surface energies are obtained, the energetics of various gas-phase precursor molecules reacting with each surface can be rapidly evaluated. Including the temperature and entropy effects is important and can be rapidly done for the gas-phase molecules. However, our calculations showed that DFT results at 0 K were enough to predict well the selective aminosilane precursor adsorption at 150 °C (Chapter 4).

8.2 Future work

In Chapter 4 we are predicting an aminosilane to react selectively with SiO_2 surface not with Si and SiC surface by calculating thermodynamical energies of the reactions. Aminosilane precursors act as sources of inert Si-H that prevent the selectivity. A possible next step would be to look at the mechanism of the N_2 plasma step that follows the aminosilane adsorption step. Further, co-reagents other than N_2 plasma could be analyzed. For instance, we can also possibly look at the NH_3 plasma reaction mechanism in order to understand why SiNx ALD using an aminosilane precursor and N_2 plasma is successful while using NH_3 is not, which still remains one of the open questions for the semiconductor industry (see Chapter 2). DFT can be used to investigate what are the possible surface terminations after the NH_3 and N_2 plasma pulse that lead/do not lead to the reactivity of the aminosilane precursor. An example of ALD plasma chemistry calculations using DFT can be found in [251].

In Chapter 7 we did a brief screening of metal-centered precursors in order to define the non-growth surface during ALD for area-selective applications. A next step for this project could be to experimentally perform TiO_2 and HfO_2 ALD growth on various surfaces in order to corroborate our theoretical results.

DFT is a precise quantum mechanical approach that allows us to predict the ALD surface and precursor structures at the electronic scale. DFT is currently limited to systems of sizes less than 1000 atoms, and therefore does not allow a description of growth over multiple ALD cycles. In order to understand the kinetics of the growth of multiple ALD cycles, multi-scale modelling such as

kinetic Monte-Carlo (KMC) of ALD should be used. [252]

Appendix A

Analysed reactions and calculated energies for SiC ALD

Table A.1: List of the analysed reactions and calculated energies (chapter 5, eq. 5.3) at $T = 1000^{\circ}$C

Reactions	ΔE_3, eV	$T\Delta S$, eV	$RT\ln Q$, eV	ΔG, eV per SiC unit
$Si_2H_6 + 2\,CH_4 \longrightarrow 2\,SiC + 6\,H_2 + H_2$	2.1	2.7	-6.4	-3.5
$2\,Si_2H_6 + 2\,C_2H_6 \longrightarrow 4\,SiC + 12\,H_2$	3.0	5.9	-11.9	-3.7
$2\,Si_2H_6 + 2\,C_2H_2 \longrightarrow 4\,SiC + 4\,H_2 + 4\,H_2$	-15.9	-0.8	-7.0	-5.5
$2\,Si_2H_6 + 2\,C_2H_4 \longrightarrow 4\,SiC + 8\,H_2 + 2\,H_2$	-0.6	2.3	-9.4	-3.1
$3\,Si_2H_6 + 2\,C_3H_8 \longrightarrow 6\,SiC + 16\,H_2 + H_2$	3.9	9.1	-17.3	-3.8
$3\,Si_2H_6 + 2\,C_3H_6 \longrightarrow 6\,SiC + 12\,H_2 + 3\,H_2$	0.7	5.5	-14.9	-3.3
$3\,Si_2H_6 + 2\,C_3H_4 \longrightarrow 6\,SiC + 8\,H_2 + 5\,H_2$	-3.5	1.7	-12.4	-2.9
$4\,Si_2H_6 + 2\,C_4H_{10} \longrightarrow 8\,SiC + 20\,H_2 + 2\,H_2$	4.9	12.3	-22.8	-3.8
$4\,Si_2H_6 + 2\,C_4H_8 \longrightarrow 8\,SiC + 16\,H_2 + 4\,H_2$	-1.4	5.9	-20.3	-3.5
$6\,Si_2H_6 + 2\,C_6H_{14} \longrightarrow 12\,SiC + 28\,H_2 + 4\,H_2$	6.7	18.7	-33.6	-3.8
$Si_2H_6 + 2\,CH_2 \longrightarrow 2\,SiC + 4\,H_2 + H_2$	-9.7	-1.0	-4.0	-6.3
$Si_2H_6 + 2\,CHCl_3 \longrightarrow 2\,SiC + 6\,HCl + H_2$	-3.5	3.0	-6.4	-6.5
$Si_2H_6 + 2\,CH_3I \longrightarrow 2\,SiC + 2\,HI + 5\,H_2$	0.6	2.8	-6.4	-4.3
$Si_2H_6 + 2\,CH_3Cl \longrightarrow 2\,SiC + 2\,HCl + 5\,H_2$	0.2	2.8	-6.4	-4.5
$Si_2H_6 + 2\,CCl_4 \longrightarrow 2\,SiC + 6\,HCl + Cl_2$	-4.0	3.1	-6.4	-6.8
$SiH_4 + CH_4 \longrightarrow SiC + 4\,H_2$	0.9	1.4	-3.5	-3.9

Table A.1: List of the analysed reactions and calculated energies (chapter 5, eq. 5.3) at T=1000°C

Reactions	ΔE_3, eV	$T\Delta S$, eV	$RT\ln Q$, eV	ΔG, eV per SiC unit
$2\,SiH_4 + C_2H_6 \longrightarrow 2\,SiC + 6\,H_2 + H_2$	1.4	2.9	-6.4	-4.0
$2\,SiH_4 + C_2H_2 \longrightarrow 2\,SiC + 2\,H_2 + 3\,H_2$	-8.0	-0.4	-4.0	-5.8
$2\,SiH_4 + C_2H_4 \longrightarrow 2\,SiC + 4\,H_2 + 2\,H_2$	-0.4	1.1	-5.2	-3.4
$3\,SiH_4 + C_3H_8 \longrightarrow 3\,SiC + 8\,H_2 + 2\,H_2$	1.9	4.5	-9.4	-4.0
$3\,SiH_4 + C_3H_6 \longrightarrow 3\,SiC + 6\,H_2 + 3\,H_2$	0.3	2.7	-8.2	-3.5
$3\,SiH_4 + C_3H_4 \longrightarrow 3\,SiC + 4\,H_2 + 4\,H_2$	-1.8	0.8	-7.0	-3.2
$4\,SiH_4 + C_4H_{10} \longrightarrow 4\,SiC + 10\,H_2 + 3\,H_2$	2.4	6.1	-12.4	-4.0
$4\,SiH_4 + C_4H_8 \longrightarrow 4\,SiC + 8\,H_2 + 4\,H_2$	-0.7	2.9	-11.2	-3.7
$6\,SiH_4 + C_6H_{14} \longrightarrow 6\,SiC + 14\,H_2 + 5\,H_2$	3.4	9.3	-18.3	-4.0
$SiH_4 + CH_2 \longrightarrow SiC + 2\,H_2 + H_2$	-5.0	-0.5	-2.2	-6.7
$SiH_4 + CH_3Cl \longrightarrow SiC + HCl + 3\,H_2$	0.0	1.4	-3.5	-4.9
$SiH_4 + CCl_4 \longrightarrow SiC + 4\,HCl$	-3.1	1.6	-3.5	-8.1
$SiH_4 + CHCl_3 \longrightarrow SiC + 3\,HCl + H_2$	-1.9	1.5	-3.5	-6.9
$SiH_4 + CH_3I \longrightarrow SiC + HI + 3\,H_2$	0.2	1.4	-3.5	-4.7
$3\,SiH_3Cl + C_3H_8 \longrightarrow 3\,SiC + 3\,HCl + 7\,H_2$	4.2	4.8	-9.4	-3.3
$SiH_3Cl + CH_4 \longrightarrow SiC + HCl + 3\,H_2$	1.7	1.4	-3.5	-3.2
$2\,SiH_3Cl + C_2H_6 \longrightarrow 2\,SiC + 2\,HCl + 5\,H_2$	2.9	3.1	-6.4	-3.3
$2\,SiH_3Cl + C_2H_2 \longrightarrow 2\,SiC + 2\,HCl + 3\,H_2$	-6.5	-0.3	-4.0	-5.1
$2\,SiH_3Cl + C_2H_4 \longrightarrow 2\,SiC + 2\,HCl + 4\,H_2$	1.2	1.3	-5.2	-2.7
$3\,SiH_3Cl + C_3H_6 \longrightarrow 3\,SiC + 3\,HCl + 6\,H_2$	2.6	3.0	-8.2	-2.8
$3\,SiH_3Cl + C_3H_4 \longrightarrow 3\,SiC + 3\,HCl + 5\,H_2$	0.5	1.1	-7.0	-2.5
$4\,SiH_3Cl + C_4H_{10} \longrightarrow 4\,SiC + 4\,HCl + 9\,H_2$	5.5	6.5	-12.4	-3.3
$4\,SiH_3Cl + C_4H_8 \longrightarrow 4\,SiC + 4\,HCl + 8\,H_2$	2.3	3.2	-11.2	-3.0
$6\,SiH_3Cl + C_6H_{14} \longrightarrow 6\,SiC + 6\,HCl + 13\,H_2$	8.0	9.8	-18.3	-3.4
$SiH_3Cl + CHCl_3 \longrightarrow SiC + 4\,HCl$	-1.1	1.6	-3.5	-6.2
$SiH_3Cl + CH_3I \longrightarrow SiC + HCl + 2\,H_2 + HI$	1.0	1.5	-3.5	-4.0
$SiH_3Cl + CH_3Cl \longrightarrow SiC + 2\,HCl + 2\,H_2$	0.8	1.5	-3.5	-4.2
$SiH_3Cl + CCl_4 \longrightarrow SiC + 3\,HCl + Cl_2$	-0.5	1.6	-3.5	-5.5
$3\,SiH_2Cl_2 + C_3H_8 \longrightarrow 3\,SiC + 6\,HCl + 4\,H_2$	6.6	5.0	-9.4	-2.6
$SiH_2Cl_2 + CH_4 \longrightarrow SiC + 2\,HCl + 2\,H_2$	2.5	1.5	-3.5	-2.5
$2\,SiH_2Cl_2 + C_2H_6 \longrightarrow 2\,SiC + 4\,HCl + 3\,H_2$	4.5	3.3	-6.4	-2.6

Table A.1: List of the analysed reactions and calculated energies (chapter 5, eq. 5.3) at T=1000°C

Reactions	ΔE_3, eV	$T\Delta S$, eV	$RT\ln Q$, eV	ΔG, eV per SiC unit
$2\,SiH_2Cl_2 + C_2H_2 \longrightarrow 2\,SiC + 4\,HCl + H_2$	-4.9	-0.1	-4.0	-4.4
$2\,SiH_2Cl_2 + C_2H_4 \longrightarrow 2\,SiC + 4\,HCl + 2\,H_2$	2.7	1.5	-5.2	-2.0
$3\,SiH_2Cl_2 + C_3H_6 \longrightarrow 3\,SiC + 6\,HCl + 3\,H_2$	5.0	3.2	-8.2	-2.1
$3\,SiH_2Cl_2 + C_3H_4 \longrightarrow 3\,SiC + 6\,HCl + 2\,H_2$	2.9	1.3	-7.0	-1.8
$4\,SiH_2Cl_2 + C_4H_{10} \longrightarrow 4\,SiC + 8\,HCl + 5\,H_2$	8.6	6.8	-12.4	-2.6
$4\,SiH_2Cl_2 + C_4H_8 \longrightarrow 4\,SiC + 8\,HCl + 4\,H_2$	5.5	3.6	-11.2	-2.3
$6\,SiH_2Cl_2 + C_6H_{14} \longrightarrow 6\,SiC + 12\,HCl + 7\,H_2$	12.7	10.3	-18.3	-2.7
$SiH_2Cl_2 + CHCl_3 \longrightarrow SiC + 3\,HCl + Cl_2$	1.5	1.6	-3.5	-3.6
$SiH_2Cl_2 + CH_3I \longrightarrow SiC + 2\,HCl + H_2 + HI$	1.7	1.5	-3.5	-3.3
$SiH_2Cl_2 + CH_3Cl \longrightarrow SiC + 3\,HCl + H_2$	1.5	1.6	-3.5	-3.5
$SiH_2Cl_2 + CCl_4 \longrightarrow SiC + 2\,HCl + 2\,Cl_2$	2.2	1.6	-3.5	-2.9
$SiHCl_3 + CH_4 \longrightarrow SiC + 3\,HCl + H_2$	3.3	1.6	-3.5	-1.8
$2\,SiHCl_3 + C_2H_6 \longrightarrow 2\,SiC + 6\,HCl + H_2$	6.0	3.5	-6.4	-1.9
$2\,SiHCl_3 + C_2H_2 \longrightarrow 2\,SiC + 4\,HCl + Cl_2$	-1.6	0.0	-4.0	-2.8
$2\,SiHCl_3 + C_2H_4 \longrightarrow 2\,SiC + 6\,HCl$	4.3	1.7	-5.2	-1.3
$3\,SiHCl_3 + C_3H_8 \longrightarrow 3\,SiC + 9\,HCl + H_2$	8.9	5.3	-9.4	-2.0
$3\,SiHCl_3 + C_3H_6 \longrightarrow 3\,SiC + 9\,HCl$	7.3	3.5	-8.2	-1.5
$3\,SiHCl_3 + C_3H_4 \longrightarrow 3\,SiC + 7\,HCl + Cl_2$	7.0	1.5	-7.0	-0.5
$4\,SiHCl_3 + C_4H_{10} \longrightarrow 4\,SiC + 12\,HCl + H_2$	11.7	7.2	-12.4	-2.0
$4\,SiHCl_3 + C_4H_8 \longrightarrow 4\,SiC + 12\,HCl$	8.5	3.9	-11.2	-1.6
$SiHCl_3 + CCl_4 \longrightarrow SiC + HCl + 3\,Cl_2$	4.8	1.6	-3.5	-0.3
$SiHCl_3 + CHCl_3 \longrightarrow SiC + 2\,HCl + 2\,Cl_2$	4.1	1.6	-3.5	-1.0
$SiHCl_3 + CH_3I \longrightarrow SiC + HI + 3\,HCl$	2.5	1.6	-3.5	-2.6
$6\,SiHCl_3 + C_6H_{14} \longrightarrow 6\,SiC + 18\,HCl + H_2$	17.3	10.9	-18.3	-2.0
$SiHCl_3 + CH_3Cl \longrightarrow SiC + 4\,HCl$	2.3	1.7	-3.5	-2.8
$SiHCl_3 + CH_2 \longrightarrow SiC + 3\,HCl$	-2.7	-0.3	-2.2	-4.6
$2\,Si_2Cl_6 + 2\,C_2H_2 \longrightarrow 4\,SiC + 4\,HCl + 4\,Cl_2$	0.5	0.0	-7.0	-1.6
$Si_2Cl_6 + 2\,CH_4 \longrightarrow 2\,SiC + 6\,HCl + H_2$	6.6	3.3	-6.4	-1.6
$2\,Si_2Cl_6 + 2\,C_2H_6 \longrightarrow 4\,SiC + 12\,HCl$	12.0	7.0	-11.9	-1.7
$2\,Si_2Cl_6 + 2\,C_2H_4 \longrightarrow 4\,SiC + 8\,HCl + 2\,Cl_2$	12.1	3.3	-9.4	-0.1
$3\,Si_2Cl_6 + 2\,C_3H_8 \longrightarrow 6\,SiC + 16\,HCl + Cl_2$	19.3	10.7	-17.3	-1.5

Table A.1: List of the analysed reactions and calculated energies (chapter 5, eq. 5.3) at T=1000°C

Reactions	ΔE_3, eV	$T\Delta S$, eV	$RT\ln Q$, eV	ΔG, eV per SiC unit
$3\,Si_2Cl_6 + 2\,C_3H_6 \longrightarrow 6\,SiC + 12\,HCl + 3\,Cl_2$	19.8	6.9	-14.9	-0.3
$3\,Si_2Cl_6 + 2\,C_3H_4 \longrightarrow 6\,SiC + 8\,HCl + 5\,Cl_2$	19.2	2.9	-12.4	0.7
$4\,Si_2Cl_6 + 2\,C_4H_{10} \longrightarrow 8\,SiC + 20\,HCl + 2\,Cl_2$	26.6	14.4	-22.8	-1.3
$4\,Si_2Cl_6 + 2\,C_4H_8 \longrightarrow 8\,SiC + 16\,HCl + 4\,Cl_2$	23.9	7.8	-20.3	-0.5
$6\,Si_2Cl_6 + 2\,C_6H_{14} \longrightarrow 12\,SiC + 28\,HCl + 4\,Cl_2$	41.1	21.7	-33.6	-1.2
$Si_2Cl_6 + 2\,CHCl_3 \longrightarrow 2\,SiC + 2\,HCl + 5\,Cl_2$	10.1	3.2	-6.4	0.3
$Si_2Cl_6 + 2\,CH_3I \longrightarrow 2\,SiC + 4\,HCl + Cl_2 + 2\,HI$	7.0	3.2	-6.4	-1.4
$Si_2Cl_6 + 2\,CH_3Cl \longrightarrow 2\,SiC + 6\,HCl + Cl_2$	6.6	3.3	-6.4	-1.6
$Si_2Cl_6 + 2\,CCl_4 \longrightarrow 2\,SiC + 7\,Cl_2$	11.5	3.1	-6.4	1.0
$SiCl_4 + CH_4 \longrightarrow SiC + 4\,HCl$	3.7	1.7	-3.5	-1.5
$2\,SiCl_4 + C_2H_6 \longrightarrow 2\,SiC + 6\,HCl + Cl_2$	8.8	3.6	-6.4	-0.6
$2\,SiCl_4 + C_2H_2 \longrightarrow 2\,SiC + 2\,HCl + 3\,Cl_2$	3.0	0.1	-4.0	-0.5
$2\,SiCl_4 + C_2H_4 \longrightarrow 2\,SiC + 4\,HCl + 2\,Cl_2$	8.8	1.7	-5.2	1.0
$3\,SiCl_4 + C_3H_8 \longrightarrow 3\,SiC + 8\,HCl + 2\,Cl_2$	13.9	5.5	-9.4	-0.3
$3\,SiCl_4 + C_3H_6 \longrightarrow 3\,SiC + 6\,HCl + 3\,Cl_2$	14.1	3.5	-8.2	0.8
$3\,SiCl_4 + C_3H_4 \longrightarrow 3\,SiC + 4\,HCl + 4\,Cl_2$	13.9	1.6	-7.0	1.8
$4\,SiCl_4 + C_4H_{10} \longrightarrow 4\,SiC + 10\,HCl + 3\,Cl_2$	19.0	7.3	-12.4	-0.2
$4\,SiCl_4 + C_4H_8 \longrightarrow 4\,SiC + 8\,HCl + 4\,Cl_2$	17.7	4.0	-11.2	0.6
$6\,SiCl_4 + C_6H_{14} \longrightarrow 6\,SiC + 14\,HCl + 5\,Cl_2$	29.2	11.1	-18.3	0.0
$SiCl_4 + CHCl_3 \longrightarrow SiC + HCl + 3\,Cl_2$	6.4	1.6	-3.5	1.3
$SiCl_4 + CH_3I \longrightarrow SiC + 3\,HCl + \frac{1}{2}\,Cl_2 + \frac{1}{2}\,I_2$	3.9	1.7	-3.5	-1.2
$SiCl_4 + CCl_4 \longrightarrow SiC + 4\,Cl_2$	7.1	1.6	-3.5	2.0
$SiCl_4 + CH_3Cl \longrightarrow SiC + 3\,HCl + Cl_2$	4.6	1.7	-3.5	-0.6
$SiF_4 + CH_4 \longrightarrow SiC + 4\,FH + 0\,F_2$	5.9	1.8	-3.5	0.6
$2\,SiF_4 + C_2H_6 \longrightarrow 2\,SiC + 6\,FH + F_2$	16.6	3.9	-6.4	3.2
$2\,SiF_4 + C_2H_2 \longrightarrow 2\,SiC + 2\,FH + 3\,F_2$	18.0	0.6	-4.0	6.7
$2\,SiF_4 + C_2H_4 \longrightarrow 2\,SiC + 4\,FH + 2\,F_2$	20.3	2.1	-5.2	6.5
$3\,SiF_4 + C_3H_8 \longrightarrow 3\,SiC + 8\,FH + 2\,F_2$	27.5	6.0	-9.4	4.0
$3\,SiF_4 + C_3H_6 \longrightarrow 3\,SiC + 6\,FH + 3\,F_2$	31.3	4.2	-8.2	6.3

Table A.1: List of the analysed reactions and calculated energies (chapter 5, eq. 5.3) at T=1000°C

Reactions	ΔE_3, eV	$T\Delta S$, eV	$RT\ln Q$, eV	ΔG, eV per SiC unit
$3\,SiF_4 + C_3H_4 \longrightarrow 3\,SiC + 4\,FH + 4\,F_2$	34.5	2.3	-7.0	8.4
$4\,SiF_4 + C_4H_{10} \longrightarrow 4\,SiC + 10\,FH + 3\,F_2$	38.3	8.1	-12.4	4.5
$4\,SiF_4 + C_4H_8 \longrightarrow 4\,SiC + 8\,FH + 4\,F_2$	40.5	4.9	-11.2	6.1
$6\,SiF_4 + C_6H_{14} \longrightarrow 6\,SiC + 14\,FH + 5\,F_2$	59.9	12.2	-18.3	4.9
$SiF_4 + CHCl_3 \longrightarrow SiC + FH + \frac{3}{2}\,F_2 + \frac{3}{2}\,Cl_2$	13.9	1.9	-3.5	8.5
$SiF_4 + CH_3I \longrightarrow SiC + 3\,FH + \frac{1}{2}\,F_2 + \frac{1}{2}\,I_2$	7.9	1.8	-3.5	2.6
$SiF_4 + CH_3Cl \longrightarrow SiC + 3\,FH + \frac{1}{2}\,F_2 + \frac{1}{2}\,Cl_2$	8.5	1.8	-3.5	3.2
$SiF_4 + CCl_4 \longrightarrow SiC + 4\,ClF$	14.1	2.1	-3.5	8.6
$SiH_3–CH_2–SiH_2–CH_3 \longrightarrow 2\,SiC + 5\,H_2$	1.5	3.0	-5.4	-3.5
$SiCH_3Cl_3 \longrightarrow SiC + 3\,HCl$	2.9	1.7	-3.0	-1.8
$CH_3–SiH_3 \longrightarrow SiC + 3\,H_2$	0.6	1.5	-3.0	-3.8
$SiH_2(CH_2)_3 \longrightarrow SiC + 2\,CH_4$	-2.3	0.5	-1.7	-4.5
$Si(CH_3)_2Cl_2 \longrightarrow SiC + CH_4 + 2\,HCl$	2.2	1.8	-3.0	-2.6
$SiCl_2(CH_2)_3 \longrightarrow SiC + C_2H_6 + Cl_2$	2.2	0.3	-1.7	0.1
$(SiCl_3)_2CH_2 \longrightarrow SiC + 2\,HC + lSiCl_4$	2.4	1.9	-3.0	-2.4
$Si(OEt)_4 \longrightarrow SiC + 3\,C_2H_5OH + CH_2O$	0.9	4.7	-4.2	-8.0
$H_2Si[N(Et)_2]_2 \longrightarrow SiC + NH(Et)_2 + CH_4 + NH_2Et$	-0.3	2.1	-3.0	-5.4
$SiH_3N(iPr)_2 \longrightarrow SiC + NH_2iPr + 2\,CH_4$	-1.5	2.3	-3.0	-6.7
$Si_2H_6 + 2\,CH_4 \longrightarrow 2\,SiC + 6\,H_2 + H_2$	2.1	1.8	-3.4	-1.5
$2\,Si_2H_6 + 2\,C_2H_6 \longrightarrow 4\,SiC + 12\,H_2$	3.0	3.9	-6.3	-1.8
$2\,Si_2H_6 + 2\,C_2H_2 \longrightarrow 4\,SiC + 4\,H_2 + 4\,H_2$	-15.9	0.3	-3.7	-5.0
$2\,Si_2H_6 + 2\,C_2H_4 \longrightarrow 4\,SiC + 8\,H_2 + 2\,H_2$	-0.6	2.0	-5.0	-1.9
$3\,Si_2H_6 + 2\,C_3H_8 \longrightarrow 6\,SiC + 16\,H_2 + H_2$	3.9	6.0	-9.2	-1.9
$3\,Si_2H_6 + 2\,C_3H_6 \longrightarrow 6\,SiC + 12\,H_2 + 3\,H_2$	0.7	4.1	-7.9	-1.9
$3\,Si_2H_6 + 2\,C_3H_4 \longrightarrow 6\,SiC + 8\,H_2 + 5\,H_2$	-3.5	2.1	-6.5	-2.0
$4\,Si_2H_6 + 2\,C_4H_{10} \longrightarrow 8\,SiC + 20\,H_2 + 2\,H_2$	4.9	8.2	-12.0	-1.9
$4\,Si_2H_6 + 2\,C_4H_8 \longrightarrow 8\,SiC + 16\,H_2 + 4\,H_2$	-1.4	4.9	-10.7	-2.1
$6\,Si_2H_6 + 2\,C_6H_{14} \longrightarrow 12\,SiC + 28\,H_2 + 4\,H_2$	6.7	12.5	-17.8	-2.0

Table A.2: List of the analysed reactions and calculated energies (chapter 5, eq. 5.3) at T=400°C

Reactions	ΔE_3, eV	$T\Delta S$, eV	$RT\ln Q$, eV	ΔG, eV per SiC unit
$Si_2H_6 + 2\,CH_2 \longrightarrow 2\,SiC + 4\,H_2 + H_2$	-9.7	2.9	-2.1	-7.4
$Si_2H_6 + 2\,CHCl_3 \longrightarrow 2\,SiC + 6\,HCl + H_2$	-3.5	2.1	-3.4	-4.5
$Si_2H_6 + 2\,CH_3I \longrightarrow 2\,SiC + 2\,HI + 5\,H_2$	0.6	1.9	-3.4	-2.3
$Si_2H_6 + 2\,CH_3Cl \longrightarrow 2\,SiC + 2\,HCl + 5\,H_2$	0.2	1.9	-3.4	-2.5
$Si_2H_6 + 2\,CCl_4 \longrightarrow 2\,SiC + 6\,HCl + Cl_2$	-4.0	2.2	-3.4	-4.8
$SiH_4 + CH_4 \longrightarrow SiC + 4\,H_2$	0.9	0.9	-1.8	-1.8
$2\,SiH_4 + C_2H_6 \longrightarrow 2\,SiC + 6\,H_2 + H_2$	1.4	1.9	-3.4	-2.0
$2\,SiH_4 + C_2H_2 \longrightarrow 2\,SiC + 2\,H_2 + 3\,H_2$	-8.0	0.1	-2.1	-5.1
$2\,SiH_4 + C_2H_4 \longrightarrow 2\,SiC + 4\,H_2 + 2\,H_2$	-0.4	0.9	-2.8	-2.0
$3\,SiH_4 + C_3H_8 \longrightarrow 3\,SiC + 8\,H_2 + 2\,H_2$	1.9	2.9	-5.0	-2.0
$3\,SiH_4 + C_3H_6 \longrightarrow 3\,SiC + 6\,H_2 + 3\,H_2$	0.3	2.0	-4.3	-2.0
$3\,SiH_4 + C_3H_4 \longrightarrow 3\,SiC + 4\,H_2 + 4\,H_2$	-1.8	1.0	-3.7	-2.1
$4\,SiH_4 + C_4H_{10} \longrightarrow 4\,SiC + 10\,H_2 + 3\,H_2$	2.4	4.0	-6.5	-2.0
$4\,SiH_4 + C_4H_8 \longrightarrow 4\,SiC + 8\,H_2 + 4\,H_2$	-0.7	2.3	-5.9	-2.2
$6\,SiH_4 + C_6H_{14} \longrightarrow 6\,SiC + 14\,H_2 + 5\,H_2$	3.4	6.1	-9.7	-2.1
$SiH_4 + CH_2 \longrightarrow SiC + 2\,H_2 + H_2$	-5.0	1.4	-1.2	-7.6
$SiH_4 + CH_3Cl \longrightarrow SiC + HCl + 3\,H_2$	0.0	0.9	-1.8	-2.8
$SiH_4 + CCl_4 \longrightarrow SiC + 4\,HCl$	-3.1	1.1	-1.8	-6.0
$SiH_4 + CHCl_3 \longrightarrow SiC + 3\,HCl + H_2$	-1.9	1.0	-1.8	-4.8
$SiH_4 + CH_3I \longrightarrow SiC + HI + 3\,H_2$	0.2	0.9	-1.8	-2.5
$3\,SiH_3Cl + C_3H_8 \longrightarrow 3\,SiC + 3\,HCl + 7\,H_2$	4.2	3.1	-5.0	-1.3
$SiH_3Cl + CH_4 \longrightarrow SiC + HCl + 3\,H_2$	1.7	0.9	-1.8	-1.1
$2\,SiH_3Cl + C_2H_6 \longrightarrow 2\,SiC + 2\,HCl + 5\,H_2$	2.9	2.0	-3.4	-1.3
$2\,SiH_3Cl + C_2H_2 \longrightarrow 2\,SiC + 2\,HCl + 3\,H_2$	-6.5	0.2	-2.1	-4.4
$2\,SiH_3Cl + C_2H_4 \longrightarrow 2\,SiC + 2\,HCl + 4\,H_2$	1.2	1.1	-2.8	-1.3
$3\,SiH_3Cl + C_3H_6 \longrightarrow 3\,SiC + 3\,HCl + 6\,H_2$	2.6	2.2	-4.3	-1.3
$3\,SiH_3Cl + C_3H_4 \longrightarrow 3\,SiC + 3\,HCl + 5\,H_2$	0.5	1.2	-3.7	-1.4
$4\,SiH_3Cl + C_4H_{10} \longrightarrow 4\,SiC + 4\,HCl + 9\,H_2$	5.5	4.2	-6.5	-1.3
$4\,SiH_3Cl + C_4H_8 \longrightarrow 4\,SiC + 4\,HCl + 8\,H_2$	2.3	2.6	-5.9	-1.5
$6\,SiH_3Cl + C_6H_{14} \longrightarrow 6\,SiC + 6\,HCl + 13\,H_2$	8.0	6.4	-9.7	-1.4
$SiH_3Cl + CHCl_3 \longrightarrow SiC + 4\,HCl$	-1.1	1.1	-1.8	-4.1

Table A.2: List of the analysed reactions and calculated energies (chapter 5, eq. 5.3) at T=400°C

Reactions	ΔE_3, eV	$T\Delta S$, eV	$RT\ln Q$, eV	ΔG, eV per SiC unit
$SiH_3Cl + CH_3I \longrightarrow SiC + HCl + 2\,H_2 + HI$	1.0	1.0	-1.8	-1.8
$SiH_3Cl + CH_3Cl \longrightarrow SiC + 2\,HCl + 2\,H_2$	0.8	1.0	-1.8	-2.1
$SiH_3Cl + CCl_4 \longrightarrow SiC + 3\,HCl + Cl_2$	-0.5	1.1	-1.8	-3.4
$3\,SiH_2Cl_2 + C_3H_8 \longrightarrow 3\,SiC + 6\,HCl + 4\,H_2$	6.6	3.3	-5.0	-0.6
$SiH_2Cl_2 + CH_4 \longrightarrow SiC + 2\,HCl + 2\,H_2$	2.5	1.0	-1.8	-0.3
$2\,SiH_2Cl_2 + C_2H_6 \longrightarrow 2\,SiC + 4\,HCl + 3\,H_2$	4.5	2.1	-3.4	-0.5
$2\,SiH_2Cl_2 + C_2H_2 \longrightarrow 2\,SiC + 4\,HCl + H_2$	-4.9	0.4	-2.1	-3.7
$2\,SiH_2Cl_2 + C_2H_4 \longrightarrow 2\,SiC + 4\,HCl + 2\,H_2$	2.7	1.2	-2.8	-0.6
$3\,SiH_2Cl_2 + C_3H_6 \longrightarrow 3\,SiC + 6\,HCl + 3\,H_2$	5.0	2.3	-4.3	-0.6
$3\,SiH_2Cl_2 + C_3H_4 \longrightarrow 3\,SiC + 6\,HCl + 2\,H_2$	2.9	1.4	-3.7	-0.7
$4\,SiH_2Cl_2 + C_4H_{10} \longrightarrow 4\,SiC + 8\,HCl + 5\,H_2$	8.6	4.5	-6.5	-0.6
$4\,SiH_2Cl_2 + C_4H_8 \longrightarrow 4\,SiC + 8\,HCl + 4\,H_2$	5.5	2.8	-5.9	-0.8
$6\,SiH_2Cl_2 + C_6H_{14} \longrightarrow 6\,SiC + 12\,HCl + 7\,H_2$	12.7	6.8	-9.7	-0.6
$SiH_2Cl_2 + CHCl_3 \longrightarrow SiC + 3\,HCl + Cl_2$	1.5	1.1	-1.8	-1.4
$SiH_2Cl_2 + CH_3I \longrightarrow SiC + 2\,HCl + H_2 + HI$	1.7	1.0	-1.8	-1.1
$SiH_2Cl_2 + CH_3Cl \longrightarrow SiC + 3\,HCl + H_2$	1.5	1.0	-1.8	-1.3
$SiH_2Cl_2 + CCl_4 \longrightarrow SiC + 2\,HCl + 2\,Cl_2$	2.2	1.1	-1.8	-0.8
$SiHCl_3 + CH_4 \longrightarrow SiC + 3\,HCl + H_2$	3.3	1.1	-1.8	0.4
$2\,SiHCl_3 + C_2H_6 \longrightarrow 2\,SiC + 6\,HCl + H_2$	6.0	2.3	-3.4	0.2
$2\,SiHCl_3 + C_2H_2 \longrightarrow 2\,SiC + 4\,HCl + Cl_2$	-1.6	0.4	-2.1	-2.1
$2\,SiHCl_3 + C_2H_4 \longrightarrow 2\,SiC + 6\,HCl$	4.3	1.3	-2.8	0.1
$3\,SiHCl_3 + C_3H_8 \longrightarrow 3\,SiC + 9\,HCl + H_2$	8.9	3.5	-5.0	0.1
$3\,SiHCl_3 + C_3H_6 \longrightarrow 3\,SiC + 9\,HCl$	7.3	2.6	-4.3	0.1
$3\,SiHCl_3 + C_3H_4 \longrightarrow 3\,SiC + 7\,HCl + Cl_2$	7.0	1.5	-3.7	0.6
$4\,SiHCl_3 + C_4H_{10} \longrightarrow 4\,SiC + 12\,HCl + H_2$	11.7	4.8	-6.5	0.1
$4\,SiHCl_3 + C_4H_8 \longrightarrow 4\,SiC + 12\,HCl$	8.5	3.1	-5.9	-0.1
$SiHCl_3 + CCl_4 \longrightarrow SiC + HCl + 3\,Cl_2$	4.8	1.1	-1.8	1.8
$SiHCl_3 + CHCl_3 \longrightarrow SiC + 2\,HCl + 2\,Cl_2$	4.1	1.1	-1.8	1.2
$SiHCl_3 + CH_3I \longrightarrow SiC + HI + 3\,HCl$	2.5	1.1	-1.8	-0.4
$6\,SiHCl_3 + C_6H_{14} \longrightarrow 6\,SiC + 18\,HCl + H_2$	17.3	7.2	-9.7	0.1
$SiHCl_3 + CH_3Cl \longrightarrow SiC + 4\,HCl$	2.3	1.1	-1.8	-0.6

Table A.2: List of the analysed reactions and calculated energies (chapter 5, eq. 5.3) at T=400°C

Reactions	ΔE_3, eV	$T\Delta S$, eV	$RT\ln Q$, eV	ΔG, eV per SiC unit
$SiHCl_3 + CH_2 \longrightarrow SiC + 3\,HCl$	-2.7	1.6	-1.2	-5.5
$2\,Si_2Cl_6 + 2\,C_2H_2 \longrightarrow 4\,SiC + 4\,HCl + 4\,Cl_2$	0.5	0.9	-3.7	-1.0
$Si_2Cl_6 + 2\,CH_4 \longrightarrow 2\,SiC + 6\,HCl + H_2$	6.6	2.2	-3.4	0.5
$2\,Si_2Cl_6 + 2\,C_2H_6 \longrightarrow 4\,SiC + 12\,HCl$	12.0	4.7	-6.3	0.2
$2\,Si_2Cl_6 + 2\,C_2H_4 \longrightarrow 4\,SiC + 8\,HCl + 2\,Cl_2$	12.1	2.7	-5.0	1.1
$3\,Si_2Cl_6 + 2\,C_3H_8 \longrightarrow 6\,SiC + 16\,HCl + Cl_2$	19.3	7.2	-9.2	0.5
$3\,Si_2Cl_6 + 2\,C_3H_6 \longrightarrow 6\,SiC + 12\,HCl + 3\,Cl_2$	19.8	5.1	-7.9	1.1
$3\,Si_2Cl_6 + 2\,C_3H_4 \longrightarrow 6\,SiC + 8\,HCl + 5\,Cl_2$	19.2	3.0	-6.5	1.6
$4\,Si_2Cl_6 + 2\,C_4H_{10} \longrightarrow 8\,SiC + 20\,HCl + 2\,Cl_2$	26.6	9.7	-12.0	0.6
$4\,Si_2Cl_6 + 2\,C_4H_8 \longrightarrow 8\,SiC + 16\,HCl + 4\,Cl_2$	23.9	6.3	-10.7	0.9
$6\,Si_2Cl_6 + 2\,C_6H_{14} \longrightarrow 12\,SiC + 28\,HCl + 4\,Cl_2$	41.1	14.6	-17.8	0.7
$Si_2Cl_6 + 2\,CHCl_3 \longrightarrow 2\,SiC + 2\,HCl + 5\,Cl_2$	10.1	2.2	-3.4	2.3
$Si_2Cl_6 + 2\,CH_3I \longrightarrow 2\,SiC + 4\,HCl + Cl_2 + 2\,HI$	7.0	2.2	-3.4	0.7
$Si_2Cl_6 + 2\,CH_3Cl \longrightarrow 2\,SiC + 6\,HCl + Cl_2$	6.6	2.2	-3.4	0.5
$Si_2Cl_6 + 2\,CCl_4 \longrightarrow 2\,SiC + 7\,Cl_2$	11.5	2.2	-3.4	2.9
$SiCl_4 + CH_4 \longrightarrow SiC + 4\,HCl$	3.7	1.1	-1.8	0.7
$2\,SiCl_4 + C_2H_6 \longrightarrow 2\,SiC + 6\,HCl + Cl_2$	8.8	2.4	-3.4	1.5
$2\,SiCl_4 + C_2H_2 \longrightarrow 2\,SiC + 2\,HCl + 3\,Cl_2$	3.0	0.5	-2.1	0.2
$2\,SiCl_4 + C_2H_4 \longrightarrow 2\,SiC + 4\,HCl + 2\,Cl_2$	8.8	1.4	-2.8	2.4
$3\,SiCl_4 + C_3H_8 \longrightarrow 3\,SiC + 8\,HCl + 2\,Cl_2$	13.9	3.6	-5.0	1.8
$3\,SiCl_4 + C_3H_6 \longrightarrow 3\,SiC + 6\,HCl + 3\,Cl_2$	14.1	2.6	-4.3	2.4
$3\,SiCl_4 + C_3H_4 \longrightarrow 3\,SiC + 4\,HCl + 4\,Cl_2$	13.9	1.5	-3.7	2.9
$4\,SiCl_4 + C_4H_{10} \longrightarrow 4\,SiC + 10\,HCl + 3\,Cl_2$	19.0	4.9	-6.5	1.9
$4\,SiCl_4 + C_4H_8 \longrightarrow 4\,SiC + 8\,HCl + 4\,Cl_2$	17.7	3.2	-5.9	2.2
$6\,SiCl_4 + C_6H_{14} \longrightarrow 6\,SiC + 14\,HCl + 5\,Cl_2$	29.2	7.4	-9.7	2.0
$SiCl_4 + CHCl_3 \longrightarrow SiC + HCl + 3\,Cl_2$	6.4	1.1	-1.8	3.4
$SiCl_4 + CH_3I \longrightarrow SiC + 3\,HCl + \frac{1}{2}\,Cl_2 + \frac{1}{2}\,I_2$	3.9	1.1	-1.8	1.0
$SiCl_4 + CCl_4 \longrightarrow SiC + 4\,Cl_2$	7.1	1.1	-1.8	4.1

Table A.2: List of the analysed reactions and calculated energies (chapter 5, eq. 5.3) at T=400°C

Reactions	ΔE_3, eV	$T\Delta S$, eV	$RT\ln Q$, eV	ΔG, eV per SiC unit
$SiCl_4 + CH_3Cl \longrightarrow SiC + 3\,HCl + Cl_2$	4.6	1.1	-1.8	1.6
$SiF_4 + CH_4 \longrightarrow SiC + 4\,FH$	5.9	2.2	-1.8	1.8
$2\,SiF_4 + C_2H_6 \longrightarrow 2\,SiC + 6\,FH + F_2$	16.6	4.1	-3.4	4.6
$2\,SiF_4 + C_2H_2 \longrightarrow 2\,SiC + 2\,FH + 3\,F_2$	18.0	1.3	-2.1	7.3
$2\,SiF_4 + C_2H_4 \longrightarrow 2\,SiC + 4\,FH + 2\,F_2$	20.3	2.6	-2.8	7.4
$3\,SiF_4 + C_3H_8 \longrightarrow 3\,SiC + 8\,FH + 2\,F_2$	27.5	6.0	-5.0	5.5
$3\,SiF_4 + C_3H_6 \longrightarrow 3\,SiC + 6\,FH + 3\,F_2$	31.3	4.5	-4.3	7.5
$3\,SiF_4 + C_3H_4 \longrightarrow 3\,SiC + 4\,FH + 4\,F_2$	34.5	3.0	-3.7	9.3
$4\,SiF_4 + C_4H_{10} \longrightarrow 4\,SiC + 10\,FH + 3\,F_2$	38.3	7.9	-6.5	6.0
$4\,SiF_4 + C_4H_8 \longrightarrow 4\,SiC + 8\,FH + 4\,F_2$	40.5	5.7	-5.9	7.2
$6\,SiF_4 + C_6H_{14} \longrightarrow 6\,SiC + 14\,FH + 5\,F_2$	59.9	11.6	-9.7	6.4
$SiF_4 + CHCl_3 \longrightarrow SiC + FH + \frac{3}{2}\,F_2 + \frac{3}{2}\,Cl_2$	13.9	1.5	-1.8	10.5
$SiF_4 + CH_3I \longrightarrow SiC + 3\,FH + \frac{1}{2}\,F_2 + \frac{1}{2}\,I_2$	7.9	2.0	-1.8	4.1
$SiF_4 + CH_3Cl \longrightarrow SiC + 3\,FH + \frac{1}{2}\,F_2 + \frac{1}{2}\,Cl_2$	8.5	2.0	-1.8	4.7
$SiF_4 + CCl_4 \longrightarrow SiC + 4\,ClF$	14.1	1.4	-1.8	10.9
$SiH_3{-}CH_2{-}SiH_2{-}CH_3 \longrightarrow 2\,SiC + 5\,H_2$	1.5	2.1	-2.9	-1.7
$SiCH_3Cl_3 \longrightarrow SiC + 3\,HCl$	2.9	1.2	-1.6	0.2
$CH_3{-}SiH_3 \longrightarrow SiC + 3\,H_2$	0.6	1.0	-1.6	-1.9
$SiH_2(CH_2)_3 \longrightarrow SiC + 2\,CH_4$	-2.3	0.6	-0.9	-3.8
$Si(CH_3)_2Cl_2 \longrightarrow SiC + CH_4 + 2\,HCl$	2.2	1.2	-1.6	-0.6
$SiCl_2(CH_2)_3 \longrightarrow SiC + C_2H_6 + Cl_2$	2.2	0.4	-0.9	0.9
$(SiCl_3)_2CH_2 \longrightarrow SiC + 2\,HCl^+ SiCl_4$	2.4	1.3	-1.6	-0.4
$Si(OEt)_4 \longrightarrow SiC + 3\,C_2H_5OH + CH_2O$	0.9	1.0	-2.2	-2.3
$H_2Si[N(Et)_2]_2 \longrightarrow SiC + NH(Et)_2 + CH_4 + NH_2Et$	-0.3	-1.0	-1.6	-0.9
$SiH_3N(iPr)_2 \longrightarrow SiC + NH_2iPr + 2\,CH_4$	-1.5	1.6	-1.6	-4.6

Appendix B

Optimized structures and adsorption energies of various Si and C precursors for SiC ALD

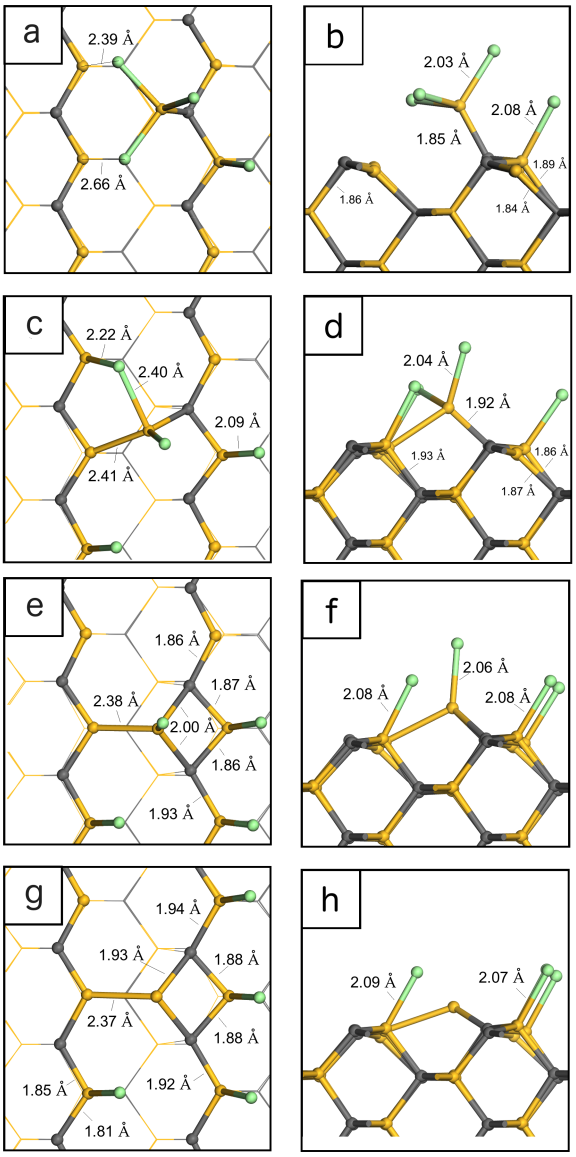


Figure B.1: Optimized structure of $SiCl_4$ adsorbing on the bare SiC surface. Left column - top view, right column - side view. Calculated adsorption energies are presented in table B.1.

Table B.1: Adsorption energies of $SiCl_4$ on the bare SiC surface. Optimized structures are presented in figure B.1. "(S)" for surface atoms.

Final structure	Figure	Adsorption energy, eV
C(S)–$SiCl_3$, Si(S)–Cl	B.1 (a, b)	-2.2
C(S)–Si(S)–C(S)–$SiCl_2$, 2 Si(S)–Cl	B.1 (c, d)	-2.8
C(S)–Si(S)–C(S)–SiCl, 3 Si(S)–Cl	B.1 (e, f)	-3.3
C(S)–Si(S)–C(S)–Si_{DB},4 Si(S)–Cl	B.1 (g, h)	-2.7

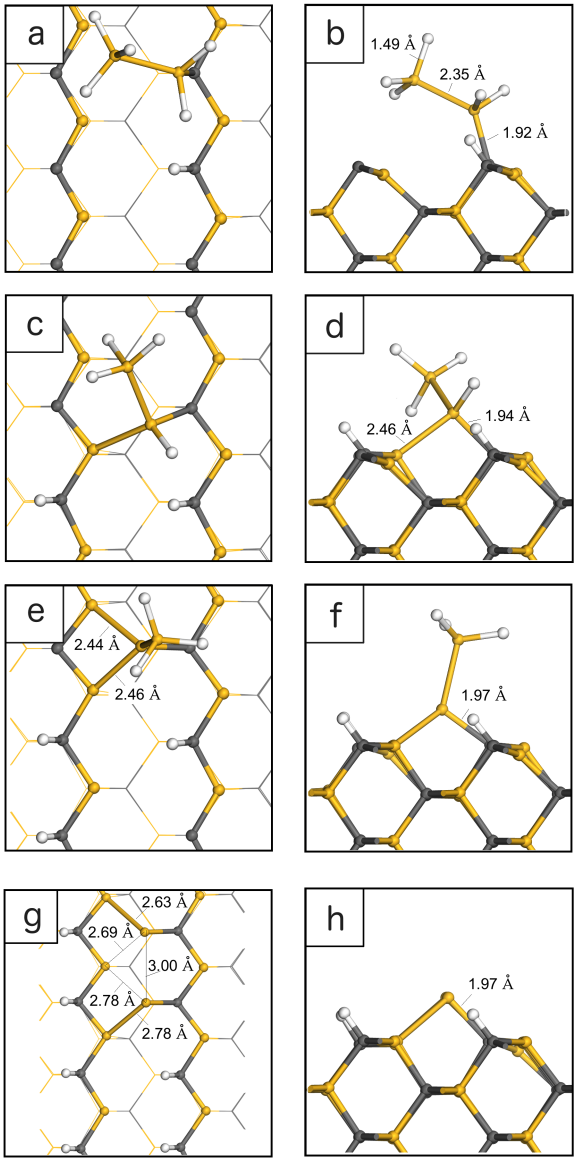


Figure B.2: Optimized structure of Si_2H_6 adsorbing on the bare SiC surface. Left column - top view, right column - side view. Calculated adsorption energies are presented in table B.2.

Table B.2: Adsorption energies of Si_2H_6 on the bare SiC surface. Optimized structures are presented in figure B.2. "(S)" for surface atoms.

Final structure	Figure	Adsorption energy, eV
C(S)–SiH_2–SiH_3, C(S)–H	B.2 (a, b)	-1.6
C(S)–Si(S)–SiH–SiH_3, 2 C(S)–H	B.2 (c, d)	-3.6
C(S)–Si(S)–Si(S)–Si–SiH_3, 3 C(S)–H	B.2 (e, f)	-4.6
2 (C(S)–Si(S)–Si(S)–Si), 6 C(S)–H	B.2 (g, h)	-7.6

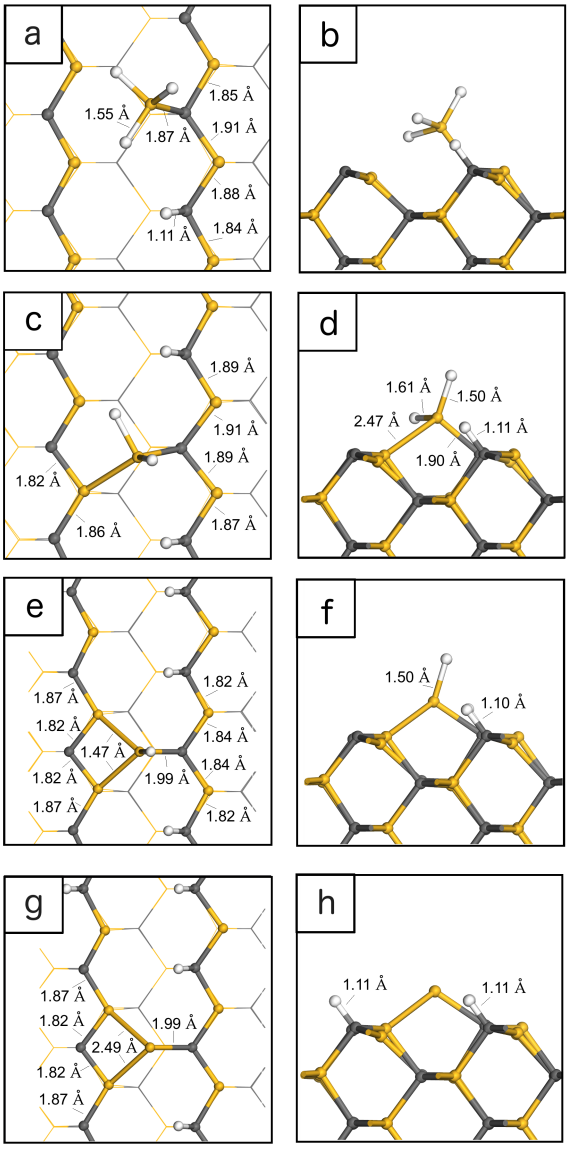


Figure B.3: Optimized structure of SiH_4 adsorbing on the bare SiC surface. Left column - top view, right column - side view. Calculated adsorption energies are presented in table B.3.

Table B.3: Adsorption energies of SiH_4 on the bare SiC surface. Optimized structures are presented in figure B.3. "(S)" for surface atoms.

Final structure	Figure	Adsorption energy, eV
C(S)–SiH_3, C(S)–H	B.3 (a, b)	-2.4
C(S)–Si(S)–SiH2, 2 C(S)–H	B.3 (c, d)	-3.6
C(S)–Si(S)–Si(S)–SiH, 3 C(S)–H	B.3 (e, f)	-4.1
C(S)–Si(S)–Si(S)–Si_{DB}, 4 C(S)–H	B.3 (g, h)	-4.4

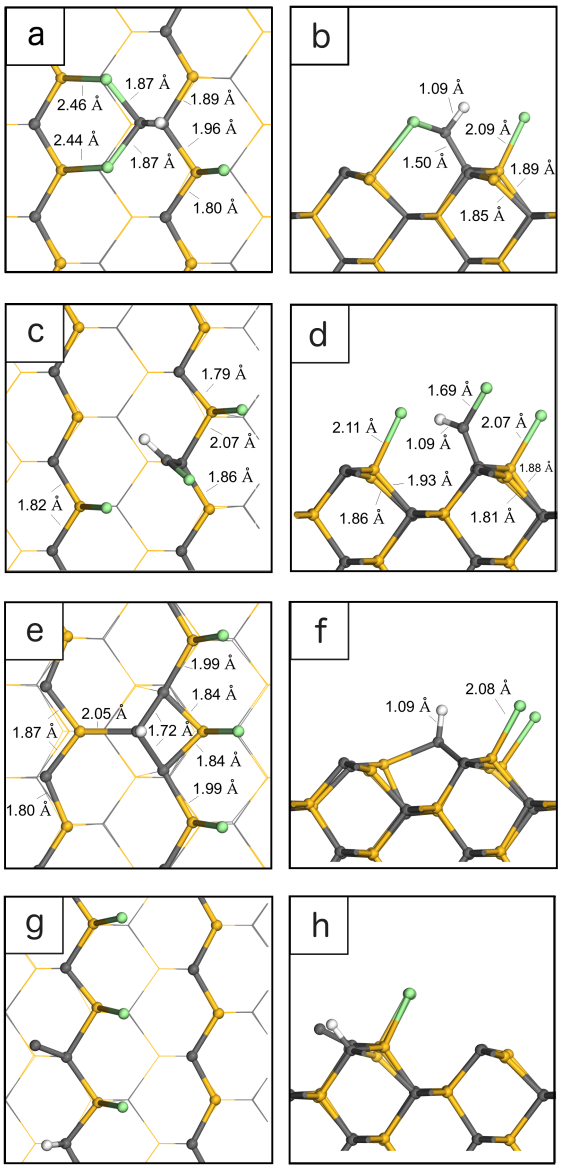


Figure B.4: Optimized structure of $CHCl_3$ adsorbing on the bare SiC surface. Left column - top view, right column - side view. Calculated adsorption energies are presented in table B.4.

Table B.4: Adsorption energies of $CHCl_3$ on the bare SiC surface. Optimized structures are presented in figure B.4. "(S)" for surface atoms.

Final structure	Figure	Adsorption energy, eV
C(S)–$CHCl_2$, Si(S)–Cl	B.4 (a, b)	-2.0
C(S)–CHCl, 2 Si(S)–Cl	B.4 (c, d)	-3.1
Si(S)–C(S)–C(S)–CH, 3 Si(S)–Cl	B.4 (e, f)	-4.1
C(S)–C_{DB}, 4 Si(S)–Cl	B.4 (g, h)	-3.5

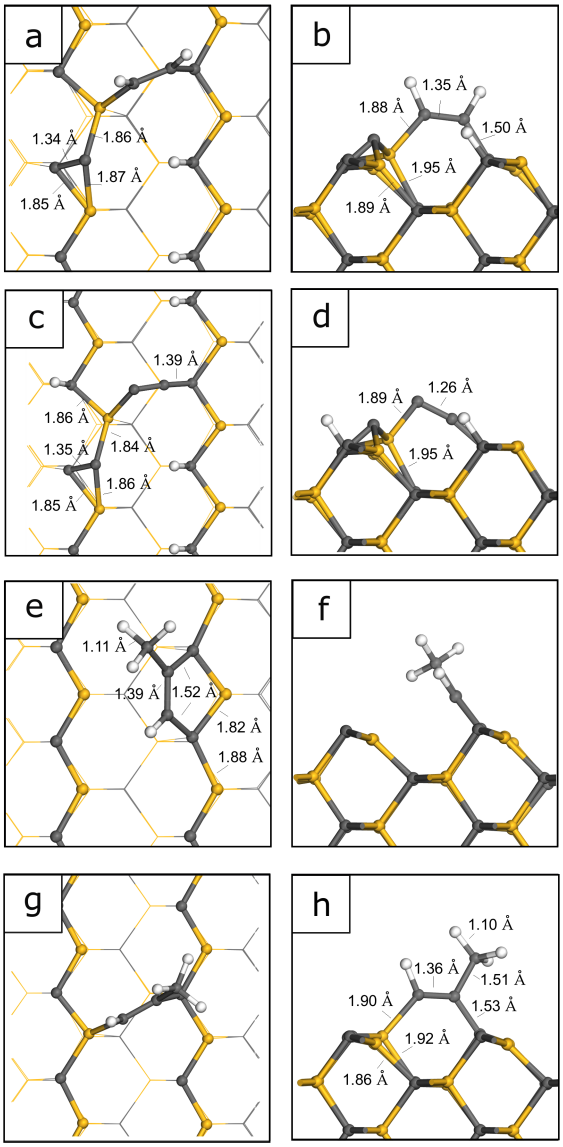


Figure B.5: Optimized structure of C_3H_4 adsorbing on the bare SiC surface. Left column - top view, right column - side view. Calculated adsorption energies are presented in table B.5.

Table B.5: Adsorption energies of C_3H_4 on the bare SiC surface. Optimized structures are presented in figure B.5. "(S)" for surface atoms.

Final structure	Figure	Adsorption energy, eV
C(S)–HC–CH–Si(S), C(S)–Si(S)–Si(S)–C_{DB}, 2 C(S)–H	B.5 (a, b)	-2.5
C(S)–C–C–Si(S), C(S)–Si(S)–Si(S)–C_{DB}, 4 C(S)–H	B.5 (c, d)	-2.3
C(S)–CH–C–CH_3–C(S) chain	B.5 (e, f)	-2.1
Si(S)–CH–C–CH_3–C(S) bridge	B.5 (g, h)	-2.6

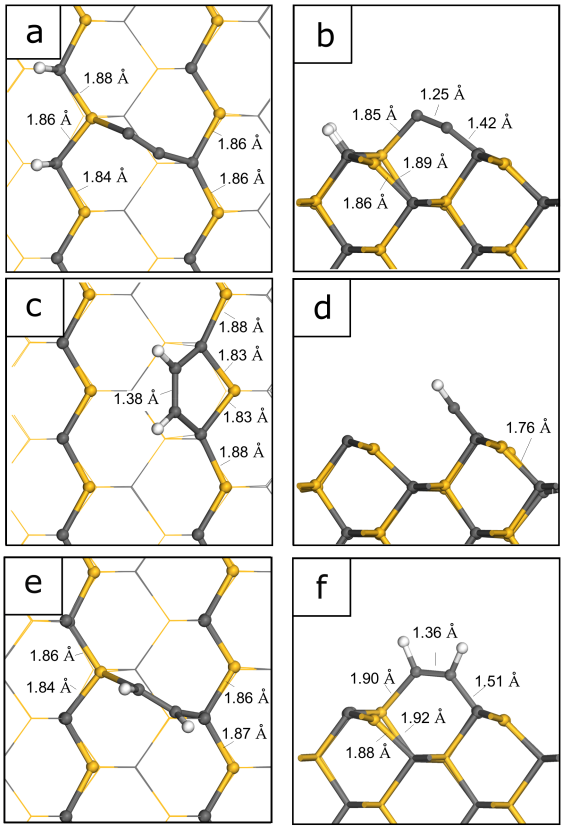


Figure B.6: Optimized structure of C_2H_2 adsorbing on the bare SiC surface. Left column - top view, right column - side view. Calculated adsorption energies are presented in table B.6.

Table B.6: Adsorption energies of C_2H_2 on the bare SiC surface. Optimized structures are presented in figure B.6. "(S)" for surface atoms.

Final structure	Figure	Adsorption energy, eV
C(S)–C–C–Si(S), 2 C(S)–H	B.6 (a, b)	-3.1
C(S)–CH–CH–C(S) chain	B.6 (c, d)	-2.3
Si(S)–CH–CH–C(S) bridge	B.6 (e, f)	-3.2

Table B.7: Adsorption energies of CCl_4 on the bare SiC surface. Optimized structures are presented in figure B.7. "(S)" for surface atoms.

Final structure	Figure	Adsorption energy, eV
C(S)–CH_2, 2 Si(S)–Cl	B.7 (a, b)	-3.5
Si(S)–C–C(S), 4 Si(S)–Cl	B.7 (c, d)	-4.8

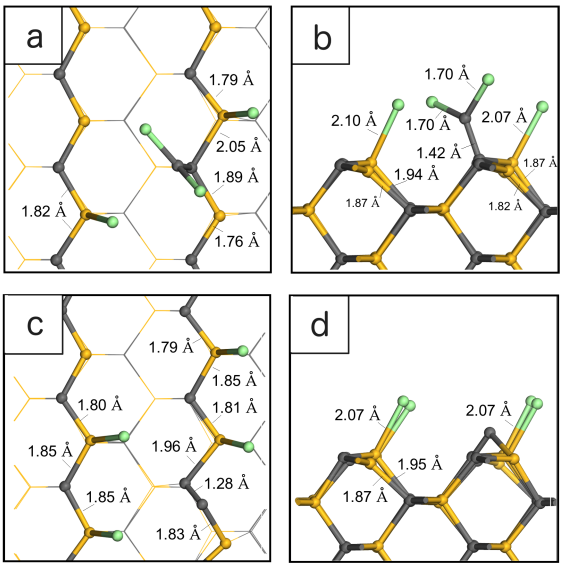


Figure B.7: Optimized structure of CCl_4 adsorbing on the bare SiC surface. Left column - top view, right column - side view. Calculated adsorption energies are presented in table B.7.

Bibliography

[1] C. A. Murray, S. D. Elliott, D. Hausmann, J. Henri, and A. LaVoie, "Effect of Reaction Mechanism on Precursor Exposure Time in Atomic Layer Deposition of Silicon Oxide and Silicon Nitride," *ACS Applied Materials and Interfaces*, vol. 6, pp. 10534–10541, 2014.

[2] K. Kano, *Semiconductor devices*. Prentice Hall, 1998.

[3] J. A. Venables, *Introduction to Surface and Thin Film Processes*. Cambridge: Cambridge University Press, 2000.

[4] K. Seshan, *Handbook of Thin Film Deposition Processes and Techniques*. Noyes Publications, 2002.

[5] J. E. Mahan, *Physical Vapor Deposition of Thin Films*. Wiley-Interscience, 2000.

[6] M. Leskelä and M. Ritala, "Atomic layer deposition chemistry: recent developments and future challenges.," *Angewandte Chemie (International ed. in English)*, vol. 42, pp. 5548–54, nov 2003.

[7] J. R. Creighton and P. Ho, "Chemical Vapor Deposition," *ASM International*, pp. 11–13, 2001.

[8] M. Hitchman and K. Jensen, *Chemical Vapor Deposition*. Academic Press, 1993.

[9] T. Suntola and J. Antson, "U.S. patent 4 058 430."

[10] V. B. Aleskovskii and S. I. Koltsov, "Some characteristics of molecular layering reactions," in *Abstract of Scientific and Technical Conference of the Leningrad Technological Institute by Lensovet*, p. 67, 1965.

[11] S. M. George, "Atomic layer deposition: an overview.," *Chemical reviews*, vol. 110, pp. 111–131, jan 2010.

[12] R. W. Johnson, A. Hultqvist, and S. F. Bent, "A brief review of atomic layer deposition: from fundamentals to applications," *Materials Today*, vol. 17, pp. 236–246, jun 2014.

[13] E. Ahvenniemi, A. R. Akbashev, S. Ali, M. Bechelany, M. Berdova, S. Boyadjiev, D. C. Cameron, R. Chen, M. Chubarov, V. Cremers, A. Devi, V. Drozd, L. Elnikova, G. Gottardi, K. Grigoras, D. M. Hausmann, C. S. Hwang, S.-H. Jen, T. Kallio, J. Kanervo, I. Khmelnitskiy, D. H. Kim, L. Klibanov, Y. Koshtyal, A. O. I. Krause, J. Kuhs, I. Kärkkänen, M.-L. Kääriäinen, T. Kääriäinen, L. Lamagna, A. A. Łapicki, M. Leskelä, H. Lipsanen, J. Lyytinen, A. Malkov, A. Malygin, A. Mennad, C. Militzer, J. Molarius, M. Norek, Ç. Özgit-Akgün, M. Panov, H. Pedersen, F. Piallat, G. Popov, R. Puurunen, G. Rampelberg, R. H. A. Ras, E. Rauwel, F. Roozeboom, T. Sajavaara, H. Salami, H. Savin, N. Schneider, T. E. Seidel, J. Sundqvist, D. B. Suyatin, T. Törndahl, J. R. van Ommen, C. Wiemer, O. M. E. Ylivaara, and O. Yurkevich, "Review Article: Recommended reading list of early publications on atomic layer deposition - Outcome of the "Virtual Project on the History of ALD"," *Journal of Vacuum Science & Technology A: Vacuum, Surfaces, and Films*, vol. 35, no. 1, p. 010801, 2017.

[14] R. Puurunen, "Surface chemistry of atomic layer deposition : a case study for the trimethylaluminum / water process," *Journal of Applied Physics*, vol. 91, pp. 121301–121301–52, 2005.

[15] M. A. Lieberman and A. J. Lichtenberg, *Principles of Plasma Discharges and Materials Processing*. New York: John Wiley & Sons, 2 ed., 2005.

[16] H. B. Profijt, S. E. Potts, M. C. M. van de Sanden, and W. M. M. Kessels, "Plasma-Assisted Atomic Layer Deposition: Basics, Opportunities, and Challenges," *J. Vac. Sci. Technol., A*, vol. 29, no. 5, p. 050801, 2011.

[17] H. Kim and I.-k. Oh, "Review of plasma-enhanced atomic layer deposition : Technical enabler of nanoscale device fabrication," *Japanese Journal of Applied Physics*, vol. 53, 2014.

[18] A. J. M. Mackus, A. A. Bol, and W. M. M. Kessels, "The use of atomic layer deposition in advanced nanopatterning," *Nanoscale*, vol. 6, no. 19, pp. 10941–10960, 2014.

[19] Chen, Rong and Kim, Hyoungsub and McIntyre, Paul C. and Porter, David

W. and Bent, Stacey F., "Achieving area-selective atomic layer deposition on patterned substrates by selective surface modification," *Applied Physics Letters*, vol. 86, pp. 191910, 2005.

[20] E. A. Filatova, D. Hausmann, and S. D. Elliott, "Investigating Routes Towards Atomic Layer Deposition of Silicon Carbide: Ab initio Screening of Potential Silicon and Carbon Precursors," *J. Vac. Sci. Technol., A*, vol. 35, pp. 1–6, 2017.

[21] E. A. Filatova, D. Hausmann, and S. D. Elliott, "Understanding the Mechanism of SiC Plasma-Enhanced Chemical Vapor Deposition (PECVD) and Developing Routes toward SiC Atomic Layer Deposition (ALD) with Density Functional Theory," *ACS Applied Materials & Interfaces*, vol. 10, pp. 15216–15225, 2018.

[22] M. Goetz, B. Lehmeier,N. Kuhn, and A. Meyer, "Silicon nitride substrates for power electronics," *PCIM Europe Conference Proceedings* p. 672-679, 2012.

[23] Nobuo Matsumoto, "Overview of Silicon-Based Materials," *Jpn. J. Appl. Phys.* p. 5425, 1998.

[24] T. Kimoto, *Jpn. J. Appl. Phys.* p. 040103, 2015.

[25] H. Matsunami, *Microelectron. Eng.* p. 2-4, 2006.

[26] N. G. Wright, A. B.Horsfall, and K. Vassilevski, *Mater. Today* p. 16-21, 2008.

[27] M. R. Baklanov, M. Van Hove, G. Mannaert, S. Vanhaelemeersch, H. Bender, T. Conard, and K. Maex, "Low temperature oxidation and selective etching of chemical vapor deposition a-SiC:H films," *Journal of Vacuum Science & Technology B: Microelectronics and Nanometer Structures*, vol. 18, no. 3, p. 1281, 2000.

[28] R. N. Wolf, Stanley, Tauber, *Silicon Processing for the VLSI Era*. Sunset Beach, CA: Lattice Press, 1986.

[29] K. Endo, Y. Ishikawa, T. Matsukawa, Y. Liu, S.-i. O'uchi, K. Sakamoto, J. Tsukada, H. Yamauchi, and M. Masahara, "Atomic Layer Deposition of SiO_2 for the Performance Enhancement of Fin Field Effect Transistors," *Japanese Journal of Applied Physics*, vol. 52, no. 11R, p. 116503, 2013.

[30] J.-E. Park, J.-H. Ku, J.-W. Lee, J.-H. Yang, K.-S. Chu, S.-H. Lee, M.-H. Park, N.-I. Lee, H.-K. Kang, and K.-P. Suh, "Mass-Productive Ultra-Low Temperature ALD SiO_2 Process Promising for Sub-90nm Memory and Logic Devices," *IEEE*, pp. 229–232, 2002.

[31] C. Wenger, J. Fompeyrine, C. Vallée, and J.-P. Locquet, "E-MRS 2012 Spring Meeting, Symposium M: More than Moore: Novel materials approaches for functionalized Silicon based Microelectronics," *IOP Conference Series: Materials Science and Engineering*, vol. 41, no. 1, p. 11001, 2012.

[32] D. H. Triyoso, K. Hempel, S. Ohsiek, V. Jaschke, J. Shu, S. Mutas, K. Dittmar, J. Schaeffer, D. Utess, and M. Lenski, "Evaluation of Low Temperature Silicon Nitride Spacer for High-k Metal Gate Integration," *ECS Journal of Solid State Science and Technology*, vol. 2, no. 11, pp. N222–N227, 2013.

[33] A. B. Sachid, Y. M. Huang, Y. J. Chen, C. C. Chen, D. D. Lu, M. C. Chen, and C. Hu, "FinFET with encased air-gap spacers for high-performance and low-energy circuits," *IEEE Electron Device Letters*, vol. 38, no. 1, pp. 16–19, 2017.

[34] S. D. Elliott, "Atomic-scale simulation of ALD chemistry," *Semiconductor Science and Technology*, vol. 27, p. 074008, jul 2012.

[35] S. Weeks, G. Nowling, N. Fuchigami, M. Bowes, and K. Littau, "Plasma enhanced atomic layer deposition of silicon nitride using neopentasilane," *Journal of Vacuum Science & Technology A: Vacuum, Surfaces, and Films*, vol. 34, no. 1, p. 01A140, 2016.

[36] C. Mui, Y. Widjajaa, J. K. Kangb, and C. B. Musgrave, "Surface reaction mechanisms for atomic layer deposition of silicon nitride," *Surface Science*, vol. 557, no. 1-3, pp. 159–170, 2004.

[37] S. W. King, "Plasma enhanced atomic layer deposition of SiN_x:H and SiO_2," *Vacuum*, vol. 97124, no. May, pp. 1–9, 2011.

[38] S. W. King, "Plasma Enhanced Atomic Layer Deposition of SiN:H using N_2 and Silane," *ECS transactions*, vol. 33, no. 2, pp. 365–373, 2010.

[39] J.-S. Park, S.-W. Kang, and H. Kim, "Growth mechanism and diffusion barrier property of plasma-enhanced atomic layer deposition Ti–Si–N

thin films," *Journal of Vacuum Science & Technology B: Microelectronics and Nanometer Structures*, vol. 24, no. 2006, p. 1327, 2006.

[40] H. Kim, H. Song, C. Shin, K. Kim, W. Jang, H. Kim, S. Shin, and H. Jeon, "Dielectric barrier characteristics of Si-rich silicon nitride films deposited by plasma enhanced atomic layer deposition," *Journal of Vacuum Science & Technology A: Vacuum, Surfaces, and Films*, vol. 35, no. 1, p. 01A101, 2017.

[41] T. Fuyuki, T. Yoshinobu, and H. Matsunami, "Atomic layer epitaxy controlled by surface superstructures in SiC," *Thin Solid Films*, vol. 225, no. 1-2, pp. 225–229, 1993.

[42] S. Hara, Y.Aoyagi, M.Kawai, S.Misawa, E.Sakuma, and S.Yoshida, "Self-limiting growth on the β-SiC(001) surface," *Surface Science*, vol. 273, p. 437, 1992.

[43] J. Sumakeris, L. Rowland, R. Kern, S. Tanaka, and R. Davis, "Layer-by-layer growth of SiC at low temperatures," *Thin Solid Films*, vol. 225, p. 219, 1993.

[44] E. Sadayuki, S. Imai, and M. Matsumura, "Sub-Atomic Layer Growth of SiC at Low Temperatures," *J. Appl. Phys.*, vol. 34, p. 6166, 1995.

[45] R. A. Ovanesyan, D. M. Hausmann, and S. Agarwal, "Challenges in atomic layer deposition of carbon-containing silicon-based dielectrics," *J. Vac. Sci. Technol., A*, vol. 35, no. 2, p. 021506, 2017.

[46] X. Meng, Y.-C. Byun, H. Kim, J. Lee, A. Lucero, L. Cheng, and J. Kim, "Atomic Layer Deposition of Silicon Nitride Thin Films: A Review of Recent Progress, Challenges, and Outlooks," *Materials*, vol. 9, no. 12, p. 1007, 2016.

[47] D. Hausmann, J. Henri, J. Sims, K. Kelchner, and S. Janjam, "Challenges with Industrialization of Atomic Layer Deposition of Silicon Nitride," 2014.

[48] J. Klaus, A. Ott, A. Dillon, and S. George, "Atomic layer controlled growth of Si_3N_4 films using sequential surface reactions," *Surface Science*, vol. 418, pp. L14–L19, 1998.

[49] A. Nakajima, T. Yoshimoto, T. Kidera, K. Obata, S. Yokoyama, H. Sunami, and M. Hirose, "Atomic-layer-deposited silicon-nitride/SiO_2 stacked gate

dielectrics for highly reliable p-metal–oxide–semiconductor field-effect transistors," *Applied Physics Letters*, vol. 77, no. 18, pp. 2855–2857, 2000.

[50] A. Nakajima, T. Yoshimoto, T. Kidera, and S. Yokoyama, "Low-temperature formation of silicon nitride gate dielectrics by atomic-layer deposition," *Applied Physics Letters*, vol. 79, no. 5, pp. 665–667, 2001.

[51] Q. D. M. Khosru, A. Nakajima, T. Yoshimoto, and S. Yokoyama, "Soft-breakdown-suppressed ultrathin atomic-layer-deposited silicon-nitride/SiO_2 stack gate dielectrics for advanced complementary metal-oxide-semiconductor technology," *Applied Physics Letters*, vol. 79, no. 21, pp. 3488–3490, 2001.

[52] A. Nakajima, Q. D. M. Khosru, T. Yoshimoto, T. Kidera, and S. Yokoyama, "NH_3-annealed atomic-layer-deposited silicon nitride as a high-k gate dielectric with high reliability," *Applied Physics Letters*, vol. 80, no. 7, pp. 1252–1254, 2002.

[53] A. Nakajima, Q. D. M. Khosru, T. Yoshimoto, T. Kasai, and S. Yokoyama, "High quality atomic-layer-deposited ultrathin Si-nitride gate dielectrics with low density of interface and bulk traps," *Applied Physics Letters*, vol. 83, no. 2, pp. 335–337, 2003.

[54] W.-J. Lee, J.-H. Lee, Y.-S. Lee, S.-K. Rha, and C.-O. Park, "A Comparative Study on the Precursors for the Atomic Layer Deposition of Silicon Nitride Thin Films," *Korean Journal of Materials Research*, vol. 14, no. 2, pp. 141–145, 2004.

[55] W. Hansch, A. Nakajima, and S. Yokoyama, "Characterization of silicon/oxide/nitride layers by x-ray photoelectron spectroscopy," *Applied Physics Letters*, vol. 75, no. 11, pp. 1535–1537, 1999.

[56] W.-J. Lee, U.-J. Kim, C.-H. Han, M.-H. Chun, S.-K. Rha, and Y.-S. Lee, "Characteristics of silicon nitride thin films prepared by using alternating exposures of SiH_2Cl_2 and NH_3," *Journal of the Korean Physical Society*, vol. 47, no. S.3, pp. 598–602, 2005.

[57] K. Park, W. D. Yun, B. J. Choi, H. D. Kim, W. J. Lee, S. K. Rha, and C. O. Park, "Growth studies and characterization of silicon nitride thin films deposited by alternating exposures to Si_2Cl_6 and NH_3," *Thin Solid Films*, vol. 517, no. 14, pp. 3975–3978, 2009.

[58] L. L. Yusup, J.-M. Park, Y.-H. Noh, S.-J. Kim, W. Lee, S. Park, and Y.-K. Kwon, "Reactivity of different surface sites with silicon chlorides during atomic layer deposition of silicon nitride," *RSC Advances*, vol. 6, pp. 68515–68524, 2016.

[59] S. Morishita, S. Sugahara, and M. Matsumura, "Atomic-layer chemical-vapor-deposition of silicon-nitride," *Applie Surface Science*, pp. 198–204, 1997.

[60] M. Edmonds, K. Sardashti, S. Wolf, E. Chagarov, M. Clemons, T. Kent, J. H. Park, K. Tang, P. C. McIntyre, N. Yoshida, L. Dong, R. Holmes, D. Alvarez, and A. C. Kummel, "Low temperature thermal ALD of a SiN_x interfacial diffusion barrier and interface passivation layer on $Si_xGe_{(1-x)}$ (001) and $Si_xGe_{(1-x)}$ (110)," *The Journal of Chemical Physics*, vol. 146, no. 5, p. 052820, 2017.

[61] S. Riedel, J. Sundqvist, and T. Gumprecht, "Low temperature deposition of silicon nitride using Si_3Cl_8," *Thin Solid Films*, vol. 577, pp. 114–118, 2015.

[62] F. Koehler, D. H. Triyoso, I. Hussain, B. Antonioli, and K. Hempel, "Challenges in spacer process development for leading-edge high-k metal gate technology," *Physica Status Solidi (C) Current Topics in Solid State Physics*, vol. 11, no. 1, pp. 73–76, 2014.

[63] S. Yokoyama, H. Goto, T. Miyamoto, N. Ikeda, and K. Shibahara, "Atomic layer controlled deposition of silicon nitride and in situ growth observation by infrared reflection absorption spectroscopy," *Applied Surface Science*, vol. 112, pp. 75–81, 1997.

[64] H. Goto, K. Shibahara, and S. Yokoyama, "Atomic layer controlled deposition of silicon nitride with self-limiting mechanism," *Applied Physics Letters*, vol. 68, no. 23, pp. 3257–3259, 1996.

[65] S. Yokoyama, N. Ikeda, K. Kajikawa, and Y. Nakashima, "Atomic-layer selective deposition of silicon nitride on hydrogen-terminated Si surfaces," *Applied Surface Science*, vol. 130-132, pp. 352–356, 1998.

[66] K. Nagata, M. Nagasaka, T. Yamaguchi, A. Ogura, H. Oji, J. Son, I. Hirosawa, Y. Watanabe, and Y. Hirota, "Evaluation of Stress Induced by Plasma Assisted ALD SiN Film K. Nagata," *ECS transactions*, vol. 53, no. 3, pp. 51–56, 2013.

[67] J. Provine, P. Schindler, Y. Kim, S. P. Walch, H. J. Kim, K. H. Kim, and F. B. Prinz, "Correlation of film density and wet etch rate in hydrofluoric acid of plasma enhanced atomic layer deposited silicon nitride," *AIP Advances*, vol. 6, no. 6, 2016.

[68] R. A. Ovanesyan, D. M. Hausmann, and S. Agarwal, "Low-temperature Conformal Atomic Layer Deposition of SiN_x Films using Si_2Cl_6 and NH_3 Plasma," *ACS Applied Materials & Interfaces*, vol. 7, no. 20, pp. 10806–10813, 2015.

[69] R. A. Ovanesyan, D. M. Hausmann, and S. Agarwal, "A Three-Step Atomic Layer Deposition Process for SiNx Using Si_2Cl_6 , CH_3NH_2 , and N_2 Plasma," *Applied Materials & Interfaces*, vol. 10, no. 22, pp. 19153–19161, 2018.

[70] X. Meng, H. S. Kim, A. T. Lucero, S. M. Hwang, J. S. Lee, Y.-C. Byun, J. Kim, B. K. Hwang, X. Zhou, and J. Young, "Hollow Cathode Plasma-Enhanced Atomic Layer Deposition of Silicon Nitride Using Pentachlorodisilane," *ACS Applied Materials & Interfaces*, vol. 10, no. 16, pp. 14116–14123, 2018.

[71] J. Klaus, O. Sneh, A. W. Otty, and S. M. George, "Atomic Layer Deposition of SiO_2 using Catalyzed and Uncatalyzed Self-limiting Surface Reactions," *Surface Review and Letters*, vol. 6, pp. 435–448, 1999.

[72] O. Sneh, M. L. Wise, A. W. Ott, L. A. Okada, and S. M. George, "Atomic layer growth of SiO_2 on Si(100) using $SiCl_4$ and H_2O in a binary reaction sequence," *Surface Science*, vol. 334, no. 1-3, pp. 135–152, 1995.

[73] J. Klaus, O. Sneh, and S. M. George, "Growth of SiO2 at Room Temperature with the Use of Catalyzed Sequential Half-Reactions," *Science*, vol. 278, no. 5345, pp. 1934–1936, 1997.

[74] J. Klaus and S. M. George, "Atomic layer deposition of SiO_2 at room temperature using NH_3-catalyzed sequential surface reactions," *Surface Science*, vol. 447, no. 1, pp. 81–90, 2000.

[75] J.-H. Lee, U.-J. Kim, C.-H. Han, S.-K. Rha, W. Lee, and C.-O. Park, "Investigation of Silicon Oxide Thin Films Prepared by Atomic Layer Deposition Using SiH_2Cl_2 and O_3 as the Precursors," *Japanese Journal of Applied Physics*, vol. 43, no. 3A, pp. L328–L330, 2004.

[76] W. Lee, C.-H. Han, J.-K. Park, Y.-S. Lee, and S.-K. Rha, "Atomic Layer Deposition and Properties of Silicon Oxide Thin Films Using Alternating Exposures to SiH_2Cl_2 and O_3 Atomic Layer Deposition and Properties of Silicon Oxide Thin Films Using Alternating Exposures to SiH_2Cl_2 and O_3," *Jpn. J. Appl. Phys.*, vol. 49, p. 071504, 2010.

[77] W. J. Lee, M. H. Chun, K. S. Cheong, K. C. Park, C. O. Park, G. Z. Cao, and S. K. Rha, "Characteristics of SiO_2 Film Grown by Atomic Layer Deposition as the Gate Insulator of Low-Temperature Polysilicon Thin-Film Transistors," *Solid State Phenomena*, vol. 124-126, pp. 247–250, 2007.

[78] S.-W. Lee, K. Park, B. Han, S.-H. Son, S.-K. Rha, C.-O. Park, and W. Lee, "Atomic layer deposition of silicon oxide thin films by alternating exposures to Si_2Cl_6 and O_3," *Electrochemical and Solid-State Letters*, vol. 11, no. 7, pp. 7–10, 2008.

[79] H. Nagasawa and Y. Yamaguchi, "Atomic level epitaxy of 3C-SiC by low pressure vapour deposition with alternating gas supply," *Thin Solid Films*, vol. 225, no. 1-2, pp. 230–234, 1993.

[80] H. Nagasawa and Y.-I. Yamaguchi, "Mechanisms of SiC growth by alternate supply of SiH_2Cl_2 and C_2H_2," *Applied Surface Science*, vol. 82-83, no. C, pp. 405–409, 1994.

[81] C. Tripp and M. L. Hair, "Chemical Attachment of Chlorosilanes to Silica: A Two-step Amine-Promoted Reaction," *J. Phys. Chem.*, vol. 97, pp. 5693–5698, 1993.

[82] J. K. Kang and C. B. Musgrave, "Mechanism of atomic layer deposition of SiO_2 on the silicon (100)-2x1 surface using $SiCl_4$ and H_2O as precursors," *J. Appl. Phys.*, vol. 91, no. 5, pp. 3408–3414, 2002.

[83] G.-Y. Fang, L.-N. Xu, L.-G. Wang, Y.-Q. Cao, D. Wu, and A.-D. Li, "Stepwise mechanism and H_2O-assisted hydrolysis in atomic layer deposition of SiO_2 without a catalyst," *Nanoscale Research Letters*, vol. 10, no. 1, 2015.

[84] G. Fang, L. Xu, J. Ma, and A. Li, "Theoretical Understanding of the Reaction Mechanism of SiO_2 Atomic Layer Deposition," *Chemistry of Materials*, vol. 28, no. 5, 2016.

[85] L. Huang, B. Han, B. Han, A. Derecskei-Kovacs, M. Xiao, X. Lei, M. L. O'Neill, R. M. Pearlstein, H. Chandra, and H. Cheng, "Density functional theory study on the full ALD process of silicon nitride thin film deposition via BDEAS or BTBAS and NH_3," *Phys. Chem. Chem. Phys.*, vol. 16, pp. 18501–12, sep 2014.

[86] J. P. Blitz, R. S. Shreedhara Murthy, and D. E. Leyden, "The role of amine structure on catalytic activity for silylation reactions with Cab-O-Sil," *Journal of Colloid And Interface Science*, vol. 126, no. 2, pp. 387–392, 1988.

[87] S. Chen, G. Fang, X. Qian, A. Li, and J. Ma, "Influence of Alkalinity and Steric Hindrance of Lewis-Base Catalysts on Atomic Layer Deposition of SiO_2," *The Journal of Physical Chemistry C*, vol. 115, pp. 23363–23373, dec 2011.

[88] T. R. Mayangsari, J. M. Park, L. L. Yusup, J. Gu, J. H. Yoo, H. D. Kim, and W. J. Lee, "Catalyzed Atomic Layer Deposition of Silicon Oxide at Ultralow Temperature Using Alkylamine," *Langmuir*, vol. 34, no. 23, pp. 6660–6669, 2018.

[89] R. Joe and M. Gandhi, "U.S. patent 7964441B2," 2007.

[90] J. D. Ferguson, E. R. Smith, a. W. Weimer, and S. M. George, "ALD of SiO_2 at Room Temperature Using TEOS and H_2O with NH_3 as the Catalyst," *Journal of The Electrochemical Society*, vol. 151, no. 8, p. G528, 2004.

[91] J. Bachmann, R. Zierold, Y. T. Chong, R. Hauert, C. Sturm, R. Schmidt-Grund, B. Rheinländer, M. Grundmann, U. Gösele, and K. Nielsch, "A practical, self-catalytic, atomic layer deposition of silicon dioxide," *Angewandte Chemie - International Edition*, vol. 47, no. 33, pp. 6177–6179, 2008.

[92] C. A. Murray, S. D. Elliott, D. Hausmann, J. Henri, and A. LaVoie, "The Effect of Reaction Mechanism on Precursor Exposure Time in Atomic Layer Deposition of Silicon Oxide and Silicon Nitride.," *ACS applied materials & interfaces*, jun 2014.

[93] B. B. Burton, S. W. Kang, S. W. Rhee, and S. M. George, "SiO_2 Atomic Layer Deposition Using Tris (dimethylamino) silane and Hydrogen Peroxide Studied by in Situ Transmission FTIR Spectroscopy," *J. Phys. Chem. C*, vol. 113, pp. 8249–8257, 2009.

[94] H. C. M. Knoops, K. De Peuter, and W. M. M. Kessels, "Redeposition in plasma-assisted atomic layer deposition: Silicon nitride film quality ruled by the gas residence time," *Applied Physics Letters*, vol. 107, no. 1, 2015.

[95] H. C. M. Knoops, E. M. J. Braeken, K. de Peuter, S. E. Potts, S. Haukka, V. Pore, and W. M. M. Kessels, "Atomic Layer Deposition of Silicon Nitride from Bis(tert-butylamino)silane and N_2 Plasma," *ACS Applied Materials & Interfaces*, vol. 7, no. 35, pp. 19857–19862, 2015.

[96] R. H. E. C. Bosch, L. E. Cornelissen, H. C. M. Knoops, and W. M. M. Kessels, "Atomic Layer Deposition of Silicon Nitride from Bis(tertiary-butyl-amino)silane and N_2 Plasma Studied by in Situ Gas Phase and Surface Infrared Spectroscopy," *Chemistry of Materials*, vol. 28, no. 16, pp. 5864–5871, 2016.

[97] Y. Kim, J. Provine, S. P. Walch, J. Park, W. Phuthong, A. L. Dadlani, H. J. Kim, P. Schindler, K. Kim, and F. B. Prinz, "Plasma-Enhanced Atomic Layer Deposition of SiN-AlN Composites for Ultra Low Wet Etch Rates in Hydrofluoric Acid," *ACS Applied Materials and Interfaces*, vol. 8, no. 27, pp. 17599–17605, 2016.

[98] T. Faraz, M. van Drunen, H. C. M. Knoops, A. Mallikarjunan, I. Buchanan, D. M. Hausmann, J. Henri, and W. M. M. Kessels, "Atomic Layer Deposition of Wet-Etch Resistant Silicon Nitride Using Di(sec-butylamino)silane and N_2 Plasma on Planar and 3D Substrate Topographies," *ACS Applied Materials & Interfaces*, vol. 9, no. 2, pp. 1858–1869, 2017.

[99] S. Suh, S. W. Ryu, S. Cho, J.-R. Kim, S. Kim, C. S. Hwang, and H. J. Kim, "Low-temperature SiON films deposited by plasma-enhanced atomic layer deposition method using activated silicon precursor," *Journal of Vacuum Science & Technology A: Vacuum, Surfaces, and Films*, vol. 34, no. 1, p. 01A136, 2016.

[100] J. M. Park, S. J. Jang, S. I. Lee, and W. J. Lee, "Novel Cyclosilazane-Type Silicon Precursor and Two-Step Plasma for Plasma-Enhanced Atomic Layer Deposition of Silicon Nitride," *ACS Applied Materials and Interfaces*, vol. 10, no. 10, pp. 9155–9163, 2018.

[101] J. W. Lim, S. J. Yun, and J. H. Lee, "Low-temperature growth of SiO_2 films by plasma-enhanced atomic layer deposition," *ETRI Journal*,

vol. 27, no. 1, pp. 118–121, 2005.

[102] Y. J. Choi, S. M. Bae, J. H. Kim, E. H. Kim, H. S. Hwang, J. W. Park, H. Yang, E. Choi, and J. H. Hwang, "Robust SiO_2 gate dielectric thin films prepared through plasma-enhanced atomic layer deposition involving di-sopropylamino silane (DIPAS) and oxygen plasma: Application to amorphous oxide thin film transistors," *Ceramics International*, vol. 44, no. 2, pp. 1556–1565, 2018.

[103] K. Pfeiffer, S. Shestaeva, A. Bingel, P. Munzert, L. Ghazaryan, C. van Helvoirt, W. Kessels, U. Sanli, C. Grévent, G. Schütz, M. Putkonen, I. Buchanan, L. Jensen, D. Ristau, A. Tünnermann, and A. Szeghalmi, "Comparative study of ALD SiO_2 thin films for optical applications," *Optical Materials Express*, vol. 6, no. 2, 2016.

[104] G. Dingemans, C. A. A. van Helvoirt, M. C. M. van de Sanden, and W. M. M. Kessels, "Plasma-Assisted Atomic Layer Deposition of Low Temperature SiO_2," *ECS transactions*, vol. 4, pp. 191–204, 2011.

[105] A. Mallikarjunan, H. Chandra, M. Xiao, X. Lei, R. M. Pearlstein, H. R. Bowen, M. L. O'Neill, A. Derecskei-Kovacs, and B. Han, "Designing high performance precursors for atomic layer deposition of silicon oxide," *J. Vac. Sci. Technol., A*, vol. 33, no. 1, p. 01A137, 2015.

[106] S.-J. Won, S. Suh, M. S. Huh, and H. J. Kim, "High-Quality Low-Temperature Silicon Oxide by Plasma-Enhanced Atomic Layer Deposition Using a Metal – Organic Silicon Precursor and Oxygen Radical," *IEEE Electron Device Lett.*, vol. 31, no. 8, pp. 857–859, 2010.

[107] M. Putkonen, M. Bosund, O. M. Ylivaara, R. Puurunen, L. Kilpi, H. Ronkainen, S. Sintonen, S. Ali, H. Lipsanen, X. Liu, E. Haimi, S.-P. Hannula, T. Sajavaara, I. Buchanan, E. Karwacki, and M. Vähä-Nissi, "Thermal and plasma enhanced atomic layer deposition of SiO_2 using commercial silicon precursors," *Thin Solid Films*, vol. 558, pp. 93–98, may 2014.

[108] Y.-S. Lee, D.-w. Choi, B. Shong, S. Oh, and J.-S. Park, "Low temperature atomic layer deposition of SiO_2 thin films using di-isopropylaminosilane and ozone," *Ceramics International*, vol. 43, no. 2, pp. 2095–2099, 2017.

[109] S. Ahn, Y. Kim, S. Kang, K. Im, and H. Lim, "Low-temperature-atomic-layer-deposition of SiO_2 using various organic precursors," *J. Vac. Sci.*

Technol., A, vol. 35, no. 1, 2017.

[110] L. Han and Z. Chen, "High-Quality thin SiO_2 films grown by atomic layer deposition using tris(dimethylamino)silane (TDMAS) and Ozone," *ECS Journal of Solid State Science and Technology*, vol. 2, no. 11, 2013.

[111] F. Hirose, Y. Kinoshita, S. Shibuya, Y. Narita, Y. Takahashi, H. Miya, K. Hirahara, Y. Kimura, and M. Niwano, "Atomic layer deposition of SiO_2 from Tris(dimethylamino)silane and ozone by using temperature-controlled water vapor treatment," *Thin Solid Films*, vol. 519, no. 1, pp. 270–275, 2010.

[112] Y. Kinoshita, F. Hirose, H. Miya, K. Hirahara, Y. Kimura, and M. Niwano, "Infrared Study of Tris(dimethylamino)silane Adsorption and Ozone Irradiation on Si(100) Surfaces for ALD of SiO_2," *Electrochemical and Solid-State Letters*, vol. 10, no. 100, p. G80, 2007.

[113] S. Kamiyama, T. Miura, and Y. Nara, "Comparison between SiO_2 films deposited by atomic layer deposition with $SiH_2[N(CH_3)_2]_2$and $SiH[N(CH_3)_2]_3$ precursors," *Thin Solid Films*, vol. 515, no. 4, pp. 1517–1521, 2006.

[114] S.-J. Won, H.-S. Jung, S. Suh, Y. Jin Choi, N.-I. Lee, C. Seong Hwang, and H. Joon Kim, "Growth and electrical properties of silicon oxide grown by atomic layer deposition using Bis(ethyl-methyl-amino)silane and ozone," *J. Vac. Sci. Technol., A*, vol. 30, no. 1, p. 01A126, 2012.

[115] J.-K. Kim, K. Jin, J. Jung, S.-K. Rha, and W.-J. Lee, "Atomic Layer Deposition of SiO_2 Thin Films Using Tetrakis(ethylamino)silane and Ozone," *Journal of Nanoscience and Nanotechnology*, vol. 12, no. 4, pp. 3589–3592, 2012.

[116] M. Degai, K. Kanomata, K. Momiyama, S. Kubota, K. Hirahara, and F. Hirose, "Non-heating atomic layer deposition of SiO_2 using tris(dimethylamino)silane and plasma-excited water vapor," *Thin Solid Films*, vol. 525, pp. 73–76, 2012.

[117] G. Dingemans, C. A. A. van Helvoirt, D. Pierreux, W. Keuning, and W. M. M. Kessels, "Plasma-Assisted ALD for the Conformal Deposition of SiO_2: Process, Material and Electronic Properties," *Journal of the Electrochemical Society*, vol. 159, no. 3, pp. H277–H285, 2012.

[118] J. Lu, B. Liu, N. P. Guisinger, P. C. Stair, J. P. Greeley, and J. W. Elam, "First-Principles Predictions and in Situ Experimental Validation of Alumina Atomic Layer Deposition on Metal Surfaces," *Chemistry of Materials*, 2014.

[119] L. Pena, C. Nanayakkara, A. Mallikarjunan, H. Chandra, M. Xiao, X. Lei, R. Pearlstein, A. Derecskei-Kovacs, and Y. Chabal, "Atomic Layer Deposition of Silicon Dioxide Using Aminosilanes Di-sec-butylaminosilane and Bis(tert-butylamino)silane with Ozone," *J. Phys. Chem. C*, vol. 120, no. 20, 2016.

[120] S.-B. Baek, D.-H. Kim, and Y.-C. Kim, "Adsorption and surface reaction of bis -diethylaminosilane as a Si precursor on an OH-terminated Si (001) surface," *Applied Surface Science*, vol. 258, no. 17, pp. 6341–6344, 2012.

[121] J. Li, J. Wu, C. Zhou, B. Han, E. J. Karwacki, M. Xiao, X. Lei, and H. Cheng, "On the Dissociative Chemisorption of Tris(dimethylamino)silane on Hydroxylated SiO_2 (001) Surface," *The Journal of Physical Chemistry C*, vol. 113, no. 22, pp. 9731–9736, 2009.

[122] B. Han, Q. Zhang, J. Wu, B. Han, E. J. Karwacki, A. Derecskei, M. Xiao, X. Lei, M. L. O. Neill, and H. Cheng, "On the Mechanisms of SiO_2 Thin-Film Growth by the Full Atomic Layer Deposition Process Using Bis(t-butylamino) silane on the," *The Journal of Physical Chemistry C*, vol. 2, no. 001, pp. 947–952, 2012.

[123] L. Huang and B. Han, "Density functional theory study on the full ALD process of silicon nitride thin film deposition via BDEAS or BTBAS and NH_3," *Physical Chemistry . . .* , vol. 16, pp. 18501–18512, 2014.

[124] L. Huang, B. Han, B. Han, A. Derecskei-Kovacs, M. Xiao, X. Lei, M. L. O'Neill, R. M. Pearlstein, H. Chandra, and H. Cheng, "First-Principles Study of a Full Cycle of Atomic Layer Deposition of SiO_2 Thin Films with Di(sec-butylamino)silane and Ozone," *The Journal of Physical Chemistry C*, vol. 117, no. 38, pp. 19454–19463, 2013.

[125] L. F. Peña, E. C. Mattson, C. E. Nanayakkara, K. A. Oyekan, A. Mallikarjunan, H. Chandra, M. Xiao, X. Lei, R. M. Pearlstein, A. Derecskei-Kovacs, and Y. J. Chabal, "In Situ Infrared Absorption Study of Plasma-Enhanced Atomic Layer Deposition of Silicon Nitride," *Langmuir*, vol. 34, no. 8, pp. 2619–2629, 2018.

[126] C. A. Murray, S. D. Elliott, D. Hausmann, J. Henri, and A. LaVoie, "The Effect of Reaction Mechanism on Precursor Exposure Time in Atomic Layer Deposition of Silicon Oxide and Silicon Nitride," *ACS applied materials & interfaces*, jun 2014.

[127] C. K. Ande, H. C. M. Knoops, K. de Peuter, M. van Drunen, S. D. Elliott, and W. M. M. Kessels, "Role of Surface Termination in Atomic Layer Deposition of Silicon Nitride," *J. of Physical Chemistry Letters*, vol. 6, pp. 3610–3614, 2015.

[128] W. Jang, H. Jeon, C. Kang, H. Song, J. Park, H. Kim, H. Seo, M. Leskela, and H. Jeon, "Temperature dependence of silicon nitride deposited by remote plasma atomic layer deposition," *Phys. Status Solidi A*, vol. 211, pp. 2166–2171, sep 2014.

[129] H. Jeon, W. Jang, H. Jeon, H. Song, H. Kim, J. Park, and H. Kim, "The effect of plasma power on the properties of low-temperature silicon nitride deposited by RPALD for a gate spacer," *Physica Status Solidi (A) Applications and Materials Science*, vol. 212, no. 12, pp. 2785–2790, 2015.

[130] J.-M. Park, S. J. Jang, L. L. Yusup, W.-J. Lee, and S.-I. Lee, "Plasma-Enhanced Atomic Layer Deposition of Silicon Nitride Using a Novel Silylamine Precursor," *ACS Applied Materials & Interfaces*, vol. 8, no. 32, pp. 20865–20871, 2016.

[131] S. D. Elliott, *Atomic Layer Deposition for Semiconductors*. New York: Springer, 2014.

[132] S. Shankar, H. Simka, and M. Haverty, "Density functional theory and beyond - opportunities for quantum methods in materials modeling semiconductor technology," *J. Phys.:Condens. Matter*, vol. 20, 2008.

[133] James B. Foresman and Eleen Frisch, *Exploring Chemistry with Electronic Structure Methods*. Pittsburgh, PA: Gaussian, Inc, 2nd editio ed., 1996.

[134] P. Henrich, V.E. and Cox, *The surface science of metal oxides*. New York: Cambridge University Press, 2000.

[135] S. D. Elliott, G. Dey, Y. Maimaiti, H. Ablat, E. A. Filatova, and G. N. Fomengia, "Modelling mechanism and growth reactions for new nanofabrication processes by Atomic Layer Deposition," *Adv. Mater.*, vol. 28, pp. 5367–5380, 2016.

[136] H. Jónsson, G. Mills, and K. W. Jacobsen, "Nudged Elastic Band Method for Finding Minimum Energy Paths of Transitions," in *Classical and Quantum Dynamics in Condensed Phase Simulations* (B. J. Berne, G. Ciccotti, and D. F. Coker, eds.), p. 385, World Scientific, 1998.

[137] G. Henkelman, B. P. Uberuaga, and H. Jónsson, "A Climbing Image Nudged Elastic Band Method for Finding Saddle Points and Minimum Energy Paths," *J. Chem. Phys.*, vol. 113, no. 22, pp. 9901–9904, 2000.

[138] D. Sheppard, R. Terrell, and G. Henkelman, "Optimization methods for finding minimum energy paths," *The Journal of Chemical Physics*, vol. 128, p. 134106, 2008.

[139] "http://theory.cm.utexas.edu/vtsttools/optimizers.html."

[140] L. H. Thomas, "The calculation of atomic fields," *Math. Proc. Camb. Phil. Soc.*, vol. 23, p. 542, 1927.

[141] E. Z. Fermi, "Eine statistische Methode zur Bestimmung einiger Eigenschaften des Atoms und ihre Anwendung auf die Theorie des periodischen Systems der Elemente," *Physik*, vol. 48, p. 73, 1928.

[142] W. Kohn and L. J. Sham, "Self-consistent equations including exchange and correlation effects," *Physical Review*, vol. 140, no. 4A, 1965.

[143] J. Perdew, *Density Functional Methods in Physics*. New York: Plenum, 1985.

[144] "https://youtu.be/ofyr1GyEZsU."

[145] D. R. Hamann, M. Schlüter, and C. Chiang, "Norm-Conserving Pseudopotentials," *Phys. Rev. Lett.*, vol. 43, no. 20, p. 1494, 1979.

[146] J. A. Appelbaum and D. R. Hamann, "Self-Consistent Pseudopotential for Si," *Phys. Rev. B*, vol. 8, p. 1777, 1973.

[147] P. E. Blöchl, "Projector augmented-wave Method," *Phys. Rev. B*, vol. 50, no. 24, pp. 17953–17979, 1994.

[148] D. Vanderbilt, "Soft self-consistent pseudopotentials in a generalized eigenvalue formalism," *Phys. Rev. B*, vol. 41, pp. 7892–7895, 1990.

[149] W. Kohn, Y. Meir, and D. E. Makarov, "van der Waals Energies in Density Functional Theory," *Phys. Rev. Lett.*, vol. 80, p. 4153, 1998.

[150] M. Lein, J. F. Dobson, and E. K. U. Gross, "Toward the description of van der Waals interactions within density functional theory," *J. Comp.Chem.*, vol. 20, no. 1, pp. 12–22, 1999.

[151] V. I. Anisimov, F. Aryasetiawan, A. Liechtenstein, and A. Lichtenstein, "First-principles calculations of the electronic structure and spectra of strongly correlated systems: the LDA+U method," *Journal of Physics: Condensed Matter*, vol. 9, no. 4, pp. 767–808, 1997.

[152] P. Ziesche, S. Kurth, and J. P. Perdew, "Density functionals from LDA to GGA," *Computational Materials Science*, vol. 11, no. 2, pp. 122–127, 1998.

[153] J. Perdew and Y. Wang, "Accurate and simple analytic representation of the electron-gas correlation energy," *Phys. Rev. B 45*, p. 13244, 1992.

[154] J. Perdew, K. Burke, and M. Ernzerhof, "Generalised gradient approximation made simple," *Phys. Rev. Lett.77*, vol. 77, p. 3865, 1996.

[155] "http://elk.sourceforge.net/CECAM/Burke-DFT.pdf."

[156] A. Mameli, B. Karasulu, M. A. Verheijen, A. J. M. Mackus, W. M. M. Kessels, and F. Roozeboom, "Area-Selective Atomic Layer Deposition: Role of Surface Chemistry," *ECS Transactions*, vol. 80, no. 3, pp. 39–48, 2017.

[157] G. Kresse and J. Furthmüller, "Efficiency of Ab-initio Total Energy Calculations for Metals and Semiconductors using a Plane-Wave Basis Set," *Comput. Mat. Sci.*, vol. 6, pp. 15–50, jul 1996.

[158] H. J. Monkhorst and J. D. Pack, "Special Points for Brillouin Zone Integrations," *Phys. Rev. B*, vol. 13, p. 5188, 1976.

[159] C. R. Hubbard, H. E. Swanson and F. A. Mauer, "A silicon powder diffraction standard reference material," *J. Appl. Crystallogr*, vol. 8, no. 45, 1975.

[160] R. Taylor, A., Jones, *Silicon Carbide: a High Temperature Semiconductor*. New York: Pergamon Press, 1960.

[161] J. D. Plummer, M. D. Deal, and P. B. Griffin, *Silicon VLSI Technology - Fundamentals, Practice and Modeling. Prentice Hall Electronics and VLSI Series* Upper Saddle River: Prentice-Hall Inc., 2000.

[162] C. M. Wang, X. Pan, M. Rühle, F. L. Riley, and M. Mitomo, "Silicon nitride crystal structure and observations of lattice defects," *Journal of Materials Science*, vol. 31, no. 20, pp. 5281–5298, 1996.

[163] N. H. D. Leeuw, F. M. Higgins, and S. C. Parker, "Modeling the Surface Structure and Stability of α-Quartz," *J. Phys. Chem. B*, vol. 103, no. 1, pp. 1270–1277, 1999.

[164] M. Morita, T. Ohmi, E. Hasegawa, M. Kawakami, and M. Ohwada, "Growth of native oxide on a silicon surface," *Journal of Applied Physics*, vol. 68, p. 1272, 1990.

[165] T. Takahagi, I. Nagai, A. Ishitani, H. Kuroda, and Y. Nagasawa, "The formation of hydrogen passivated silicon single-crystal surfaces using ultraviolet cleaning and HF etching," *Journal of Applied Physics*, vol. 64, no. 7, pp. 3516–3521, 1988.

[166] E. Yablonovitch, D. L. Allara, C. C. Chang, T. Gmitter, and T. B. Bright, "Unusually Low Surface-Recombination Velocity on Silicon and Germanium Surfaces," *Physical Review Letters*, vol. 57, no. 2, p. 249, 1986.

[167] L. Huang, Q. Zhu, M. Gao, F. Qin, and D. Wang, "Cleaning of SiC surfaces by low temperature ECR microwave hydrogen plasma," *Applied Surface Science*, vol. 257, no. 23, pp. 10172–10176, 2011.

[168] E. Langereis, S. B. Heil, H. C. Knoops, W. Keuning, M. C. Van De Sanden, and W. M. Kessels, "In situ spectroscopic ellipsometry as a versatile tool for studying atomic layer deposition," *Journal of Physics D: Applied Physics*, vol. 42, no. 7, 2009.

[169] L. Huang, B. Han, B. Han, A. Derecskei-kovacs, M. Xiao, X. Lei, M. L. O. Neill, R. M. Pearlstein, H. Chandra, and H. Cheng, "First-Principles Study of a Full Cycle of Atomic Layer Deposition of SiO_2 Thin Films with Di(sec -butylamino) silane and Ozone," *J. Phys. Chem. C*, vol. 117, pp. 19454–19463, 2013.

[170] l. J. Jr., Little and M. M. Jones, "A complete table of electronegativities," *J. Chem. Educ.*, vol. 37, no. 5, p. 231, 1960.

[171] P. G. Neudeck, *The VLSI Handbook*. Florida: CRC Press, 2 ed., 2007.

[172] T. Rana, M. V. S. Chandrashekhar, and T. S. Sudarshan, "Elimination of Silicon Gas Phase Nucleation Using Tetrafluorosilane (SiF_4) Precursor

for High Quality Thick Silicon Carbide (SiC) Homoepitaxy," *Phys. Status Solidi A*, vol. 209, pp. 2455–2462, dec 2012.

[173] C. Hallin, I. Ivanov, T. Egilsson, A. Henry, O. Kordina, and E. Janzén, "The Material Quality of CVD-grown SiC Using Different Carbon Precursors," *J. Cryst. Growth*, vol. 183, no. 1-2, pp. 163–174, 1998.

[174] I. Chowdhury, M. Chandrashekhar, P. B. Klein, J. D. Caldwell, and T. Sudarshan, "High Growth Rate 4H-SiC Epitaxial Growth Using Dichlorosilane in a Hot-wall CVD Reactor," *J. Cryst. Growth*, vol. 316, pp. 60–66, feb 2011.

[175] H. Matsunami, S. Nishino, M. Odaka, and T. Tanaka, "Epitaxial Growth of α-SiC Layers by Chemical Vapor Deposition Technique," *J. Cryst. Growth*, vol. 31, pp. 72–75, dec 1975.

[176] Y. Furumura, M. Doki, F. Mieno, T. Eshita, T. Suzuki, and M. Maeda, "Heteroepitaxial β-3-SIC on Si," *J. Electrochem. Soc.*, vol. 135, no. 5, pp. 1255–1260, 1987.

[177] M. F. MacMillan, M. J. Loboda, G. Chung, E. Carlson, and J. Wan, "Homoepitaxial Growth of 4H-SiC Using a Chlorosilane Silicon Precursor," *Mater. Sci. Forum*, vol. 527-529, pp. 175–178, 2006.

[178] S. Leone, M. Mauceri, G. Pistone, G. Abbondanza, F. Portuese, G. Abagnale, G. L. Valente, D. Crippa, M. Barbera, R. Reitano, G. Foti, and F. La Via, "SiC-4H Epitaxial Layer Growth using Trichlorosilane (TCS) as Silicon Precursor," *Mater. Sci. Forum*, vol. 527-259, pp. 179–182, 2006.

[179] H. S. Kong, Y. C. Wang, J. T. Glass, and R. F. Davis, "The Effect of off-axis Si (100) Substrates on the Defect Structure and Electrical Properties of β-SiC Thin Films," *J. Mater. Res.*, vol. 3, no. 100, pp. 521–530, 1988.

[180] A. Henry, J. ul Hassan, J. P. Bergman, C. Hallin, and E. Janzén, "Thick Silicon Carbide Homoepitaxial Layers Grown by CVD Techniques," *Chem. Vapor Depos.*, vol. 12, pp. 475–482, sep 2006.

[181] S. Leone, *Advances in SiC growth using chloride-based CVD*. PhD thesis, Linkoping University, 2010.

[182] H. Pedersen, S. Leone, A. Henry, F. Beyer, V. Darakchieva, and E. Janzén, "Very high growth rate of 4H-SiC epilayers using the chlorinated precur-

sor methyltrichlorosilane (MTS)," *J. Cryst. Growth*, vol. 307, pp. 334–340, sep 2007.

[183] S. Kotamraju, B. Krishnan, and Y. Koshka, "Use of chlorinated carbon and silicon precursors for epitaxial growth of 4H-SiC at very high growth rates," *Phys. Status Solidi - R*, vol. 157, p. 3, 2009.

[184] H. Pedersen, S. Leone, O. Kordina, A. Henry, S. Nishizawa, Y. Koshka, and E. Janzén, "Chloride-based CVD growth of silicon carbide for electronic applications," *Chemical reviews*, vol. 112, pp. 2434–53, apr 2012.

[185] C. S. Roper, C. Carraro, R. T. Howe, and R. Maboudian, "Silicon Carbide Thin Films using 1,3-Disilabutane Single Precursor for MEMS Applications – A Review Christopher S. Roper," *Elec.Soc.S.Trans.*, vol. 3, no. 10, pp. 267–280, 2006.

[186] C. W. Liu and J. C. Sturm, "Low temperature chemical vapor deposition growth of β-SiC on (100) Si using methylsilane and device characteristics," *J. Appl. Phys.*, vol. 82, no. 9, p. 4558, 1997.

[187] D.-C. Lim, H.-G. Jee, J. Kim, J.-S. Moon, S.-B. Lee, S. Choi, and J.-H. Boo, "Deposition of epitaxial silicon carbide films using high vacuum MOCVD method for MEMS applications," *Thin Solid Films*, vol. 459, pp. 7–12, jul 2004.

[188] B.-T. Lee, D.-K. Kim, C.-K. Moon, and J. K. Kim, "Microstructural investigation of low temperature chemical vapor deposited 3C-SiC/Si thin films using single-source precursors," *J. Mater. Res.*, vol. 14, no. 1, p. 24, 1999.

[189] A. J. Steckl, C. Yuan, J. P. Li, and M. J. Loboda, "Growth of crystalline 3C-SiC on Si at reduced temperatures by chemical vapor deposition from silacyclobutane," *Applied Physics Letters*, vol. 63, no. 24, p. 3347, 1993.

[190] R. Ahlrichs, M. Bär, M. Häser, H. Horn, and C. Kölmel, "Electronic Structure Calculations on Workstation Computers: The Program System Turbomole," *Chem. Phys. Lett.*, vol. 162, pp. 165–169, oct 1989.

[191] J. Perdew, K. Burke, and M. Ernzerhof, "Generalized Gradient Approximation Made Simple," *Physical review letters*, vol. 77, pp. 3865–3868, oct 1996.

[192] R. Ahlrichs and F. Weigend, "Balanced Basis Sets of Split Valence, Triple Zeta Valence and Quadruple Zeta Valence Quality for H to Rn: Design an Assessment of Accuracy," *Phys. Chem.*, vol. 7, p. 3297, 2005.

[193] K. Eichkorn, O. Treutler, H. Öhm, M. Häser, and R. Ahlrichs, "Auxiliary Basis Sets to Approximate Coulomb Potentials," *Chem. Phys. Lett.*, vol. 240, pp. 283–290, jun 1995.

[194] M. Sierka, A. Hogekamp, and R. Ahlrichs, "Fast Evaluation of the Coulomb Potential for Electron Densities using Multipole Accelerated Resolution of Identity Approximation," *The Journal of Chemical Physics*, vol. 118, no. 20, p. 9136, 2003.

[195] W. V. Muench and I. Pfaffeneder, "Epitaxial deposition of silicon carbide from silicon tetrachloride and hexane," *Thin Solid Films*, vol. 31, pp. 39–51, 1976.

[196] G. Dhanaraj, M. Dudley, Y. Chen, B. Ragothamachar, B. Wu, and H. Zhang, "Epitaxial growth and characterization of silicon carbide films," *J. Cryst. Growth*, vol. 287, pp. 344–348, jan 2006.

[197] D. Thompson, "patent WO2012039833A2," 2012.

[198] H. Pedersen, S. Leone, A. Henry, A. Lundskog, and E. Janzén, "Growth characteristics of chloride-based SiC epitaxial growth," *Phys. Status Solidi - R*, vol. 2, pp. 278–280, dec 2008.

[199] T. Rana, H. Z. Song, M. Chandrashekhar, and T. S. Sudarshan, "Comparison of 4H Silicon Carbide Epitaxial Growths at Various Growth Pressures Using Dicholorosilane and Silane Gases," *Mater. Sci. Forum*, vol. 717-720, pp. 117–120, may 2012.

[200] S. F. Cogan, D. J. Edell, A. A. Guzelian, Y. Ping Liu, and R. Edell, "Plasma-Enhanced Chemical Vapor Deposited Silicon Carbide as an Implantable Dielectric Coating," *J. Biomed. Mater. Res., Part A*, vol. 67, no. 3, pp. 856–867, 2003.

[201] T. Rajagopalan, X. Wang, B. Lahlouh, C. Ramkumar, P. Dutta, and S. Gangopadhyay, "Low Temperature Deposition of Nanocrystalline Silicon Carbide Films by Plasma Enhanced Chemical Vapor Deposition and Their Structural and Optical Characterization," *J. Appl. Phys.*, vol. 94, no. 8, pp. 5252–5260, 2003.

[202] C.-K. Jung, D.-C. Lim, H.-G. Jee, M.-G. Park, S.-J. Ku, K.-S. Yu, B. Hong, S.-B. Lee, and J.-H. Boo, "Hydrogenated Amorphous and Crystalline SiC Thin Films Grown by RF-PECVD and Thermal MOCVD; Comparative Study of Structural and Optical Properties," *Surf. Coat. Technol.*, vol. 171, no. 1-3, pp. 46–50, 2003.

[203] S. Bau, S. Janz, T. Kieliba, C. Schetter, S. Reber, and F. Lutz, "Application of PECVD-SiC as Intermediate Layer in Crystalline Silicon Thin-Film Solar Cells," in *3rd World Conference on Photovoltaic Energy Conversion*, pp. 1178–1181, 2003.

[204] R. Robertson and A. Gallagher, "Mono and Disilicon Radicals in Silane and Silaneargon dc Discharges," *J. Appl. Phys.*, vol. 59, no. 10, pp. 3402–3411, 1986.

[205] J. M. Jasinski and S. M. Gates, "Silicon Chemical Vapor Deposition One Step at the Time: Fundamental Studies of Silicon Hydride Chemistry," *Acc. Chem. Res.*, vol. 24, pp. 9–15, 1991.

[206] T. Kuwahara, H. Ito, K. Kawaguchi, Y. Higuchi, N. Ozawa, and M. Kubo, "Different Crystal Growth Mechanisms of Si (001) - (2x1):H during Plasma-Enhanced Chemical Vapor Deposition of SiH_3 and SiH_2 Radicals : Tight-Binding Quantum Chemical Molecular Dynamics Simulations," *J. Phys. Chem. C*, vol. 117, no. 001, p. 15602, 2013.

[207] T. Kuwahara, H. Ito, K. Kawaguchi, Y. Higuchi, N. Ozawa, and M. Kubo, "The Reason Why Thin-Film Silicon Grows Layer by Layer in Plasma-Enhanced Chemical Vapor Deposition," *Scientific reports*, vol. 5, p. 9052, 2015.

[208] S. Cereda, M. Ceriotti, F. Montalenti, M. Bernasconi, and L. Miglio, "Quantitative Estimate of H Abstraction by Thermal SiH_3 on Hydrogenated Si(001)(2x1)," *Phys. Rev. B*, vol. 75, p. 235311, 2007.

[209] E. Kalered, H. Pedersen, E. Janzén, and L. Ojamäe, "Adsorption and Surface Diffusion of Silicon Growth Species in Silicon Carbide Chemical Vapour Deposition Processes Studied by Quantum-Chemical Computations," *Theoretical Chemistry Accounts*, vol. 132, p. 1403, oct 2013.

[210] H. H. and R. Ahlrichs, M. Bär, M. Häser and C. Kölmel, "Electronic Structure Calculations on Workstation Computers: The Program System TURBOMOLE," *Chem. Phys. Lett.*, vol. 162, p. 165, 1989.

[211] A. Kasden, E. Herbst, and W. C. J. Lineberger, "Laser Photoelectron Spectrometry of the Negative Ions of Silicon and its Hydrides," *Chem. Phys.*, vol. 62, p. 541, 1975.

[212] D. Lespiaux and F. Langlais, "Chemisorption on β-SiC and Amorphous SiO2 During CVD of Silicon-Carbide from the Si-C-H-Cl System - Correlations with the Nucleation Process," *Thin Solid Films*, vol. 265, no. 1-2, pp. 40–51, 1995.

[213] J. Olander and K. Larsson, "Influence of Adsorbed Species on the Reconstruction of 4H-SiC(0001) Surfaces," *J. Phys. Chem. B*, vol. 105, pp. 7619–7623, 2001.

[214] P. Sukkaew, Ö. Danielsson, O. Kordina, E. Janzén, and L. Ojamäe, "Ab Initio Study of Growth Mechanism of 4H-SiC: Adsorption and Surface Reaction of C_2H_2, C_2H_4, CH_4, and CH_3," *J. Phys. Chem. C*, vol. 121, no. 2, pp. 1249–1256, 2017.

[215] R. L. Cicero, C. E. D. Chidsey, G. P. Lopinski, D. D. M. Wayner, and R. A. Wolkow, "Olefin additions on H-Si(111): Evidence for a surface chain reaction initiated at isolated dangling bonds," *Langmuir*, vol. 18, no. 2, pp. 305–307, 2002.

[216] J. Olander and K. Larsson, "An Ab Initio Study of 4H-SiC(0001) and (0001) Surface Processes at Experimental Temperatures," *Thin Solid Films*, vol. 458, pp. 191–196, jun 2004.

[217] H. Ito, T. Kuwahara, K. Kawaguchi, Y. Higuchi, N. Ozawa, and M. Kubo, "Tight-binding Quantum Chemical Molecular Dynamics Simulations for the Elucidation of Chemical Reaction Dynamics in SiC etching with SF_6/O_2 Plasma," *Phys. Chem. Chem. Phys.*, vol. 18, pp. 7808–7819, 2016.

[218] B. A. Sawrey, H. E. O'Neal, M. A. Ring, and D. Coffey, "The Gas-Phase Decomposition of Methylsilane. Part I. Mechanism of Decomposition under Shock-Tube Conditions," *J. Chem. Kinet.*, vol. 16, p. 31, 1984.

[219] I. M. T. Davidson and R. J. Scampton, "Quantitative Aspects of Some Unimolecular Isomerization Reactions of Organosilicon Intermediates," *J. Organomet. Chem.*, vol. 271, p. 249, 1984.

[220] J. M. Jasinski, R. Becerra, and R. Walsh, "Direct Kinetic Studies of Silicon Hydride Radicals in the Gas Phase," *Chemical Reviews*, vol. 95, no. 5, pp. 1203–1228, 1995.

[221] Y.-R. Luo, *Comprehensive Handbook of Chemical Bond Energies*. CRC Press, 2007.

[222] C. A. Murray and S. D. Elliott, "Density functional theory predictions of the composition of atomic layer deposition-grown ternary oxides," *ACS applied materials & interfaces*, vol. 5, pp. 3704–15, may 2013.

[223] A. Sharma, V. Longo, M. A. Verheijen, A. A. Bol, and W. M. M. E. Kessels, "Atomic layer deposition of HfO_2 using $HfCp(NMe_2)_3$ and O_2 plasma," *Journal of Vacuum Science & Technology A: Vacuum, Surfaces, and Films*, vol. 35, no. 1, p. 01B130, 2017.

[224] S. Consiglio, R. D. Clark, G. Nakamura, C. S. Wajda, and G. J. Leusink, "Evaluation of high thermal stability cyclopentadienyl Hf precursors with H2O as a co-reactant for advanced gate logic applications," *Journal of Vacuum Science & Technology A: Vacuum, Surfaces, and Films*, vol. 30, no. 1, p. 01A119, 2012.

[225] R. Hussin, K. L. Choy, and X. H. Hou, "Growth of TiO2 Thin Films by Atomic Layer Deposition (ALD)," *Advanced Materials Research*, vol. 1133, pp. 352–356, 2016.

[226] S. McDonnell, R. C. Longo, O. Seitz, J. B. Ballard, G. Mordi, D. Dick, J. H. G. Owen, J. N. Randall, J. Kim, Y. J. Chabal, K. Cho, and R. M. Wallace, "Controlling the Atomic Layer Deposition of Titanium Dioxide on Silicon: Dependence on Surface Termination," *J. Phys. Chem. C*, vol. 117, no. 39, p. 20250, 2013.

[227] T. P. Holme and F. B. Prinz, "Atomic Layer Deposition and Chemical Vapor Deposition Precursor Selection Method Application to Strontium and Barium Precursors," *The Journal of Physical Chemistry A*, vol. 111, no. 33, pp. 8147–8151, 2007.

[228] I. Kazadojev, D. J. Otway, and S. D. Elliott, "Modeling of Precursors for Atomic Layer Deposition of Magnesium and Calcium Oxide," *Chem. Vapor Depos.*, vol. 19, pp. 117–124, jun 2013.

[229] S. D. Elliott, "Improving ALD growth rate via ligand basicity: Quantum chemical calculations on lanthanum precursors," *Surface and Coatings Technology*, vol. 201, no. 22-23 SPEC. ISS., pp. 9076–9081, 2007.

[230] C. Elschenbroich, *Organometallics*. Weinheim: WILEY-VCH Verlag, 2006.

[231] K. Woo-Hee, P. Sang-Joon, K. DoYoung, and K. Hyungjun, "Atomic Layer Deposition of Ruthenium and Ruthenium-oxide ThinFilms by Using a $Ru(EtCp)_2$ Precursor and Oxygen Gas," *Journal of the Korean Physical Society*, vol. 55, no. 1, p. 32, 2009.

[232] S. S. Yim, D. J. Lee, K. S. Kim, S. H. Kim, T. S. Yoon, and K. B. Kim, "Nucleation kinetics of Ru on silicon oxide and silicon nitride surfaces deposited by atomic layer deposition," *Journal of Applied Physics*, vol. 103, no. 11, 2008.

[233] J. H. Kim, D. S. Kil, S. J. Yeom, J. S. Roh, N. J. Kwak, and J. W. Kim, "Modified atomic layer deposition of RuO_2 thin films for capacitor electrodes," *Applied Physics Letters*, vol. 91, no. 5, pp. 2005–2008, 2007.

[234] D. Z. Austin, M. A. Jenkins, D. Allman, S. Hose, D. Price, C. L. Dezelah, and J. F. Conley, "Atomic Layer Deposition of Ruthenium and Ruthenium Oxide Using a Zero-Oxidation State Precursor," *Chemistry of Materials*, vol. 29, no. 3, pp. 1107–1115, 2017.

[235] T. Aaltonen, A. Rahtu, M. Ritala, and M. Leskelä, "Reaction Mechanism Studies on Atomic Layer Deposition of Ruthenium and Platinum," *Electrochemical and Solid-State Letters*, vol. 6, no. 9, p. C130, 2003.

[236] S. J. Park, W. H. Kim, W. J. Maeng, Y. S. Yang, C. G. Park, H. Kim, K. N. Lee, S. W. Jung, and W. K. Seong, "Effect oxygen exposure on the quality of atomic layer deposition of ruthenium from bis(cyclopentadienyl)ruthenium and oxygen," *Thin Solid Films*, vol. 516, no. 21, pp. 7345–7349, 2008.

[237] M. E. Donders, M. C. M. Van, W. M. M. Kessels, H. C. M. Knoops, and P. H. L. Notten, "Remote Plasma Atomic Layer Deposition of Co_3O_4 Thin Films," *Journal of The Electrochemical Society*, vol. 158, no. 4, p. G92, 2011.

[238] S.-H. Kim, D. Kim, J. Yoon, H. Kim, H.-B.-R. Lee, and T. Cheon, "Atomic Layer Deposition of Co Using N_2/H_2 Plasma as a Reactant," *Journal of The Electrochemical Society*, vol. 158, no. 11, p. H1179, 2011.

[239] M. F. Vos, G. Van Straaten, W. M. Kessels, and A. J. Mackus, "Atomic Layer Deposition of Cobalt Using H_2-, N_2-, and NH_3-Based Plasmas: On the Role of the Co-reactant," *Journal of Physical Chemistry C*, vol. 122, no. 39, pp. 22519–22529, 2018.

[240] H.-B.-R. Lee and H. Kim, "High-Quality Cobalt Thin Films by Plasma-Enhanced Atomic Layer Deposition," *Electrochemical and Solid-State Letters*, vol. 9, no. 11, p. G323, 2006.

[241] H. A. Skinner and J. A. Connor, "Metal—ligand bond-energies in organometallic compounds," *Pure & Appl. Chem*, vol. 57, no. 1, pp. 79–88, 1985.

[242] J. A. Simões and J. L. Beauchamp, "Transition Metal–Hydrogen and Metal–Carbon Bond Strengths: The Keys to Catalysis," *Chemical Reviews*, vol. 90, no. 4, pp. 629–688, 1990.

[243] R. R. Reddy, Y. N. Ahammed, K. R. Gopal, P. A. Azeem, and S. Anjaneyulu, "Rkrv potential energy curves, dissociation energies, γ-centroids and franck-condon factors of YO, CrO, BN, ScO, SiO and AlO molecules," *Astrophysics and Space Science*, vol. 262, pp. 223–240, 1999.

[244] E. G. Lee, J. Y. Seto, T. Hirao, P. F. Bernath, and R. J. L. Roy, "FTIR Emission Spectra , Molecular Constants , and Potential Curve of Ground State GeO," *Journal of Molecular Spectroscopy*, vol. 194, pp. 197–202, 1999.

[245] C. Naulin, I. M. Hedgecock, and M. Costes, "The dissociation energy of TiO determined from a crossed-beam study of the Ti + NO > TiO + N reaction," *Chem. Phys. Lett.*, vol. 266, no. February, pp. 335–341, 1997.

[246] V. Blagojevic, G. K. Koyanagi, V. V. Lavrov, G. Orlova, and D. K. Bohme, "Ion – molecule reactions of W^+ and WO^+ : new and improved values for IE (WO), D_{298} (W^+–O), D_{298}(W-O) $\Delta_f H^0{}_{298}$WO," *Chem. Phys. Lett.*, vol. 389, pp. 303–308, 2004.

[247] F. Liu, F.-X. Li, and P. B. Armentrout, "Guided ion-beam studies of the reactions $Co^+{}_n$(n=2-20) of with O_2 : Cobalt cluster-oxide and -dioxide bond energies," *J. Chem. Phys.*, vol. 064304, no. May, 2005.

[248] M. T. Rodgers, B. Walker, and P. B. Armentrout, "Reactions of Cu^+(^{1}S and ^{3}D) with O_2 , CO, CO_2, N_2, NO, N_2O, and NO_2 studied by guided ion beam mass spectrometry," vol. 183, no. 2, pp. 99–120, 1999.

[249] R. R. Reddy, Y. N. Ahammed, B. S. Devi, K. R. Gopal, P. A. Azeem, and T. V. R. Rao, "Spectroscopic studies on astrophysically interesting TaO, TaS, ZrS and SiO^+ molecules," *Astrophysics and Space Science*, vol. 281, pp. 729–741, 2002.

[250] J. Aarik, A. Aidla, T. Uustare, M. Ritala, and M. Leskela, "Titanium isopropoxide as a precursor for atomic layer deposition: characterization of titanium dioxide growth process," *Applied Surface Science*, vol. 161, pp. 385–395, 2000.

[251] G.N. Fomengia, M.Nolan, S.D. Elliott, "First principles mechanistic study of self-limiting oxidative adsorption of remote oxygen plasma during the atomic layer deposition of alumina," *Physical Chemistry Chemical Physics*, vol. 20, pp. 22783-22795, 2018.

[252] M. Shirazi, S.D. Elliott, "Atomistic kinetic Monte Carlo study of atomic layer deposition derived from density functional theory," *Journal of computational chemistry*, vol. 35, pp. 244–59, 2014.